Paulina Zielińska

Heat resistance of SiC/SiC ceramic composites

DOCTORAL THESIS

(prepared as part of the 4th edition of the 'Industrial Doctorate' programme)

Supervisor: DSc Maciej Motyka

Assistant supervisor: PhD Waldemar Ziaja

Rzeszow 2025

This work was carried out as part of a scientific collaboration with MTU Aero Engines Polska Sp. z o.o.

Academic supervisor from MTU Aero Engines Polska Sp. z o.o.:
Dr Aleksandra Kloc

Acknowledgements

I would like to express my sincere gratitude to Dr Benedikt Albert for his invaluable help, support, and guidance throughout the preparation of my doctoral thesis. My special thanks go to Dr Aleksandra Kloc, whose encouragement and assistance inspired me to undertake this challenge and supported me at every stage of my doctoral journey.

I am deeply grateful to all my colleagues and friends, especially those from the Data Analysis and Material Damage Department and the Material Analytics team, for their inspiring collaboration, valuable assistance, and constant support.

I also wish to thank my colleagues from the Department of Materials Science at the Rzeszów University of Technology for their advice and encouragement.

Finally, I would like to thank my husband, Bartosz, for his unwavering support, patience, and belief in me throughout the entire doctoral process.

Table of Contents

1 Introduction

The success of modern aircraft engines largely depends on increasing their efficiency while simultaneously reducing fuel consumption. In addition to the expected economic benefits, a significant reduction in the emission of CO_2 and NOx oxides harmful to the atmosphere, as well as a decrease in the noise generated by aircraft, is also expected. Increasing the efficiency of aircraft engines is associated with increasing the temperature at which they operate. The gas temperature in the turbine can reach temperature above 2100 °C, but the turbine blades are most often made of nickel-based superalloys, which have a limited operating temperature range of 1100 °C. In addition, continuous forced cooling with air and coatings are required to prevent them from overheating. As a consequence, the temperature in the combustion chamber is lowered and it is not possible to increase fuel combustion efficiency. Increasing the operating temperature of aircraft engine components therefore requires the development of new, innovative materials such as composites.

Ceramic matrix composites (CMCs) reinforced with continuous ceramic fibers are considered promising structural materials for high-temperature applications. Suitable selection of the matrix material and reinforcing phase, as well as the development of innovative microstructure, has significantly increased the resistance to catastrophic cracking of CMC composites compared to monolithic ceramics. These composites have high strength properties at high temperature - compared to currently used superalloys, they have much greater durability at high temperature and lower density (usually <3 g/cm^3). Among the low-density materials for long-term operation at extremely high temperature, ceramic composites with a silicon carbide (SiC/SiC) matrix reinforced with continuous, polycrystalline SiC fibers with a small diameter (~10-15 μm) seem to be a potential candidate for application in the aviation industry. The maximum operating temperature of SiC/SiC composites already introduced into the production of structural components for military and commercial aircraft engines is currently 1250 °C. It is assumed that in the near future it may increase to 1600 °C.

2 Motivation

CMCs are a relatively new group of engineering materials, and there is little data available in publicly accessible literature regarding their behavior at high temperature. Therefore, there is a justified need for conducting such research to develop their thermo-mechanical characteristics, which are necessary for their application in aircraft engines. A comprehensive description of the material's microstructure after tests simulating operating conditions will allow for the identification of critical flaws in the material that need to be detected in finished parts before their implementation in the turbine. Additionally, the conducted research will allow for the development of a methodology for detecting critical features using 2D microstructure analysis.

The research part of this dissertation will be preceded by an in-depth literature study, which will verify the current state of knowledge in the area of mechanical properties of SiC/SiC CMC, especially at high temperature. Particular emphasis will be placed on publications describing the microstructure of the material and its influence on mechanical properties. The research will be carried out on a SiC/SiC ceramic composite that is produced in accordance to aerospace standards (AS9100). The research subject will be a potential material that has a high chance of being adapted by MTU Polska for the production of turbine components. The first stage of the research will involve a thorough characterization of the selected material, including qualitative and quantitative description of its microstructure. The result of this stage will be the creation of a catalog of microstructure components characteristic for the tested SiC/SiC material and the selection of their critical features that determine the behavior of the material at elevated temperature. An attempt will be made to develop a repeatable method for describing porosity and cracks in the material, as well as automating this process using advanced computer image analysis methods. In the next part of the research, a series of creep tests will be conducted at high temperature. The tests will be performed for at least two temperature values. Samples after mechanical properties tests will be subjected to detailed analysis, including characterization of fracture surfaces. Ceramographic analysis also will be conducted to determine the effect of temperature and load on the microstructure of the tested composite. It is assumed that quantitative analysis of the microstructure will allow for a systematic cataloging of the consequences of damage and degradation of the material. The obtained results will be compared with the

characteristics of the material in its initial state. Additionally, heat treatment tests will be performed at the same temperature and time as the mechanical properties tests, and the microstructure will be characterized. This will allow for the identification of microstructure changes that occur at high temperature and simultaneous mechanical loading.

The scientific objective of the implementation doctoral thesis is to describe the microstructural behavior of the SiC/SiC composite under the influence of synergistically acting factors in operating conditions, such as temperature and load. This will allow the identification and characterization of critical features of the material's microstructure that should be considered in the quality assessment procedures for this type of composites. The uniqueness of the composite chosen for the research makes it innovative on a global scale. The obtained results will facilitate a full understanding of the behavior of SiC/SiC composites at elevated temperature and significantly accelerate their application in the design of aircraft turbines.

3 Literature review

3.1 CMC - historical overview, types (Ox/Ox, SiC/SiC), general properties

The term “Ceramic” can be adjusted to a large range of materials. Ceramics materials are typically non-metallic and inorganic in nature [1]. They exhibit high hardness, high compressive strength and high heat resistance. They are the only class of materials that can be used in the temperature above 1100 °C. On the other side, ceramics tend to be brittle, with low damage tolerance and low fracture toughness. What is more, ceramics do not show signs of plastic deformation and fail in a catastrophic way, which makes the application of monolithic ceramics in the load bearing structures almost impossible [2].

A composite material is *“a system consisting of two or more phases on a macroscopic scale, whose mechanical performance and properties are designed to be superior to those of the constituent materials acting independently”* [3]. In ceramic matrix composites are two phases in the material system: a continuous matrix phase and a discontinuous reinforcement phase (Figure 1). This combination allows obtaining a material that has low density, high strength at elevated temperature (~1250 °C, depending on the actual matrix and fiber type) and has a high fracture toughness.

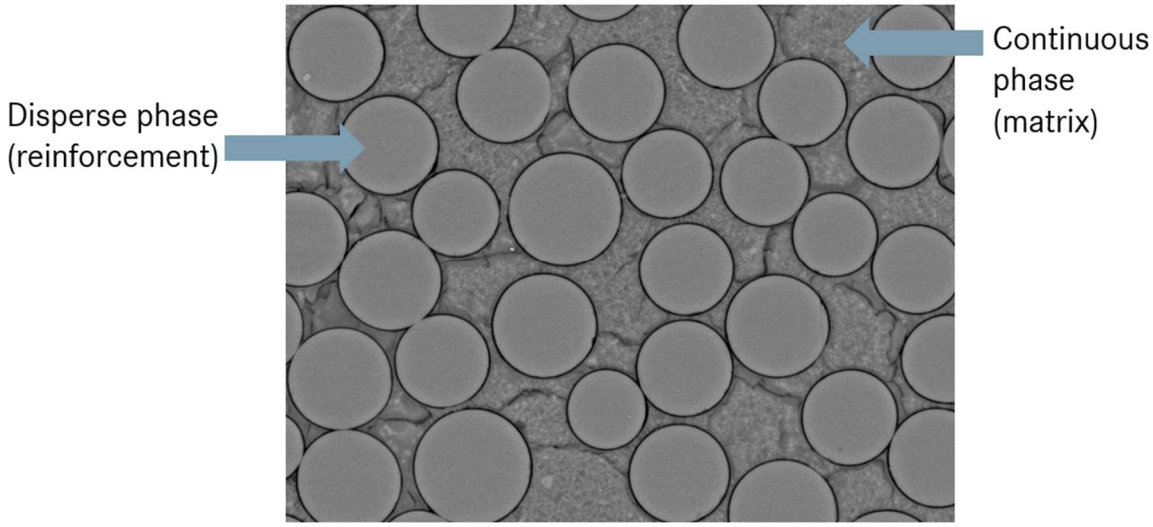

Figure 1 Phases of typical composite

There are many different types of ceramic matrix composites. Classification generally can be done based on fiber and matrix materials. Non-oxide fibers are usually made out of silicon carbide or carbon. Oxide fibers are mainly made out of silica and alumina oxides. Non-oxide matrices are usually made of carbon, silicon carbide and mixtures of silicon and silicon carbide.

Oxide matrices are mostly zirconia, alumina and mixtures of alumina and silicates. Usually, non-oxide fibers are combined with non-oxide matrices and oxide fibers with oxide matrices. The most common ceramic matric composites reinforced by fibers types are: C/C, C/SiC, SiC/SiC and Ox/Ox [4].

Ceramic matrix composites are usually porous materials. Ceramic fibers have significantly higher tensile strength and elastic modulus compared to the matrix. The tensile strength of CMC fibers is between 1000 and 7000 MPa and the elastic modulus is between 200 and 900 GPa. Due to that fact, selecting the types of fiber has to be done very carefully. Depending on the fibers quality, fibers material and the atmosphere, fiber degradation can occur usually at the temperature between 1000 and 2100 °C (C-Fibers, depending on the atmosphere can be damaged at much lower temperature ~400 °C). The maximum service temperature of the fibers, affects the maximum service temperature of the whole part made from a CMC material. Fibers can be handled using various textile techniques such as weaving, braiding, stitching, or filament winding [5].

The difference between CMC materials and other composite materials with polymer or metal matrix is that the fibers do not automatically represent the significantly stronger and stiffer phase in the composite material. The reinforcing effect of ceramic fibers aims to achieve a quasi-ductile behavior of the material. This prevents catastrophic brittle fracture, while increasing fracture toughness, thermal shock resistance, and dynamic load capacity. In this regard, the interface between the fiber and the matrix plays a crucial role. Unlike polymer composite materials, where the bond between the fiber and the matrix must be strong to transfer forces from the matrix to the fibers, CMCs generally require a sufficiently weak bond between the fiber and the matrix. This can be achieved by different concepts, either a weak matrix (Ox/Ox) or a weak interphase concept (SiC/SiC). The functioning of the interface, leading to the quasi-ductile behavior of CMC materials, is schematically illustrated in Figure 2 a. By having a sufficiently weak bond between the fiber and the matrix, growing cracks at the interface are redirected. This redirection allows for partial sliding of the fiber within the matrix, dissipating energy and reducing the energy at the crack tip, thereby slowing down crack growth. At the same time, the fibers counteract further crack opening at the crack flanks. As the crack continues to grow, fiber fractures occur, followed by fiber pull-out (Figure 2 b). However, the fiber/matrix bond must not be too weak, as it needs to transfer stresses from the matrix to the fiber under loading. The described mechanism can be achieved through various adjustments of the interface,

as schematically shown in Figure 2 a. For SiC/SiC materials, the strategy of using a suitable fiber coating to adjust the fiber-matrix bond is preferred (Figure 2 b). The coating, often consisting of many very thin individual layers, ensures that the bond is not so strong that a crack propagates completely through the matrix and fiber. In oxide CMC materials, the sufficiently weak bond between the fibers and the matrix is achieved through a porous matrix. By having high proportion of microporosity (15% up to 40%; depending on the manufacturer and material system), a weak matrix is established. However, the matrix still needs to be strong enough to ensure transfer of forces to the fibers and to provide strength across the fiber direction.

a)

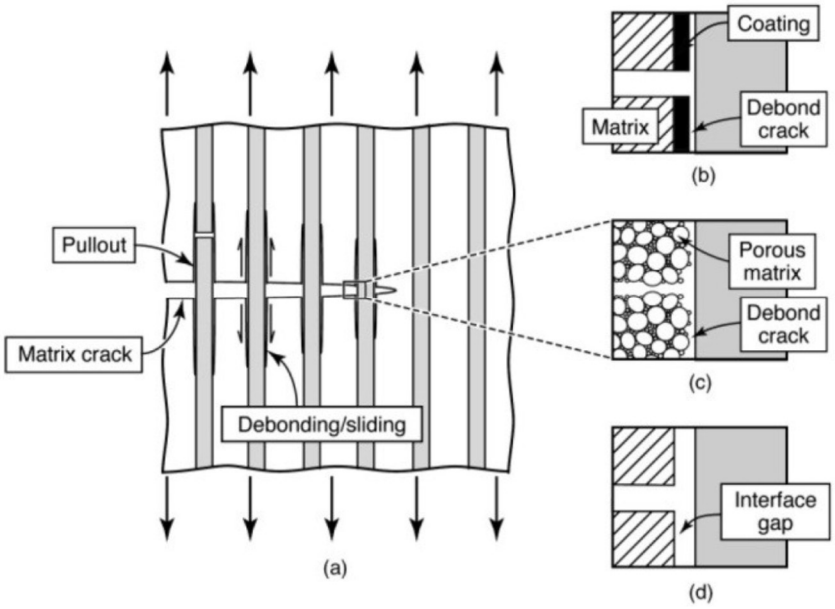

b)

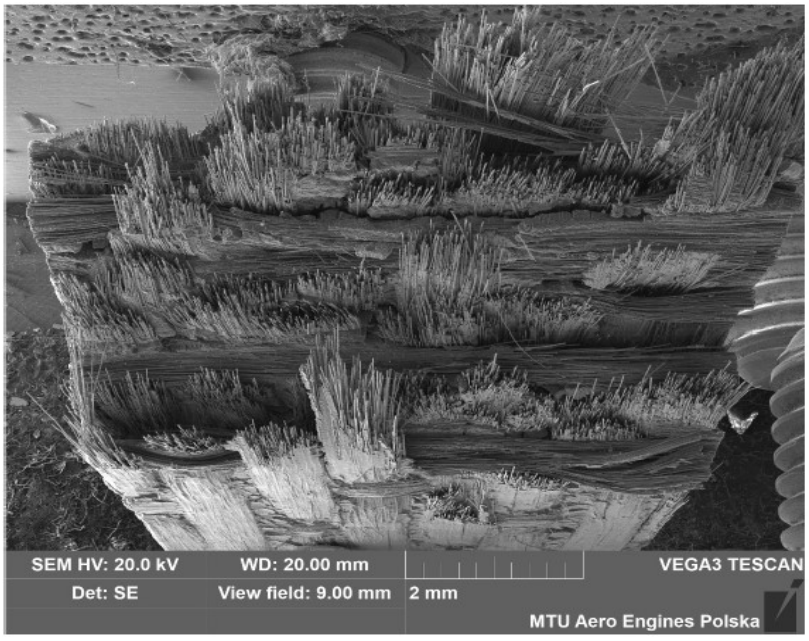

Figure 2 Schematic representation of crack diversion mechanisms in a CMC material (a) [6] and fracture surface of the composite material with fiber pull-out (b)

Table 1 shows the typical properties of different ceramic matrix composites. Compared to the other materials, for example metals used at high temperature applications, ceramic matrix composites have a significantly lower density and much higher operating temperature, which is very important for lightweight constructions working at elevated temperature, like aircraft turbines. What is more, CMCs are wear resistant and can work in aggressive chemicals environment. Production of ceramic matrix composites is very expensive and depends strongly on the composition of the composite and manufacturing routes. To conclude, CMCs, and especially SiC/SiC composites usually are very expensive, but compared to metals they show longer service life and unique performance. Either oxide and non-oxide composites are being developed and introduced into a new field of application and for sure they are the future of new, high tech materials.

Table 1 Material properties of typical ceramic matrix composites (Ox/Ox covers alumina fibers and alumina or alumina-silicate matrix) [5]

Property	Unit	SiC/SiC	C/SiC	C/C	Ox/Ox
Fiber content	Vol.-%	40-60	10-70	40-60	30-50
Porosity	Vol.-%	10-15	1-20	8-23	10-40
Density	g/cm^3	2,3-2,9	1,8-2,8	1,4-1,7	2,1-2,8
Tensile strength	MPa	150-360	80-540	14-1100	70-280
Bending strength	MPa	280-550	80-700	120-1200	80-630
Strain-to-failure	%	0,1-0,7	0,5-1,1	0,1-0,8	0,12-0,4
Young's modulus	GPa	70-270	30-150	10-480	50-210
Fracture toughness	$MPa*m^{1/2}$	25-32	25-30	5,7-3	58-69
Thermal conductivity	W/m *K	6-20	10-130	10-70	1-4
Coefficient of thermal expansion	Ppm/K	2,8-5,2	0-7	0,6-8,4	2-7,5
Maximum service temperature	°C	1100-1600	1350-2100	2000-2100	1000-1100

3.2 SiC fibers

High-performance SiC fibers have very high mechanical properties. Their tensile strength is higher than 2 GPa and stiffness exceeds 400 GPa. What is more, SiC fibers are thermally stable at elevated temperature – up to 1900 °C (Tyrrano SA3). Non-oxide ceramic fibers are perfect as reinforcement for ceramic matrix composites. These lightweight fibers with diameter <20 µm can be weaved and shaped into a complex parts.

Polymer-derived SiC fibers are now commercially available and they are an excellent example of a combination of material science, engineering and polymer chemistry for the development of manufacturing processes on an industrial scale. SiC fibers present a strong correlation between thermal properties, mechanical properties and microstructure conditions. To obtain very high tensile strength, SiC fibers needs to have an ultra-fine microstructure. The creep and thermal properties of SiC fibers are mainly determined by the oxygen content and stoichiometry.

The low oxygen content of SiC fibers results in better creep properties and stability at elevated temperature. In the first generation of commercial SiC fibers, high properties were not realized. Continued development of those fibers resulted in the commercialization of second new generations of ceramic fibers and finally the most advanced third generation of SiC fibers [7].
The first generation ceramic fibers were manufactured by spinning in inert atmosphere, but the curing process was performed before pyrolysis in an air atmosphere. As a consequence, the oxygen was not removed at the pyrolysis steps which resulted in the formation of an amorphous Si-O-C phase. If the temperature of the pyrolysis process is higher than 1200 °C, then the amorphous phase releases the gases and crystallizes, causing degradation of SiC fibers. As a consequence, the non-stoichiometric amorphous composition from the first generation of ceramic fibers did not have enough high thermal and mechanical properties [8,9].
In the second generation of SiC fiber, the oxygen content was reduced by curing the fibers with an electron beam or γ-ray irradiation in inter atmosphere. The oxygen content was almost completely removed which resulted in higher thermal resistance and microstructure with almost no amorphous phase. This allowed the formation of bigger SiC grains during the pyrolysis process. Nevertheless, the free carbon which was in the fibers limited the growth of the ceramic grains and the process needs to be carried at about 1300 °C [9,10,11,12].
The first and second generation of ceramic fibers did not fulfill high temperature requirements for advanced applications. As a result, the third generation of ceramic fibers was made on the basics of highly crystalline ceramic materials, which are unchanged in air up to 1400 °C. To achieve more stoichiometric crystalline SiC fibers and to improve mechanical properties at elevated temperature, manufacturing temperature was raised up to more than 1500 °C [9,11,12] Production details and properties of the fibers are shown in the Table 2.

Table 2 Production details and properties of commercial SiC fibers [12]

	Trade name (manufacturer)	Curing method	Max. Temp.[°C][a]	Production temperature	Density [g/cm³]	Avr. Diameter [µm]/fibers per tow	Tensile strength [GPa]	Elastic modulus [GPa]
First Generation	Nicalon 200N (Nippon-Carbon)	Oxygen		1200 °C	2.55	14/500	3.0	210
	Tyranno Lox-M (UBE Industries)	Oxygen		1200 °C	2.48	11/800	3.3	180
	Tyranno S (UBE Industries)	Oxygen		1200 °C	2.35	11/800 8.5/1600	3.2	170
Second Generation	Hi-Nicalon (Nippon-Carbon)	Electron irradiation	1450	1300 °C	2.74	14/500	2.8	270
	Tyranno ZMI (UBE Industries)	Oxygen		1300 °C	2.48	11/800	3.4	190
Third Generation	Hi-Nicalon S (Nippon-Carbon)	Eletron irradiation	1650	>1500 °C	3.10	12/500	2.6	420
	Tyranno SA-3 (UBE Industries)	Oxygen	1900	>1700 °C	3.10	10/800 7.5/1600	2.8	380
	Sylramic (COI Ceramics)	Oxygen	1850	>1700 °C	3.2	10/800	3.2	~400
	Sylramic iBN (COI Ceramics)	Oxygen	1800	>1700 °C	3.2	10/800	3.2	~400

a- Maximum temperature for loss of > 10% of as produced strength after 10h exposure

Nicalon fibers

The first company which introduced polymer-derived continuous ceramic SiC fibers to the world market was Nippon Carbon Corporation Ltd from Japan. Name Nicalon is the family name of three grades of ceramic fibers - Nicalon, Hi-Nicalon and Hi-Nicalon Type-S (HNS). While the Hi-Nicalon Type S fiber fulfills many practical requirements for fibers, such as its wide availability in commercial quantities, there are still some significant microstructural requirements that it does not fully meet. The production process of the Hi-Nicalon Type S fiber is similar to its precursor, the Hi-Nicalon fiber. Initially, it is created by spinning an organometallic "pre-ceramic" polymer precursor, which is then cross-linked or cured using electron irradiation. Subsequently, the fiber undergoes high-temperature pyrolysis and heat treatment to eliminate excess carbon found in the Hi-Nicalon fiber (C/Si~1.3) and transform it into a nearly stoichiometric (C/Si~1.05) β-phase SiC fiber [13]. Despite the use of irradiation instead of oxidative curing, the Hi-Nicalon Type S fiber still retains residual oxygen content (~0.7 wt %), primarily in the form of a silicon-oxycarbide impurity phase. When subjected to high temperature above approximately 1600 °C, this phase decomposes, releasing SiO and CO gases. This decomposition process leads to the formation of pores within the fiber, ultimately resulting in a reduction in fiber strength [14]. The as-produced HNS (NOX grade) fiber has a surface rich in carbon, which can be adversely affected when exposed to combustion environments [15]. To

address this issue in turbine applications, it is advisable to use HNS (OX grade) fibers where the carbon surface has been removed, either by the fiber manufacturer or the end-user before CMC fabrication. Nevertheless, this removal process can reduce the fiber's strength by approximately 10% due to the exposure of surface flaws. Applying an interfacial coating, such as BN, may mitigate this issue by covering the entire fiber surface and helping to minimize the impact of these flaws. In terms of structural performance at elevated temperature, the as-produced HNS fiber has a thermal limit of approximately 1600 °C for retaining strength. To achieve this, the grain size within the fiber remains below ~20 nm on average [15] and oxide-based impurities persist at the grain boundaries [16]. Recent research conducted by NASA [17] indicates that these two factors are key contributors to undesirable fiber creep and impose a structural temperature limit of less than ~1450 °C for this fiber type. To explore this limitation further, Figure 3 illustrates the creep behavior of polymer-derived SiC fibers tested individually under constant stress (σ) of 270 MPa and a constant temperature of 1400 °C in air. The data reveal that all polycrystalline SiC fibers exhibit a time-dependent transient or primary creep strain (εp), and transition into a near-steady-state secondary creep strain (εs). NASA has determined that the primary mechanism driving secondary-stage creep in these fine-grained SiC fibers is Interface Controlled Diffusional (ICD) creep. In this process, grain-boundary diffusion governs the concentration of vacancies that facilitate fiber creep, with the fine grain size acting as a limiting factor [17]. In this context, the rate of secondary-stage creep strain rate ($\dot{\varepsilon}_s$) can be expressed analytically as:

$$\dot{\varepsilon}_s = \left(\frac{C}{d}\right)\sigma^3 \exp\left[-\frac{Q}{RT}\right] \quad (1)$$

Where the key factors in determining creep behavior are:

- C is the composition-dependent diffusion constant,
- d is the activation energy controlling steady-state creep,
- Q is the activation energy for the diffusion process,
- R=8,314 J/mol*K is the universal gas constant.

According to Equation (1), for a given stress and temperature, increasing the grain size of HNS fibers from 20 nm to 200 nm could potentially reduce the secondary creep strain rate by an order of magnitude. However, heat treatments exceeding approximately 1600 °C, while beneficial for increasing grain size and enhancing creep resistance, lead to the decomposition of the silicon-oxycarbide phase in the fiber, resulting in a significant reduction in fiber strength [14].

In addition to restricting grain size, the oxide-based phase present in HNS fibers contributes to a significant primary creep stage, which is undesirable for this type of fibers [18].This effect can be conveniently observed in Table 3, which provides a comparison of the parameter *m* obtained from a Bend Stress Relaxation (BSR) test [19) after heat treatment in elevated temperature for 1 hour in argon atmosphere. The table includes (m) values not only for HNS fibers but also for Tyrranno Sa3 and Sylramic-iBN, which contain lower oxygen levels following fabrication. As stress relaxation is directly linked to creep, the primary creep strain ($\dot{\varepsilon}_p$) of a fiber can be reasonably estimated for (m) values greater than 0.5 using the following equation (2).

$$\dot{\varepsilon}_p = \varepsilon_e[\left(\frac{1}{m}\right) - 1] \tag{2}$$

Where is the elastic strain of the fibers ($\varepsilon_e = \frac{\sigma}{E}$). Table 3 reveals that the as-produced HNS fiber exhibits primary creep starting at temperature 1100 °C, where its (m) value drops below one after just 1 hour of exposure. In contrast, this behavior is not observed in the other two fiber types in this temperature. It is assumed that this creep behavior results from grain boundary sliding facilitated by the low-viscosity silicon-oxycarbide phase present within the HNS fiber boundaries [20]. What is more, Equation (2) and Table 3 indicate that after only 1 hour at approximately 1450 °C (m=0.5), the HNS fiber's primary creep strain is nearly equivalent to its elastic strain. This represents a 50% reduction in fiber stiffness or modulus within that short time frame, which could lead to a stress overload on the matrix, potentially causing it to crack. To address the limitations of HNS fibers, achieving SiC/SiC composites with enhanced structural performance and temperature resistance requires the development of SiC fibers with minimal or no low-viscosity phases in their grain boundaries and an average grain size of up to approximately 500 nm. This guideline is equally critical for minimizing creep in the SiC matrix.

Table 3 Average BSR (m) values for single near-stoichiometric SiC based fibers measured after 1 h exposure in argon at various temperatures [20]

Fiber Type	1100°C	1200°C	1300°C	1400°C	1500°C
Tyrrano SA3	—	0.90	0.74	0.45	—
HNS	0.96	0.89	0.83	0.64	0.40
Sylramic-iBN	1.00	0.97	0.91	0.84	0.74

A well-established method for producing SiC fibers with higher temperature capabilities compared to HNS fibers involves thermally treating the fibers to decompose the silicon-oxycarbide phases typically formed during fabrication. This process releases gases, leaving behind a weak SiC fiber with fine pores. These pores can then be eliminated by introducing sintering aids,

either directly into the fiber pre-ceramic polymer [21, 22] or through gaseous infiltration after the decomposition of a SiCO fiber [23, 24]. Subsequent sintering treatment at a temperature of 1800 °C or higher results in high-density, near-stoichiometric SiC fibers with minimal residual oxide phases and average grain sizes exceeding 100 nm. These key microstructural characteristics are not present in HNS fibers. Moreover, this sintering method has the significant advantage of producing strong fibers even at elevated production temperature. This greatly extends the temperature range for the fabrication and use of ceramic matrix composites while avoiding microstructural instabilities in the fiber reinforcement.

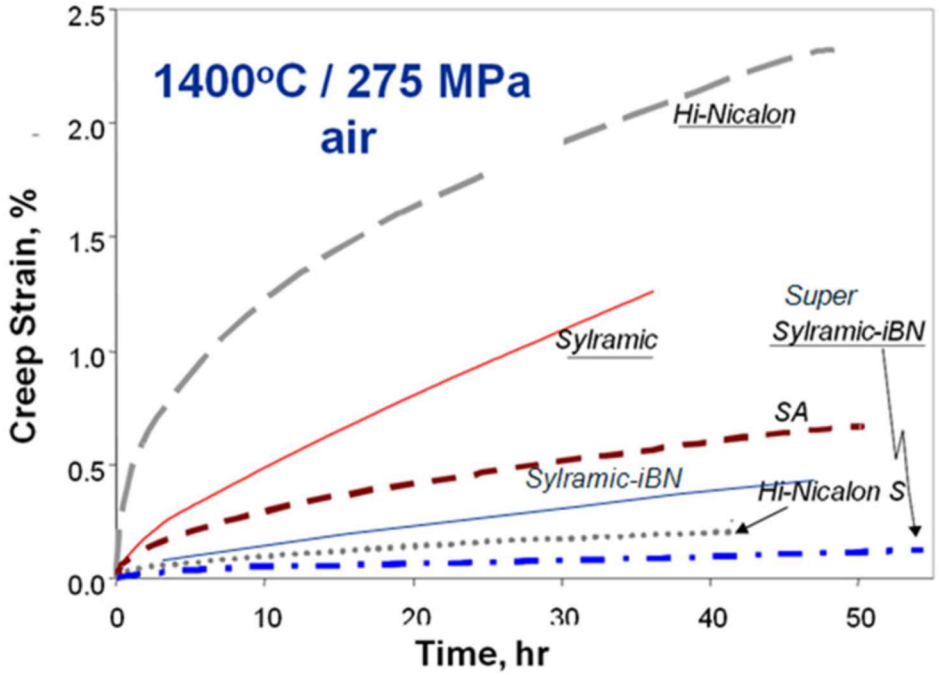

Figure 3 Creep strain behavior of various SiC fiber types in single fiber form [18]

Currently, two commercially available SiC fiber types utilize this sintering process. The first is the "Tyranno SA3" fiber, developed by UBE Industries, where an aluminum-based sintering aid is incorporated into a SiC-forming pre-ceramic polymer [25]. The second is the "Sylramic" fiber, initially produced by Dow Corning and now manufactured by ATK-COI Ceramics in San Diego, California, which uses a boron-based sintering aid introduced into the pores of a decomposed SiCO precursor fiber [24]. Table 2 highlights key properties of these fibers, while Figure 3 compares their tensile creep performance and HNS fibers under identical test conditions (1400 °C, 270 MPa, and laboratory air). Although both Tyranno SA and Sylramic fibers are near-stoichiometric, exceeds excellent strength and thermal conductivity, but their high-temperature tensile creep performance is inferior to that of HNS fibers. This suboptimal

creep resistance is attributed to residual aluminum and boron-based sintering aids in their grain boundaries, which promote grain boundary sliding. To address this issue, NASA developed high-temperature thermal treatments in controlled environments to remove or modify these residual sintering aids. It was observed that while the creep resistance of the fibers improved with grain growth, the tensile strength of the Tyranno SA3 fibers further deteriorated following thermal treatment. Conversely, boron in the Sylramic fiber's sintering aids could be effectively removed in nitrogen or argon atmospheres while retaining high tensile strength (~3 GPa) and significantly enhancing creep resistance [26]. In nitrogen at atmospheric pressure, this treatment led to the formation of a thin, uniform in-situ BN (iBN) coating around each fiber, even those in close contact within woven tows. The resulting fiber is referred to as “Sylramic-iBN” [27]. At higher nitrogen pressures, fibers with even greater creep resistance, known as “Super Sylramic-iBN,” were produced [28].Table 2 and Figure 3 illustrate the improved properties and tensile creep resistance of Sylramic-iBN (iBN fiber) and Super Sylramic-iBN fibers compared to their precursor Sylramic fiber.

Figure 3 reveals an interesting observation: during creep testing at 1400 °C, the iBN fiber shows slightly less resistance to creep than the HNS fiber, while the Super iBN fiber exhibits slightly better creep resistance. According to Equation (1), this outcome is surprising if grain size were the sole factor, as both iBN fibers have an average grain size at least ten times larger than that of the HNS fiber. However, bend stress relaxation (BSR) results in Table 3 indicate that iBN fiber demonstrates significantly better primary-stage creep resistance than HNS fiber.

NASA research explains this apparent contradiction by noting that, after sintering, both Sylramic and Tyranno SA fibers exhibit a no uniform cross-sectional microstructure. This microstructure consists of large grains forming a thin shell at the fiber surface and a core region composed of smaller grains and fine pores [29]. It appears that the shell forms before or during sintering due to the concentration of grain growth aids near the fiber surfaces. At high temperature, more creep-prone core region within the fibers transfers its load to the creep-resistant shell, which constitutes 30% of the total cross-sectional area. Consequently, the stress on the shell can be up to approximately three times greater than that experienced by the HNS fiber, which has a more consistent cross-sectional structure [29]. Based on Equation (1), this leads to the iBN fiber having a tensile steady-state creep rate approximately 33 times higher than HNS fiber with the same grain size. As a result, the potential tensile creep advantage provided by the iBN fiber's larger grain size is effectively nullified by its no uniform cross-

section. Additionally, since the BSR test primarily evaluates the creep-resistant shell region, it is expected that the BSR data for the iBN fiber could show significantly better creep resistance compared to the HNS fiber. The iBN fiber, unlike the Super Sylramic-iBN fiber, has advanced from development stage to commercial production due to its easier manufacturing process, which does not require high-pressure nitrogen. For nearly a decade, the iBN fibers have been commercially available as multifilament tows and have been used in SiC/SiC CMC panels, both as 2D-woven fabric and 3D-woven preforms for CVI-MI and other matrix infiltration methods. This enabled a direct comparison of properties between CMCs reinforced with HNS and iBN fibers. For instance, in creep-rupture tests conducted at 1315 °C in laboratory air [30], the CMC reinforced with HNS fibers exhibited a noticeably higher initial creep strain than the CMC reinforced with iBN fibers when the applied on-axis stress was raised from 103 to 138 MPa.

Each kind of CMC was manufactured using the non-reactive melt infiltration (NRMI) process, incorporating 2D-woven balanced fabric with approximately 18% fiber content aligned in the load-bearing direction. This behavior seems to result from the lower matrix cracking strength of the HNS CMC and/or the more pronounced primary creep phase of the HNS fiber. This subsequent mechanism is supported by the BSR data in Table 2, which indicates that after 1 hour at 1300 °C, the iBN fiber exhibits significantly less creep compared to the HNS fiber. Consequently, during the initial loading of the CMC, the primary creep of the HNS fiber caused the NRMI matrix to surpass its micro-cracking strain limit of approximately 0.05% (CMC modulus ~265GPa) before it could relax the stress and transfer the majority of the load to the fiber. Therefore, the increased creep behavior of the HNS CMC at 138 MPa likely reflects localized matrix cracking, forcing the crack-bridging fibers to bear much higher stress levels than they would in an intact CMC [31]. Conversely, matrix cracking likely did not occur in the iBN CMC, enabling its fibers to creep under lower stress levels and resulting in reduced overall creep for the CMC.

For melt infiltrated (MI) CMC specimens subjected to low stresses without matrix cracking, NASA's analytical creep models, based on the creep behavior of individual HNS and iBN fibers, can reliably predict steady-state creep behavior. These models assume that over time, all fibers bear the full load of the CMC [18]. This assumption holds true not only for CMCs produced via the NMI method but also for those fabricated using HNS fibers through the RMI process [32]. This suggests that in the laboratory air, the rupture life of these ceramic matrix composites can be estimated by analyzing the intrinsic rupture properties of the two fiber types.

Nevertheless, while the rupture characteristics of individual HNS and iBN fibers have been evaluated under varying stress and temperature conditions [12], it is important to recognize that the conditions experienced by fibers within a cracked CMC during high-temperature applications may differ significantly from those in standard creep-rupture tests conducted on single fibers. For instance, the condition of maintaining a constant tensile stress over time and along the fiber's length is unlikely to occur within a CMC. This is due to the curvature of fibers caused by their architecture and the common presence of matrix micro-cracks in CMCs. In these micro-cracks, fiber stresses are highest and then diminish in the intact matrix segments. Additionally, under these CMC conditions, the fiber gauge length is significantly smaller than the 25 or 100 mm typically used in single-fiber creep-rupture tests, and rupture is governed by bundles of fibers rather than individual fibers. Furthermore, if the testing environment influences fiber rupture, results obtained in laboratory air may differ from those in specific composite application environments. To address this, NASA has found it more practical to investigate and empirically model the overall rupture characteristics of different fiber types by studying CMC specimens with specific conditions:

- the reinforcing fibers are aligned with the primary loading direction at a known fiber content,
- the fibers are predominantly straight in the loading direction,
- the matrix contributes little or no load due to being more susceptible to creep than the fibers.

In summary, compared to the HNS fiber, the iBN SiC fiber demonstrates greater thermal stability due to its higher production temperature. This enables the fabrication and operation of SiC/SiC composites at elevated temperature without degradation of the fibers due to tensile strength. The higher production temperature also leads to lower oxygen content, resulting in a reduced primary creep phase, as well as larger grains that significantly enhance thermal conductivity and offer the potential for improved creep performance if the grain size distribution can be made more uniform. Moreover, the in-situ grown BN layer led to superior environmental resistance compared to the non-carbon-rich or carbon-rich surfaces of the HNS fiber and the CVI-produced BN-based interfacial coatings, which often fail to fully cover the fiber surface. Nevertheless, despite these advantages, certain limitations hinder the optimal use of the iBN fiber. For instance, its larger grain size compared to the HNS fiber often creates rougher fiber surfaces. While this can enhance interfacial stress and restrict crack opening, it

may also lead to fiber-fiber abrasion and fiber breakage during weaving or braiding into complex preforms. Furthermore, the larger grains appear to limit the maximum creep strain the fiber can achieve before rupture. Lastly, the higher production temperature of sintered fibers contribute to increased acquisition costs. Currently, the Sylramic precursor fibers used for iBN SiC fibers are manufactured through a combination of batch and continuous processing methods. This production approach restricts their availability in the quantities needed for large-scale, production-ready components.

3.3 Manufacturing methods of SiC/SiC composites

The manufacturing of SiC/SiC composites for engines is done by different densification methods to create a matrix surrounding the fiber/fiber preform. The different techniques are densification via infiltration of either a liquid phase (PIP, Silicon infiltration) or a gaseous phase (CVI).

Chemical Vapor Infiltration (CVI) processing involves the ongoing deposition of SiC to extensively fill the pores within a 3D pre-form coated at the interface (full CVI process). The advantages of this process is that the full CVI technique for matrix infiltration offers the flexibility to produce SiC/SiC components of irregular, large and intricate shapes with nearly exact shape replication. Generally, the high temperature properties are commendable as it enables the production of high purity matrices with precisely controlled microstructures. Despite some trapped porosity (around 10 to 15 vol. %), this method typically yields a SiC matrix material characterized by good thermal conductivity and superior creep resistance in various directions. Furthermore, CVI is conducted at relatively low temperature (below 1000 °C), which minimizing the risk of fiber damage. Moreover, the fiber-matrix interface can be customized by precoating the fiber preform during an initial CVI step using different reagents within the same reactor. On the other hand, one of the significant problems of this process is the deposition times needed for the densification process (typically greater than 100 hours), which significantly increases the cost of the production. In addition, ongoing deposition often results in irregular regions of the matrix containing large and distinct pores forming between the tows. These trapped pores, which have irregular sizes and shapes significantly reduce the mechanical properties of CMC in a various directions. Consequently, achieving completely dense matrices is unattainable through the Full CVI method [12].

Polymer infiltration and pyrolysis (PIP) is a process that involves multiple cycles of infiltration. Each cycle includes filling the remaining porosity of the 3D pre-form with a polymer which transforms into silicon carbide (SiC) as a result of high-temperature pyrolysis. The main

benefit of the Full PIP approach is that this process uses methods which are well established and employed in the production of polymer matrix. Unlike the Full CVI approach, the dimensions of CMC parts are not constrained by the dimensions of the CVI reactor. On the other hand, the main disadvantage of the PIP process is the lengthy processing time and repeated infiltration required to achieve adequate matrix density. The next drawback of this process is matrix microcracking, which causes fine cracks in the composite. Re-infiltration partially fills the cracks, but the strength of matrix and the thermal conductivity typically remain lower compared to the composite made by the Full CVI approach. Ultimately, because of the presence of oxygen in the polymer and the repeated cycles from room temperature to high temperature, oxygen tends to accumulate within the fine cracks. This accumulation can lead to the degradation of the interphase and fibers [33].

CVI-PIP approach refers to the combination of these two processes, usually beginning with CVI process to partially fill the pre-form porosity, followed by subsequent multiple PIP cycles to fill the remaining porosity to the fullest extent. The combination of these two methods enables the attainment of many benefits. First is obtaining high strength, creep resistant and highly thermally conductive SiC matrix by reducing the deposition time and risk of forming large inter-tow porosity. Furthermore, the incomplete SiC matrix obtained during CVI process, offers protection against environmental factors for the fibers and interphase during next infiltration steps. Using the PIP method to fill the remaining matrix enables the incorporation of highly conductive SiC particles without oxygen absorption during multiple PIP cycles. While fine cracks will persist between the particles, they are significantly smaller than those formed during the cracking of the CVI matrix, allowing them to seal much faster in high-temperature oxidizing conditions. However, despite the numerous benefits of the hybrid approach, it still does not produce matrix with zero or near zero porosity.

Presently, the advanced SiC/SiC composites utilized in the hot sections of aircraft engines are manufactured using CVI-MI matrices, which result in reduced porosity compared to fully CVI matrix composites. The production ceramic matrix composites typically involves a series of steps, though there may be variations based on the manufacturer and the specific component needed:

- Weaving SiC tows into a preform, either in 2D or 3D configurations, followed by the removal of fiber sizing,

- Applying one or more interfacial functionalization and protective layers through CVD/CVI on all the fibers of the preform,
- Filling the remaining porosity with SiC powders, for instance, using the slurry casting method,
- Achieving densification through liquid silicon infiltration,
- Applying a silicon-based layer to serve as a bonding coat,

The purpose of Environmental Barrier Coatings (EBCs) is to shield ceramic matrix composites from water corrosion and the harmful effects of calcium-magnesium alumino-silicate (CMAS) melts that can result from exposure to dust, sand, or ash. EBCs are typically applied using air plasma spraying techniques [34]. In a manufacturing variation known as "prepreg MI" the protective fiber layers and matrix slurry are continuously applied to a moving fiber tow before the preform is shaped [35, 36].

3.4 Interfacial fiber coatings

In order to produce a strong composite material, the loads should be held by the strong fibers, while the matrix should hold the composite together as well as transfer the loads between the fibers and protect them from the influence of the environment. Usually, the failure strain of the matrix is lower than that of the fibers, which results in cracking of the matrix before the composite fails. It can be especially problematic when the composite is exposed to elevated temperature, because the difference in coefficients of thermal expansion between the fibers and matrix can lead to microcracking of the material. To prevent this, the zone between the matrix and the fibers needs to be designed to allow for debonding [37]. (Figure 4 a)

When matrix does not break away, cracks formed in the matrix can propagate to the fiber, resulting in a brittle fracture of the composite. Coatings are applied to the fibers before introducing the matrix to allow for debonding and sliding between the fiber and matrix. This sliding effect is crucial as it affects the strength, failure strain, crack spacing, and toughness of the material. It is also important to prevent oxygen from reaching non-oxide fibers, like SiC fibers. Oxygen can react with SiC and form SiO_2. which can weaken the composite [38]. Therefore, coatings are selected to ensure debonding between the matrix and fiber and protect the fiber from environmental effects.

In the past, graphite was commonly used as the interphase because of its excellent lubrication properties. However, it is susceptible to oxidation, which can lead to bridging and oxidation of

the fibers. Boron nitride (BN) was introduced as an alternative coating due to its greater oxidation resistance compared to graphite. BN has similar lubrication properties to graphite and allows for crack deflection within the interphase. If the interphase is well-bonded to the fiber, the load transfer effect from microcracks within the interphase will be maintained, protecting the fibers from the oxidation effects [37].

Oxygen may react with the BN and forming boron oxide (B_2O_3, also known as boria) in the area previously held by the interphase and within the matrix cracks. The boria can then react with the SiC fibers and matrix, leading to the formation of borosilicate glass. However, it has been observed that BN can volatilize, and sometimes, oxygen has no effect on BN. Boron oxide layer produces a glassy sealant, which prevents additional oxygen from reaching the fibers and has the potential to self-heal [39].

Moreover, BN and SiC remain stable when in contact with one another, which makes BN an ideal option for a protective coating. Determining the optimal coating thickness is very important, because too thin coatings can led to the early failure due to insufficient fiber/matrix debonding, whereas overly thick coatings can caused failure due to interlinear shear [39]. Overall, the interfacial coatings play a crucial role in ensuring the strength and durability of the composite material, protecting the fibers from environmental attack, and allowing for debonding and sliding between the fiber and matrix.

3.5 Oxidation resistance of SiC/SiC with BN coating

SiC-based composites are considered top candidates for applications involving extreme conditions of temperature, time and oxidative environment. They provide superior oxidation resistance compared to C/C composites and can withstand higher temperature than nickel-based super alloys used in the hot sections of jet engines [40]. Nevertheless, because these composite systems are made of non-oxide materials, they remain vulnerable to oxidation and corrosive degradation when exposed to water vapor, oxygen, or corrosive environment like Na_2SO_4 and CMAS. The extent of degradation in composites and the mechanisms behind it vary based on the composite's composition, as well as the surrounding environment and temperature. When degradation becomes excessively harmful, the application of protective coatings, known as environmental barrier coatings, becomes essential. To fully understand the impact of time, stress, temperature, and environmental factors on the degradation of SiC-based ceramic matrix composites, it is crucial to comprehend the mechanisms that lead to degradation under specific time-stress-temperature-environment conditions, and the characteristics of the composite

system itself. This is important because certain degradation mechanisms are influenced by the materials comprising the composite components (such as the fiber, interphase, or matrix) and, to some degree, the structural design of the composite system [41].

There are two main types of environmental degradation mechanisms: surface recession and internal oxidation, which can occur through cracks which are located closed to the surface of the composite or other channels that connect the material to the environment. The first mechanism is largely independent of stress; however, the second typically requires the presence of matrix cracks, which are induced by stresses that lead to cracking in the matrix. Both mechanisms can have a harmful impact on mechanical properties. The first mechanism leads to a reduction in the composite's cross-sectional area, while the second one either removes or replaces the interphase by the oxidation product, which changes the essential interfacial properties needed for effective load transfer and robust composite behavior, frequently resulting in more brittle mechanical characteristics. It is also quite possible for both mechanisms to occur simultaneously. The temperature to which the composites are subjected also influences the characteristics of the mechanisms, as it affects both chemical and mechanical interactions. The following temperature classification was proposed by Morscher [43]:

- Low temperature: This refers to temperature below which there is no time-dependent degradation, usually because environmental effects are absent.
- Intermediate temperature: This refers to temperature in the range in which the influence of time-dependent creep in the fibers and/or matrix is either absent or very limited, which means that the mechanical degradation mainly results from environmental mechanisms. In this range, degradation is primarily influenced by the interphase and environmental factors, like slow crack growth or oxidation of the fibers. For SiC-based composites, this temperature can be up to 450 °C due to the oxidation of BN, resulting in the formation of boria liquid or volatile gases like $H_xB_yO_z$ to around 500 °C for carbon interphases (leading to the formation of volatile CO or CO_2).
- High temperature: This refers to the temperature at which intrinsic time-dependent creep and/or fatigue mechanisms of the reinforcing fibers and matrix become activated. While mechanical degradation can happen in a non-reactive environment, it is intensified by oxidizing or corrosive environment. In this temperature range,

both surface recession and internal oxidation mechanisms can be present. It depends on the chemical composition of the environment and the applied stress state.

Various mechanisms of surface recession can take place, influenced by temperature, environmental factors, and the composition of the materials involved. The surface oxidation of the SiC/SiC composite results from the interaction between the solid components and oxidizing gas phases (such as O_2 and/or H_2O), leading to the formation of liquid, solid, and/or gaseous reaction products. At a temperature exceeding 900 °C, SiC can experience either active or passive oxidation [42]:

$$SiC(s) + 2SiO_2(s) \rightarrow 3SiO(g) + CO(g) \quad (3)$$

$$SiC(s) + O_2(g) \rightarrow SiO(g) + CO(g) \quad (4)$$

During passive oxidation, a protective layer of SiO_2 develops on the surface as follows:

$$SiC(s) + \rightarrow \frac{3}{2}O_2(g) \rightarrow SiO_2(s) + CO(g) \quad (5)$$

$$SiC(s) + 2O_2(g) \rightarrow SiO(g) + CO(g) \quad (6)$$

In most CMCs, under the assumption of a high concentration of oxidizing agents (O_2 and/or H_2O), the outer surface is typically composed of SiC, with the reaction products including solid SiO_2, CO gas, H_2 gas, and/or $Si(OH)_4$. As a result of oxidation, a thin layer of SiC may form on the surface of the composite. This surface layer can act as some protection for composite. On the other hand, when the oxidation front reaches the interphase, there is a significant increase in the oxidation rate due to a direct oxidation reaction occurring in the matrix, leading to substantial material loss. When the environment can infiltrate the interior of SiC composites (such as fibers or interphases) through surface-exposed cracks, internal oxidation of the fibers, interphase, and matrix may lead to a decrease in load-carrying capacity. Several mechanisms can lead to diminished mechanical properties, depending on the specific matrix phases, fibers and interphases. The possible mechanisms include:

- Fiber volatilization, which results in a decrease in the fiber's cross-sectional area and a reduction in load-carrying capacity over time due to the decline in fiber strength.
- Formation and/or growth of fiber surface flaws arising from localized surface oxidation mechanisms.
- Interphase volatilization, which leads to time-dependent lengths of fiber detaching from the matrix and reduced interfacial sliding strengths.

- Formation of solid oxide reaction products in the interphase region due to the oxidation of the interphase, fiber, and matrix.

In the SiC/SiC composite with BN interphase, the main mechanism for degradation due to stressed oxidation involves the oxidation of the SiC fibers, matrix and BN interphase, which occurs through surface-exposed matrix cracks. This results in a solid oxidation reaction product that bonds fibers to adjacent fibers and/or the matrix [43]. Several reactions take place, including the oxidation of BN that forms boria liquid, the oxidation of matrix and fibers producing SiO_2, and the melting of boria that can further enhance SiC oxidation by fluxing with SiO_2. Preliminary oxidation within the matrix occur as deboning between the fiber and the BN interface and the initial oxidation takes place at the fiber-BN interface and on the surface of the BN interface. In some instances, a thin carbon layer on the fibers can worsen oxidation between the fiber and BN interface [44]. As the SiO_2 content in the borosilicate melt increases, its viscosity rises, eventually solidifying into a glass with high SiO_2 content. Additionally, this process is accelerated by the presence of small concentrations of H_2O gas in the atmosphere, where boron reacts with H_2O to create volatile species containing $H_xB_yO_z$ (such as HBO_2, H_3BO_3, and $H_3B_3O_6$,), which depletes the boron content in the borosilicate and speeds up the solidification of the melt [45]. If the temperature is sufficiently low and if the environment contain enough H_2O, the volatilization of the boria liquid can occur rapidly while the oxidation of SiC is slow, leading to BN depletion that resembles the slower volatilization of carbon. When a solid oxide glass forms as the reaction product at the interphase, it creates areas of tightly bonded fibers within the matrix cracks. Upon examination after failure, these areas appear as flat sections on the fracture surface. The magnitude of these “embrittled” zones within the matrix cracks is influenced by the rate-limiting reactions and the reduction of oxidizing species in the environment. The nearest-neighbor fibers, which have the thinnest layers of BN separating them, are the most prone to forming strong bonds between fibers. In SiC/BN/SiC composites, the mechanism behind fiber failure and the development of unbridged matrix cracks involves the failure of at least one strongly bonded fiber, which leads to stress concentration on the nearest-neighbor fibers. Given the statistical nature of fiber failure, a local fiber may fail due to a minor increase in stress and/or due to weakening from either intrinsic or extrinsic mechanisms related to slow-crack growth or creep-induced strength degradation. When a local fiber fails, it transfers the load to the nearest-neighbor fibers because of the absence of global load sharing resulting from

strong fiber-to-fiber or matrix bonding. This can trigger a series of failures among the strongly bonded fibers, leading to an unbridged section of the transverse crack [46].

In literature, a few examples of studies on the impact of the oxidative environment on SiC fibers can be found. Castello and Tressler [47] investigated the oxidation behavior of sintered SiC and chemical vapor deposition (CVD) SiC at temperature ranging from 1200 to 1500 °C in the environment of dry oxygen. It was noted a parabolic oxidation pattern and proposed that the oxidation process is governed by the permeation of oxygen ions through the developing oxide film. Nevertheless, the oxidation rates for CVD SiC were greater than those for sintered SiC because of the presence of free silicon. Schiroky [48] investigated the oxidation behavior of chemical vapor deposition SiC at temperature ranging from 1200 to 1800 °C. At a temperature exceeding 1500 °C, it was noted the formation of uniform layers of amorphous silica, along with the emergence of bubbles between 1700 and 1800 °C, which was attributed to elevated CO pressure at the SiC-SiO_2 interfaces. The oxidation of CVD SiC was also studied by Narushima et al. [49] at a temperature between 1550 and 1700 °C. It was found that the parabolic oxidation behavior of CVD SiC is divided into two stages (stage I and stage II), which is attributed to a change in the diffusion rate of oxygen within the SiO_2 film caused by the crystallization process from amorphous silica to β-cristobalite.

There are only a limited number of studies on the oxidation of SiC/SiC composites documented in the literature. Kleykamp et al. [50] were pioneers in examining the effect of oxidation on carbon-coated SiC fibers in air at temperature ranging from 550 to 1520 °C. It was found that between 870 and 985 °C, amorphous SiO_2 converts to tetragonal cristobalite, and the oxidation kinetics exhibit a quadratic rate law at temperature above 1000 °C. Sheldon et al. [51] examined the oxidation resistant of SiC fibers with BN interfaces in the SiC/SiC composite in the temperature range 1000-1450 °C. It was observed that the oxidation of the CMC is derived into 3 stages. In the first stage, the oxidized SiC forms SiO_2 and solid carbon. In the second stage, the oxidized carbon produces CO, and in the third stage, the BN coating undergoes the oxidation process. Narsin Al Nasiri et al [42] investigated the oxidation behavior of BN-coated SiC/SiC ceramic matrix composites when exposed to air at high temperature ranging from 1200 to 1400 °C, for 1, 5, 24, and 48 hours. To carry out the research, the authors used several analytical techniques including weight gain and oxide layer thickness measurements, X-ray diffraction (XRD), X-ray photoelectron spectroscopy (XPS), energy dispersive spectroscopy (EDS), transmission electron microscopy (TEM), and electron energy loss spectroscopy (EELS). The results

showed that the oxidation process followed parabolic kinetics, meaning it depended on both time and temperature. A silicon dioxide (SiO_2) oxide layer formed on the surface of the composites, and its thickness increased from 1 μm after 48 hours at 1200 °C to 8 μm after 48 hours at 1400 °C. The boron nitride (BN) coating around the SiC fibers remained intact and resistant to oxidation, even after 48 hours at 1400 °C. Furthermore, the activation energy for the oxidation process was calculated to be 619 kJ/mol. This value is higher than those reported for monolithic SiC, indicating that the SiC/SiC composites studied in this work possess superior oxidation resistance.

3.6 Effect of high temperature static loads on SiC/SiC composites

3.6.1 Creep properties of SiC/SiC composites

Creep is characterized by time-dependent, permanent deformation of a material over time when exposed to high temperature and mechanical stress. This irreversible deformation occurs due to temperature-induced changes in the material's microstructure. When a material experiences time-dependent elongation that exceeds acceptable limits during operation, the primary concern is often the rate at which this deformation occurs, known as the creep rate. Creep rate equations are derived from deformation curves obtained through constant-load testing. Nevertheless, creep can also result in material failure. Therefore, predicting or determining the time to rupture under stress is essential in cases where dimensional changes are permissible, but structural failure must be avoided. Creep deformation typically can be observed at temperature exceeding approximately 35% of the absolute melting point for metals and about 45% for ceramics [52]. Creep testing usually involves applying a constant load or stress under tension, compression or bending at elevated temperature. Tests conducted at a constant strain rate are also used, as they are faster and simpler to perform. Creep behavior under a constant strain rate is represented by a nonlinear stress-strain curve. However, a more detailed analysis of creep behavior requires tests under constant load or stress. Stress rupture tests, on the other hand, focus on determining the time to failure under specific stress and temperature conditions.

Creep curves for monolithic ceramic represent the relationship between strain and time. Under constant load conditions, these curves typically display three distinct stages (Figure 4 a):

- an instantaneous strain,
- a nonlinear region representing the primary stage of creep (stage I)
- a linear region corresponding to the steady-state or secondary stage (Stage II),

- nonlinear region with upward curvature, known as the tertiary stage (Stage III), leading to fracture.

After the load is removed, (Figure 4 b) can be observed changes of deformation. The first is elastic deformation, which is instantly recovered and the sample returns to its original shape. The second is time-dependent reversible deformation that occurs during primary creep, where the material slowly returns to its initial state over time. Lastly, there is permanent deformation observed during secondary creep, which does not recover and remains in the material even after the load is removed.

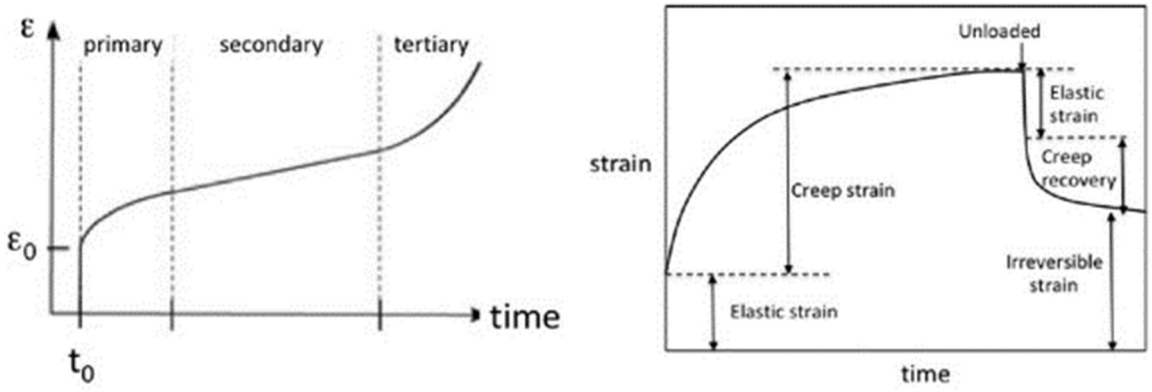

a) b)

Figure 4 Schematic illustrations of the creep curves obtained from tests conducted under condition of constant load (a) and constant strain over time (b) [53]

The deformation caused by creep is influenced by three primary factors: the applied stress (σ), time (t) and temperature (T). The relationship between these factors can be represented mathematically as the product of different functions, which varies depending on the specific properties of the material:

$$\varepsilon_c = f(\sigma).g(t).h(T) \quad (7)$$

Primary creep: during the primary stage of creep, the rate of deformation initially decreases over time until it reaches a minimum point (Figure 4a). This stage is characterized by a viscoelastic deformation mode. t is important to note that only a portion of the strain accumulated during this stage can be recovered when the load is removed, due to the presence of both reversible (elastic or viscoelastic) and irreversible (plastic) deformation. The strain rate during this stage is inversely proportional to time.

Secondary creep: during the second stage of creep, the strain rate remains constant. This stage is primarily governed by diffusion mechanisms. The steady-state creep, which occurs during

this stage, is the most well-understood. In many high-temperature creep mechanisms, the steady-state creep rate can be described by the following expression [53]:

$$\dot{\varepsilon}_S = \frac{ADGb}{kT}\left(\frac{b}{d}\right)^q\left(\frac{\sigma}{G}\right)^{n'} \quad (8)$$

Where A is a dimensionless constant, D is the diffusion coefficient, G is shear modulus, b is the Burgers vector, k is the Boltzmann constant, d is the grain size, q is the exponent of the inverse grain size and n' is the stress exponent.

Tertiary creep: during the third stage of creep, the deformation is primarily influenced by cavitation. As the creep progresses into the tertiary stage, necking phenomena or internal voiding occur, resulting in a decrease in the effective area of the specimen. The plot of the steady-state creep rate against the time until rupture is typically described by the Monkman-Grant law of creep rupture [53]:

$$t_f = C\dot{\varepsilon}_{min}^{-m} \quad (9)$$

Where: t_f is creep rupture time, C is the material constant, $\dot{\varepsilon}_{min}$ is the minimum strain rate and m is minimum strain rate exponent.

The Larson-Miller parameter (LM) is a mathematical expression that combines temperature (T in Kelvin) and the logarithm of time. It is commonly used to assess the equivalence of time at a specific temperature in the context of thermally activated creep and stress rupture in steel materials. This parameter is particularly useful for predicting stress and time required for long-term durability based on shorter-term data. By utilizing the Larson-Miller parameter, it becomes possible to calculate the equivalent times needed for stress rupture to occur at different temperature. The general form of this parameter is as follows:

$$LM = T\left(logt_f + C\right) \quad (10)$$

Where: t_f is the rupture time in h for an isothermal condition, C is the material constant and T is the temperature in ºC.

The majority of research papers on the creep behavior of fiber-reinforced ceramic matrix composites were published between the years 1990 and 2000. There are two main approaches to study the creep behavior of fiber-reinforced composites: macroscopic approaches and micro-macro approach:

- The macroscopic approach treats the composite as a bulk material and draw inspiration from creep studies conducted on monolithic ceramics. These approach utilize concepts and equations at the macroscopic length scale of the composite.

- The micro-macro approach focuses on understanding the creep behavior of individual constituents within the composite. While more attention has been given to studying the creep behavior of fibers, less emphasis has been placed on the matrices. Nevertheless, a significant amount of creep data has been obtained from monolithic ceramics, which can provide valuable insights into the behavior of matrices. Models have been developed to establish relationships between the creep behavior of the constituents and the overall composite behavior.

Creep tests serve the purpose of assessing the creep behavior under specific controlled atmosphere by measuring dimensional changes at a constant high temperature and constant strain or load. These tests are valuable for modeling applications that are subject to long-term strain limitations. By conducting creep tests, one can predict the expected lifespan of a material before it is put into service. To accurately determine the intrinsic time-dependent creep properties, it is necessary to conduct tests in an inert atmosphere: vacuum or argon. However, tests can also be conducted in specific atmospheres that simulate the conditions experienced during actual service, such as air or steam. For instance, SiC/SiBC, SiC/Si-B-C, and enhanced SiC/SiC composites, as well as oxide composites that are known to be resistant to oxidation, are tested at air to assess their creep behavior [54,55,56,57]. In-depth creep studies typically favor tests conducted at a constant load or stress instead of tests at a constant strain rate or cyclic fatigue. Tensile tests are commonly employed for ceramic matrix composites, while there are no reported studies that provide creep results from compression tests. Only a limited number of authors have determined creep data through 3-point [58] or 4-point bending tests [59]. The creep behavior is typically described using load-displacement (or deflection) curves. However, it is worth noting that bending tests are not recommended for composites materials since the elastic beam theory is not an appropriate basis for determining stresses in this context. Standards provide detailed specifications and procedures for conducting tensile testing on ceramic matrix composites [60]. A technique for conducting tensile creep testing is discussed in [61]. Two types of installations can be utilized for this purpose: a test machine or a creep-testing rig. The testing process involves heating the unloaded specimen to the desired test temperature and measuring the gauge length. Then, a predetermined load is applied rapidly but without causing shock. This load is maintained at a constant level for a specified duration or until rupture occurs. Throughout the test, the change in gauge length is recorded over time. Creep tests typically involve long-term testing with low loads. The deformations that occur during these tests are

small, requiring precise strain measurements. From the test results, creep stress, strain, and strain rate can be determined. The creep constants can then be calculated based on the creep strain rate using the equations mentioned earlier. The focus is often on identifying the minimum strain rate at a given stress and temperature. The tests are usually stopped before failure occurs, as the objective is not to determine the time-to-failure. In the case of creep rupture tests, the emphasis is on determining the time-to-failure at a specific stress and temperature. This information is then used to create a stress-rupture time diagram. Higher loads are typically employed in these tests to reduce the duration of the creep testing process. Conducting creep tests at elevated temperature (>1200 °C) poses various practical challenges. These tests demand meticulous attention to detail and precise strain measurement techniques while also necessitating the avoidance of any artifacts that could affect the accuracy of the results. In an accidental discovery [62], it was demonstrated that even a small oxygen concentration of approximately 20 parts per million (ppm) in an argon environment was enough to facilitate oxidation and have a similar impact on creep behavior and failure times as composites tested at air. Tensile tests conducted under a constant force are favored for fiber materials. Specifics regarding this testing method can be found in various papers [63,64,65,66,67,68]. For instance, in [68], creep tests were conducted using a specially designed tensile device capable of testing carbon fibers at temperature up to 3000 °C. The fiber was heated by applying electric tension in a secondary vacuum environment with a residual pressure of approximately 10^{-4} Pa. In the article [69], two different types of tensile tests were employed to generate stress-rupture time diagrams: stress rupture tests, where a constant stress and temperature were applied, and slow warm-up tests, where a constant stress was applied with a constant rate of temperature change.

Numerous creep test results have been reported for commercial composites manufactured by different companies. Consequently, these composites may exhibit variations in microstructure and composition, especially at the interface between the fiber and matrix or within the matrix itself. Detailed information regarding the composition is often unavailable. In the article [70], Chermant consolidated the findings from over a decade of in-house research on the creep behavior of various lots of CMCs reinforced with carbon or SiC (Nicalon or Hi-Nicalon) continuous fibers and glass matrix. The temperature ranges for testing were 1273-1673 K for SiC-based matrices and 1173-1473 K for glass-matrix composites (MLAS, YMAS). The tensile creep curves, depicting strain or strain rate over the time, exhibited primary creep followed by

a steady/pseudo-steady creep stage, without any tertiary creep observed. These tests were conducted in argon for most of the CMCs, while the SiC/Si-B-C composites were tested at air. When tested at air at temperature of 1600 °C and stresses above 90 MPa, SiC/SiC, SiC/SiBC, Enhanced SiC/SiC and SiC/Al_2O_3 reinforced with Nicalon and Hi Nicalon fibers exhibited only the transient creep stage [55,56,71,72]. For SiC/SiC composites at low stress, three stages of creep can be observed, but there is no secondary and tertiary stage at high stress [72]. In the case of melt infiltrated Hi-Nicalon S/SiC at 1615 °C in air, a decrease in creep rate was observed at stress below 168 MPa [73]. Tests that were interrupted after 100 hours did not reveal a distinct secondary creep stage. Specimen rupture occurred at a stress of 172 MPa after an increasing rate of deformation over time. The composite was deemed relatively resistant to creep at stress up to 103 MPa, which can be attributed to the creep-resistant characteristics of the reinforcing fiber. This behavior aligns with that of similar SiC/SiC composite.

Strain recovery during unloading: Recovery is the process by which a material regains part or all of the strain accumulated during loading once the load is removed. This time-dependent strain recovery is a characteristic feature of the viscoelastic behavior during primary creep stage. The investigation of creep recovery in ceramic matrix composites have been relatively overlooked, with limited experimental data available [74,75,76]. Holmes et al. conducted research on the creep recovery behavior of 0 ° and 0/90 ° SiC/CAS and SiC/Si_3N_4 composites at high temperature [76]. For unidirectional and 2D woven SiC/Si_3N_4 composites, 50% of the total creep strain accumulated after 200 hours of loading at 200 MPa and 1200 °C was recovered after 25 hours after unloading. A similar recovery pattern was noted for unidirectional and 2D woven SiC/CAS composites tested at 1200 °C. In another loading scenario including 100 hours of creep testing at 60 MPa and followed by 100 hours of recovery at 2 MPa, around 27% of the previous creep strain was regained for the 0 ° composite, while 49% was regained for the 0 °/90 ° composite. The strain recovery observed in the CMCs studied by Holmes et al. [76] was significantly greater than that of monolithic ceramics. The creep recovery behavior of 2D woven enhanced Nicalon/SiC at 1200 °C was investigated in a study [74]. The specimen was subjected to a creep stress of 140 MPa at 1200 °C and held at that stress for around 2 hours. After that, the specimen was unloaded and kept at zero stress for the same duration. After the recovery period, the specimen was loaded to a higher stress level and this process was repeated until failure occurred. The researchers observed from the creep curves that the material showed a tendency to recover both the instantaneous and accumulated creep strain over time, regardless of

the applied load during creep [74]. However, these conclusions are questionable due to the possibility of irreversible deformation near fracture stress. Recovery tests were conducted on a 2D woven N720/Alumina composite at 1200 °C in air and steam environment. The procedure involved loading the specimen at a rate of 200 MPa/sec to a creep stress of either 100 or 125 MPa. After a 1-hour hold time, the specimen was unloaded at the same rate to a minimum stress of 2 MPa. The obtained strain-time curves showed noticeable recovery at 2 MPa. This led to two significant observations: a reduction in primary creep with cycles and a reduction in overall strain accumulation [75]. The recovery trends can be explained by considering the underlying creep behavior. The creep curves for the enhanced Nicalon/SiC composite at 1200 °C showed a predominant primary creep stage, with the duration of this stage decreasing as the applied stress increased [74]. Recovery, which relies on viscoelastic response, is influenced by the ratio of hold time to primary creep time and the applied stress. At higher stresses, the primary creep time becomes shorter, potentially shorter than the hold time, resulting in a viscoplastic response and partial recovery. At lower stresses, where the primary creep time exceeds the hold time, the response upon unloading is viscoelastic, allowing for complete recovery. In the case of the 2D woven N720/Alumina composite, the primary creep time was significantly longer than the hold time (around 20 hours compared to 1 hour) [75]. This suggests that the response during unloading was likely viscoelastic, leading to complete recovery. Recovery tests serve as a reliable technique for distinguishing between viscoelasticity and viscoplasticity in creep behavior.

In the case of most ceramic matrix composites the secondary and tertiary creep stages are typically not observed. Similar to conventional materials, creep analysis for CMCs involves plotting the minimum creep strain rate against stress and also creating stress rupture time diagrams. While transient creep strain was predominantly observed, some researchers estimated the stress exponents by analyzing the slope of logarithmic plots of minimum strain rate against stress, following the steady-state power law equations Equation (8) [71,77,78,79]. Zhu et al. [71,78] obtained high stress exponent values (8-9) for enhanced and standard Nicalon/SiC composites in both air and argon. These values were significantly higher than the stress exponent ($n' = 1- 2.5$) for creep of Nicalon™ fibers [64,65,80]. In a severe-matrix-cracked Al_2O_3/SiC composite, the estimated stress exponent for creep of the composite aligned with that of the Al_2O_3 fiber [81]. In Nicalon/glass-ceramics, the stress exponent for creep was found to be the same as that of Nicalon™ fibers [72]. Based on the comparison of the slope of the logarithmic

plots of minimum strain rate against stress with the stress exponent of the fibers, it was suggested that the fiber controlled the creep behavior of the composite, either partially or entirely. However, this approach lacks a solid physical foundation and has not been supported by other researchers. It is based on Equation (8), which is derived for steady-state creep in homogeneous materials like ceramics or metals. This equation cannot be directly applied to analyze creep rate data during the time-dependent primary stage. To properly analyze composite creep data, robust models specifically designed for composite creep behavior are required.

3.6.2 Microstructural changes in SiC/SiC composites after creep testing

The transfer of stress plays a crucial role in managing creep in ceramic matrix composites. Over time, the component (either the fiber or the matrix) that is less resistant to creep gradually transfers the load to the component that is more resistant to creep. The influence of a mismatch in creep rates between the fibers and matrix can be understood by considering the creep mismatch ratio (CMR), which is defined as the ratio of the creep strain rates for the fiber and matrix [82]. When CMR < 1, indicating that the fibers have greater creep resistance than the matrix and the matrix unloads onto the fibers. This phenomenon in present in SiC/CAS, composites, where the creep properties of the fibers control the composite response [83]. In the scenario of an elastic fiber, the process of creep comes to a halt when the matrix fully transfers its load onto the fiber. On the other hand, when CMR > 1, it indicates that the fibers have lower creep resistance than the matrix and they unload onto the matrix. The behavior of the composite is still controlled by the fibers if the matrix has high compliance, such as in SiC/C composites, but the matrix may crack if it has high stiffness like the CVI SiC matrix [83]. Additionally, the creep resistance of the SiC matrix can vary depending on its composition, with the presence of free Si or Si-rich, MI or enhanced, or SiBC, or Si-B-C matrices resulting in higher or lower creep resistance. The mismatch in thermal expansion coefficients between the fibers and the matrix can result in the generation of stresses. When the coefficient of thermal expansion of the fibers (α_f) is greater than coefficient of thermal expansion of matrix (α_m), and CMR is less than 1, the comparative deformation of the fibers increases at elevated temperature beyond the processing temperature. This leads to the reloading and further unloading of the matrix. Conversely, when α_f is less than α_m for CMR less than 1 or when the temperature at which creep takes place is lower than the processing temperature, the opposite effect occurs. In the case of SiC/Si_3N_4 and SiC/CAS composites, where α_f is greater than α_m and CMR is less than 1, the residual stresses that form in

the composite can serve as an additional driving mechanism for the recovery of strain, complementing the inherent recovery process observed in monolithic ceramic [76]. However, in SiC/SiC composites, the SiC fibers have a slightly lower coefficient of thermal expansion compared to the matrix. Consequently, the thermally induced residual stresses in SiC/SiC composites are relatively low. If present, tensile stresses may develop in the fiber at elevated temperature. The subsequent behavior of the matrix and fibers is influenced by the stress versus strength relationship for cracking, as well as the temperature for thermal degradation. Matrix cracking results in increased loading on fibers that have become debonded. After the initial matrix cracking, further degradation of the composite can occur through various mechanisms. The debonding of the fiber/matrix interface can happen due to differences in the radial creep strain between the fibers and the matrix [114,115]. In oxidizing environments, the properties of the interface (and consequently the creep behavior) can be changed through the damage of the interface layer or by the sealing of the interface due to oxygen influence on the fiber and/or matrix. Creep fracture occurs when the stress on fibers exceeds their strength, either due to the reloading of fibers or their weakening caused by the growth of flaws induced by creep or oxidation in the SiC fibers [83,84,85,86]. The creep behavior of CMCs can fall into different regimes, but it is influenced by temperature, stress state and time, leading to potential variations in the creep mismatch ratio (CMR), especially in situations where the initial mismatch in creep resistance is small [87]. The principles mentioned above are insufficient for predicting the creep behavior of composites. Additionally, there are other factors that affect composite creep, such as interfaces and fiber volume fraction, which are not taken into account.

The findings presented in [58], which involved a comprehensive microscopy examination (optical, SEM, TEM) of ceramic matrix composites subjected to creep testing in an argon environment, uncovered various types of damage. These included debonding between fibers and matrix, microcracking in the matrix, debonding between yarns, bridging between fibers and yarns, fiber pull-out and fiber fracture, among others. These damage modes have also been observed by other researchers in different types of CMCs, such as SiC/Si_3N_4, SiC/C, SiC/Al_2O_3, SiC/mullite, and Al_2O_3/SiC [58]. The microcracking sequence observed in C/SiC and SiC/SiC composites tested at an argon environment involved the creation of initial microcracks, followed by the propagation of transverse microcracks and the development of longitudinal cracks between yarns [88,89]. Importantly, no new matrix microcracks were observed during the creep testing.

Microscopic analysis revealed that the matrix cracks in SiC/Si-B-C composites tested at temperature below 1573 K in the air environment are filled with a glassy phase [58]. This glassy phase acts as a protective barrier against oxidation for the fibers. Further examination using TEM and HREM techniques identified several changes at smaller length scales, including the extension of interlayer microcracks in the multilayered SiBC matrix, which involved deflection and bridging by carbon ribbons [58]. Lenticular pores were observed in the pyrocarbon interphases, and the growth of SiC nanocrystals within the SiC fibers was observed. Additionally, the growth and alignment of basic structural units were observed in the carbon fibers. No movement of dislocations was observed, and it is unexpected to observe diffusion phenomena at temperature below 1828 K for SiC and 2423 K for carbon. Based on this phenomenological approach, Chermant concluded that the creep behavior of SiC-based matrix composites in an argon environment is governed by a damage creep mechanism [58]. In glass CMC's, where the matrix becomes viscous at temperature above 1273 K, the creep of the composite is regulated by the fibers. Chermant proposed the following sequence of events for SiC-based CMC's: initial saturated matrix cracking (with no new cracks), followed by the propagation of transverse microcracks and resulting debonding between yarns, as well as microcracking in the matrix along the longitudinal yarns. Depending on the temperature and stress levels, the SiC fibers may experience creep, while the carbon fibers do not exhibit creep below 1873 K.

4 Objectives, scope and research hypotheses

The primary objective of this doctoral research is to comprehensively investigate the mechanical and thermal resistance of the SiC/SiC (S200H) composite, with a particular focus on its potential application in aircraft engine components produced by MTU Aero Engines Polska. As part of an industrial PhD program, this study aims to develop a set of microstructural evaluation criteria and analytical tools that can be implemented in quality control and certification processes within an industrial environment.

The research will focus on identifying key mechanisms of microstructural degradation under high-temperature and mechanical loading conditions, and on assessing the material's suitability for operation in real engine environments. Automated methods for porosity and crack analysis will be developed, and high-temperature creep and heat treatment tests will be conducted to isolate and understand the effects of thermal and mechanical exposure.

In order to guide the experimental and analytical work, the following research hypotheses have been formulated:

1. The mechanical and thermal resistance of the SiC/SiC composite is primarily governed by the properties of the SiC fibers.
2. The SiC matrix significantly contributes to the overall durability of the composite, providing structural support and resistance to oxidation and crack propagation.
3. Temperature is the dominant factor driving microstructural degradation in SiC/SiC composites.
4. Mechanical stress is a critical factor influencing microstructural damage in SiC/SiC composites.

Based on above discussion and in light of observation that the effect of oxidation and the influence of static loads on the fiber and matrix constituents of the SiC/SiC composite had not been studied, it was decided to conduct research following the scheme presented in Figure 9 in chapter 5.2.7. Based on the analysis of the current state of the literature on the subject, the following objectives of the study were formulated:

1. Conduct an in-depth literature review to verify the current state of knowledge on the mechanical properties of SiC/SiC ceramic matrix composites (CMCs), particularly at high temperature and to emphasize publications describing the relationship between microstructure and mechanical properties.

2. Characterize the SiC/SiC (S200H) composite material produced according to AS9100 aerospace standards to create a qualitative and quantitative description of its microstructure, to build a catalog of characteristic microstructural components an to identify critical microstructural features that affect material behavior at elevated temperature.
3. Develop a repeatable and automated method for describing porosity and cracks using advanced computer image analysis techniques.
4. Perform high-temperature creep tests at a minimum of two temperature values to evaluate the material's mechanical properties under operating conditions.
5. Analyze samples after mechanical tests to characterize fracture surfaces, to conduct ceramographic tests determining the effects of temperature and loading on microstructure and to systematically catalog damage and degradation effects via quantitative microstructure analysis.
6. Compare microstructure after testing to initial material state to assess the degree of change due to mechanical and thermal exposure.
7. Conduct separate heat treatment tests (without load) at the same temperature and duration as mechanical tests, to isolate and analyze microstructural changes caused by thermal exposure.
8. Formulate a phenomenological description of the changes occurring in the composite's microstructure under synergistic effects of temperature and load and to identify and characterize microstructural features critical for quality control and material certification.
9. Analyze the tested material under aircraft engine operating conditions in order to determine the feasibility of using this material in components manufactured by MTU.

5 Experimental research

5.1 Material

The material studied in this research effort was manufactured by COI Ceramic S by Polymer Infiltration and Pyrolysis process (PIP). The commercial name of this material is S200H. The composite consisted of eight plies of High-Nicalon™ [0 °/90 °] fabric woven in an 8 harness satin weave (8HSW). The fibers are made out of SiC and the matrix is made out of SiNC. The fibers are coated with CVD processed boron nitride (BN) and silicon nitride Si_3N_4. The purpose of the BN is to promote deboning between the fiber and the matrix, while the Si_3N_4 is theoretically designed to shield the BN from deterioration during both processing and service. The matrix material was produced by the polymer infiltration and pyrolysis method (PIP). The initial infiltration step utilized a slurry composed of crystalline Si_3N_4 particles dispersed in a preceramic polymer The fiber tow fineness was 1800 DEN. The selected physical and mechanical properties of S200H composite are presented in Table 4 and Table 5.

Table 4 Physical Properties of S200H CMC. Source: S200H Brochure ATK Space System

Physical properties	
Fiber	Hi-Nicalon™
Fiber coating	BN
Matrix	SiNC
Filler	Si_3N_4
Typical ply thickness. mm	0.32
Bulk density. g/cm³	2.3
Fiber volume fraction	0.42
Open porosity. %	<5

Table 5 Mechanical Properties of S200H CMC. Source: S200H Brochure ATK Space System

Mechanical properties	
Tensile matrix cracking stress. MPa	131
Tensile strength. 20°C (1300°C). MPa	262 (241)
Tensile modulus. 20°C (1300°C). MPa	172 (144)
Tensile strain at failure. 20°C. %	0.35
Interlaminar tensile strength. MPa	23
Flexure strength. MPa	358
Shear strength. interlaminar. MPa	71
Poisson's ratio	0.19

This work focuses on Ceramic Matrix Composite known as S200H. Throughout the text, the terms Ceramic Matrix Composite, SiC/SiC composite, CMC and S200H will be used interchangeably to refer to this material.

5.2 Methodology

The research presented in this work was conducted across multiple locations in collaboration with Rzeszów University of Technology (RUT), MTU Aero Engines Polska (MTU), Warsaw University of Technology (WUT), and Element Materials Technology in Lancaster. Oxidation tests were partially carried out at MTU and partially at RUT. All microscopic investigations were performed at MTU. DTA/TG and X-ray diffraction (XRD) analyses were conducted at RUT. Density measurements using the Archimedes method were carried out in collaboration with WUT. Creep tests were conducted by Element Materials Technology.

5.2.1 Light and electron microscopy

The samples for the microstructure evaluation were cut out from the plate in accordance with the cutting guidelines described in the internal company instruction. Due to its characteristics, the SiC/SiC material cannot be cut well with standard cutting processes. In order to avoid delamination and potential cracks, the cutting is generally done with a low speed cutting grinder with diamond-studded circular blade. The samples must be cut in such a way that the sample later cross sections yields a cross sectional surface parallel or with a right angle to the fiber layers (Figure 5).

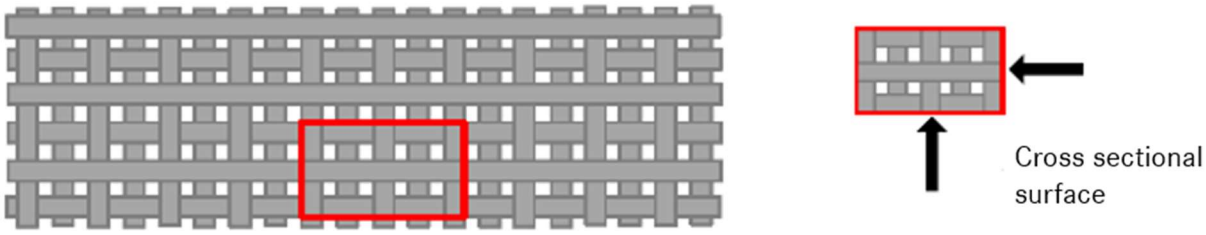

Figure 5 A sketch of an optimal sampling method

Afterward the samples were cold mounted in accordance to internal company procedure. Cold mounting is a sealing without pressure or supplementary temperature. The most suitable embedding compound for CMC is transparent epoxy-resin.

Subsequently, the samples were grinded and polished according to the internal standards which are in line with ISO 20580/2022 on machine Struers Abrapol 10 with an automatic dosing system for the lubricant and diamond suspensions. CMC composites were a new material at MTU, and therefore, their preparation was previously unknown to the employees. The sample preparation methodology was developed in collaboration with Struers company.

Observations of the microstructure using stereoscopic microscope (SM - Stereo Microscopy) and light microscopy (LM - Light Microscopy) were conducted with metallographic microscopes - Leica M205 C and Leica DM4M respectively equipped with image recording system. Examinations using scanning electron microscope (SEM – Scanning Electron Microscopy) were performed with a Tescan Vega 3 microscope, applying an accelerating voltage of 15kV and using detectors for secondary electrons (SE) and backscattered electrons (BSE).

The chemical composition of the material was analyzed using energy dispersive spectroscopy including both elemental mapping and point spectra measurements. Elemental mapping was performed to visualize the distribution of key elements, including oxygen, nitrogen, carbon, and silicon. Both point and line scans were acquired to provide detailed insight into the local chemical variations. The analysis focused on three distinct regions to evaluate the effects of oxidation: the oxidized surface layer, the reinforcing fibers, and the matrix. All measurements were conducted on the pristine sample, samples subjected to oxidation and creep processes, as well as a sample exposed to conditions simulating those found in an aircraft engine environment.

SEM observations were conducted in three areas using a working distance (WD) of 8.00 mm to 10.00 mm. The images were captured at different magnifications, as indicated by the varying fields of view and the imprinted scale bars (Table 6).

Table 6 Used view fields in SEM observations

View fields	2.5 mm	1.25 mm	500 µm	250 µm	125 µm	50 µm	25 µm	10 µm

The above view fields can be derived into following classification:

- Macroscale (mm – order of magnitude)
- Mesoscale (500µm – 125 µm)
- Microscale (50µm- 25 µm)
- Nanoscale (above view fields stop at 10 µm)

In the macroscale the entire surface of the sample, Interlaminar pores between plies and voids can be observed (Figure 6 a-d). In the mesoscale voids, SiC fibers, matrix, matrix cracks and pores can be seen (Figure 6 e-g). In microscale shrinkage cracks and Si_3N_4 coating can be observed (Figure 6 h-i). For nanoscale Si_3N_4 and BN coatings can be observed (Figure 6 j).

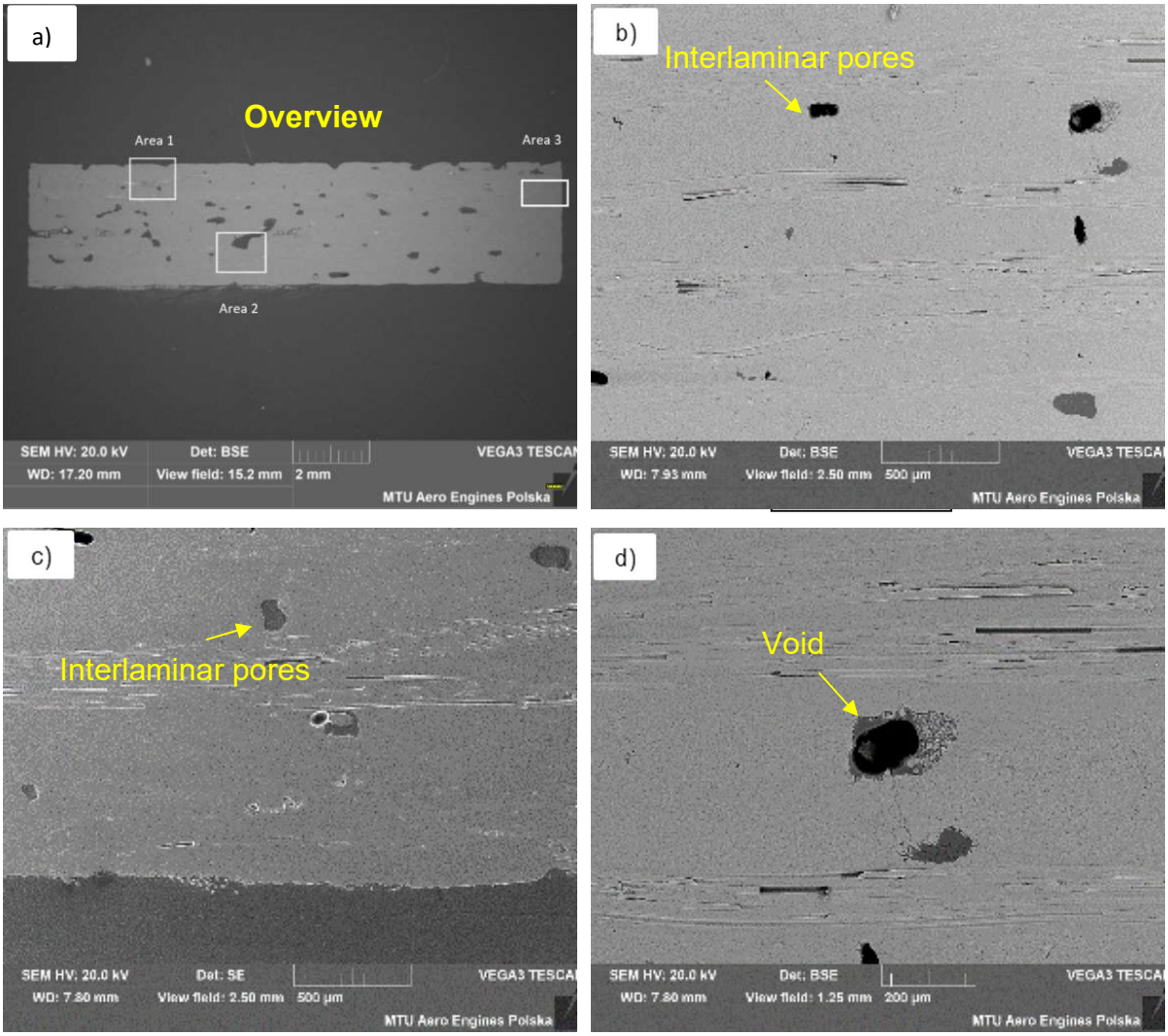

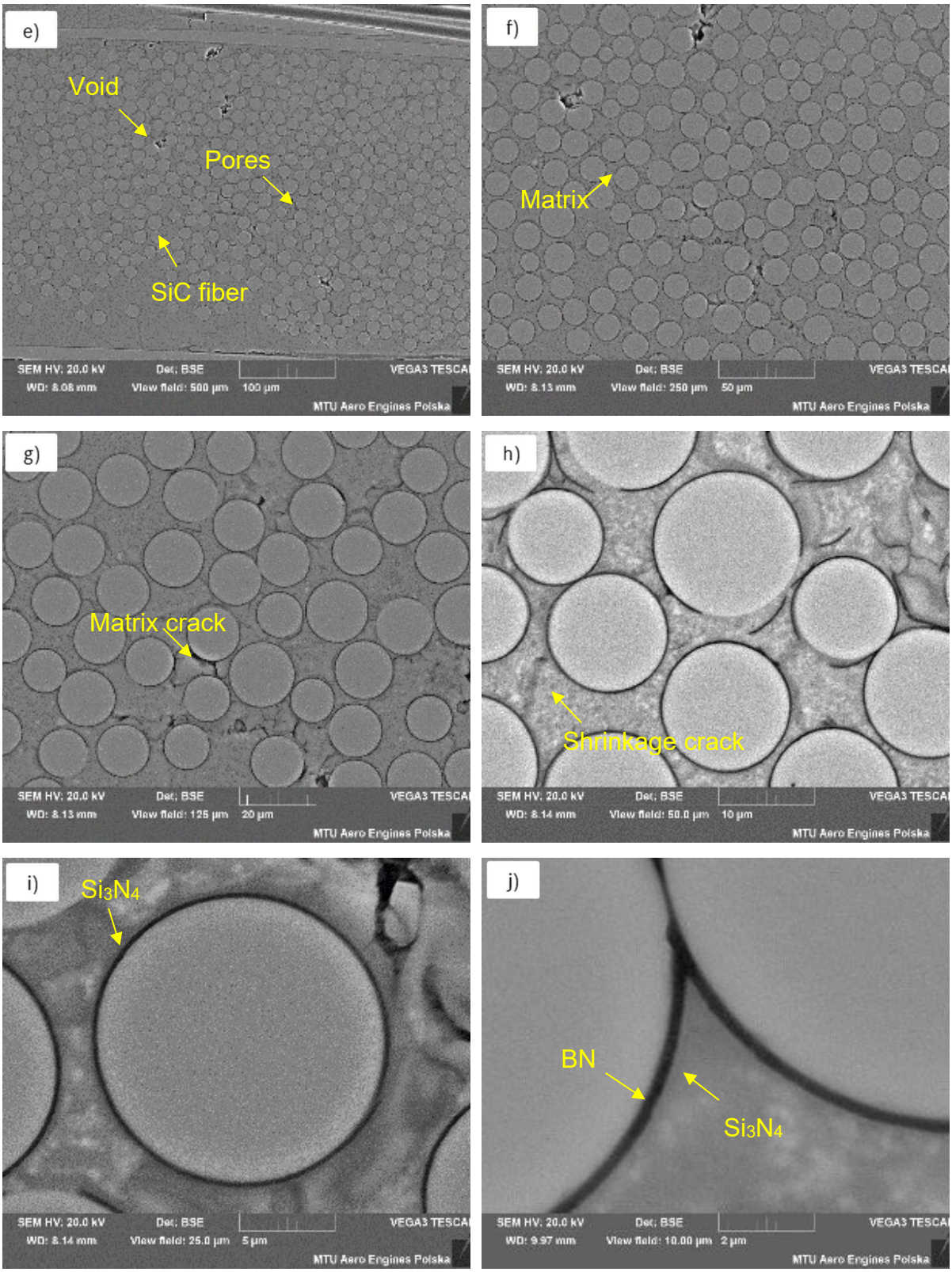

Figure 6 S200H sample: a) overview with observed areas (1,2 and 3), b) 2.5 mm, BSE mode, c) 2.5 mm, SE mode, d) 1.25mm BSE mode, e) 500 µm BSE mode, f) 250 µm BSE mode, g) 125 µm BSE mode, h) 50 µm BSE mode, i) 25 µm BSE mode, j) 2 µm BSE mode

5.2.2 Thermal analysis

For dilatometry tests, square samples were cut using the electro-spark method. Measurements were conducted using a Netzsch DIL 402C dilatometer. The characteristic temperature values of phase transitions were determined using the three-tangent method [111].

The analysis of phase transitions in the tested material, using the differential scanning calorimetry method (DSC – Differential Scanning Calorimetry), was performed with a NETZSCH STA 449 F3 Jupiter device. Both the dilatometric and DSC tests were carried out in an argon stream, during heating and cooling at a rate of 10 K/min.

5.2.3 X-ray diffraction (XRD)

Phase composition analysis were conducted using a Miniflex II X-ray diffractometer from Rigaku (Japan) Filtered X-ray radiation from a CuKα1 lamp with $\lambda = 0.154$ nm was used in Bragg-Brentano diffraction geometry. Following parameters were selected to obtain diffractograms: the angular range of the diffractogram was $2\theta = 20\text{-}100$ °, the angular step size was $2\theta = 0.02$, and the counting time per angular step was t = 3s.

Phase composition was determined using the Powder Diffraction File (PDF) database developed and published by the International Centre for Diffraction Data (ICDD). Phase identification involved matching the measured diffractogram based on the calculated interplanar spacings dhkl for individual reflections and their intensities to the data contained in the ICDD database. XRD measurements were performed on two distinct surfaces of the same SiC/SiC sample. The first measurement was taken on the as-received surface provided by the supplier, corresponding to the shorter side of the sample. The second measurement was conducted on a freshly cut surface along the longer edge of the specimen, prepared specifically for this analysis (Figure 7). This approach allowed for the assessment of potential differences in phase composition or texture between different orientations of the material.

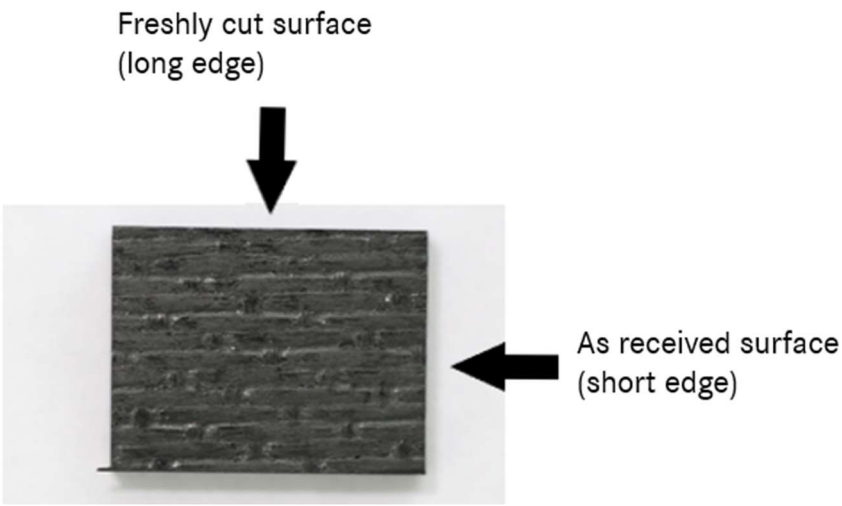

Figure 7 XRD measurement of longer and shorter plane of SiC/SiC Composite

5.2.4 Density measurements

The density of the ceramic matrix composite samples was determined using the Archimedes method, in accordance with ISO 1183-1 and ISO 18754. This method relies on the principle of buoyancy, where the sample is weighed both in air and in liquid of known density. Before measurement, the samples were thoroughly cleaned and dried at 105 °C for 24 hours to eliminate any moisture. After cooling in a desiccator, each sample was weighed in air using an analytical balance with an accuracy of 0.0001 g, and the obtained mass was recorded. The sample was then immersed in distilled water at approximately 23 °C, ensuring that no air bubbles remained trapped by applying vacuum degassing or gently tapping the sample. The submerged mass was then recorded. Based on the obtained measurements, the density of the tested CMC samples was determined.

The Archimedes method provided a fast and reliable assessment of the density of the CMC samples, offering valuable insights into their structural properties.

5.2.5 Heat treatment

The heat treatment conditions of the SiC/SiC composite were selected based on the characteristic operating temperature of typical aircraft engine components. Annealing for oxidation of the samples was carried out by heating them to temperature of 980, 1100, and 1300 °C, holding them for 20, 40, 80, and 100 hours, and then cooling in a furnace (Table 7). The average cooling rate was estimated to be around -1.15 °C/s. Dimensions and mass of the samples are presented in Table 7 and shown in (Figure 8). The annealing at 980 and 1100 °C was conducted at MTU

Aero Engines Polska in a chamber furnace from ThermConcept. The annealing at 1300 °C was carried out at the Rzeszow University of Technology in a chamber furnace from Nabertherm.

Table 7 Annealing conditions for CMC composite

Temperature [°C]	Time [h]	Lenght [mm]	Width [mm]	Thickness [mm]	Weight [g]
980	20	14.980	13.990	2.560	1.280
		14.980	14.350	2.510	1.280
		15.370	15.060	3.440	1.870
	40	18.730	15.000	2.570	1.730
		19.170	14.980	2.560	1.770
		19.850	14.980	2.550	1.830
	80	19.350	15.030	2.560	1.790
		18.630	14.960	2.500	1.690
		20.560	14.950	2.510	1.860
	100	15.020	15.090	3.350	1.820
		14.110	15.000	3.380	1.750
		15.020	15.050	3.360	1.820
1100	20	14.970	15.020	2.560	1.370
		14.480	14.980	2.590	1.310
		14.320	15.030	3.400	1.750
	40	19.060	15.000	3.140	2.150
		19.560	15.010	3.110	2.200
		20.070	15.040	3.150	2.290
	80	19.380	15.020	3.070	2.160
		19.230	15.060	3.140	2.180
		19.840	15.050	3.100	2.190
	100	14.570	14.960	2.460	1.290
		14.240	15.010	2.550	1.310
		15.120	15.110	3.330	1.800
1300	20	19.020	15.030	3.110	1.799
		20.010	15.030	3.140	2.283
		19.580	15.020	3.120	2.151
	40	18.910	15.010	3.140	2.151
		19.980	15.040	3.130	2.142
		19.120	15.010	3.140	2.268
	80	19.360	15.060	2.540	1.790
		19.400	14.970	2.570	1.780
		19.360	15.000	2.550	1.770
	100	19.767	14.933	3.160	2.154
		19.467	14.933	3.120	2.245
		18.983	14.940	3.120	2.225

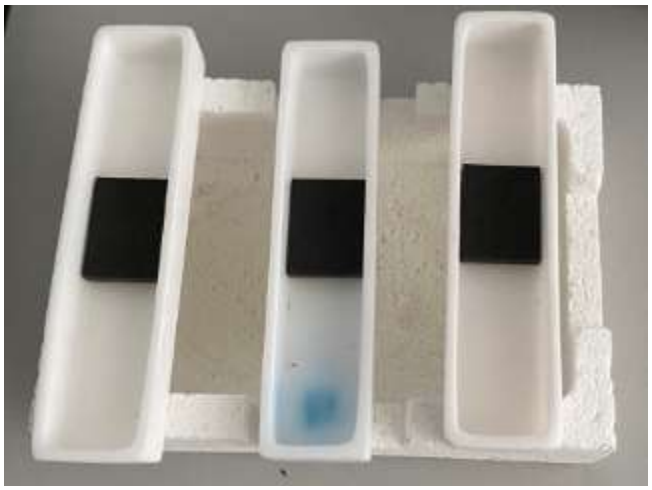

Figure 8 CMC samples in ceramic crucibles before being placed in the furnace

5.2.6 Creep testing

The 16 samples were tested at two temperature: eight at 980 °C and eight at 1100 °C. The creep tests were carried out in accordance with the ASTM C1337-17 standard. All tests were carried out in load control with a loading rate of 0.1 kN/s. The strain was monitored using an Epsilon side-contacting Axial Furnace Extensometer with 25.4 mm gauge length. For tests conducted at elevated temperature, a short profile, 2-zone "zip" furnace was used. The specimen was cold-gripped outside of the furnace.

Tests were discontinued upon reaching one of the following criteria:

- 200 hours at load,
- 2% total strain.

All testing was conducted under the laboratory's UKAS Flexible Scope in accordance with internal procedure - CMC Strain Monitored, Load Controlled Axial Creep Tests.

5.2.7 Research plan

An depth analysis of the SiC/SiC material was divided into following stages shown in Figure 9. All studies were conducted in accordance with the outlined workflow to thoroughly characterize the most critical features of the Ceramic Matrix Composite.

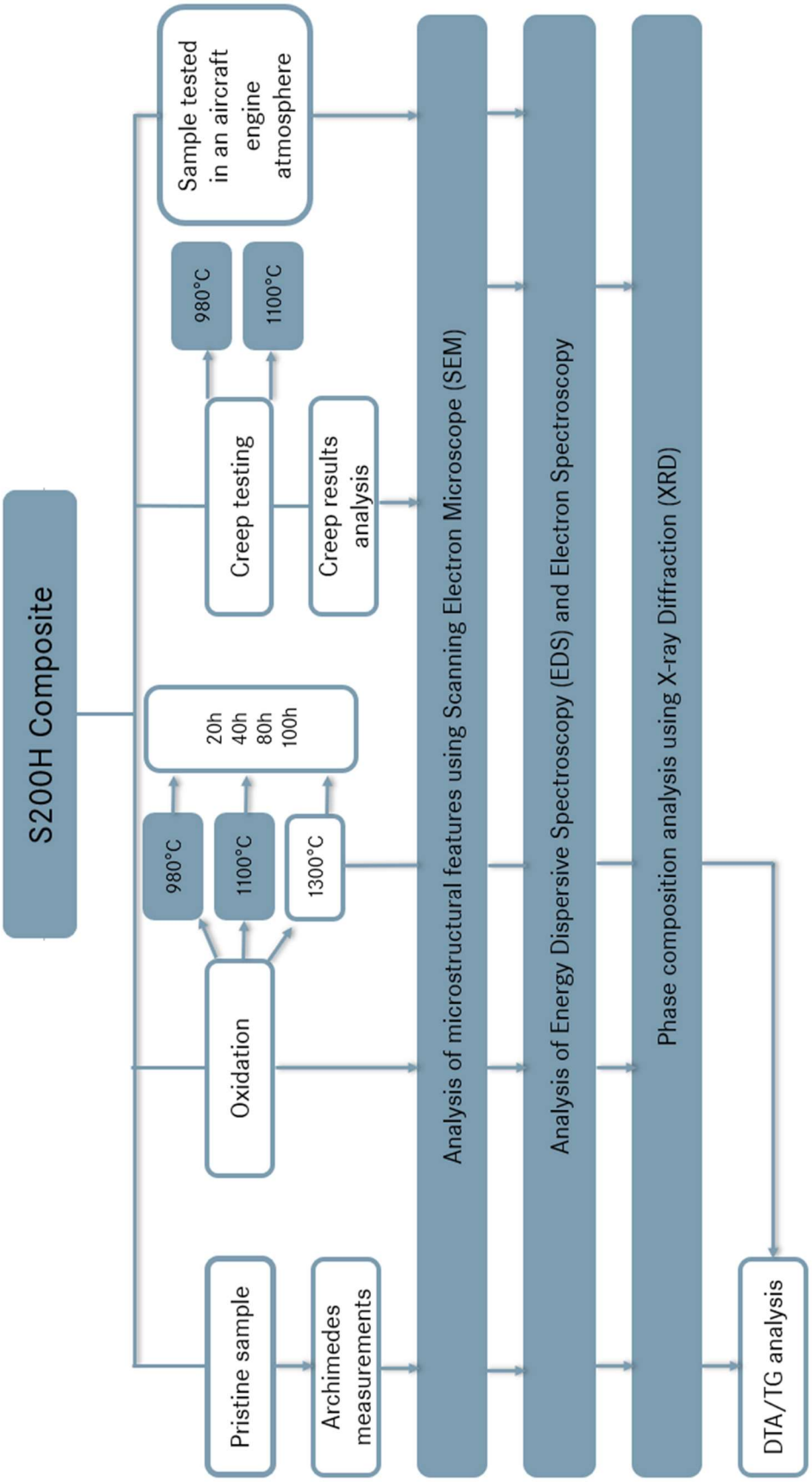

Figure 9 Research work scheme on the SiC/SiC composite

6 Results and discussion

Microstructural characterization is a very important part of developing and understanding the SiC/SiC composite. Microstructure investigation methods like Scanning Electron Microscopy and Light Microscopy can be used for characterization of the received material quality. The preferred microstructure has been determinate by the association of mechanical properties and microstructure. The high quality of the SiC/SiC material is extraordinarily important in aero engines production [90]. An depth analysis of the SiC/SiC material was divided into following stages showed in the Figure 9. Characterization of the as-received composite should bring to the point where laboratory engineers can easily recognize which features are the most critical and can be fast stopped so that they do not proceed to the next stages of production. This analysis included the measurement of the SiC/SiC composite density using the Archimedes method, microstructure analysis using SEM, EDS analysis, XRD analysis, as well as DTA and TG analysis. The description of the collected results will allow for the assessment of the quality of delivered material and enable a comparison of the effects of high temperature and load on the microstructure of the SiC/SiC composite. This will help characterize the key microstructural features that may influence the strength of the material operating under high-temperature and load conditions. Additionally, it will allow for the determination of the material's failure mechanism and the boundary conditions to which the SiC/SiC composite may be subjected. Finally, the collected conclusions will be compared with the microstructural analysis of the material used during aircraft engine tests under conditions simulating those present during engine operation in an aircraft. This work will enable the assessment of the possibility of using the SiC/SiC composite in an aircraft engine manufactured by MTU company.

6.1 As received composite SiC/SiC

An in depth analysis of the source material has been divided into the following stages:

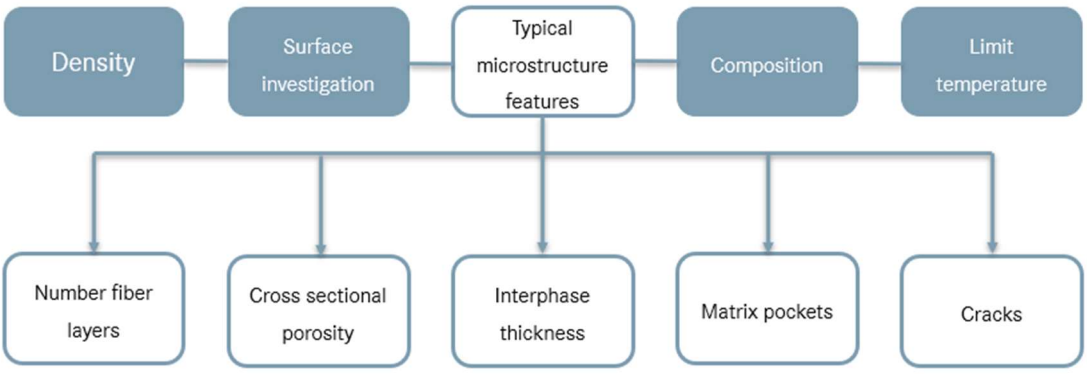

Figure 10 Analysis of the source SiC/SiC composite

A thorough material analysis will enable a reliable assessment of the actual condition of the CMC composite delivered by the supplier to MTU. It will also allow for the creation of technical documentation that will allow the laboratory engineer to assess whether the delivered material complies with the applicable requirements set for the supplier. The above classification will be extensively described in the subsequent steps of the work. Such an in-depth investigation is essential for gaining a comprehensive understanding of the material and the changes it undergoes under various conditions. As a newly developed Ceramic Matrix Composite, the material exhibits a high degree of complexity and variability due to its heterogeneous structure. For this reason, a detailed characterization of the initial (pristine) state is of critical importance and has been given significant attention in this study.

Density

Density measurement was conducted using the Archimedes method. The measurements were done on 10 samples. Material's density was calculated using Equation 11 and the open porosity was determined based on Equation 12.

$$d_a = \frac{m_{dry}}{m_{wet} - m_{water}} * d_{water} \tag{11}$$

$$d_a = \frac{m_{dry}}{m_{wet} - m_{water}} * d_{water} \tag{12}$$

Table 8 Archimedes measurements on 10 samples from SiC/SiC composite

Sample number	m_{dry} [g]	m_{water} [g]	m_{wet} [g]	da [g/cm^3]	Moisture absorption [%]	Open porosity Po [%]
1	0.9981	0.607	1.0137	**2.45**	1.56	**3.84**
2	0.992	0.603	1.0071	**2.45**	1.52	**3.74**
3	1.1611	0.7049	1.1818	**2.43**	1.78	**4.34**
4	1.0837	0.6596	1.1029	**2.44**	1.77	**4.33**
5	1.0152	0.6181	1.0324	**2.45**	1.69	**4.15**
6	0.9221	0.5606	0.9375	**2.45**	1.67	**4.09**
7	0.9788	0.5957	0.9968	**2.44**	1.84	**4.49**
8	1.1302	0.6879	1.1515	**2.44**	1.88	**4.59**
9	1.0602	0.6417	1.0788	**2.43**	1.75	**4.26**
10	1.0295	0.6256	1.0496	**2.43**	1.95	**4.74**

Open porosity in CMCs refers to the volume of pores that are connected to the surface and can interact with the environment, such as gases or liquids. Total porosity includes both open and closed pores, the latter being isolated within the material and not accessible from the outside. The difference between the two is important, as open porosity affects permeability and chemical resistance, while total porosity influences mechanical strength and density [91].

Based on the results obtained from the Archimedes density measurement method, it can be concluded that the measured density of the material is slightly higher than that provided by the manufacturer. The measured density is approximately 0.15 g/cm³ higher (Table 8).

The open porosity, calculated based on the results of the Archimedes method measurements, falls within the range specified by the supplier <5%. It should be noted, however, that the manufacturer did not specify the method used to determine the reference density value, which makes a direct one-to-one comparison difficult. Therefore, the observed difference may result from the use of different measurement technique.

Surface investigation

Surface investigation was done under Stereo Microscope. All samples had a dark gray color, which is related to the presence of silicon carbide. In some areas of the samples, lighter gray regions could be observed, which may appear due to oxidation, surface defects or variations in the matrix composition or very fine particles. Additionally, the samples have a matte surface (Figure 11).

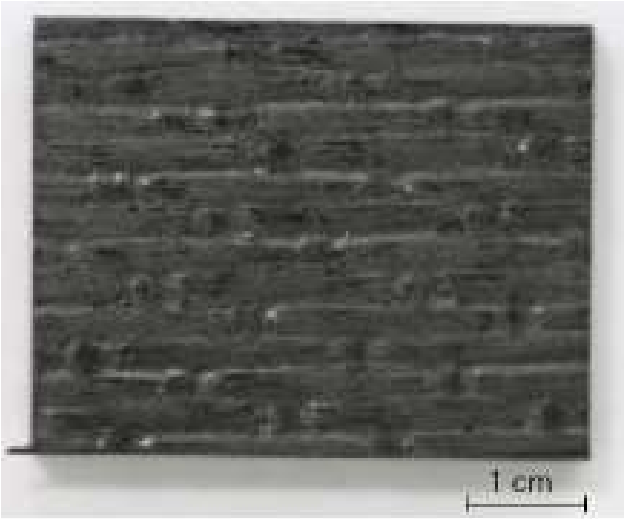

Figure 11 Stereo photography of pristine Sample S200H.

The surface appear uneven or textured because of the alignment and distribution of the silicon carbide fibers or particles embedded in the matrix. The fibers can create a rough, fiber-reinforced texture on the surface, giving it a non-smooth feel. The surface roughness caused by misaligned or unevenly distributed silicon carbide fibers is not necessarily beneficial - in fact, such irregularities can reduce the composite's mechanical performance, as fibers that are not ideally oriented contribute less effectively to load-bearing. However, the non-uniform distribution of the reinforcing phase throughout the material may further contribute to the irregular surface appearance. The distribution of the silicon carbide fibers or particles is not always uniform throughout the material. This can lead to variations in the surface texture, where some areas may show more pronounced fiber alignment or concentration (Figure 12 a-b), while others may have a more random arrangement. This inhomogeneity in structure often results in slight differences in appearance and performance across the material. Depending on the processing method (e.g., infiltration), surface porosity may also be present. The pores can create a pitted or uneven surface, contributing to roughness and inhomogeneity (Figure 12 c-e) [92].

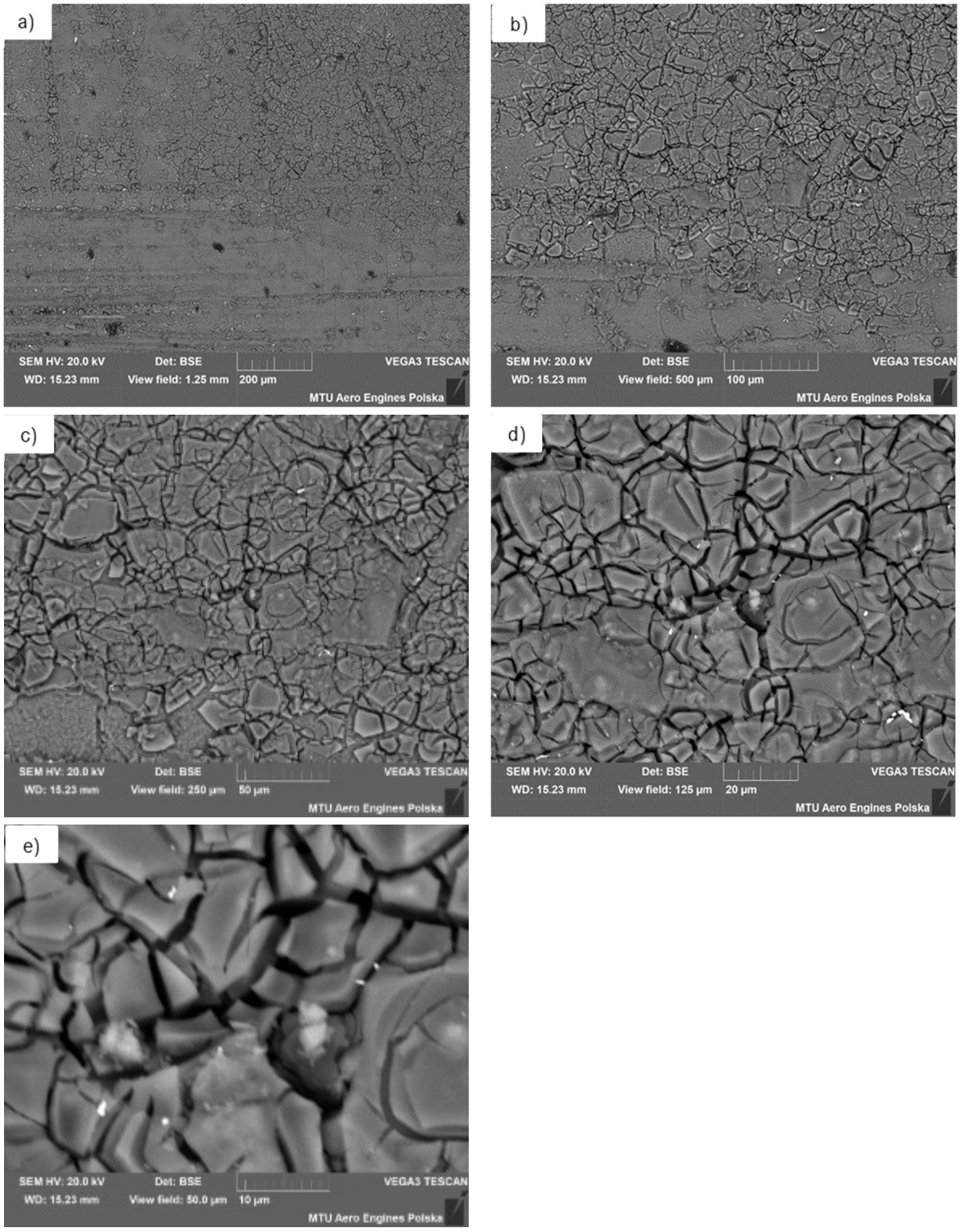

Figure 12 Surface SEM pictures a) View field 1250 µm, b) 500 µm, c) 250 µm, d) 125 µm, e) 50 µm

Typical microstructure features

Typical microstructure features which were selected for observation under Scanning Electron Microscope are shown in Figure 13 a, b and c. Fibers in the material are located longitudinal and transverse due to 8HS satin weave. The longitudinal fibers normally are continuous in

length, but due to the sample preparation process might be broken (during grinding and polishing longitudinal fibers are parallel to the grinding and polishing loads). Transverse fibers should be located singularly, but sometimes fibers may also touch each other. This fiber interconnection results in a lower coating content on fibers. The coating on the fibers usually should be homogenous in thickness, but due to the sample preparation process and manufacturing process it might be delaminated (Figure 13 c). The matrix of S200H material has porosity below 5% and visible closed cracks produced during PIP process. The matrix during PIP process is infiltrated several times. During this manufacturing process, cracks are formed during pyrolysis and later are healed due to next steps of infiltration. Another important features of the material are matrix pockets. Matrix pockets are the matrix rich location in the material. They can form as interlaminar layers between plies or as localized accumulations within a single ply.

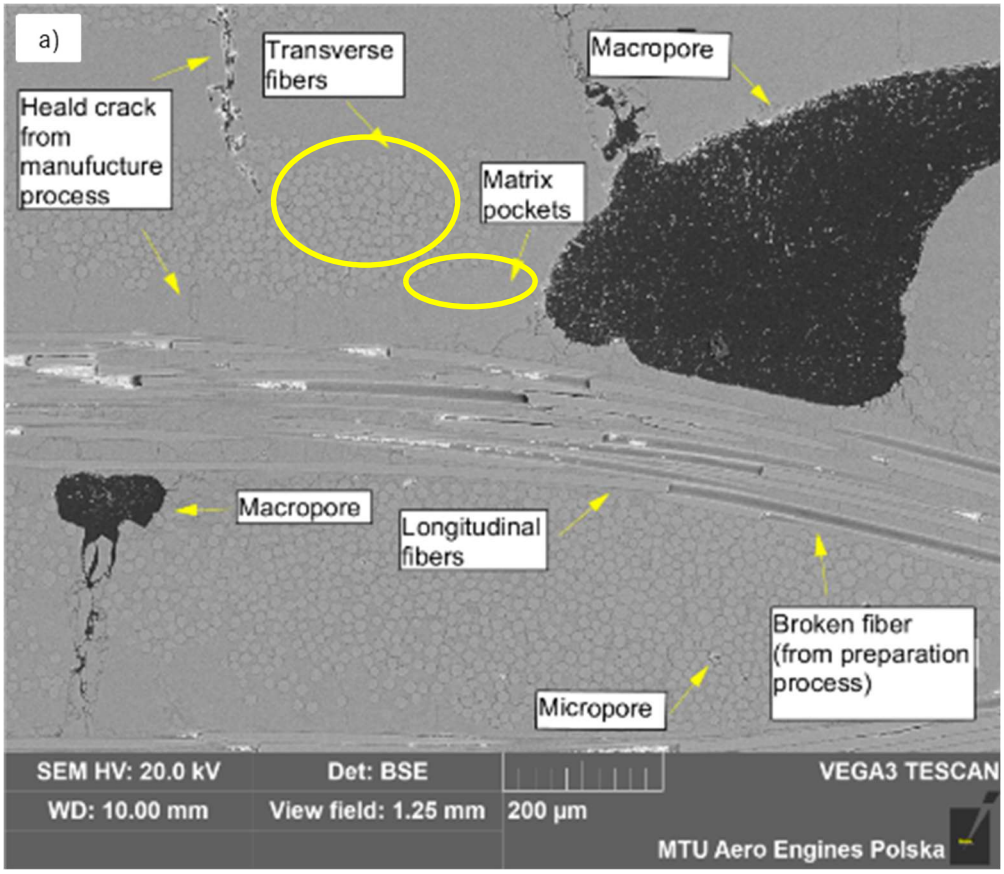

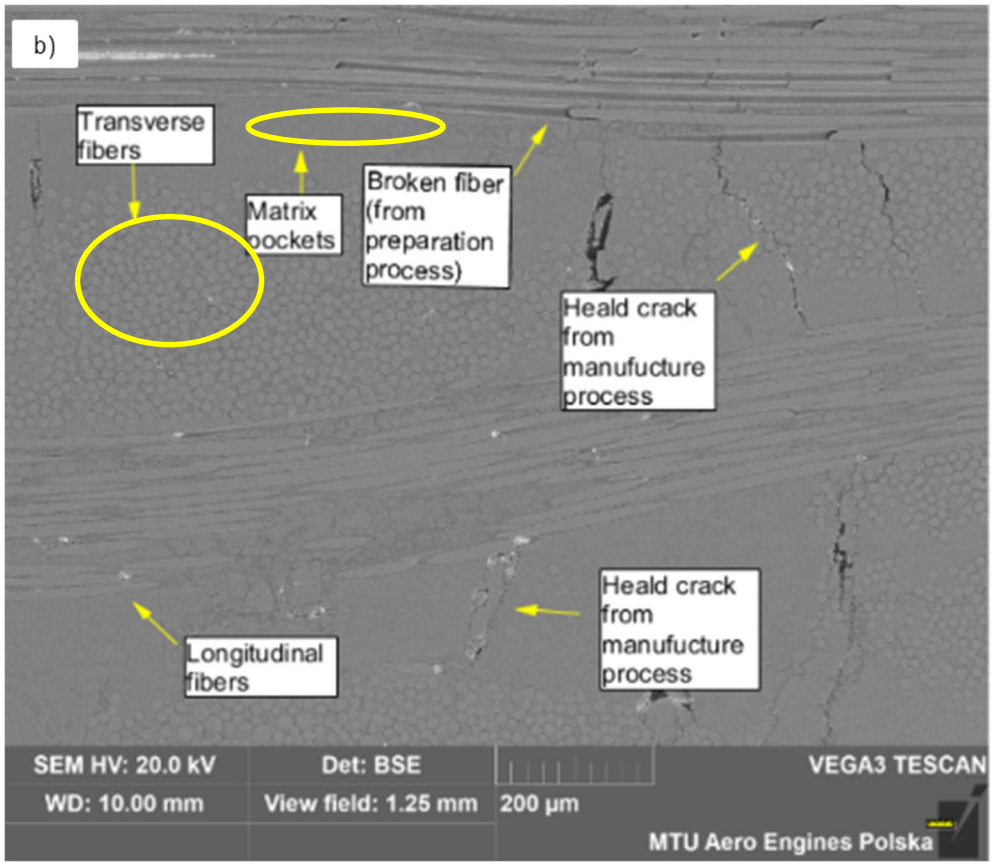

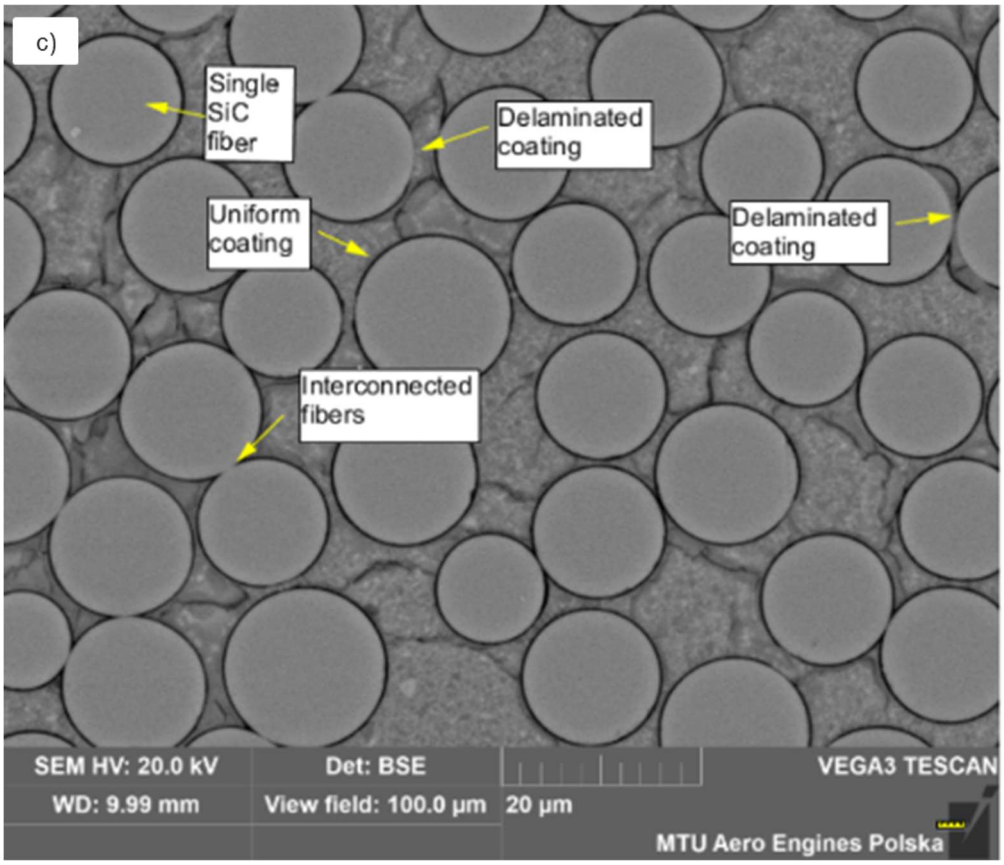

Figure 13 Typical microstructure features of S200H

The number of fiber layers

Material S200H have 8 fiber layers which can be easily visible and countable on the Figure 14. Verifying the number of fiber layers is essential, as it directly influences the structural integrity and performance of the composite. A reduced number of layers may significantly compromise the mechanical properties of the material, such as tensile strength, stiffness, and fracture toughness. Moreover, insufficient reinforcement can negatively affect the material's resistance to operational conditions, including thermal stress, mechanical loading, and environmental degradation. Therefore, confirming the correct number of fiber layers is a critical step in quality control and ensures the composite meets its intended performance requirements.

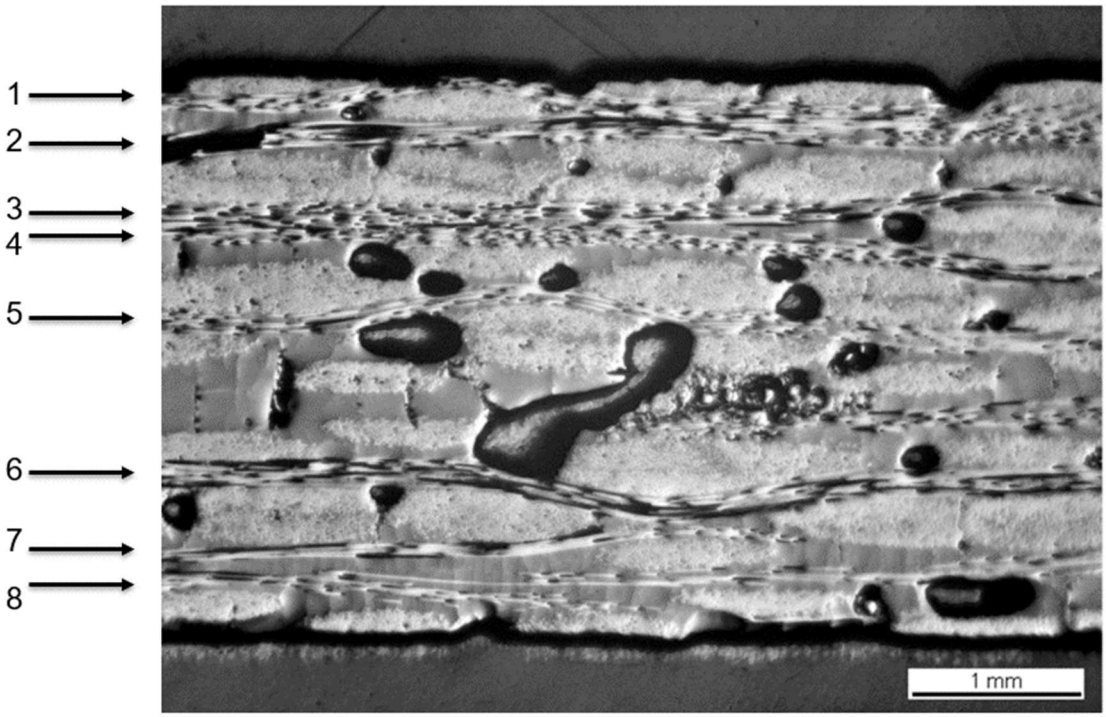

Figure 14 Stereoscopy photo of fiber layers of S200H material

Cross-sectional porosity

Porosity investigation in ceramic matrix composites is very important. Size, distribution and number of pores have significant influence on mechanical properties and oxidation resistance of S200H material. According International Union of Pure and Applied Chemistry pores are classified to the following definitions:

- Macropores – Pores with a diameter greater than 50 nm. These large pores allow for easy fluid and gas flow and are commonly found in ceramics, catalysts, and porous composites.

- Mesopores – Pores with a diameter between 2 nm and 50 nm. They play a crucial role in adsorption, catalysis, and mass transport in porous materials.
- Micropores – Pores with a diameter less than 2 nm. These extremely small pores significantly impact material properties such as gas storage and selective adsorption.
- Nanopores – A broad term referring to pores in the nanometer scale, often overlapping with micropores and mesopores. They are relevant in nanotechnology, biomaterials, and filtration applications [93].

This classification is widely used in materials science, particularly in the context of porous ceramics. However, it does not fully reflect the scale and morphology of pores observed in fiber-reinforced ceramic composites such as S200H. Therefore, in this work, the literature-based classification is included only for reference and comparison purposes. The actual classification used for the analysis of S200H was developed based on the observed pore sizes in the material, the available magnification range of the imaging techniques used (e.g., SEM), and the relevance of pore size to mechanical performance in this specific composite system. The working classification used in this study is presented in Table 9, where pores are grouped based on their longitudinal axis.

Table 9 Classification of the pores in S200H

Classification	Pores sizes (µm)
Macroporosity	>100
Mesoporosity	100-10
Microporosity	10-0.1
Nanoporosity	<0.1

The classification of pores in composites can be based on various criteria, including detection techniques, impact on mechanical properties, and morphological characteristics. Pores can be classified based on origin (natural pores, which arise from production processes, and artificial pores, which are intentionally created to improve the properties of the composite), size, shape (regularly shaped pores, which can have a cylindrical or spherical shape, making them easier to model and predict their impact on mechanical properties, and irregularly shaped pores, which can lead to complicated stress distribution and affect properties in unpredictable way), as well as based on their location (surface pores, which are located on the surface of the composite and can influence adhesion and interactions with the environment, and internal pores, which are located within the structure and have the greatest impact on the material's strength and stability). Pores can also be classified according to detection techniques, such as scanning electron microscopy (SEM), nuclear magnetic resonance (NMR) or computed tomography (CT). Each of

these methods has different capabilities in terms of resolution and the ability to identify specific types of pores. Pores in composites have a crucial impact on their mechanical properties, such as tensile strength, hardness, and fatigue resistance. Depending on their size, shape, and distribution, pores can weaken the material or, if properly designed, enhance its functionality for example, by reducing weight, increasing thermal or acoustic insulation, improving surface area for catalytic or filtration applications, and enabling better adhesion of coatings or bonding agents. The morphology of the pores and their distribution, can be analyzed using various techniques, allowing for a better understanding of their influence on the behavior of the composite under load.

In this work, the focus was on the classification of pores according to their size, shape, and location. A large amount of macropores and mesopores may lead to reduced material strength and initiation of crack propagation. What is more, pores can be the most oxidized area when material is operating in an oxidizing environment. For these reasons, an in-depth analysis of the pores in the material is very important and necessary.

Pore sizes were described by Maximum Feret diameter according to ISO 21363:2020 (Figure 15). Feret Diameter is not a diameter in its literal meaning, but the common group of diameters obtained from the distance between two tangents to the end contour of the particle in a well-defined orientation. In another word, this method corresponds to the slide gauge principle. Generally is defined as the distance between two parallel tangents of the particle at an arbitrary angle. The Feret diameters are calculated and their maximum value is selected. If a particle has no regular shape, the Feret diameter differs more than with regular shaped particles. For irregularly shaped particles, the maximum Feret diameter tends to exceed the equivalent diameter, whereas for regular shapes, the values may be comparable [94].

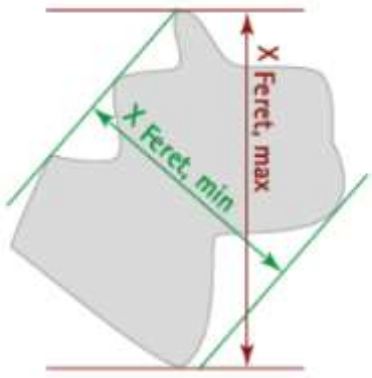

Figure 15 Definition of the Feret Diameters

During analysis, the focus was on macroporosity and mesoporosity resulting from the inability to observe smaller-sized pores. Moreover, larger pores are known to have a more pronounced impact on the mechanical properties of the composite, as well as on its resistance to oxidation, making their characterization particularly important. Porosity can be observed inside the tows and in the matrix. Pores can be spherical or elliptical in shape, elongated in one direction, longitudinal to the material plies or perpendicular to the material plies (Figure 16 a-f). The analysis of pores and different types of porosity will be examined in a later part of the work, especially the impact of various types of porosity on oxidation resistance and loads in the SiC/SiC composite.

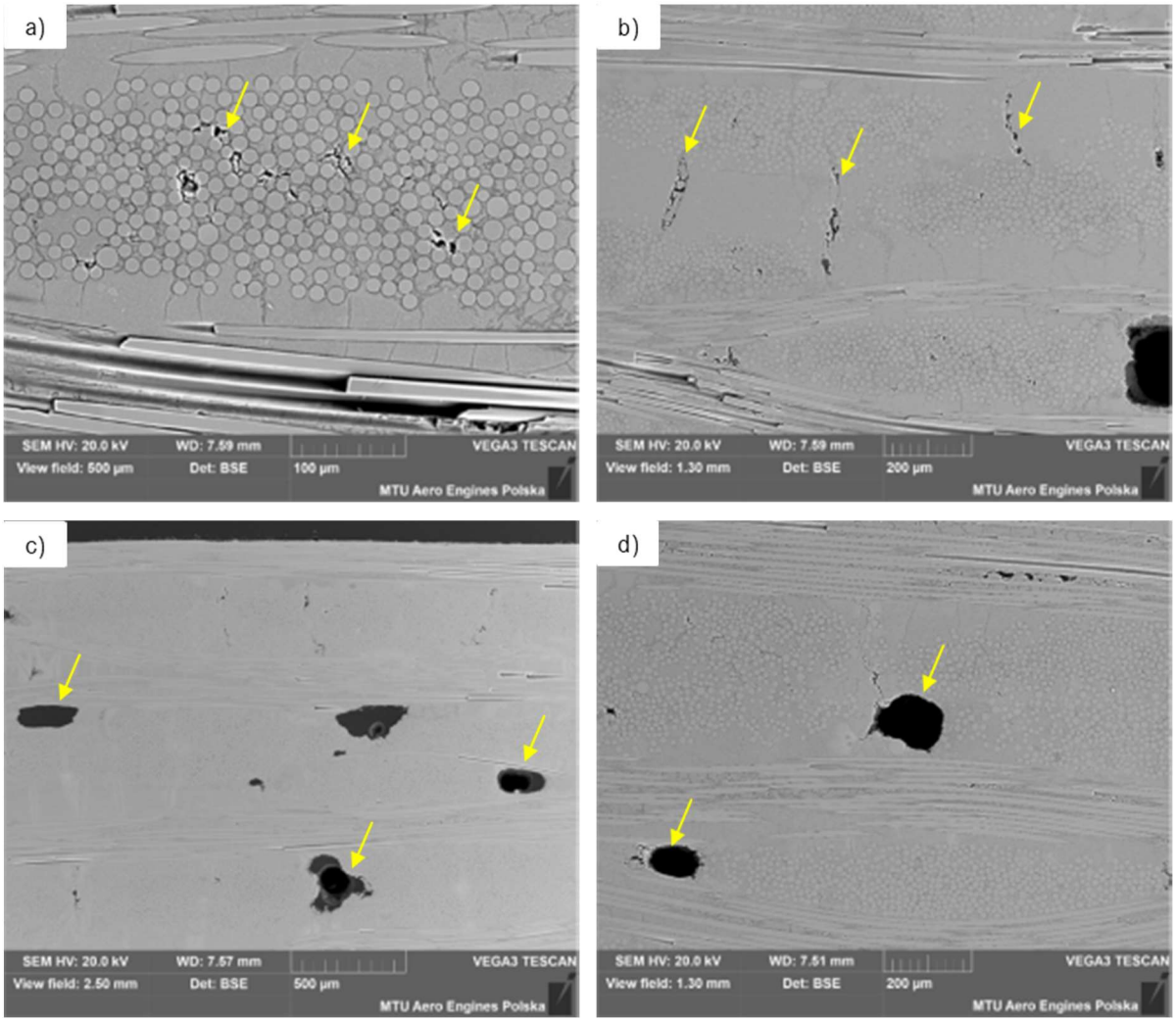

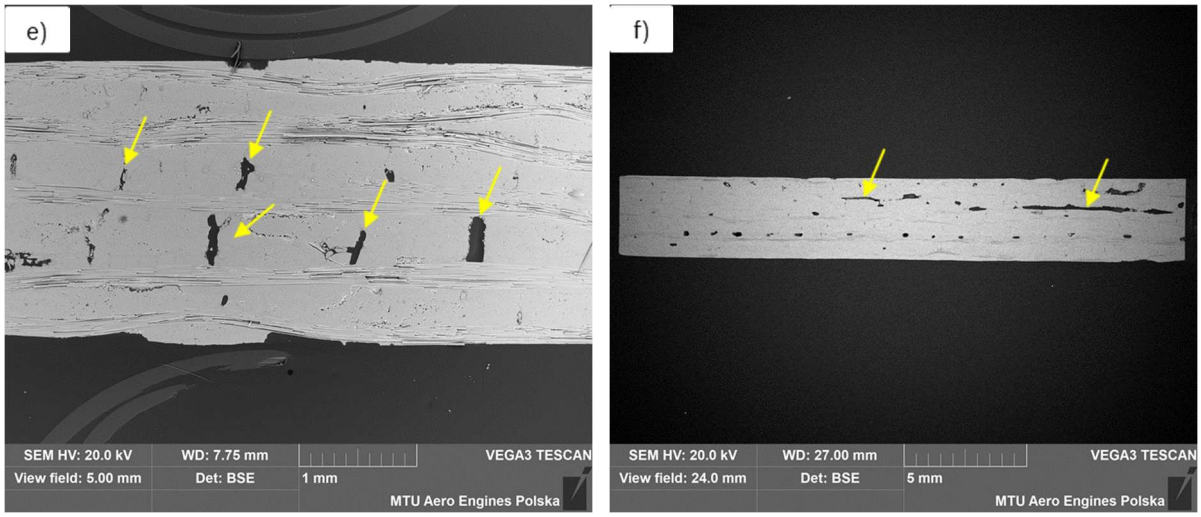

Figure 16 Pores in S200H, a) inside tows, b) in the matrix, c) elliptical in shape, d) spherical in shape, e) perpendicular to material plies, f) longitudinal to material plies

The method of analyzing pores has not been previously described; therefore in this work proposes a research method that allows for determining the dimensions and size of pores in the SiC/SiC material was proposed. Analysis of the size and shape of the pores was done in the Image IMS program (Figure 17). The cross-sections from 6 samples were analyzed. SEM images were taken of each sample, after which the sample was ground and polished, and subsequent cross-section areas of the sample were analyzed to check the porosity within the material. In total, measurements were made on 34 photos (1500 mm^2). During observation only closed porosity was included in the calculation. Moreover due to the presence of a large number of small defects and the limited resolution of the images, only the pores whose Feret max was greater than 20 µm were analyzed. Pores which are greater than 20 µm can have significant influence on the mechanical properties of composites. Large pores can create weak points in the composite structure, leading to a reduction in its tensile, bending, and compressive strength. In areas where pores are present, stress concentration may occur, increasing the risk of cracks and damage [95]. Pores contribute to a decrease in the material's density, which in turn leads to a reduction in the stiffness of the composite. Lower stiffness can negatively affect its ability to bear loads. Large pores can also lead to faster development of microcracks as a result of cyclic loading, which can result in material fatigue and reduction in its lifespan. What is more, they can be very important for oxidation. Large pores can increase the surface area available for reactions with oxygen, which may lead to faster oxidation of the material. This phenomenon is particularly significant in high-temperature applications. Pores can act as traps for oxidizing gases, leading to localized chemical changes and reduction of the material's stability. Pores can

also affect thermal conductivity of the composite. In the case of high-temperature applications, a large number of pores can lead to thermal instability, which in turn affects oxidation resistance.

Figure 17 IMS analysis of microporosity in the SiC/SiC composite

During the analysis the focus was on parameters such as area of pores, area fraction of pores, Feret Max, Feret Min and circularity. In total, over 4000 individual pores were analyzed. Most of them can be classified as mesoporosity (Figure 18 a). The friction of mesoporosity (20-100µm) in the area of all porosity in the material was below 10%. The area friction of pores larger than 500 µm is equaled to 21%. In mesoporosity the most frequently observed were pores with Feret Max 20-40 µm (59%) and the most rarely were pores with Feret Max 80-100 µm (8%). In macroporosity the most frequent were pores with Feret Max 10-200 µm (52%) and the most rare were pores with Feret Max 400-500 µm (4%) (Figure 18 b and c).

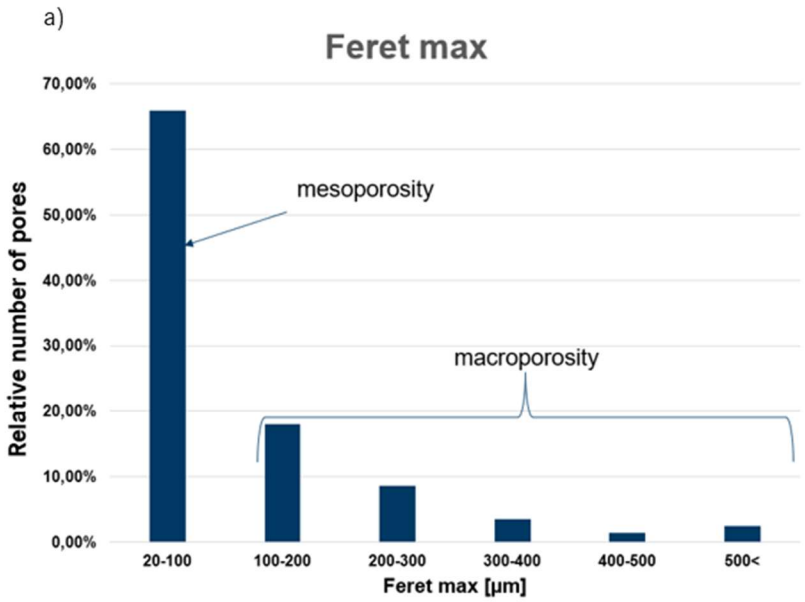

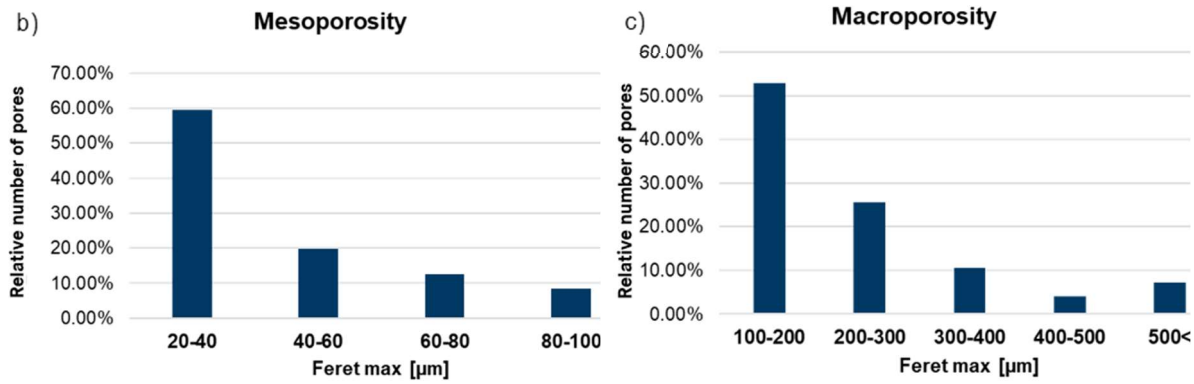

Figure 18 Pore size distribution depending on the Feret Max a) in the SiC/SiC composite, b) mesoporosity, c) macroporosity

The shape of pores was described by the ratio of the minimum and the maximum Feret diameter (Figure 19). This shape parameter is used in stereological analysis for evaluating the degree to which a particle is stretched or how similar its projected contour is to a circle. The highest frequency had pores with shape parameter 0.4 and the most rare were pores with shape parameter 0-0.2 (Figure 20). The largest pores were characterized by the largest elongation (Figure 21). In ceramic matrix composites pore shape plays a critical role in determining mechanical performance. Highly elongated pores (with low shape parameter values) tend to act as more severe stress concentrators compared to more equiaxed or circular pores. This can lead to localized stress intensification, promoting crack initiation and propagation under mechanical loading. As a result, materials with a higher proportion of elongated pores may exhibit reduced tensile strength, lower fracture toughness, and diminished fatigue resistance. Furthermore, elongated pores can facilitate faster oxygen ingress along their length, potentially accelerating oxidation processes and degrading the fiber–matrix interface, especially under high-temperature service conditions [96]. Therefore, controlling not only the size but also the shape of pores is essential for optimizing the durability and reliability of CMCs.

$$Shape\ parameter = \frac{Feret\ max}{Feret\ min} \tag{13}$$

Figure 19 Graphical representation of shape parameter

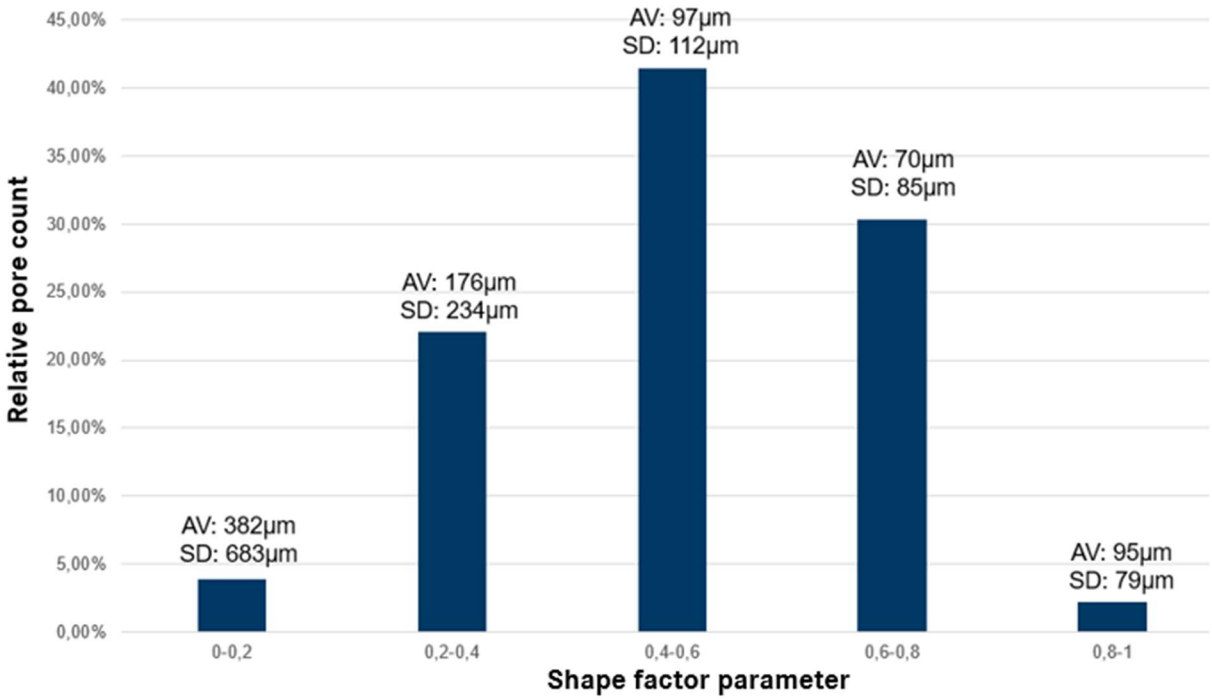

Figure 20 Cumulative distribution of pores shape in S200H

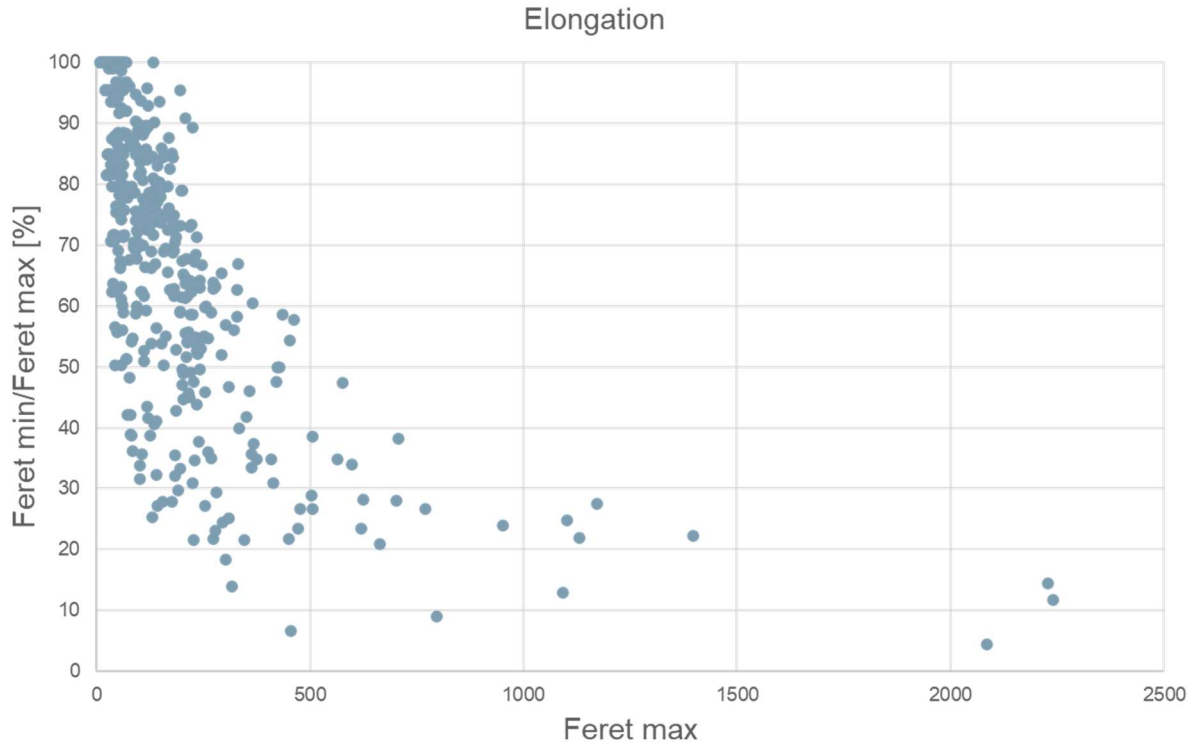

Figure 21 Correlation between pore size and shape in S200H

Interphase thickness

The interphase thickness on the SiC fibers is very important information about the quality of the CMC material. In such materials, the mechanical behavior depends on the interaction of the matrix with the fiber/matrix interfacial zone. Interphase of SiC/SiC composite is made out of BN/Si_3N_4. The fibers should be covered with a homogeneous and coherent BN/Si_3N_4 interphase with the appropriate width. Generally, the thickness of the interphase in composite materials can range from a few nanometers to several tens of nanometers. In the case of ceramic composites, this thickness can be adjusted based on the requirements for strength, flexibility, and resistance to cracking. The interphase in CMC is responsible for:

- acting as a mechanical fuse, i.e. to deflect the matrix microcracks,
- maintain a good load transfer between the fibers and the matrix.

What is more, the interphase could act as a buffer, absorbing partially the residual stresses at the fiber/matrix interfaces resulting from Coefficient Thermal Expansion incompatibility. To meet those functions, the interphase has to be thick enough and compliant. Too narrow or too thick interphase may not provide sufficient bonding to the fiber which can reduce the mechanical properties of the CMC composite. In addition, the interphase may act as a diffusion barrier for non-oxide fibers embedded in a silica glass-ceramic matrix. Finally, Ceramic matrix composites are used in elevated temperature and in the oxidizing atmospheres therefore the interphase should be resistant to oxidation. This last requirement is very important because CMCs are often microcracked and the microcrack network facilitates the in-depth diffusion of oxygen towards the interphases and the fibers [97]. Because of all those reasons, interphase thickness on SiC fibers needs to be checked.

The method of measuring the interface thickness has not been previously described in MTU therefore, this work proposes a research method that allows for determining this characteristic. During interphase thickness investigation of S200H material, 3 samples were checked. The samples were observed under SEM. The photos were done in high resolution mode with a view field: 5 μm. The measurements of interphase thickness were done in the IMS program. The measurements were conducted exclusively on the BN (boron nitride) coating, as it appears darker and thicker in SEM images, making it more distinguishable and easier to analyze. In contrast, the Si_3N_4 (silicon nitride) interphase exhibits a bright, thin outline that closely resembles the surrounding SiC matrix in morphology and contrast (Figure 24 a-c). Due to the limited

resolution and contrast capabilities of the available SEM equipment, it was not possible to reliably measure the Si_3N_4 layer. The cross section area of analyzed samples was divided into three sections: I, II and III (Figure 22). For the two extreme sections, two areas were selected for the location of the fibers for coating thickness measurements. In the middle section (II) one area was taken for coating thickness measurements.

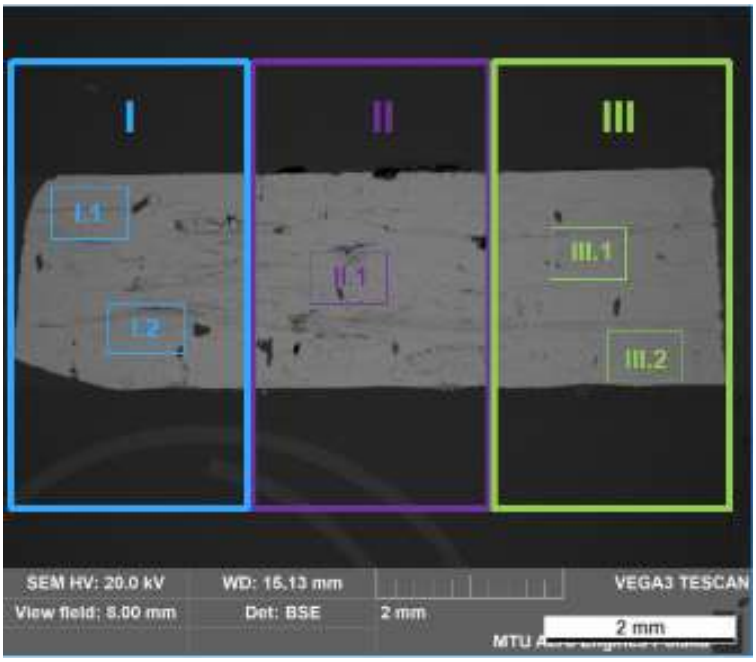

Figure 22 Exemplary area which was chosen for interphase thickness measurements.

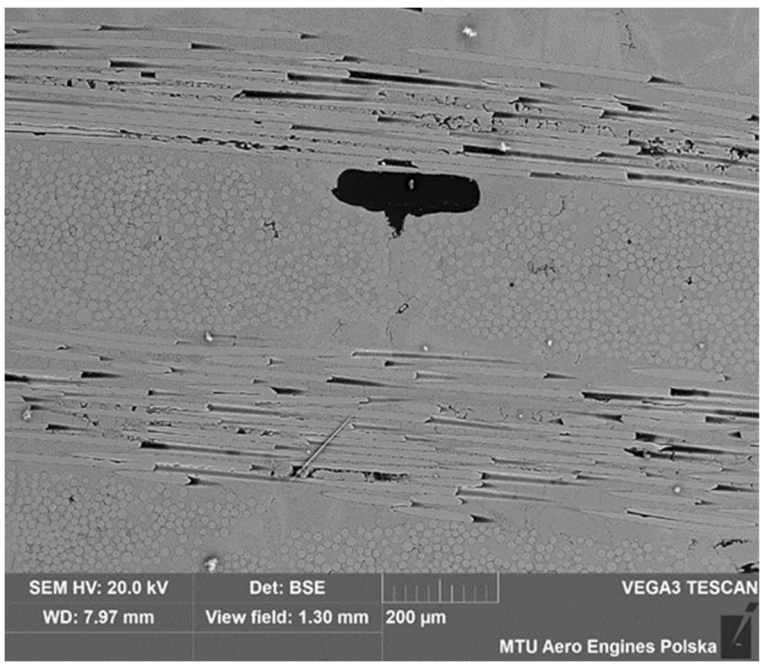

Figure 23 SEM Exemplary area chosen for the interphase thickness measurements.

For each areas, five fibers were measured (Figure 23). The fibers were at a distance of at least 5 times the fiber diameter from each other. Three interphase thickness measurements were done on each fiber (Figure 24 a, b and c).

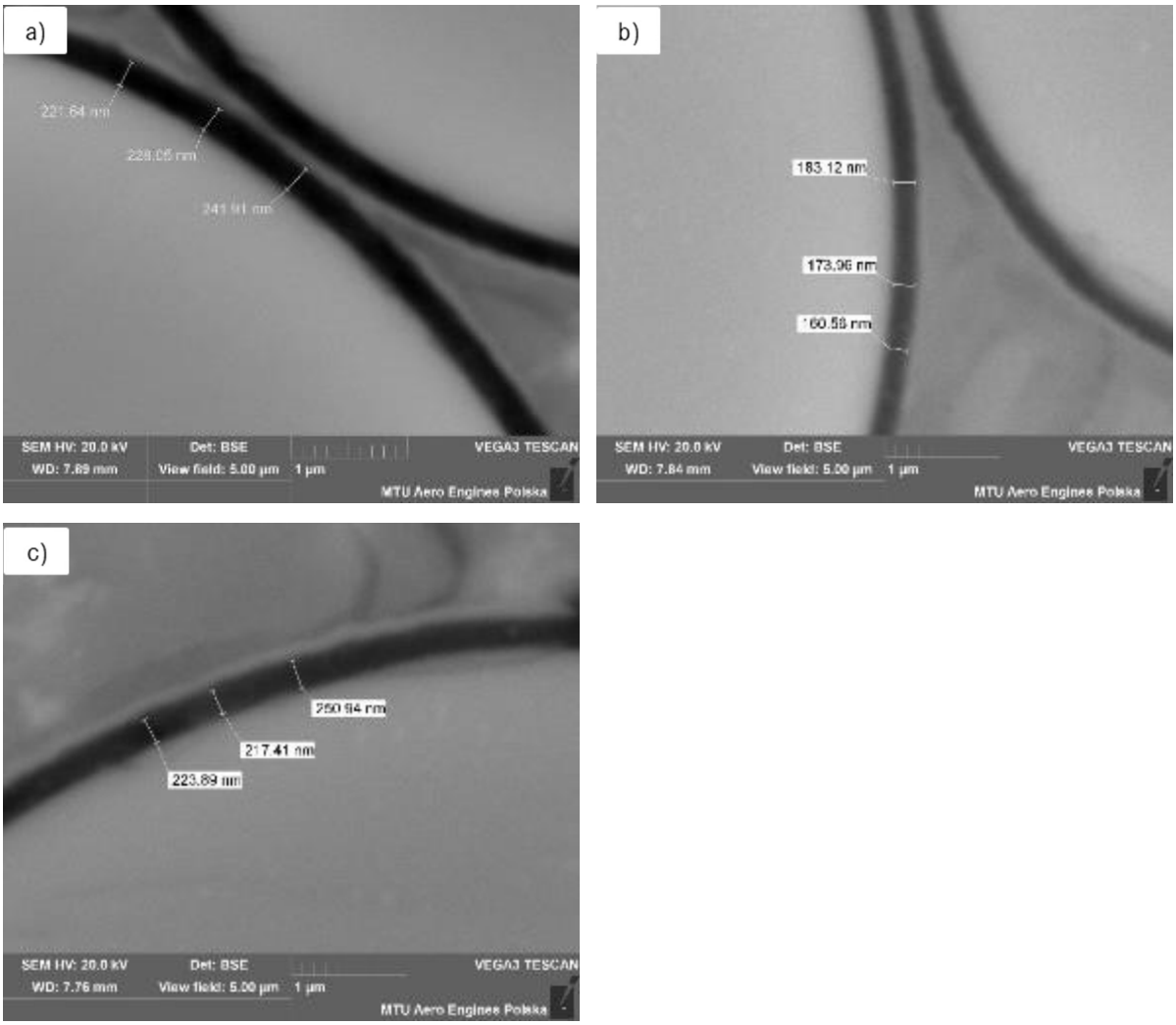

Figure 24 Interphase thickness measurements a), b) and c).

In total, 75 interphase thickness measurements were performed. For all measured fibers, interfacial fiber coating thickness (BN only) was in the range 193.83 nm to 258.32 nm in average (Table 10).

Table 10 Interphase thickness measurement of 3 samples

	Average interphase thickness [nm]	Average interphase thickness [nm]	Average interphase thickness [nm]	Average interphase thickness [nm]	Average interphase thickness [nm]
Fiber 1	227.70	214.39	230.53	186.70	239.24
Fiber 2	221.24	218.73	229.56	240.00	224.67
Fiber 3	221.70	209.84	176.16	224.22	238.10
Fiber 4	186.92	236.78	228.71	220.48	191.68
Fiber 5	231.42	227.88	231.77	236.41	212.76
Total	217.80	221.53	219.35	221.56	221.29
Fiber 1	240.57	196.40	131.21	207.92	196.73
Fiber 2	188.49	221.37	212.24	217.61	221.76
Fiber 3	211.69	216.40	197.38	206.45	211.45
Fiber 4	211.63	215.58	218.01	218.79	220.42
Fiber 5	212.81	216.95	210.29	215.30	205.09
Total	**213.04**	**213.34**	**193.83**	**213.21**	**211.09**
Fiber 1	284.29	255.75	258.98	233.42	222.43
Fiber 2	228.09	257.67	274.67	219.04	234.12
Fiber 3	261.95	265.36	253.06	247.90	231.40
Fiber 4	243.25	222.32	248.55	228.24	234.82
Fiber 5	227.69	227.88	256.35	234.61	221.61
Total	**249.05**	**245.80**	**258.32**	**232.64**	**228.88**

Variations in the thickness of the BN interfacial coating may result from several factors, including inconsistencies in the deposition process (e.g., chemical vapor deposition parameters such as temperature, gas flow rate, and time), surface roughness of the fibers, or local differences in fiber orientation and spacing. Additionally, the geometry of the fiber bundle and the accessibility of the coating precursor to inner fibers can lead to non-uniform coating distribution. Another important factor is the variation in fiber weave architecture, which can influence local fiber packing density and exposure during coating, thereby affecting the uniformity and thickness of the deposited interphase. These variations in coating thickness can significantly influence the mechanical behavior of the composite. A thicker BN layer may enhance crack deflection and energy dissipation at the fiber–matrix interface, improving fracture toughness. However, if the coating is too thick, it may reduce load transfer efficiency between the matrix and the fibers, leading to premature interfacial debonding. Conversely, a thinner or uneven coating may not provide sufficient interfacial protection, reducing oxidation resistance and increasing the risk of fiber damage during thermal or mechanical loading [95]. Therefore, maintaining a controlled

and uniform interphase thickness is critical for optimizing the performance and reliability of SiC/SiC composites.

Matrix pockets

Matrix pockets in ceramic matrix composite are regions within the composite were the matrix phase is more concentrated and consist less fibers compared to the rest of the material. Matrix pockets are forming during manufacturing process during the infiltration of the matrix into fiber preform and during densification stages. Matrix rich pockets play a very important role in the overall behavior of the CMC. Matrix pockets can influence the stress distribution, mechanical properties like tensile strength or fracture toughness, crack propagation and overall performance of the composite. It is essential to understand and manage the formation of matrix pockets during the manufacturing process to achieve the desired properties and performance of the final composite material. This influence arises from the inherent differences in mechanical and thermal behavior between the matrix and the reinforcing fibers. In matrix-rich regions, the absence of sufficient fiber reinforcement leads to localized variations in stiffness and strength, which can result in stress concentrations under mechanical loading. These stress concentrations may serve as initiation sites for microcracks, especially under cyclic or high-temperature conditions. Furthermore, the lack of fibers in these pockets reduces the material's ability to deflect or bridge cracks, thereby facilitating faster crack propagation. Crack bridging is a toughening mechanism in which intact fibers span across a crack and hold the two faces of the crack together. This mechanism helps to slow down or even arrest crack growth, significantly improving the fracture toughness and damage tolerance of the composite. In matrix-rich areas, where fibers are sparse or absent, this beneficial mechanism is limited or entirely missing, making the material more susceptible to brittle failure [98]. From a thermal perspective, matrix pockets may exhibit different thermal conductivity and expansion behavior compared to fiber-rich areas, potentially leading to thermal gradients and residual stresses during service. Overall, while matrix pockets are often an unavoidable consequence of the manufacturing process, their presence must be carefully controlled and understood, as they can critically affect the structural integrity and reliability of ceramic matrix composites in demanding applications.

Matrix pockets can occur as inter-lamellar matrix layers between plies or as interlaminar matrix pockets within a single layer (Figure 25).

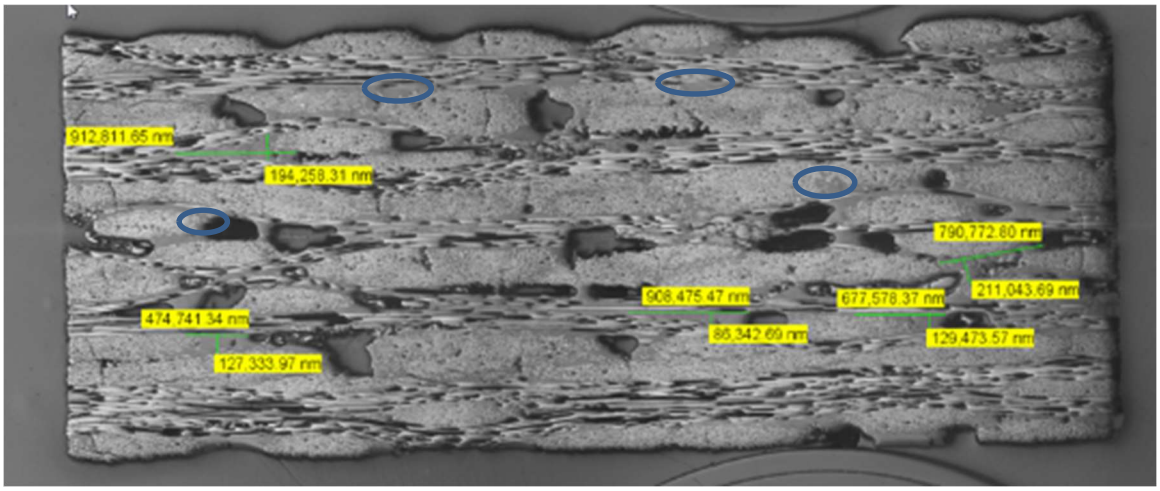

Figure 25 Matrix rich pockets in CMC Composite

Since the method for measuring matrix pockets has not been previously described in MTU, this study proposes a research approach that enables the determination of this characteristic. The verification of the areas and total number of matrix pockets was carried out using the IMS program. This program is designed to identify and calculate the matrix rich pockets automatically. Unfortunately, the low contrast between matrix and fibers makes impossible to automatically differentiate them and additional manual coloring was needed. Below, the following steps have been presented:

1. Manual identification of matrix rich pockets areas
2. Threshold range
3. Region of interest
4. Corrections
5. Results

Using the previously proposed research method, 3 samples were analyzed (Figure 26 a, b and c), and their results are presented below (Table 11):

Table 11 Results for matrix rich pockets

Sample number	Effective Area	Area Fraction	
	mm^2	%	mm^2
1	86.8	18.5	16.1
2	75.5	6.0	4.5
3	24.8	8.6	2.1

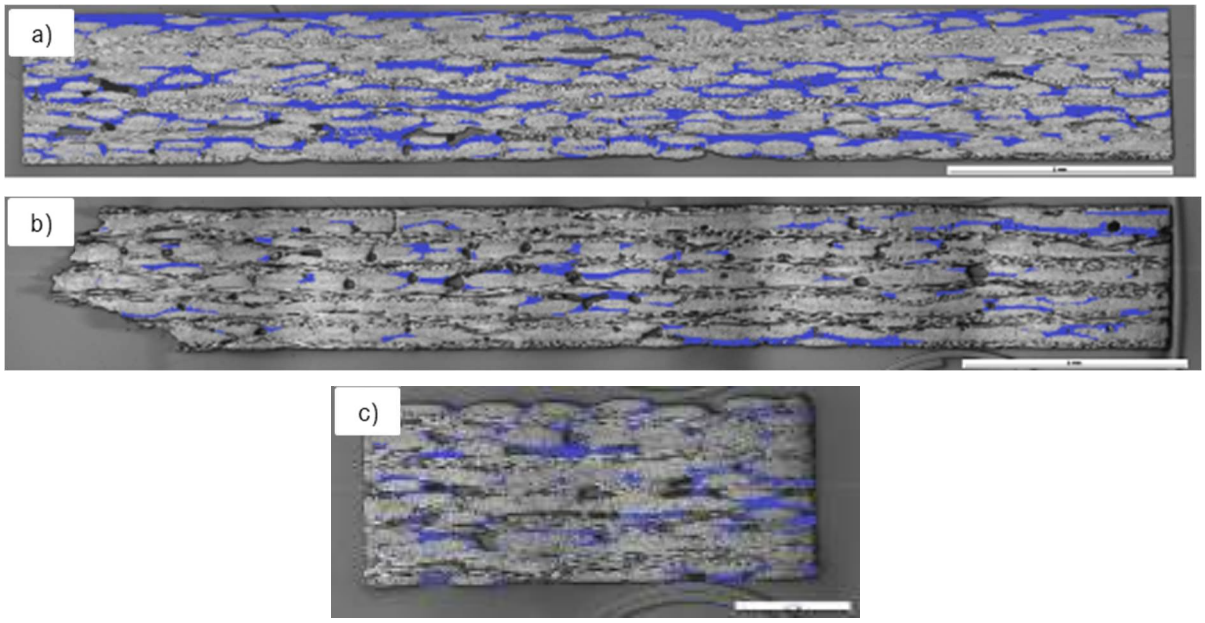

Figure 26 SEM pictures a) sample number 1, b) sample number 2, c) sample number 3

The area fraction of matrix rich pockets for the analyzed samples was in the range of 5.9-18.5% with reference to the entire surface of the sample. The observed differences in the area fraction values can be primarily attributed to the variation in the effective area analyzed for each sample. As shown in Table 11, Sample 1 had the largest effective area (86.8 mm²) and exhibited the highest matrix-rich pocket fraction (18.5%), while Sample 3, with the smallest effective area (24.8 mm²), showed a lower fraction (8.6%). This trend suggests that larger analyzed areas are more likely to intersect a greater number of matrix-rich regions, which are typically distributed non-uniformly throughout the composite microstructure. Consequently, the probability of detecting such features increases with the size of the observed area. Interestingly, Sample 2, despite having a relatively large effective area (75.5 mm²), exhibited the lowest matrix-rich pocket fraction (6.0%). This result may be explained by the more uniform microstructure in the analyzed region of this sample. It is possible that the matrix infiltration process in Sample 2 was more homogeneous, resulting in fewer localized accumulations of matrix material. Additionally, the analyzed area may have coincided with a region of the composite that naturally contained fewer matrix-rich zones due to better fiber packing or more efficient densification during processing. In addition to the influence of effective area and local microstructure, other factors such as fiber orientation, compaction quality, and processing conditions (e.g., temperature gradients or infiltration rate) may also contribute to the observed differences in matrix distribution.

Cracks

Figure 27 presents SEM images of the SiC/SiC composite microstructure at two view fields: a) 5 mm and b) 500 µm. Within these images, several linear features can be observed in the matrix phase. Although these features visually resemble cracks, a detailed analysis indicates that they are not open or structurally critical defects. Instead, they are most likely closed microcracks or matrix discontinuities that developed during earlier stages of processing and were subsequently healed during the matrix infiltration phase. These features are characterized by their sharp, linear morphology and their alignment with the local fiber architecture. Importantly, there is no evidence of contrast variation or voids along their length, which would typically indicate the presence of open cracks. Furthermore, no signs of delamination, fiber pull-out, or crack branching were observed, which confirms that these features do not propagate through the composite structure. The absence of both transverse and longitudinal open cracks in the analyzed regions suggests that the composite underwent effective densification and that the infiltration process successfully filled any microstructural discontinuities. The matrix appears continuous and well bonded to the fibers, with no visible signs of interfacial degradation. Although the term "crack" is used throughout the text for consistency, it is important to emphasize that the observed features do not compromise the structural integrity of the material. Rather, they represent typical microstructural characteristics of ceramic matrix composites. Their presence does not indicate damage or failure but reflects the complex nature of the composite's internal structure and the effectiveness of the manufacturing process in mitigating critical defects.

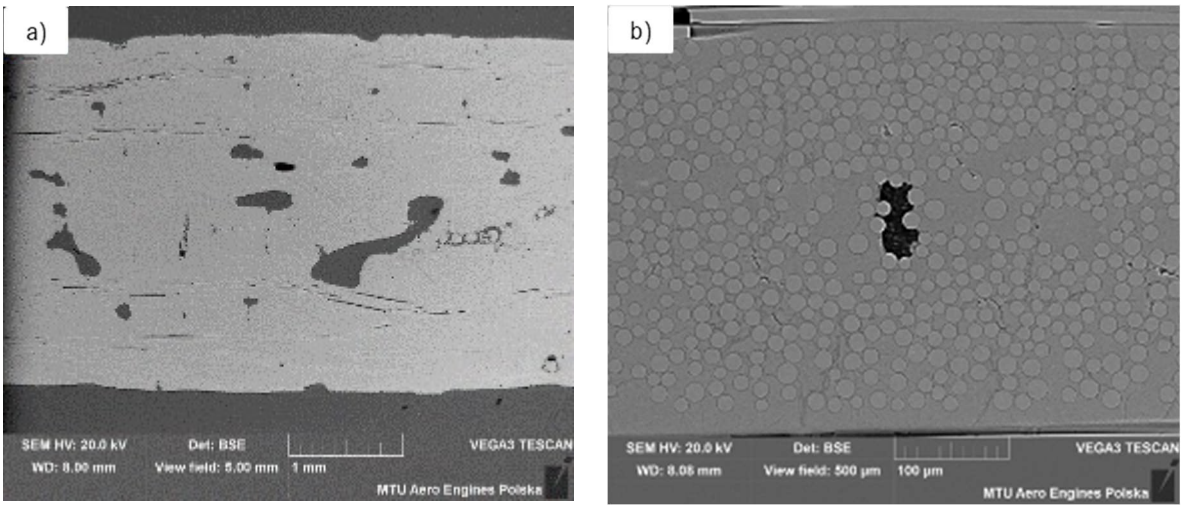

Figure 27 Cured cracks in matrix in the SiC/SiC material, a) view field 5 mm, b) view field 500 µm

Composition

XRD pattern obtained for pristine sample is shown in Figure 28. SiC/SiC composite reveals SiC (Hexagonal, P63mc) and Si_3N_4 (Hexagonal, P31c), where the main peaks are at 2θ of 35.7 º and 20.6 º respectively. The identified hexagonal SiC corresponds to the α-SiC polytype, which is consistent with the findings reported in the literature [42]. No additional phases were detected. Although the composite contains elements such as nitrogen and boron, these were not identified as separate phases in the XRD pattern. This is due to the nature of XRD, which detects only crystalline structures with long-range atomic order. If nitrogen is present in an amorphous form or as part of a disordered phase, it would not produce distinct diffraction peaks. Therefore, elemental nitrogen is not visible in the XRD spectrum. Similarly, boron was not detected. This can be explained by the fact that boron in the composite is present in the form of boron nitride (BN), which is often poorly crystalline or turbostratic when used as a fiber coating. Such disordered or nanocrystalline forms of BN produce very weak or broad diffraction signals that may fall below the detection threshold of the instrument or overlap with stronger peaks from SiC and Si3N4. According to the manufacturer of the S200H material, the matrix is composed of silicon carbonitride (SiNC). No diffraction peaks corresponding to the SiNC matrix were observed. This is most likely due to the amorphous crystalline nature of the SiNC phase, which is typically formed by pyrolysis of polymer-derived precursors. Such materials lack long-range atomic order and therefore do not produce sharp diffraction peaks in XRD. Instead, they may generate broad, low-intensity halos that are often indistinguishable from the background or masked by the intense signals from crystalline SiC and Si_3N_4.

Furthermore, the influence of the sample surface on the XRD results was analyzed. Measurements were carried out on two different surfaces of the same CMC SiC/SiC sample: one corresponding to the original surface provided by the supplier (shorter plane (Figure 7)), and the other being a freshly cut surface along the longer edge of the sample (longer plane (Figure 7)). The XRD patterns obtained from both surfaces revealed identical peak positions, indicating no differences in phase composition or crystallographic structure between the analyzed areas (Figure 29). This confirms that the material exhibits the same crystalline characteristics regardless of the surface being measured. However, a significant difference in peak intensity was observed. Firstly, the cut surface had a larger area exposed to the X-ray beam, which allowed a greater volume of the microstructure to be analyzed. As a result, more components of the composite - such as fibers, fiber coatings, and the matrix-contributed to the diffraction signal. It is also worth

noting that a slight difference in surface chemistry may have contributed to the observed intensity variation. The original surface, as delivered by the supplier, may have been subtly oxidized due to exposure to air during storage or handling. In contrast, the freshly cut surface was free from such surface oxidation, potentially resulting in a cleaner and more representative diffraction signal. Additionally, the freshly cut surface was likely smoother and more uniform, which enhanced X-ray reflection and reduced scattering. In contrast, the original surface may be rougher or have some oxygen content due to storage of the samples, which can attenuate the signal. Despite this difference in intensity, the consistent peak positions confirm that the surface type does not affect the accuracy of phase identification. Therefore, in the subsequent analysis: the influence of surface type (cut vs. uncut) on XRD results is considered negligible and will be omitted.

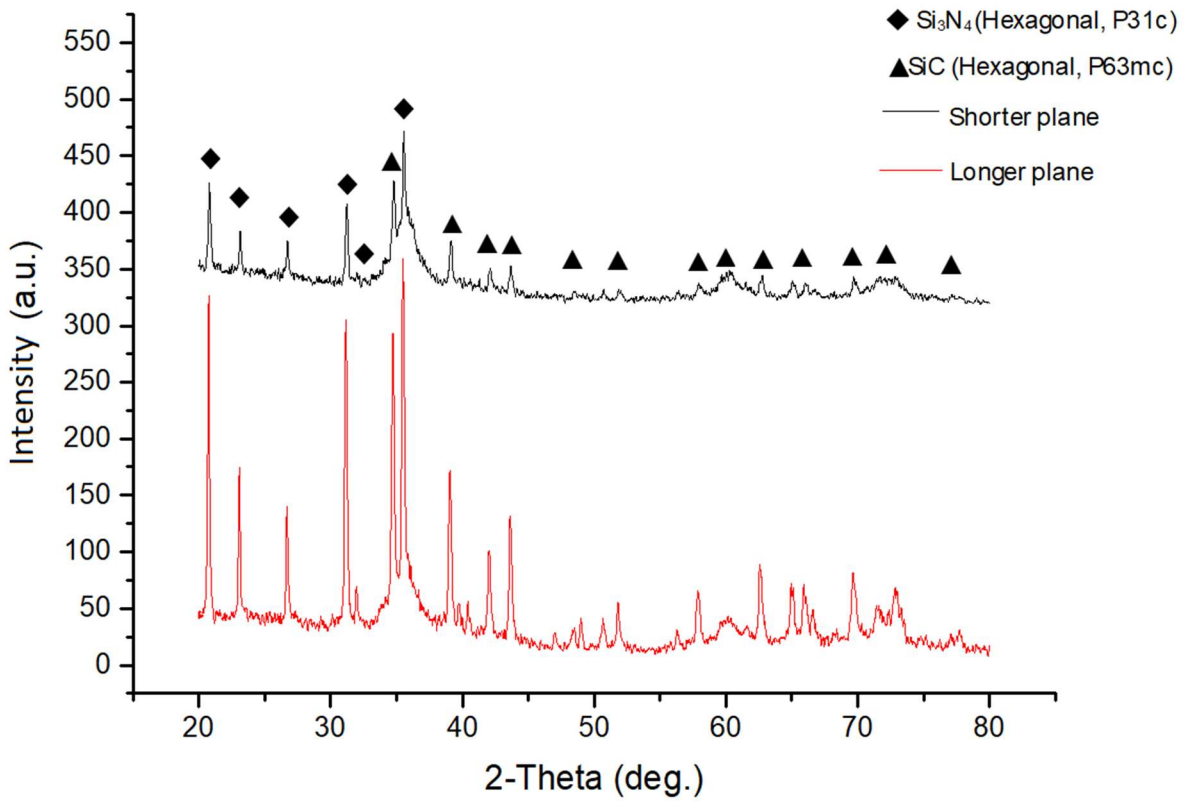

Figure 28 XRD of SiC/SiC composite, as received sample

Energy Dispersive Spectroscopy (EDS) measurements were done using Aztec program. Analysis of EDS measurements showed the presence of elements: Si, C, O and N (Figure 29, Figure 30, Figure 32, Figure 33). Silicon is the dominant element because it is a primary component

of SiC/SiC composite as well as carbon. Characteristic peaks (Figure 31, Figure 34) for silicon carbon, nitrogen and oxygen are visible at specific energy values:

- Silicon (Si): Si-kα is around 1.70 keV.
- Carbon (C): C-kα is around 0.35 keV
- Nitride (N): N-kα is around 0.40 keV
- Oxygen (O): O-kα is around 0.50 keV

To ensure a comprehensive understanding of the material's microstructure and chemical uniformity, EDS measurements were conducted in multiple regions of the sample, including areas near the fiber–matrix interface to assess the integrity of the fiber coatings and detect any elemental diffusion or reaction zones, regions with visible or suspected microcracks to verify whether the cracks were sealed or filled with matrix material and to check for any signs of oxidation or contamination, bulk matrix regions to confirm the low oxygen content and the homogeneity of the SiNC phase, as well as surface and subsurface zones to compare the elemental composition and detect any surface oxidation or environmental degradation. One of the key objectives of the EDS analysis was to verify the low oxygen content in the composite, which is critical for high-temperature stability and oxidation resistance. The results confirmed that oxygen was present only in trace amounts, likely limited to the outermost surface layers, possibly due to brief exposure to air during sample preparation or handling. Additionally, no foreign elements or unexpected inclusions were detected, and the elemental maps showed an uniform distribution of Si, C, and N, indicating that the material is chemically homogeneous and free from significant defects or contamination. The EDS analysis also supported the absence of structural damage in the analyzed regions. In areas where healed-cracks were observed under SEM, the EDS data revealed that these were either sealed by matrix infiltration or did not show signs of oxidation, suggesting that the material retained its structural integrity. It is important to note that EDS is a qualitative or semi-quantitative technique, meaning it provides information about the presence and relative distribution of elements but does not offer precise quantitative data on their concentrations. For accurate elemental quantification, more advanced analytical techniques such as Wavelength Dispersive X-ray Spectroscopy (WDS), Inductively Coupled Plasma Optical Emission Spectroscopy (ICP-OES), or X-ray Photoelectron Spectroscopy (XPS) would be more suitable. However, these methods are not available in the current laboratory setup.

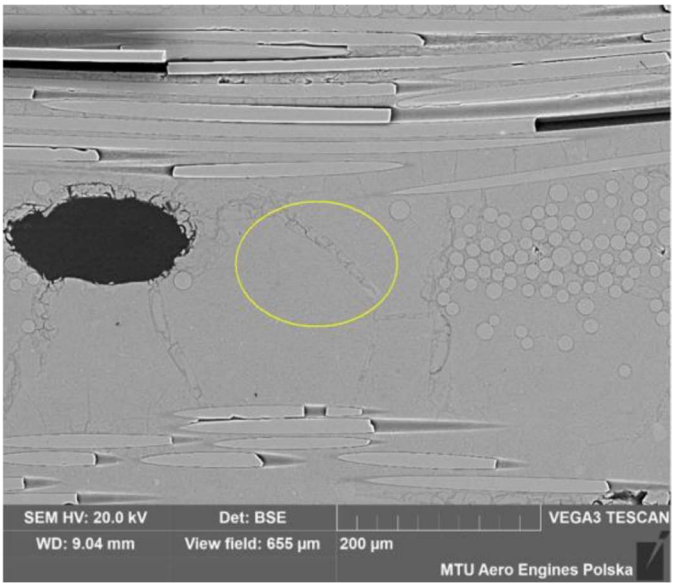

Figure 29 Area 1 selected for ESD analysis, view field 655 µm

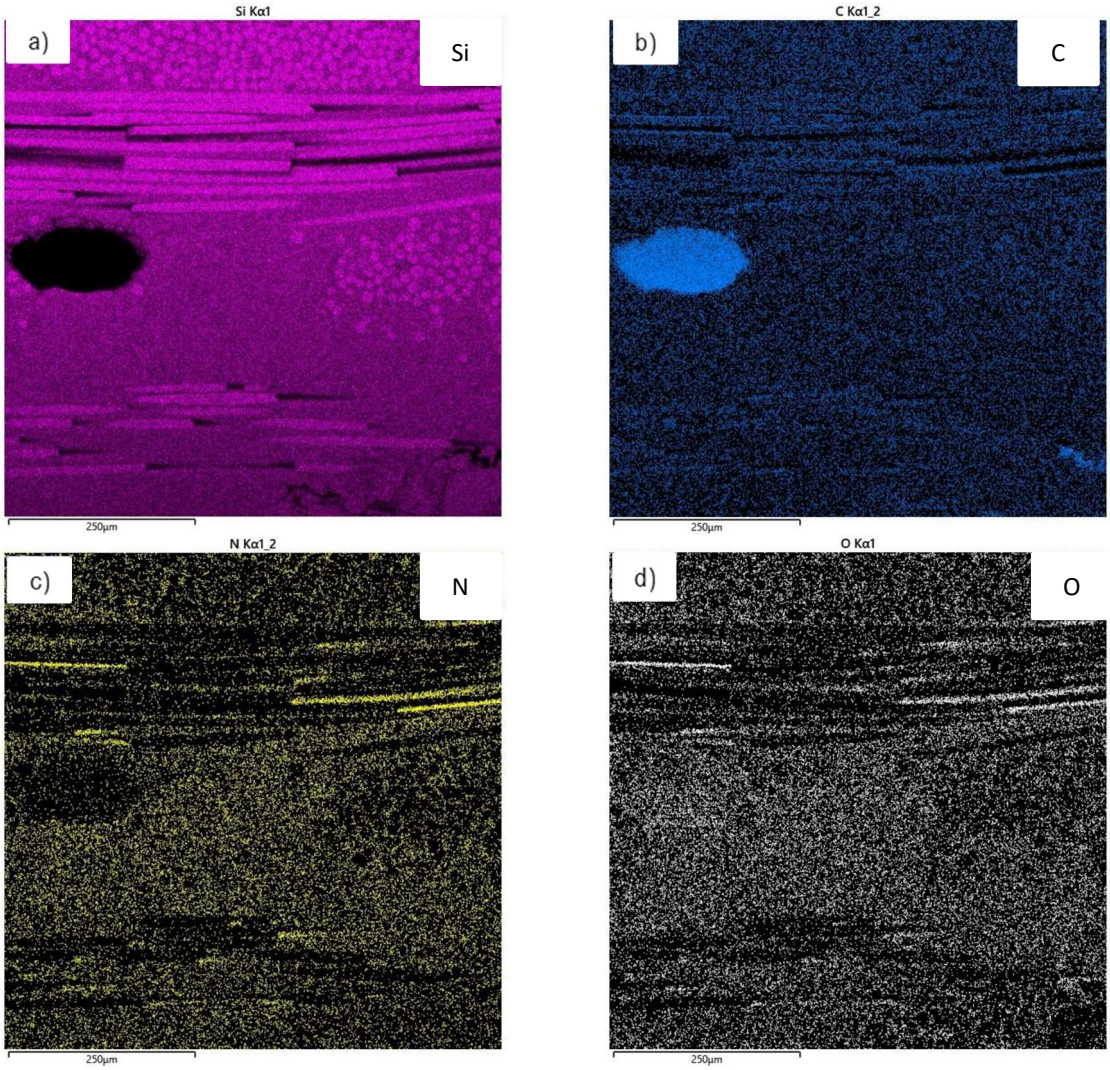

Figure 30 EDS elemental mapping of S200H composite (area 1) : a) Si, b) C, c) N, d) O

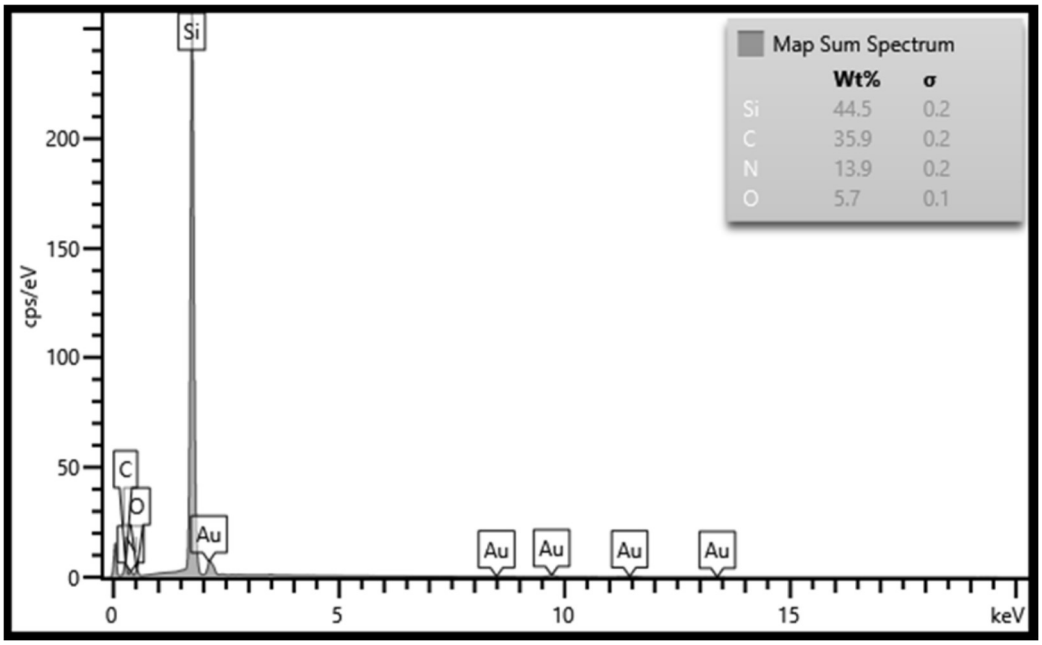

Figure 31 Spectrogram of SiC/SiC composite

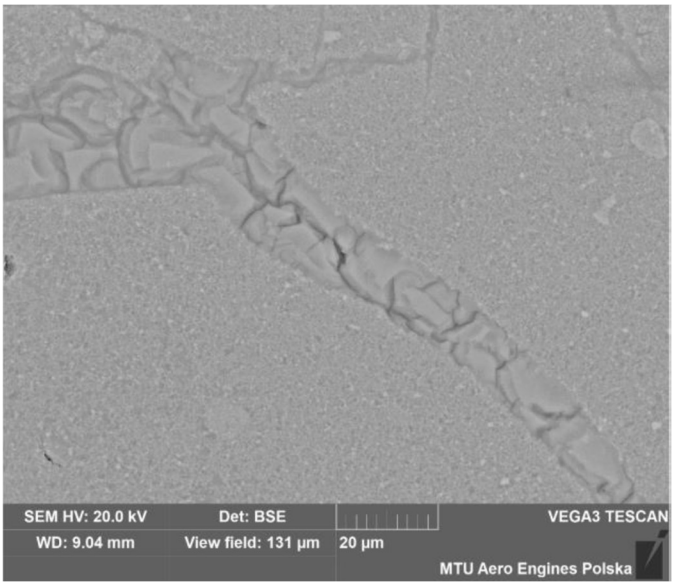

Figure 32 Area 2 selected for ESD analysis, view field 131 µm

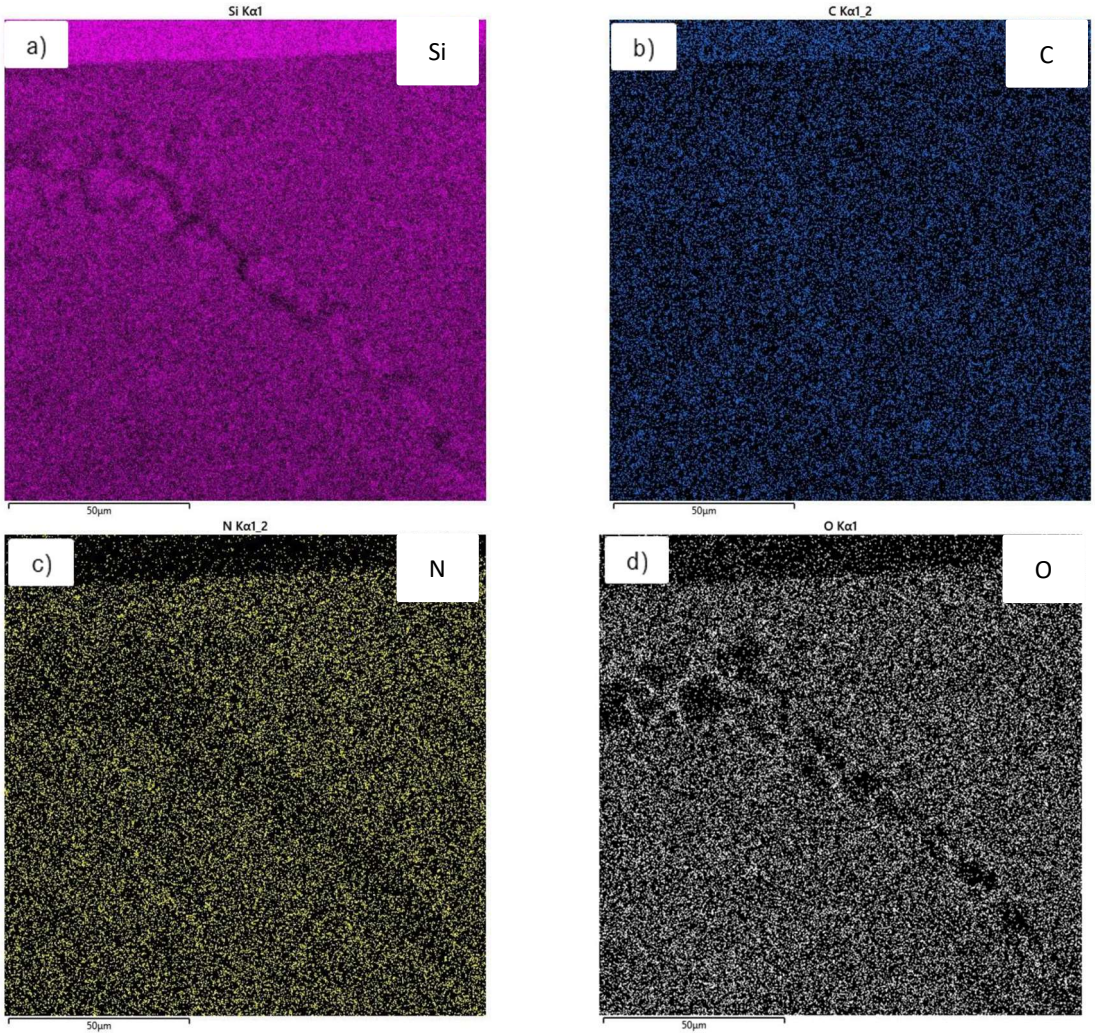

Figure 33 EDS elemental mapping of S200H composite (area 2) : a) Si, b) C, c) N, d) O

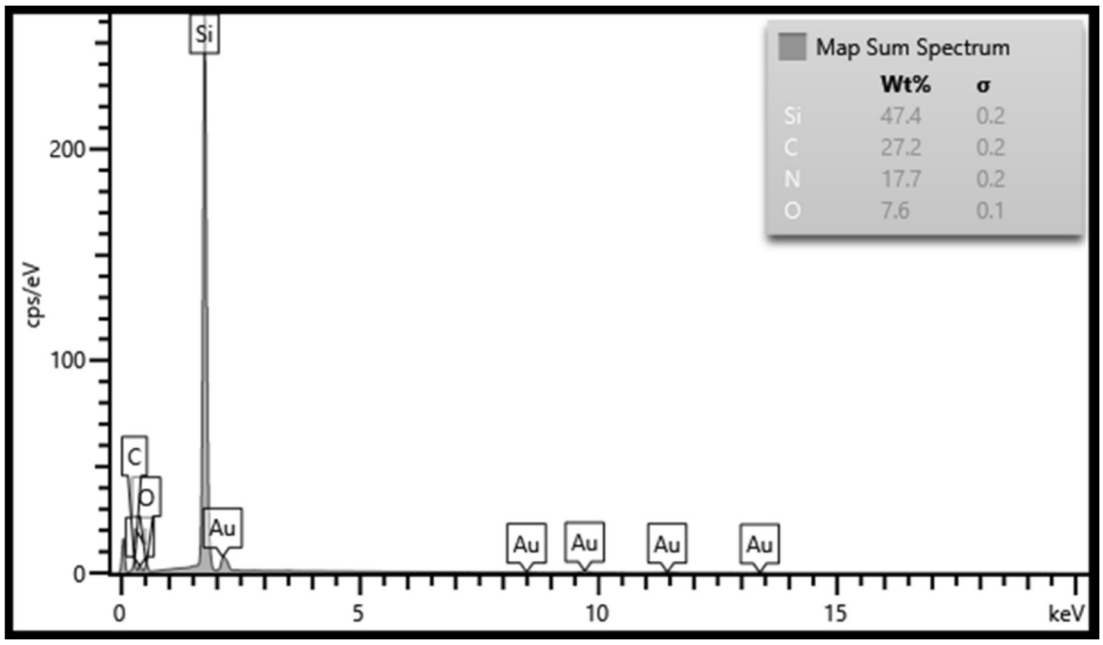

Figure 34 Spectrogram of SiC/SiC composite

Thermal Analysis:

The thermal behavior of the SiC/SiC composite, consisting of a silicon carbonitride (SiNC) matrix and SiC fibers coated with boron nitride (BN) and silicon nitride (Si_3N_4), was investigated using simultaneous thermogravimetric analysis (TGA) and differential scanning calorimetry (DSC). The DSC curve complements the TGA data by providing insight into the thermal events associated with these processes (Figure 35).

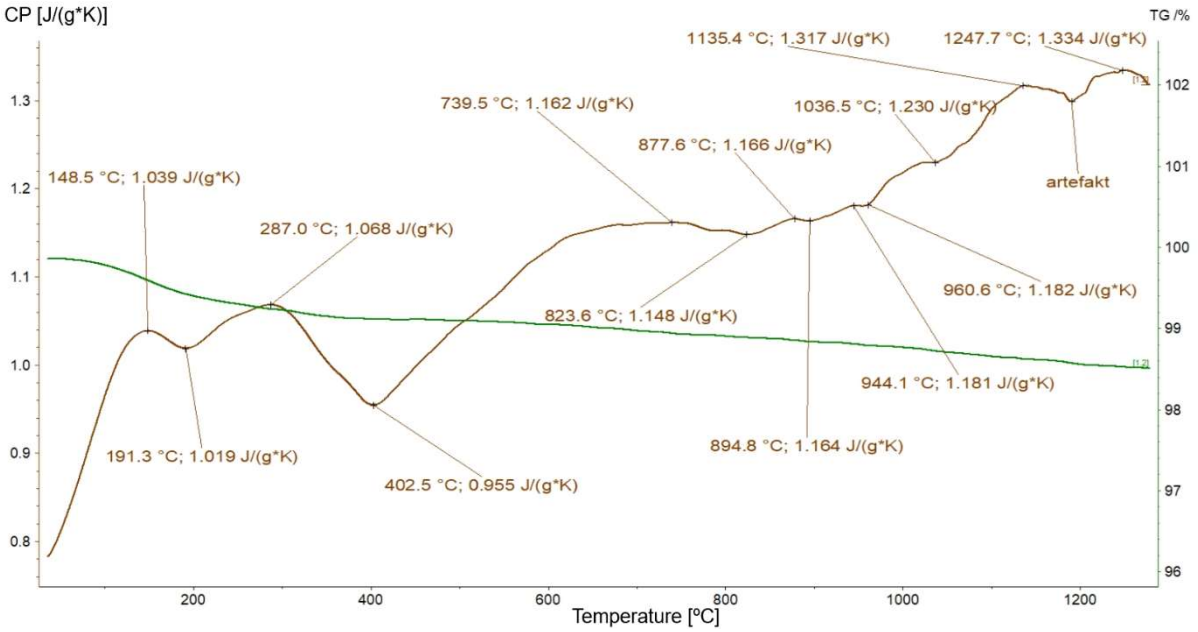

Figure 35 DSC and TGA curves for S200H composite tested atthe temperature range 0-1200 °C

The first three peaks, occurring at 148.5, 191.3, and 287.0 °C, are relatively minor and likely correspond to the removal of adsorbed moisture, low-temperature desorption of surface-bound species, or the release of residual solvents or processing by-products from the matrix or fiber coatings. These are typical for materials that have undergone prior processing and may still contain trace volatiles. The peak at 402.5 °C, which shows a slight decrease in Cp, may indicate the onset of structural relaxation or the beginning of oxidation of more reactive components in the matrix, such as free carbon or nitrogen-rich phases in the SiNC. This could also be associated with the initial formation of a thin oxide layer on the surface of SiC or Si_3N_4. Between 739.5 and 944.1 °C, a series of small but consistent increases in Cp are observed. These likely reflect the progressive oxidation of the matrix and coatings, particularly the formation of silica (SiO_2) from SiC and Si_3N_4, and boron oxide (B_2O_3) from BN. These reactions are typically exothermic but may appear as gradual Cp changes due to overlapping processes and the slow kinetics of oxide scale growth. The absence of sharp peaks suggests that the oxidation is relatively uniform and does not involve abrupt phase transitions. Above 1000 °C, the DSC curve

shows a more pronounced increase in Cp, with notable features around 1038 and 1135 °C. These may correspond to the breakdown or destabilization of the oxide scale, increased oxidation rates, or the onset of volatilization of oxidation products such as SiO and B_2O_3. The sharp rise in Cp at these temperature could also indicate the formation of glassy or liquid phases, particularly if B_2O_3 begins to melt or interact with silica, forming a viscous surface layer.

The microstructural characterization of the SiC/SiC composite in the as-received condition provides valuable insights into the quality of the material delivered by the supplier. The results indicate high quality, which is essential for aero engine production by MTU. The analysis allows for identifying critical features that may influence the material's strength under high-temperature and load conditions. This information is crucial for determining the material's failure mechanism and boundary conditions. The findings from this research will be beneficial for MTU in approving the material from the supplier. The technical documentation based on these results will enable laboratory engineers to assess whether the delivered material complies with the applicable requirements.

6.2 Oxidation

The oxidation studies of the SiC/SiC composite were conducted as described in Chapter 5.2.7 and according to Scheme Figure 9. The microstructural examination of the samples after oxidation processes were conducted as described in Chapter 5.2.1. The XRD measurements were carried out according to the procedure described in 5.2.3. In this work, the results were divided into three main subsections based on the oxidation temperature: 980, 1100 and 1300 °C, which were further categorized based on the oxidation times: 20, 40, 80 and 100 hours. In addition to observing the microstructural features of the samples after the oxidation process, the weight of the samples was measured before and after each oxidation process. Based on these results, the activation energy of oxidation was calculated based on the equation 14. The relationship between the change in mass divided by the cross-section of the sample and the oxidation time for each of the three temperature was presented in Figure 37. The XRD measurements were compiled into three aggregate graphs for each oxidation temperature, illustrating the effect of oxidation time on the elemental content in the SiC/SiC composite (Figure 36).

X-ray diffraction (XRD) analysis was conducted on S200H ceramic matrix composite subjected to oxidation at three different temperature: 980, 1100 and 1300 °C. For each temperature, measurements were taken after 20, 40, 80, and 100 hours of exposure. The results were compared to the as-received material to evaluate the evolution of crystalline phases during oxidation. In all oxidized samples, new diffraction peaks appeared that were not present in the as-received material. These peaks, most notably the one at approximately 2θ 22.95 °, were identified as belonging to silicon dioxide (SiO_2) (Figure 36). The emergence of SiO_2 peaks indicates the formation of an oxide layer on the surface of the composite as a result of high-temperature oxidation. As the oxidation time increased, the intensity of the SiO_2 peaks also increased, reflecting the progressive growth of the oxide layer. Concurrently, a gradual decrease in the intensity of Si_3N_4 peaks was observed, suggesting partial degradation or transformation of this phase during oxidation. The SiC peaks remained present but showed a slight reduction in intensity, likely due to the overlaying SiO_2 layer, which attenuates the signal from the underlying material. When comparing the results at 1100 and 1300 °C, the differences in oxidation behavior become more pronounced (Figure 36 b) and c)). At 1100 °C, the formation of SiO_2 is evident but moderate, with peak intensities increasing steadily over time. In contrast, at 1300 °C, the SiO_2 peaks are significantly more intense and appear earlier, indicating a more aggressive and accelerated oxidation process. Additionally, the suppression of Si_3N_4 and SiC peaks is more substantial at

1300 °C, confirming that higher temperature promote more extensive structural and compositional changes in the composite. These findings demonstrate that both oxidation time and temperature have a direct impact on the phase composition of the SiC/SiC composite, with SiO_2 formation being a key indicator of oxidation progression.

a)

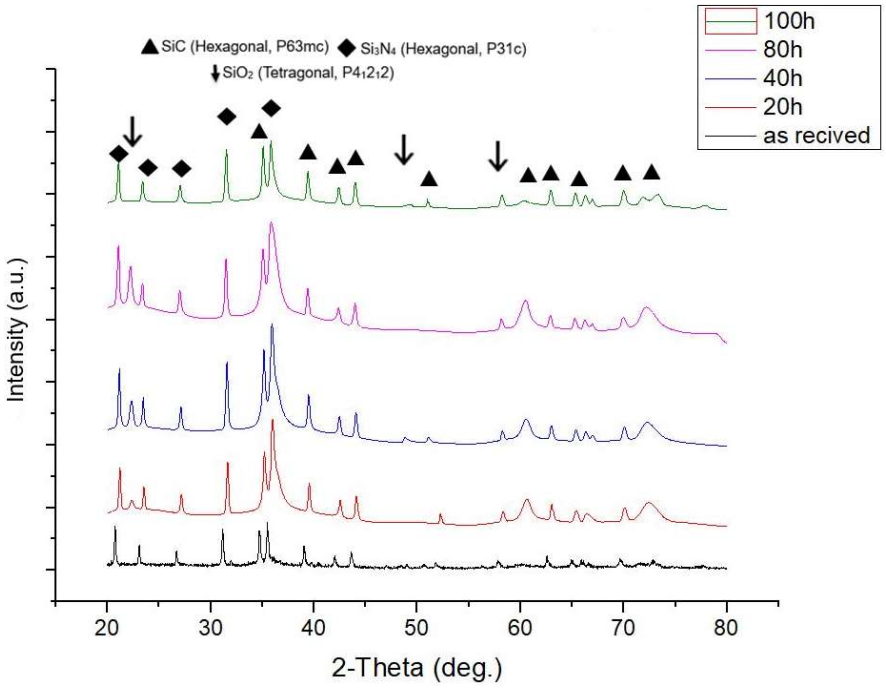

b)

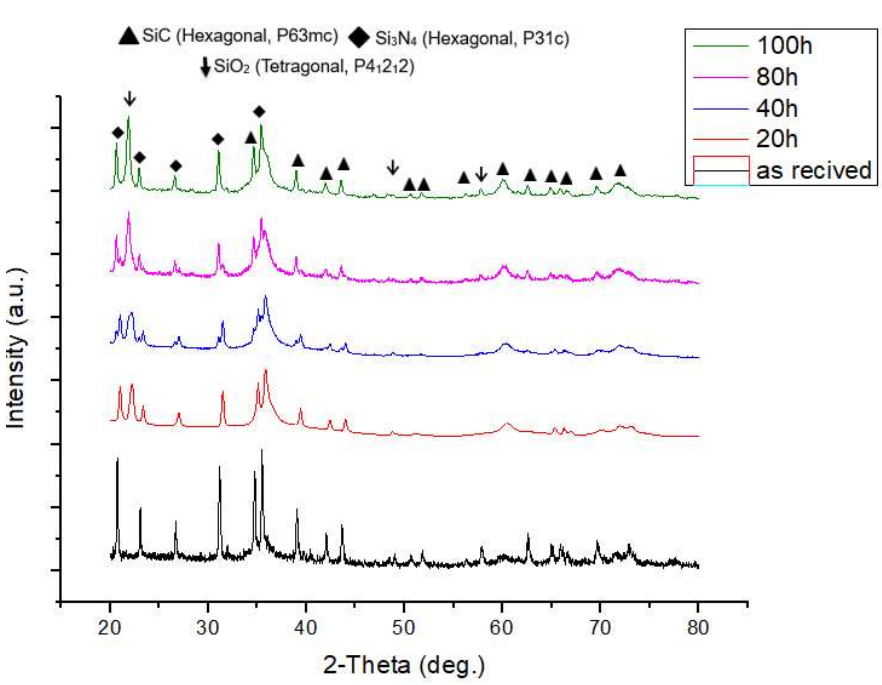

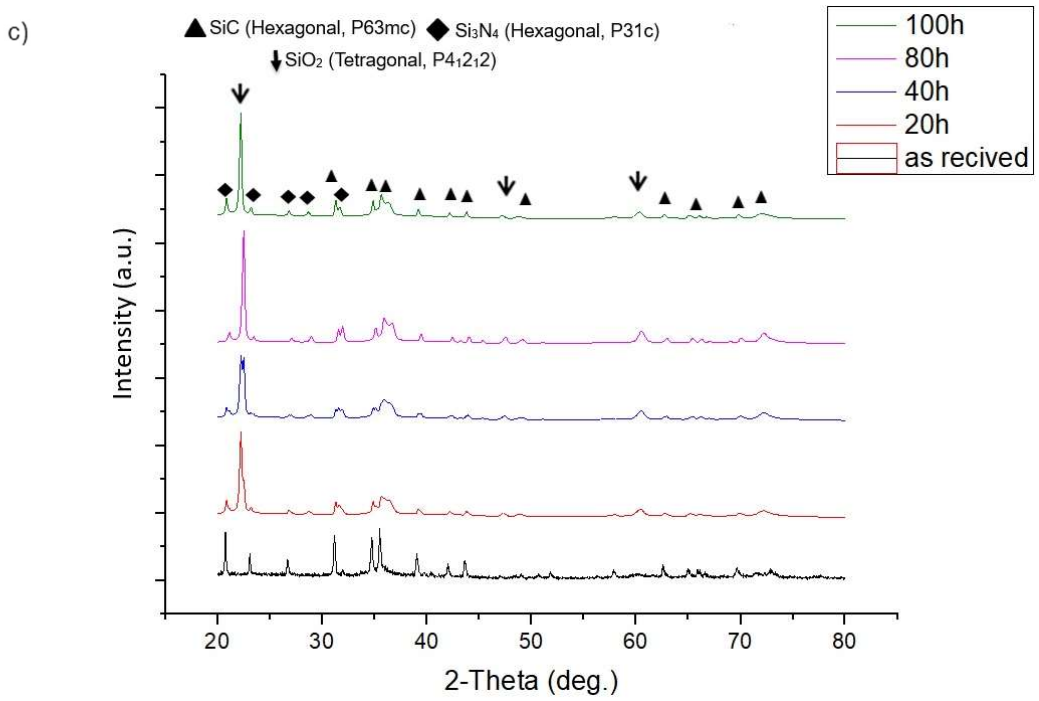

Figure 36 XRD patterns of S200H composite oxidized at: a) 980 ºC, b) 1100 ºC and c) 1300 ºC

Oxidation kinetics refers to the study of the rate and mechanisms by which materials react with oxygen or other oxidizing agents, typically at elevated temperature. This process leads to the formation of an oxide layer on the material's surface, which may act as a protective barrier or, conversely, contribute to structural degradation. Understanding oxidation kinetics is crucial in materials engineering, especially in the design of materials resistant to high temperature corrosion. This is particularly important for components operating under extreme conditions, such as gas turbine blades, aircraft engine parts, and nuclear reactor elements. The most commonly used method for studying oxidation kinetics is thermogravimetric analysis (TGA), which involves measuring the mass gain of a sample over time during oxidation. The collected data allows to determine the kinetic law governing the process - this may follow linear, parabolic, logarithmic, or more complex behaviors [99]. The mass gain is directly related to the amount of oxygen absorbed and the growth of the oxide scale. When the oxide layer is dense and adherent, it can slow down further oxidation, leading to a change in the reaction mechanism.
Oxidation kinetics can be analyzed by using a parabolic power law [42]:

$$\left(\frac{\Delta w}{A}\right) = \sqrt{k * t} \tag{14}$$

Where: Δw is the weight change during oxidation process, A is the oxidized surface area, k is the parabolic rate constant and t is the oxidation time.

The rate of oxidation is strongly temperature - dependent and is typically described by the Arrhenius equation [100]:

$$k = A * e^{(-\frac{E}{RT})} \quad (15)$$

Where, A is a constant, R is the gas constant, T is the oxidation temperature.

Activation energy is the minimum amount of energy that reacting molecules must possess in order for a chemical reaction to occur. It represents the energy barrier that must be overcome for reactants to be transformed into products. The magnitude of the activation energy determines the rate of the reaction - the higher the activation energy, the slower the reaction at a given temperature.

To evaluate the oxidation resistance of S200H composites, the primary focus was placed on measuring the mass change of the samples after exposure to high temperature in air. Each sample was weighed before oxidation using a precision analytical balance to determine its initial mass. After oxidation, the samples were cooled to room temperature and weighed again to determine the final mass. The weight change (Δw) was calculated as:

$$\Delta w = w_{after} - w_{before} \quad (16)$$

Oxidation kinetics at 980, 1100 and 1300 °C are illustrated in Figure 37 a), b) and c), in which mass gain per unit area is presented with best fitting curves according to equation 14. The mass change per unit area (Δw/A) was recorded and plotted as a function of time. To interpret the oxidation kinetics, the experimental data were fitted using a parabolic oxidation model ($\Delta m^2 \propto t$), which reflects diffusion-controlled oxide growth.

a)

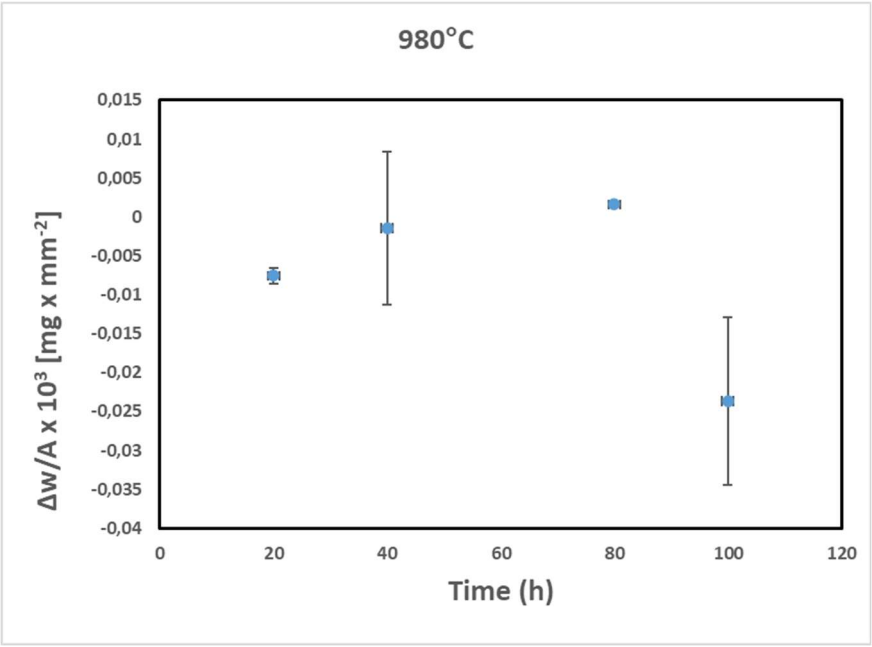

b)

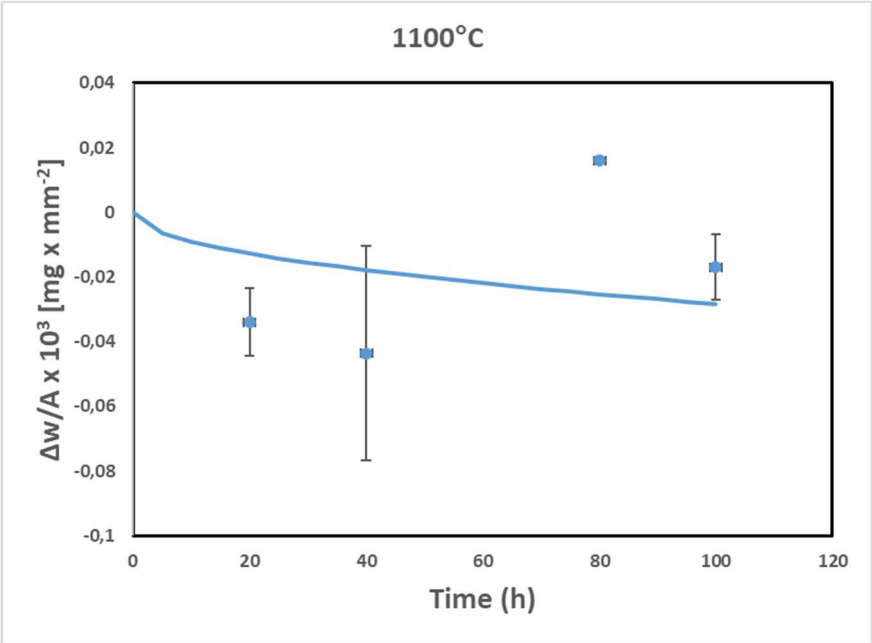

c)

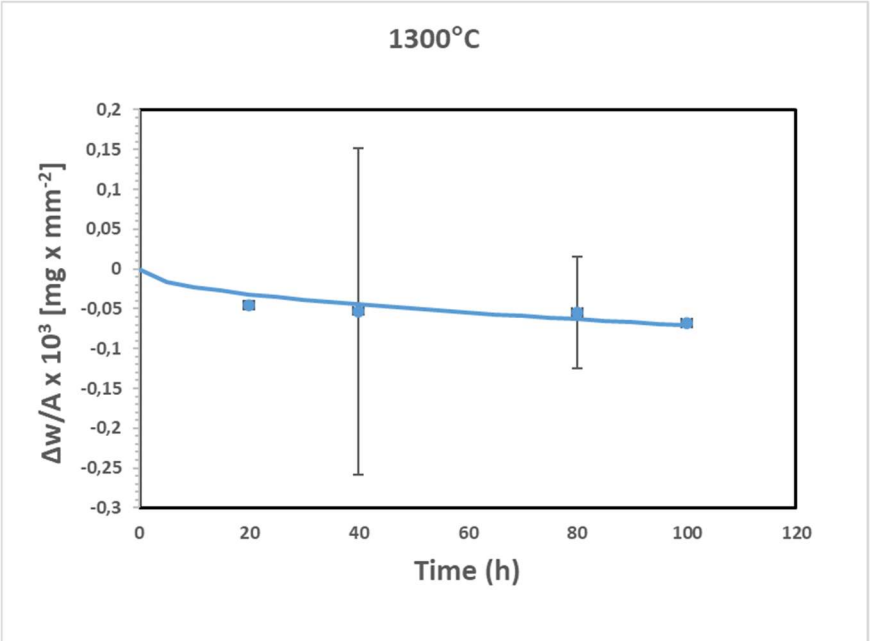

Figure 37 Mass gain versus time at a) 980 °C, b) 1100 °C and c) 1300 °C for S200H composites.

Despite the fact that the experimental data for the oxidation of the SiC/SiC composite indicated a net mass loss, a parabolic kinetic model was applied to describe the oxidation behavior. According to the literature, parabolic oxidation kinetics are typically associated with mass gain, resulting from the formation and growth of a protective oxide scale, such as SiO_2, under diffusion-controlled conditions. In the present study, the observed mass loss suggests that the oxidation mechanism may involve active oxidation and the formation of volatile species (e.g., SiO, CO), which are not consistent with the assumptions underlying the parabolic model. According

to NASA technical reports, passive oxidation of SiC typically results in mass gain due to the formation of a protective SiO_2 layer, whereas active oxidation at higher temperature or low oxygen partial pressures can lead to mass loss through the formation of volatile species such as SiO and CO [101]. Alternative kinetic models, including linear and logarithmic fits, were also considered during the analysis. However, the parabolic model was ultimately retained to enable comparison with existing literature and to provide a simplified framework for describing the oxidation behavior, despite its limitations in accurately capturing the underlying mechanism in this specific case. It is therefore emphasized that the use of the parabolic model in this context should be interpreted with caution, and further investigation is required to develop a more representative kinetic description of the oxidation process under the tested conditions.

During the oxidation tests, the samples were placed in ceramic holders (Figure 8). As a result, the surface area in direct contact with the holders was excluded from the oxidation surface calculations The data are summarized in Table 12.

Table 12 Oxidation kinetics in term of mass gain of S200H composite at 980 - 1300 °C

Oxidation time [h]	980°C	1100°C	1300°C
	Δw (mg)		
20	0.000	-0.010	-0.019
	0.000	-0.010	-0.025
	-0.010	-0.020	-0.023
40	-0.001	-0.016	-0.034
	0.000	-0.021	0.101
	-0.001	-0.030	-0.145
80	-0.005	0.031	-0.070
	0.006	-0.008	-0.003
	0.001	0.001	-0.002
100	-0.010	0.000	-0.034
	-0.010	-0.010	-0.035
	-0.010	-0.010	-0.035

At 980 °C the oxidation process was minimal. The mass change values fluctuated slightly around zero, indicating a very slow growth of the oxide layer or a balance between oxidation and potential mass loss due to volatile species. Although a parabolic fit was initially considered, it did not accurately reflect the oxidation behavior at this temperature. The data showed no clear trend, and the microstructural analysis confirmed that oxidation was limited to isolated regions, with no significant degradation of the fiber coatings. Therefore, no kinetic model was applied for this temperature, as the oxidation process was too weak and irregular to be meaningfully described by a diffusion-based law (Figure 37 a).

At 1100 °C, the oxidation rate increased, and the mass change data followed a parabolic trend. The parabolic fit captured the general trend of decreasing mass gain over time, suggesting that the dominant process was the evaporation of composite constituents and the resulting increase in porosity, rather than the growth of a SiO_2 layer through oxygen diffusion. However, the fit did not perfectly match all individual data points. Notably, a deviation was observed at 40 hours, where the experimental value fell below the fitted curve. This indicates that while the parabolic model provides a reasonable approximation of the overall behavior, it does not fully account for local variations in oxidation kinetics, which may arise from microstructural heterogeneities or measurement uncertainties. Microstructural analysis supports the diffusion-controlled oxidation mechanism. Oxygen ingress was most pronounced in matrix-rich pockets and along matrix cracks-regions characterized by higher matrix phase content and structural discontinuities. These features acted as preferential pathways for oxygen transport, facilitating localized oxidation. Despite the onset of interfacial degradation, the fiber coatings (BN and Si_3N_4) remained largely intact at this stage, and the composite preserved its structural integrity. While the parabolic model is traditionally associated with mass gain due to protective oxide scale formation, in this study it was used to approximate the mass loss behavior observed at 1100 °C. The fit suggests a diffusion - controlled process, likely governed by oxygen ingress through microstructural defects and the subsequent evaporation of volatile oxidation products. SEM analysis supports this interpretation, revealing preferential oxidation in matrix-rich regions and along cracks, which act as diffusion pathways. Therefore, despite the net mass loss, the oxidation kinetics may still be governed by diffusion, justifying the use of a parabolic approximation.

At 1300 °C, the oxidation became significantly more aggressive and penetrative. The mass loss increased rapidly over time, and although a parabolic model was applied, the data deviated from good parabolic behavior, indicating a transition to a more complex oxidation regime (Figure 37 c). This suggests that a textbook oxidation model may not be fully applicable due to the presence of multiple phases and microstructural features that influence oxidation behavior in different ways. Microstructural analysis revealed extensive degradation: a thick oxide scale formed on the surface, and deep oxygen penetration was observed along matrix cracks and in matrix-rich zones. The matrix underwent severe oxidation, forming a dense SiO_2 network and releasing gaseous byproducts (CO, N_2), which contributed to internal porosity and embrittlement. Cracking became widespread, facilitating further oxygen ingress. The BN and Si_3N_4 fiber coatings degraded significantly-BN oxidized which either evaporated or reacted with SiO_2 to

form borosilicate glass, while Si_3N_4 oxidized to SiO_2, releasing nitrogen-containing gases. These reactions compromised the protective function of the interphases, exposing the SiC fibers to oxidation. In some cases, silica was observed penetrating into the fiber structure, indicating advanced degradation. Despite these changes, the composite did not experience catastrophic failure. The SiC fibers remained structurally intact and continued to provide mechanical reinforcement, demonstrating the material's inherent damage tolerance. However, the observed degradation mechanisms - particularly the oxidation of the matrix and fiber coatings, oxygen ingress through cracks, and the formation of volatile or glassy oxidation products-highlight the limitations of unprotected use in harsh environments.

Based on the experimental observations, a degradation mechanism is proposed in which oxidation at 1300 °C proceeds through a combination of matrix oxidation, volatile product formation, and interphase degradation. Oxygen ingress is facilitated by microstructural defects such as cracks and matrix-rich zones, leading to the formation of porous oxide networks and the loss of protective coatings. This complex interplay of chemical and structural changes cannot be fully captured by classical oxidation models, underscoring the need for a more nuanced approach to describing high-temperature behavior in SiC/SiC composites. The applied parabolic model should be regarded as an empirical approximation rather than a mechanistically accurate representation of the oxidation process. While it provides a useful framework for comparing trends and estimating oxidation rates, its validity is limited by the observed deviations and the complex nature of the degradation mechanisms. To improve the reliability of kinetic modeling, further analysis involving a larger number of samples and extended exposure times is recommended. This would allow for better statistical evaluation and potentially support the development of more representative, mechanism-based models.

The parabolic rate constant (k) for the oxidation of S200H composite are given by the slopes of (Figure 37 a b and c) and plotted in an Arrhenius plot (Figure 38). From the slope of figure and using the equation 15, an activation energy for the oxidation of S200H composites is calculated as $\underline{107\ kJ*mol^{-1}}$. Although the oxidation process resulted in a net mass loss, the calculated activation energy reflects the temperature dependence of the overall reaction rate, including oxygen ingress and the formation of volatile oxidation products. The calculated activation energy falls within the range reported in the literature for similar composite materials.

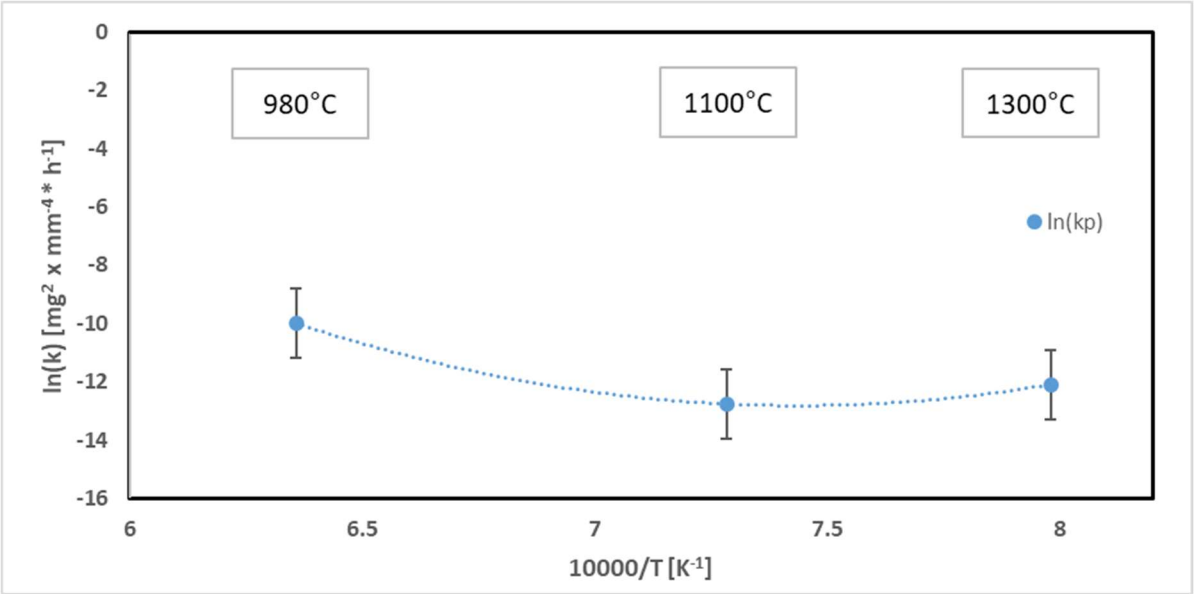

Figure 38 Parabolic rate constant for the oxidation of S200H composite

For comparison, the activation energy for SiC produced by CVD and oxidized in dry oxygen ranges from 120 to 345 kJ/mol^{-1} [102,103]. For sintered SiC oxidized in oxygen or air, values typically range from 130 to approximately 300 kJ/mol^{-1} [104,47].

In the case of sintered Si_3N_4, depending on the oxidation environment, the activation energy can vary from 20 to 227 kJ/mol^{-1} [105]. However, it is important to note that most literature data refer to mass gain during oxidation, typically associated with the formation of a protective SiO_2 scale under passive oxidation conditions. In contrast, in present study a net mass loss was observed, suggesting that the oxidation mechanism is governed by active oxidation and the formation of volatile products such as SiO and CO. Despite this difference in oxidation behavior, the activation energy remains physically meaningful. It reflects the temperature dependence of the overall oxidation rate, including oxygen ingress, matrix degradation, and the volatilization of reaction products. The fact that the process results in mass loss does not imply a negative activation energy; rather, the positive value of Ea indicates that the reaction rate increases with temperature, as expected for thermally activated processes. The differences between the obtained value and those reported in the literature may result from several factors. First, the tested S200H composite is not a bulk, single-phase material, but a complex multiphase system composed of SiC fibers coated with BN and Si_3N_4, and a matrix consisting of a silicon carbonitride (SiNC) phase mixture. Moreover, the supplier did not specify the exact phase composition of the matrix, making precise phase identification difficult. Additionally, the material exhibits approximately 5% porosity, and its properties are strongly influenced by microstructural features

such as matrix cracking and matrix-rich pockets. The oxidation environment also plays a crucial role in determining the activation energy. In this study, oxidation was conducted in a furnace, but the presence of water vapor (H_2O) in the atmosphere was not monitored, even though it can significantly affect oxidation kinetics. It is also important to note that the samples used for testing had very small surface areas and volumes, which may have influenced local oxidation conditions and, consequently, the measured activation energy. In summary, although the obtained activation energy lies within the range reported in the literature, it cannot be directly compared to values from other studies due to the composite's complex structure and differences in experimental conditions.

The thermogravimetric analysis (TGA) of the SiC/SiC composite revealed a total mass loss of approximately 1.35% during continuous heating up to 1200 °C (Figure 39). The mass decreased gradually across the entire temperature range, with a slight initial drop below 200 °C - likely due to the evaporation of adsorbed moisture or volatile surface contaminants. Between 200 and 1200 °C, the mass continued to decline steadily, suggesting ongoing oxidation processes accompanied by the volatilization or decomposition of reaction products. Notably, no significant mass gain was observed, indicating that the formation of a stable, protective oxide layer was either limited or offset by concurrent mass loss mechanisms. Based on the composition of the SiC/SiC composite-containing SiC fibers coated with BN and Si_3N_4, and a SiNC (silicon carbonitride) matrix - the most likely causes of mass loss observed during thermogravimetric analysis (TGA) are related to the oxidation and volatilization of specific components at elevated temperature. One of the primary contributors to mass loss is the formation and evaporation of silicon monoxide (SiO). This volatile species can form during the oxidation of SiC, Si_3N_4, or the SiNC matrix, especially under conditions where the protective silica (SiO_2) layer is either thin, porous, or locally disrupted. SiO is gaseous at high temperature and readily escapes from the material, leading to a measurable decrease in mass. Another significant factor is the oxidation of the BN coating. Upon oxidation, BN converts to B_2O_3, a glassy and hygroscopic compound with a high boiling point (~1500–1860 °C). Although B_2O_3 is not volatile under standard conditions, it can be gradually lost at elevated temperature through evaporation or reaction with moisture, particularly above 1000 °C. This may contribute to localized degradation of the fiber/matrix interface. However, given the relatively small amount of BN in the composite, its contribution to the overall mass loss is likely limited, though not negligible in terms of structural

integrity. Additionally, the carbon and nitrogen components of the SiNC matrix may oxidize to form gaseous products such as CO, CO_2, and NO_x. These gases are not retained in the material and are immediately released, further reducing the sample's mass during heating. Together, these mechanisms-SiO volatilization, B_2O_3 evaporation, and the release of gaseous oxidation products from the matrix-explain the gradual and continuous mass loss observed in the TGA curve. These processes are consistent with the material's composition and the oxidative environment of the test.

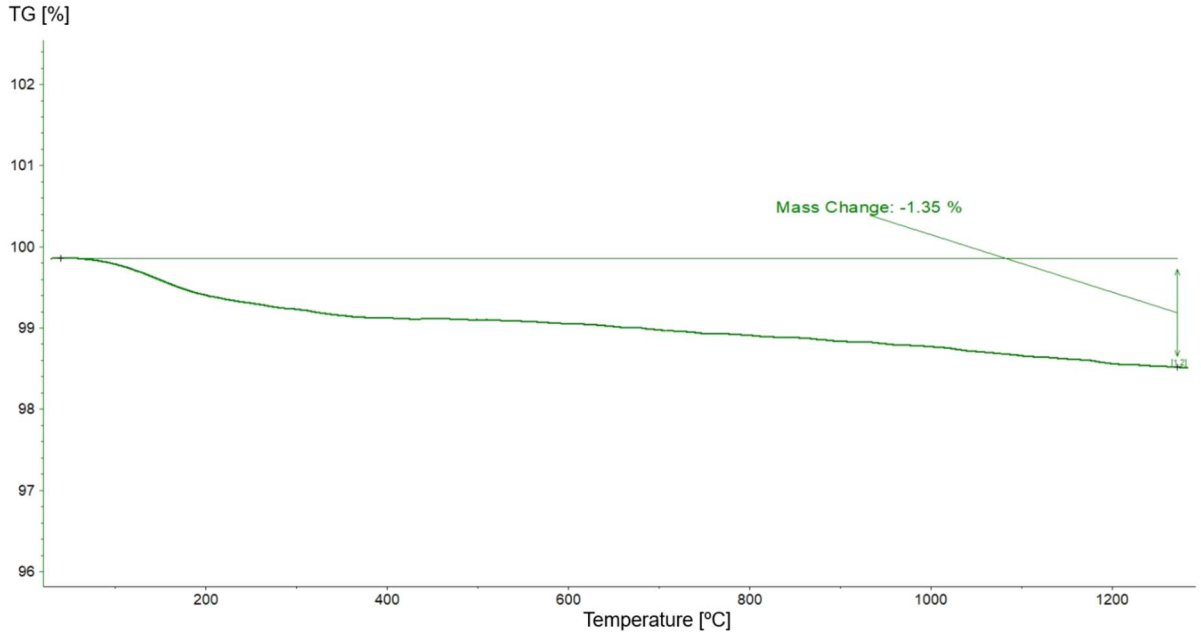

Figure 39 Thermogravimetric curve (TGA) of S200H composite

The mass change behavior of the SiC/SiC composite was investigated using two complementary approaches: thermogravimetric analysis (TGA) and isothermal oxidation tests conducted at 980, 1100 and 1300 °C for durations of 20, 40, 80, and 100 hours. While both methods aim to assess the oxidation resistance and thermal stability of the material, the results obtained from each differ due to fundamental differences in test conditions and mechanisms involved. The discrepancies between the TGA and isothermal test results can be explained by several factors. First, the duration of exposure in TGA is much shorter, which limits the extent of oxide scale growth and degradation. Second, the small sample size in TGA reduces the likelihood of thermal gradients and mechanical stresses that can lead to cracking or spallation. Third, the isothermal tests are more susceptible to environmental influences such as contact with ceramic holders, local variations in gas flow, and differences in surface morphology, all of which can affect oxidation behavior and mass change. TGA provides valuable insights into the initial stages of

oxidation and the volatilization behavior of the composite, while the isothermal oxidation tests capture the long-term stability and mechanical integrity of the oxide scale under more realistic service conditions.

Surface features of the samples were compared in three conditions: pristine (without oxidation), after oxidation at 1100 °C for 100 hours, and after oxidation at 1300 °C for 100 hours. Surface observations were performed using a Scanning Electron Microscope (SEM) in both Backscattered Electron (BSE) and Secondary Electron (SE) modes. Various view fields were utilized, ranging from overview to high magnification (view filed 10 µm). Images were captured on unmounted samples, cross-sections, and surface in three different areas (Figure 40). The pristine sample exhibited a smooth and uniform black surface without visible defects (Figure 11). In contrast, the oxidized sample at 1100 °C for 100 hours showed a dark gray surface with a white bloom (Figure 41 a). At high magnification a net-like structure began to appear on the surface. On the cross-section, this net structure was visible at 125 µm view field, with dimensions approximately 3-12 µm in height/width (Figure 41 b, d. f). The sample oxidized at 1300 °C for 100 hours displayed a gray surface with a more pronounced white bloom. The higher temperature oxidation resulted in a more distinct and visible net structure on both the surface and cross-section. The dimensions of the net structure were similar to those observed in the 1100 °C sample but were more clearly defined (Figure 40 c, e, g). The oxidation on the surface of the SiC/SiC samples affected both the matrix and the composite fibers.

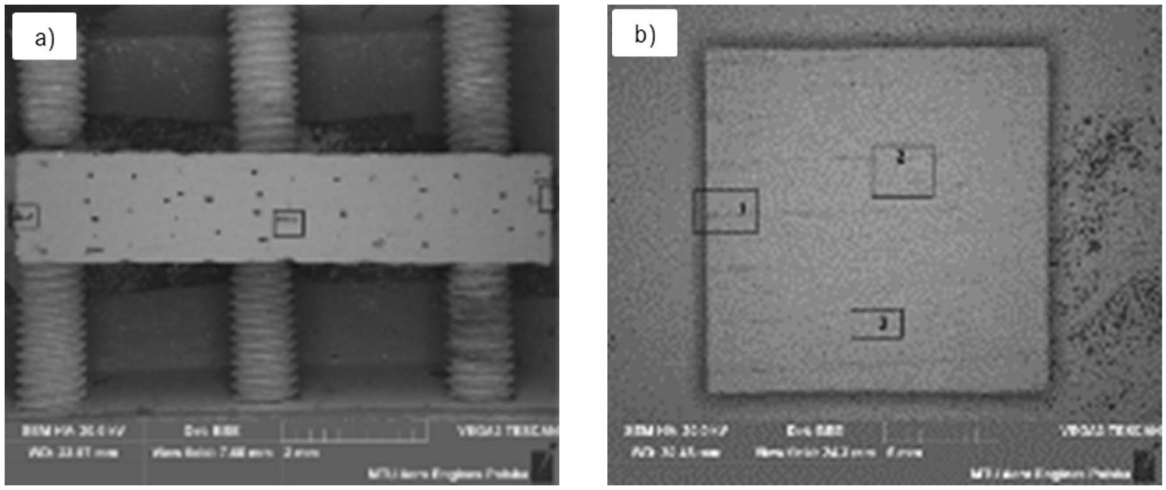

Figure 40 Investigation area of SiC/SiC samples, a) cross-section, b) surface area after oxidation

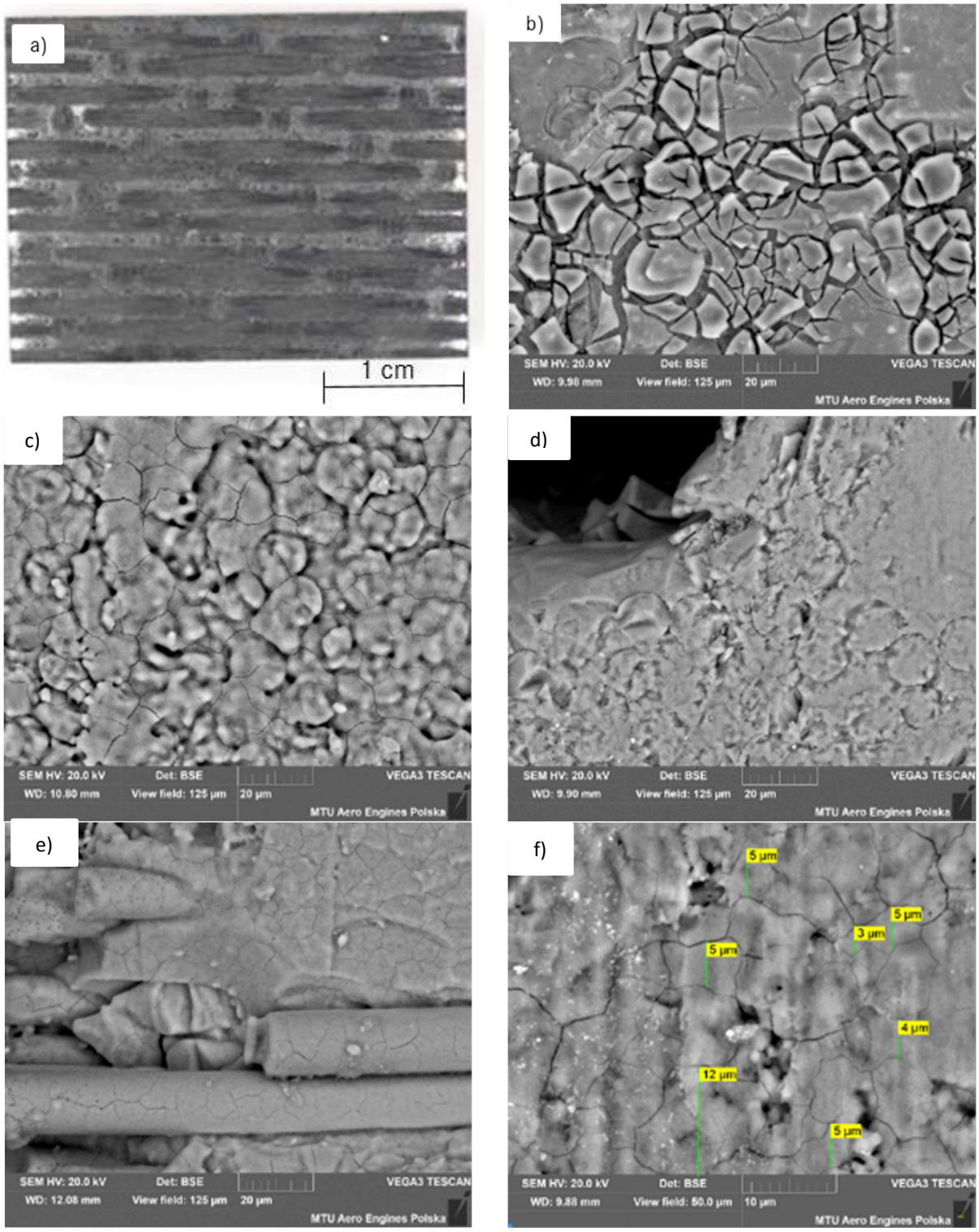
a)
1 cm
b)
SEM HV: 20.0 kV
Det: BSE
VEGA3 TESCAN
WD: 9.96 mm
View field: 125 µm
20 µm
MTU Aero Engines Polska
c)
SEM HV: 20.0 kV
Det: BSE
VEGA3 TESCAN
WD: 10.00 mm
View field: 125 µm
20 µm
MTU Aero Engines Polska
d)
SEM HV: 20.0 kV
Det: BSE
VEGA3 TESCAN
WD: 9.90 mm
View field: 125 µm
20 µm
MTU Aero Engines Polska
e)
SEM HV: 20.0 kV
Det: BSE
VEGA3 TESCAN
WD: 12.08 mm
View field: 125 µm
20 µm
MTU Aero Engines Polska
f)
5 µm
5 µm
3 µm
5 µm
4 µm
12 µm
5 µm
SEM HV: 20.0 kV
Det: BSE
VEGA3 TESCAN
WD: 9.88 mm
View field: 50.0 µm
10 µm
MTU Aero Engines Polska

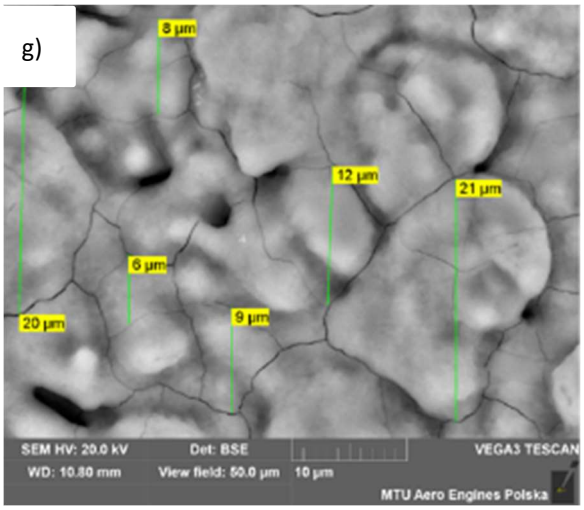

Figure 41 Surface features of SiC/SiC sample after oxidation at 1100 ℃ for 100 h a, c, e, g and after oxidation at 1300 ℃ for 100 h b, d, f

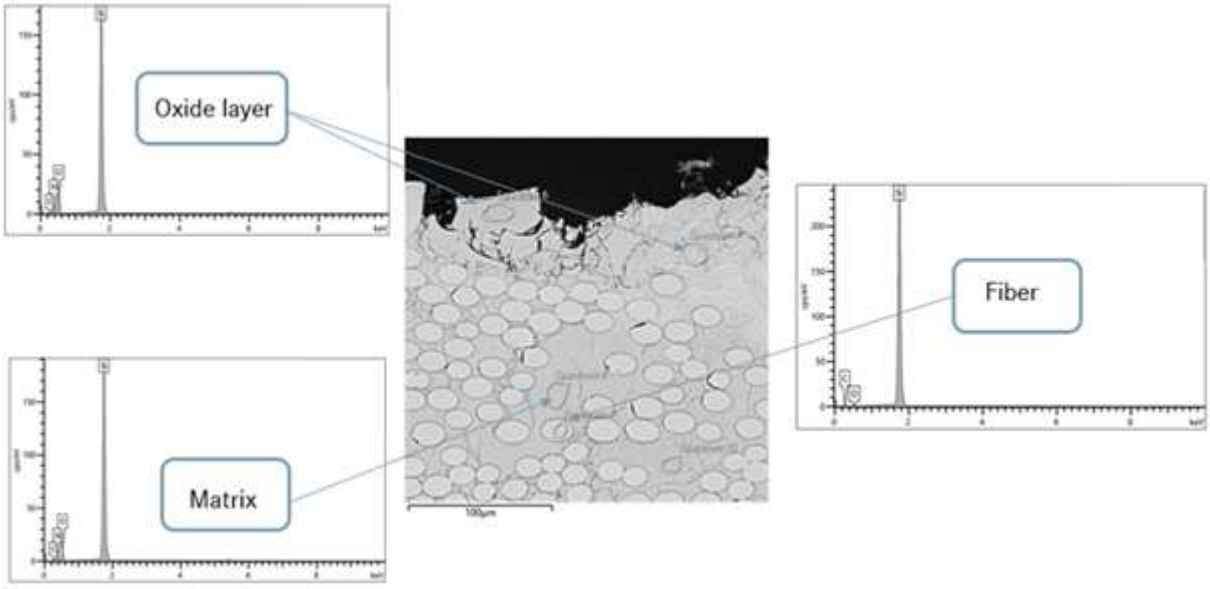

Figure 42 Example of Electron Spectroscopy measurements for SiC/SiC composites

EDS point spectra were obtained for all oxidation times and temperature. Three main areas were identified and examined for the impact of oxidation on chemical composition: the oxidized layer, the fibers, and the matrix (Figure 42). All measurements taken were compiled into Table 13.

The spectroscopic analysis of the SiC/SiC composite, which consists of SiC fibers coated with Si_3N_4 and BN and embedded in a SiNC matrix, was performed. The results revealed the presence of nitrogen (N), silicon (Si), and carbon (C), which are present in their atomic form. This is due to the nature of the analytical methods used - such as Electron Spectroscopy methods which detect and quantify elements based on their characteristic energy signatures rather than their chemical bonding states. As a result, the data reflect the elemental composition of the

sample surface or near-surface region, without directly identifying the specific compounds in which these elements are present. Although the elements originate from well-defined compounds such as Si_3N_4, BN, and SiC, the spectroscopic output does not distinguish between these phases unless additional chemical state analysis is conducted. Therefore, the elemental results are reported as atomic percentages, providing insight into the overall distribution of elements within the composite

As expected the oxide layer demonstrates the highest oxygen concentration among all locations, with values ranging from 14 to 50 wt.%. It should be noted, however, that these values represent relative concentrations derived from EDX measurements, which are influenced by the spot size, interaction volume, and local topography of the sample. Therefore, the reported oxygen contents should be interpreted as semi - quantitative, providing comparative rather than absolute information about elemental distribution. A clear temperature dependence is observed, with specimens tested at 1300 °C showing significantly higher oxygen content (40-46 wt.%) compared to those tested at lower temperature. This suggests enhanced oxidation kinetics at elevated temperature. Time exposure also plays a crucial role in oxygen enrichment of the oxide layer. At 1300 °C, oxygen content increases from moderate levels at shorter times to 44 wt.% at 80h and 46 wt.% at 100h. This time-dependent behavior is less pronounced at 980 °C, where oxygen content fluctuates between 14 and 29 wt.% without a clear trend. The silicon content in the oxide layer shows an inverse relationship with oxygen concentration. As oxygen content increases with higher temperature, silicon percentage decreases from approximately 45-50 wt.% at 980 °C to 36-43 wt.% at 1300 °C (Figure 43). This suggests that silicon is being consumed in the oxidation process, potentially forming silicon dioxide (SiO_2), but also leading to the formation of less stable silicon oxides such as Si_2O_3 or SiO. When the amount of silicon is relatively low-either due to a limited initial quantity or partial evaporation at elevated temperature-the excess oxygen from the environment drives the formation of more oxidized species. Some of these, like SiO_2, may exist in the gas phase, making them difficult to detect using conventional analytical methods. This behavior highlights the complex interaction between silicon availability and oxygen concentration during the oxidation process.

Nitrogen content in the oxide layer exhibits a marked decrease with increasing temperature, dropping from 9.6-24.4 wt.% at 980 °C to only 1.3-4.7 wt.% at 1300 °C. This indicates that nitrogen may be released from the material during high-temperature oxidation [106]. The matrix region shows considerable variability in oxygen content (2.0-36.8 wt.%) without a clear

correlation to either temperature or time. This heterogeneity suggests that oxidation in the matrix is influenced by local microstructural features rather than solely by processing parameters. Silicon content in the matrix remains relatively stable (approximately 48-53 wt.%) across most conditions, though specimens treated at 1300 °C for 40h show somewhat reduced silicon levels (38-39 wt.%). This relative stability indicates that silicon in the matrix is less affected by the oxidation process compared to other elements. Nitrogen concentration in the matrix is generally high (10-25 wt.%) and does not show a strong dependence on temperature or time. This suggests that nitrogen detected in the matrix region originates from the presence of Si_3N_4, where it is chemically bonded within the crystal structure. In contrast, the oxide layer lacks such nitrogen-containing phases, resulting in significantly lower nitrogen signals in that region. Therefore, the observed nitrogen distribution reflects the phase composition rather than differences in bonding strength or diffusion behavior.

Fibers consistently maintain the lowest oxygen content (1.5-2.8 wt.%) regardless of temperature and exposure time, demonstrating remarkable oxidation resistance. The minimal variation in oxygen content suggests that fibers have inherent protection against oxidation.

Silicon content in fibers is consistently high (56-60 wt.%) and remains stable across all conditions, indicating that silicon is a major constituent of the fiber composition and is not significantly affected by the oxidation process.

Carbon content in fibers is also high (38-59 wt.%) and relatively stable, further supporting the conclusion that fibers maintain their compositional integrity even under severe oxidation conditions. The observed results can be attributed to the presence of a protective coating of BN (boron nitride) and Si_3N_4 (silicon nitride) on the fibers. This coating effectively shields the fibers from the oxidative effects of elevated temperature, thereby enhancing their resistance to oxidation. In contrast, the matrix is not protected by any thermal barrier coatings (TBC), which makes it the most susceptible to oxidation. Temperature appears to have a more significant impact than time on oxygen content, particularly in the oxide layer. The most pronounced oxidation effects are observed at 1300 °C, where oxygen levels in the oxide layer reach their maximum values. While time does influence oxidation, its effect is more evident at higher temperature. At 1300 °C, longer exposure times generally lead to higher oxygen content in the oxide layer, suggesting a cumulative oxidation process.

As oxidation progresses with increasing temperature and time, the oxide layer becomes relatively enriched in oxygen, reflecting the formation of SiO_2 and the concurrent loss of nitrogen

and silicon through the volatilization of reaction products such as N_2 and SiO. This compositional shift highlights the ongoing chemical transformations, including the breakdown of Si_3N_4 and the evolution of a porous or glassy oxide network.

The findings indicate that higher temperature lead to an increased oxygen content in the samples. For instance, samples oxidized at 1300 °C exhibited oxygen levels exceeding 45% in certain locations, such as the oxide layer at 80 hours. In contrast, samples subjected to oxidation at the lower temperature of 980 °C displayed significantly lower oxygen content, particularly in the matrix and fiber locations.

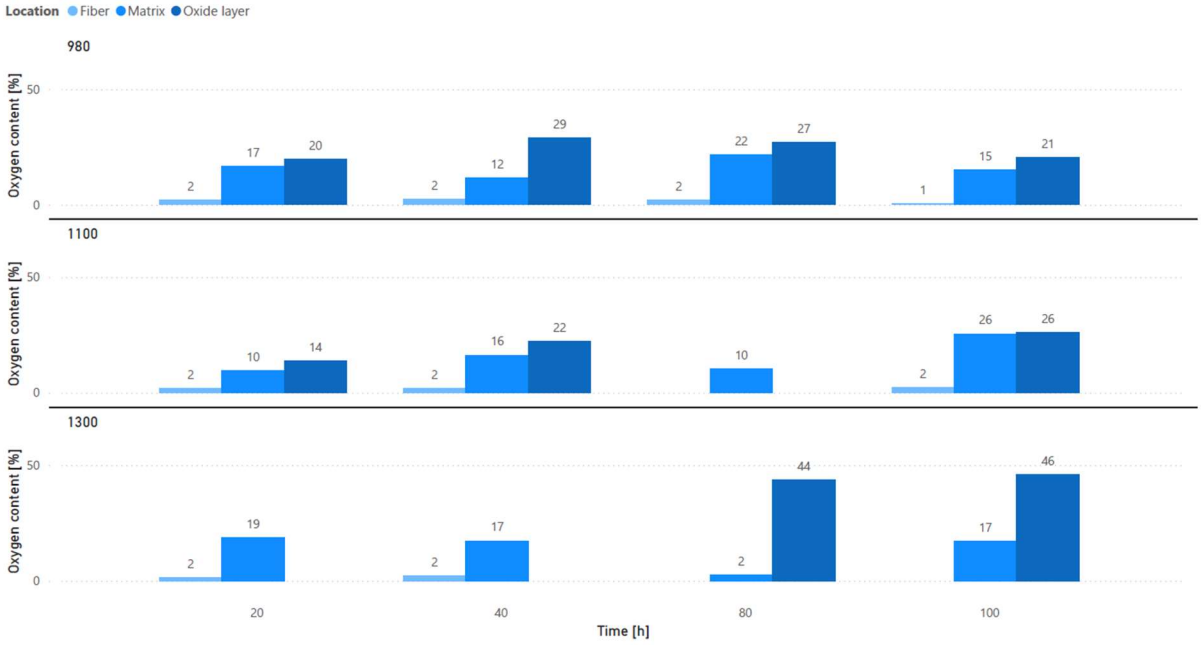

Figure 43 Oxygen content after oxidation of S200H composite at 980, 1100 and 1300 °C

Table 13 Results for CMC tested at oxidation environment

Tempertaure [°C]	Time [h]	Spectrum numer	Location	C [%]	O [%]	Si [%]	N [%]	Total [%]
980	20	7	Fiber	40.2	2.0	57.8	-	100
		8	Matrx	23.8	2.6	51.9	21.7	100
		9	Oxide layer	15.2	29.3	45.9	9.6	100
		10	Oxide layer	26.6	14.1	40.8	18.6	100
		11	Matrix	8.0	13.3	53.3	25.4	100
		12	Oxide layer	10.3	16.1	49.2	24.4	100
		13	Matrix	14.6	33.8	43.6	8.0	100
	40	6	Matrix	22.6	4.6	53.5	19.5	100
		7	Oxide layer	9.4	28.8	48.3	13.5	100
		8	Matrix	10.5	15.04	51.0	23.1	100
		9	Fiber	38.2	2.4	59.4	-	100
		10	Matrix	11.4	15.6	50.5	22.6	100
	80	7	Oxide layer	29.9	27.1	37.6	5.5	100
		8	Matrix	20.2	13.3	48.0	18.5	100
		9	Fiber	40.6	2.2	57.2	-	100
		10	Matrix	8.5	22.7	48.5	20.3	100
		11	Matrix	14.1	28.9	46.2	10.7	100
	100	1	Oxide layer	34.1	20.5	31.1	14.3	100
		2	Fiber	38.8	0.6	60.6	-	100
		3	Matrix	20.2	15.1	52.5	12.2	100
		4	Matrix	18.8	15.3	53.5	12.3	100
1100	20	1	Matrix	22.5	3.7	53.2	20.5	100
		2	Matrix	22.2	3.7	53.6	20.5	100
		3	Oxide layer	13.8	13.9	50.1	22.1	100
		4	Matrix	6.4	21.8	51	20.8	100
		5	Fiber	58.7	1.9	58.7	-	100
	40	47	Oxide layer	0.9	21	61.0	17	100
		48	Oxide layer	0.8	23.7	53.5	22.1	100
		49	Matrix	0.9	16.3	59.5	23.3	100
		50	Fiber	58.7	1.9	58.7	-	100
	80	4	Matrix	23	2.1	53.2	21.7	100
		5	Matrix	17.8	26.9	45.5	9.8	100
		6	Matrix	23.6	2.0	53.2	21.2	100
	100	1	Oxide layer	20.1	26.1	43.0	10.8	100
		2	Matrix	17.2	19.0	47.0	16.9	100
		3	Matrix	24.1	32.1	38.3	5.5	100
		4	Fiber	40.3	1.9	57.8	-	100
		5	Fiber	40.5	2.8	56.7	-	100
1300	20	2	Matrix	26.7	16.5	34.7	22.2	100
		3	Matrix	12.6	10.7	51.3	25.4	100
		4	Fiber	40.6	1.5	57.9	-	100
		5	Matrix	16.6	29.2	44.2	10.0	100
	40	7	Matrix	22.1	2.5	53.8	21.6	100
		8	Matrix	22.6	2.3	53.3	21.7	100
		9	Matrix	24.4	36.8	38.9		100
		10	Matrix	20.7	34.0	38.6	6.7	100
		11	Matrix	10.8	14.1	5`1.3	23.8	100
		12	Matrix	11.1	14.3	50.3	24.3	100
		13	Fiber	40.4	2.1	57.5	-	100
	80	14	Oxide layer	10	47.6	40.2	2.1	100
		15	Matrix	22.6	2.4	52.7	22.3	100
		16	Oxide layer	11.8	39.9	43.6	4.7	100
		17	Oxide layer	13.3	43.6	41.7	1.3	100
	100	26	Oxide layer	17.7	45.9	36.4	-	100
		27	Matrix	7.3	21.1	51.5	20.1	100
		28	Matrix	11.0	13.2	51.5	24.3	100

EDS studies were conducted for all samples oxidized at three temperature and four times. During the measurements, the distribution of oxygen, nitrogen, carbon, and silicon was analyzed, as shown in Figure 44. In the subsequent analysis, not all collected EDS maps were presented; however, those that showed the presence of oxygen resulting from the oxidation process were selected.

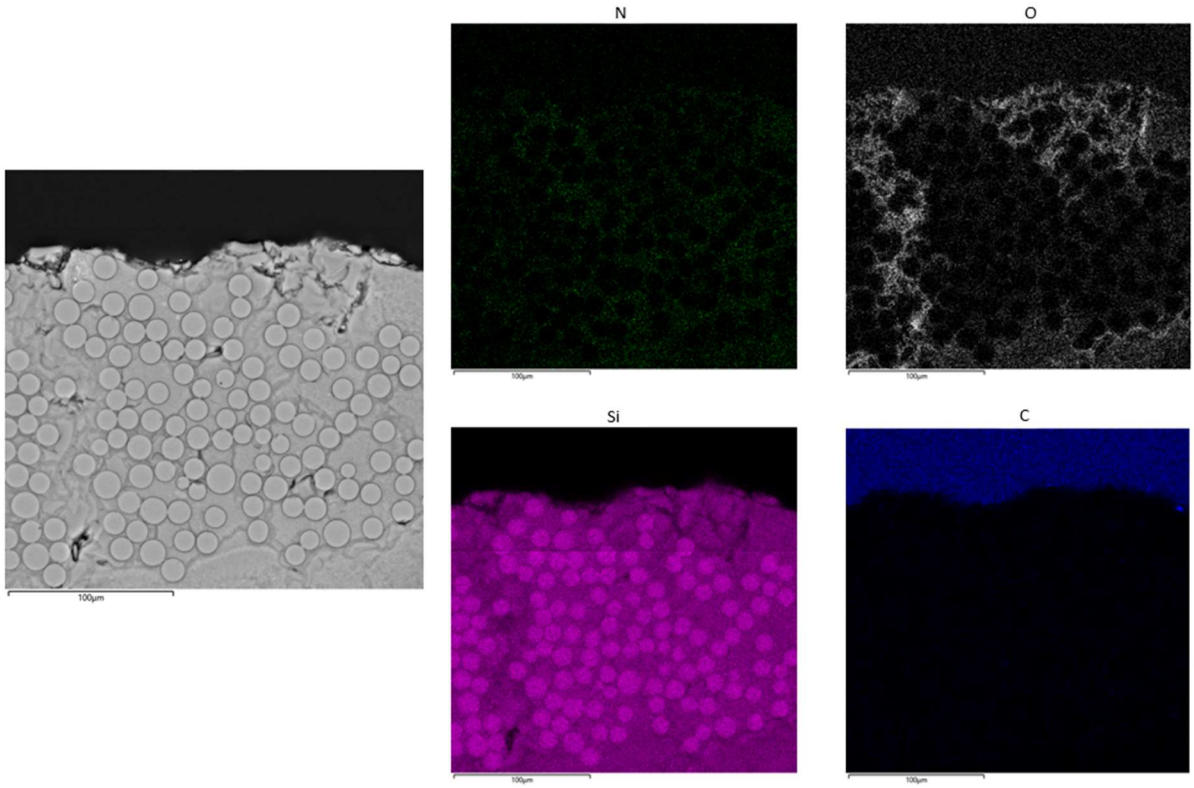

Figure 44 EDS elemental mapping for SiC/SiC composite tested at 980 ºC for 80h

It is important to emphasize that EDS is primarily a qualitative or semi-quantitative analytical technique. While EDS can provide estimates of the relative abundance of elements within a sample, it is not considered a fully quantitative method. This limitation arises from several factors, including matrix effects, variations in X-ray generation efficiency, detector sensitivity, and surface topography. These variables can significantly influence the intensity of the detected signals, leading to inaccuracies in the calculated elemental concentrations. Furthermore, EDS does not account for the chemical bonding states of the elements, nor does it distinguish between different compounds containing the same elements. For example, silicon detected in the sample may originate from SiC, Si_3N_4, or SiO_2, but EDS cannot differentiate between these phases without additional complementary techniques. Similarly, EDS point analysis generated from EDS measurements are used to identify the presence of specific elements based on their

characteristic X-ray peaks. These spectra serve as a qualitative fingerprint of the sample's composition. However, the peak intensities should not be interpreted as precise quantitative values, especially when comparing elements with significantly different atomic numbers or X-ray emission efficiencies.

6.2.1 Oxidation at 980 °C

The oxidation process conducted at 980 °C did not result in any observable changes in the number of fiber layers within the SiC/SiC composite. This indicates that the laminate structure of the material remained structurally stable under the applied thermal conditions. The preservation of the fiber layering suggests that the composite exhibits satisfactory resistance to oxidation-induced delamination or degradation at this temperature. However, localized detachment of surface fibers was observed in the oxidized region. These fibers, situated at the outermost layer directly exposed to the oxidizing atmosphere, appeared to have separated from the bulk material. It is important to note that this phenomenon is not necessarily a direct consequence of the oxidation process itself. Rather, it is likely associated with a reduction in interfacial strength or local embrittlement of the surface region, which may have rendered the fibers more susceptible to mechanical damage during post-oxidation sample preparation, such as cutting or polishing (Figure 45).

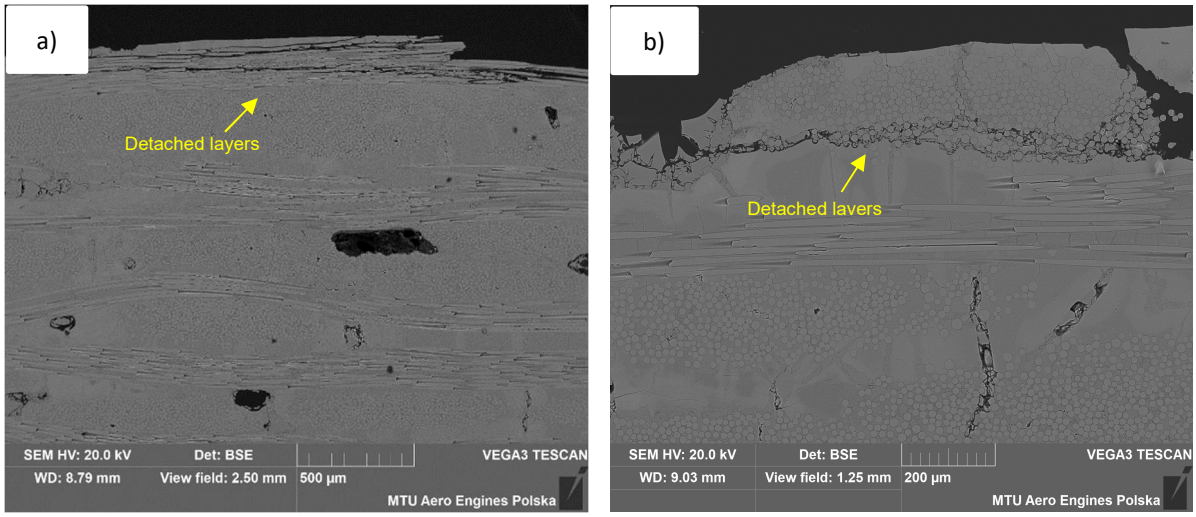

Figure 45 Detached fibers in SiC/SiC composite after oxidation process at 980 °C, 20h

As in the pristine state, the pores observed in the SiC/SiC composite after oxidation at 980 °C retained their characteristic morphology. The pores were predominantly elliptical or elongated, with orientations both longitudinal and transverse relative to the fiber plies. However, it was

observed that pores connected to matrix microcracks became active pathways for oxygen diffusion into the interior of the material. This connectivity between pores and cracks effectively bypassed the protective surface oxide layer, enabling localized oxidation of internal phases (Figure 46 a) and b)).

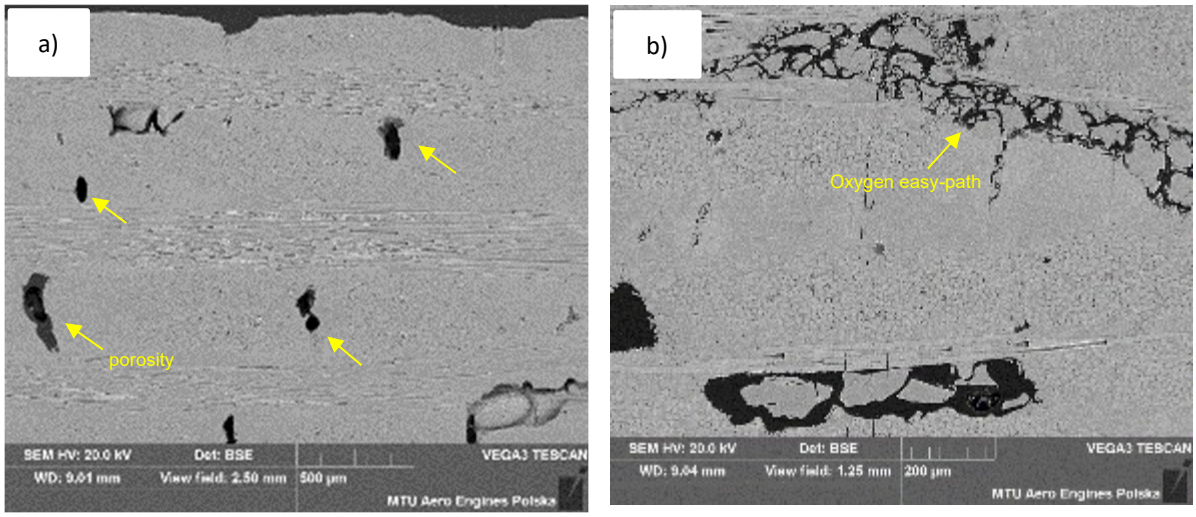

Figure 46 Macroporosity in SiC/SiC composite oxidized at 980 °C, a) 40h, b) 100h

Matrix-rich pockets located near the surface of the SiC/SiC composite, and thus directly exposed to the oxidizing environment, were particularly susceptible to oxygen ingress. These regions, characterized by a high local concentration of matrix material and a lack of reinforcing fibers, exhibited a distinct tendency to crack under thermal stress during oxidation at 980 °C. The absence of fibers in these zones significantly reduced their mechanical constraint and structural reinforcement, making them more prone to microcracking (Figure 47 a and b). The formation of cracks in matrix-rich pockets is likely associated with the inability of the matrix to accommodate thermal and chemical strains during oxidation and cooling. In the absence of reinforcing fibers, which typically help redistribute stresses, the matrix alone may be more susceptible to localized cracking. While thermal residual stresses due to CTE mismatch may contribute, they are not necessarily the dominant factor. Additional mechanisms, such as oxidation-induced volume changes and microstructural constraints, may also play a significant role. The cracks, once formed, provided direct and unimpeded pathways for oxygen diffusion into the interior of the material. In contrast, matrix-rich pockets located deeper within the composite and surrounded by fibers remained intact and unoxidized. The fibers in these regions acted as both a mechanical barrier and a diffusion shield, limiting the propagation of cracks and impeding the inward migration of oxygen (Figure 47 c and d). This protective effect was consistent

across all oxidation durations tested (20, 40, 80, and 100 h), indicating that the spatial distribution of fibers plays a critical role in determining the oxidation resistance of the composite.

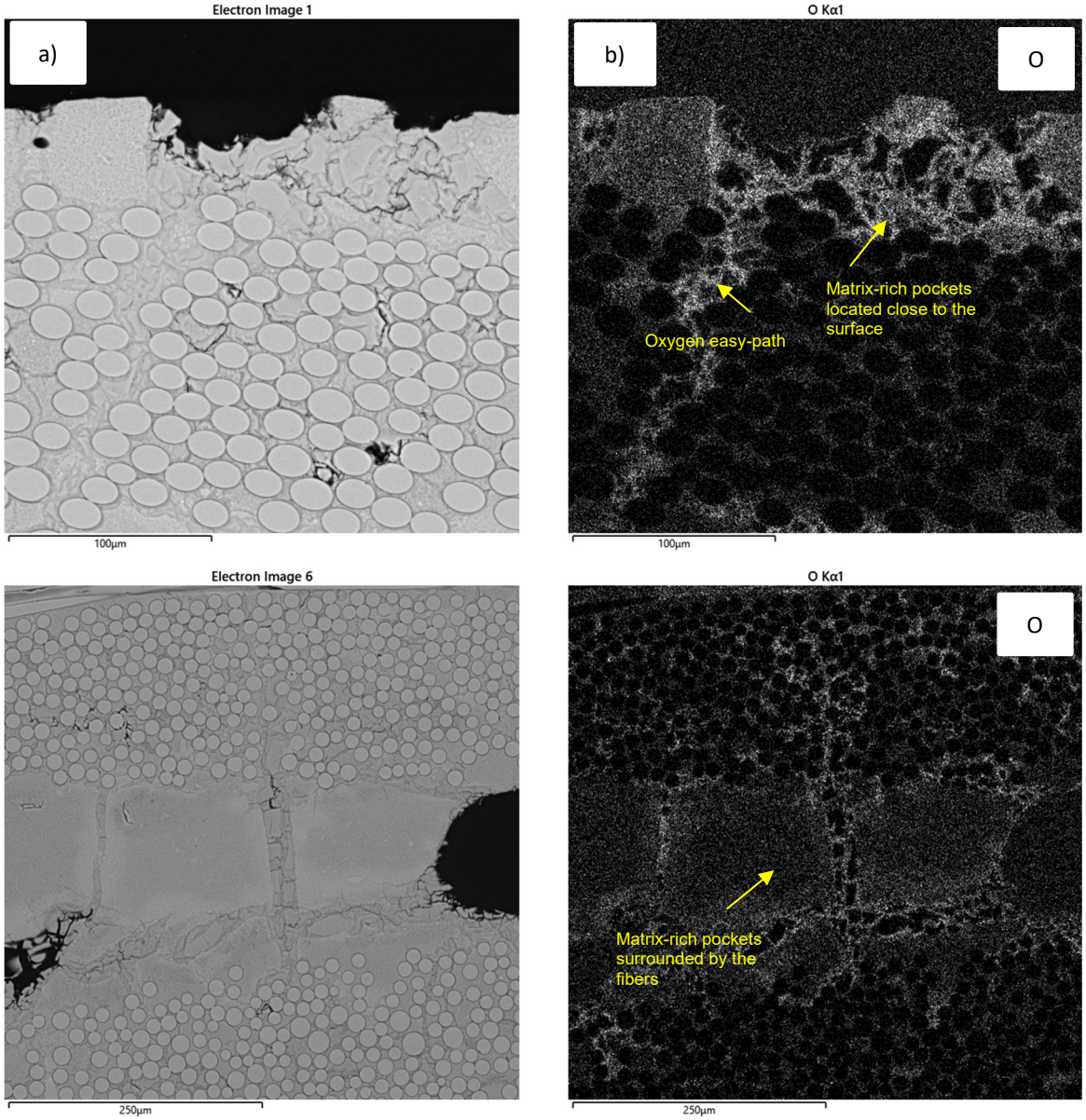

Figure 47 Oxidized a) and b) and not oxidized matrix rich pockets c) and d) in SiC/SiC composite tested at 980 °C

The SiC/SiC composite matrix was identified as the most oxidation-sensitive microstructural feature at 980 °C. The matrix (SiNC) produced by PIP process is expected to allow gas into the material without applied load. The results is that, the PIP-derived SiC/SiC composites may degrade even under stresses below the proportional limit [110]. Cracks that had previously been sealed through matrix infiltration during oxidation process (20, 40, 80, and 100 hours) were observed to reopen, forming continuous pathways for oxygen ingress into the material (Figure 48 d). These cracks were both transverse and longitudinal, and were observed to propagate

along the fiber direction as well as perpendicular to the plies, particularly in matrix-rich pockets and near the oxidized surface (Figure 48 a, c, e, f, g). The cracks typically initiated in fiber-depleted regions, where the absence of reinforcement limited the ability of the material to re-distribute thermal and chemical stresses. While thermal residual stresses are often attributed to mismatches in the coefficient of thermal expansion (CTE), in this case, the CTE of the SiC matrix and SiC fibers are relatively similar ($3.5–4.9 \times 10^{-6}\ K^{-1}$) [107], and the BN/$Si_3N_4$ interphases are too thin to dominate the stress field. Therefore, the observed cracking is more likely associated with oxidation-induced volume changes, local stiffness mismatches, and the absence of fiber bridging, rather than classical CTE mismatch mechanisms [108]. Despite the propagation of cracks along the fiber direction, they did not penetrate the SiC fibers themselves, nor did they disrupt the protective interphase layers. The fibers in this composite were coated with a dual-layer interphase system consisting of boron nitride (BN) and silicon nitride (Si_3N_4), each serving a distinct and complementary function: The inner BN layer acts as a mechanical debonding interface, enabling fiber sliding (fiber pull-out) during crack propagation. Its low interfacial shear strength and layered structure reduce stress transfer between the matrix and the fiber, enhancing damage tolerance and energy dissipation. The outer Si_3N_4 layer serves as a chemical barrier, protecting the fiber and the BN layer from oxidation. Due to its high oxidation resistance and intermediate CTE, it also helps mitigate thermal mismatch stresses at the fiber–matrix interface. As a result, although the matrix experienced oxidation-induced cracking, the fiber coatings remained intact, and no degradation of the SiC fibers was observed. This confirms the effectiveness of the BN/ Si_3N_4 interphase system in maintaining the structural and chemical integrity of the reinforcement under oxidative conditions. Furthermore, the reopening of cracks correlates with the oxidation products identified through XRD and DSC analysis. The formation of SiO_2 as a passive oxidation product of SiC was confirmed, and DSC data revealed exothermic peaks associated with oxidation reactions. However, the presence of amorphous or turbostratic BN and low-crystallinity Si_3N_4 may have limited the formation of a dense, continuous oxide scale, particularly in cracked regions. This allowed oxygen to bypass the surface barrier and reach the interior matrix. (Figure 48 b).

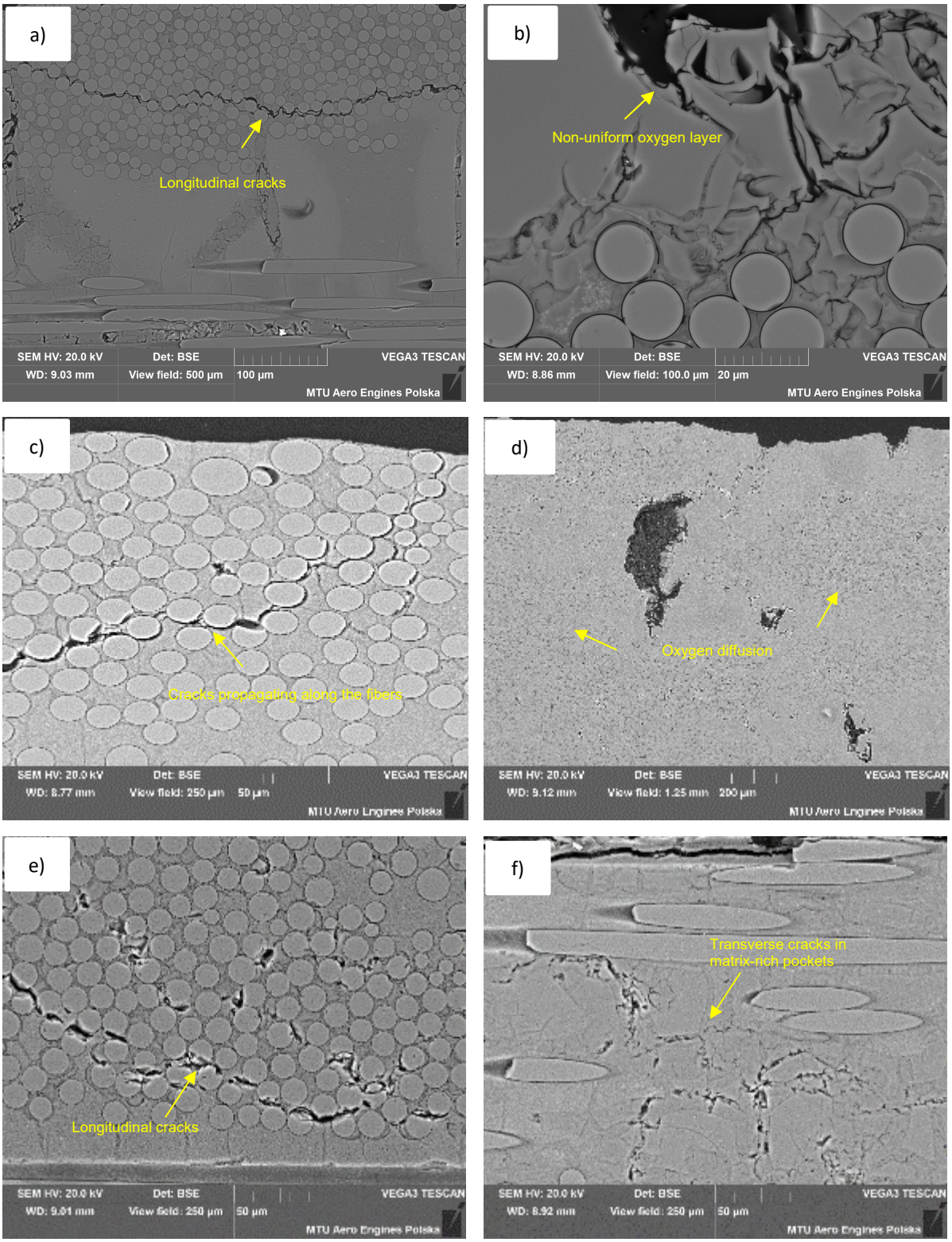
a)
Longitudinal cracks
SEM HV: 20.0 kV
Det: BSE
VEGA3 TESCAN
WD: 9.03 mm
View field: 500 µm
100 µm
MTU Aero Engines Polska
b)
Non-uniform oxygen layer
SEM HV: 20.0 kV
Det: BSE
VEGA3 TESCAN
WD: 8.86 mm
View field: 100.0 µm
20 µm
MTU Aero Engines Polska
c)
Cracks propagating along the fibers
SEM HV: 20.0 kV
Det: BSE
VEGA3 TESCAN
WD: 8.77 mm
View field: 250 µm
50 µm
MTU Aero Engines Polska
d)
Oxygen diffusion
SEM HV: 20.0 kV
Det: BSE
VEGA3 TESCAN
WD: 9.12 mm
View field: 1.25 mm
200 µm
MTU Aero Engines Polska
e)
Longitudinal cracks
SEM HV: 20.0 kV
Det: BSE
VEGA3 TESCAN
WD: 9.01 mm
View field: 250 µm
50 µm
MTU Aero Engines Polska
f)
Transverse cracks in matrix-rich pockets
SEM HV: 20.0 kV
Det: BSE
VEGA3 TESCAN
WD: 8.92 mm
View field: 250 µm
50 µm
MTU Aero Engines Polska

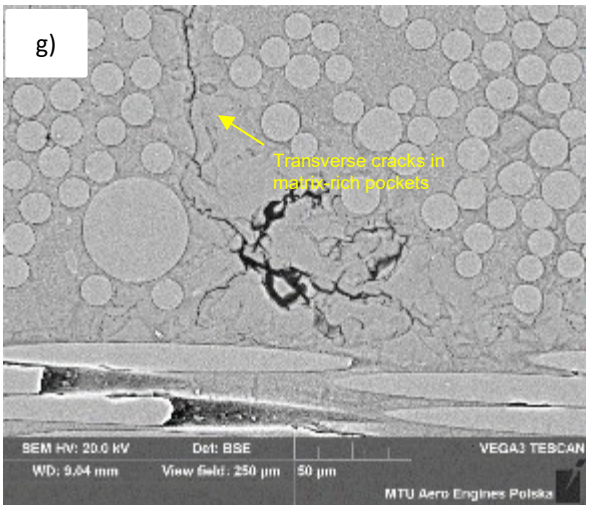

Figure 48 Cracks in the composite matrix subjected to heating at a temperature of 980 °C for a, b) 20h, c, d) 40h, e, f) 80h, g) 100h

EDS maps for the composite oxidized at a temperature of 980 °C over periods of 20, 40, 80 and 100 hours confirmed the highest concentration of oxygen in the cracks of the SiC/SiC composite matrix and demonstrated that these cracks provide an easy pathway for oxygen diffusion into the material (Figure 49).

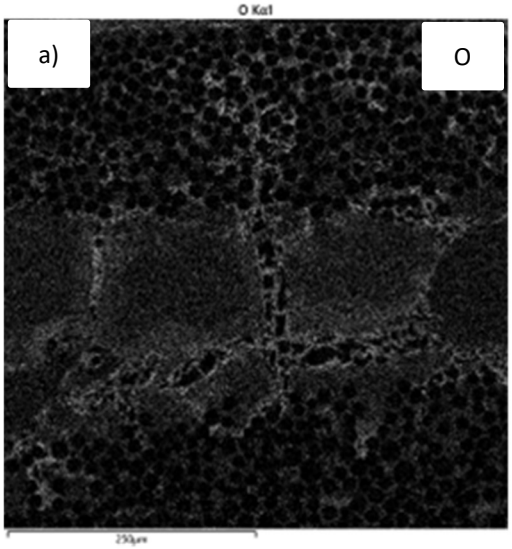

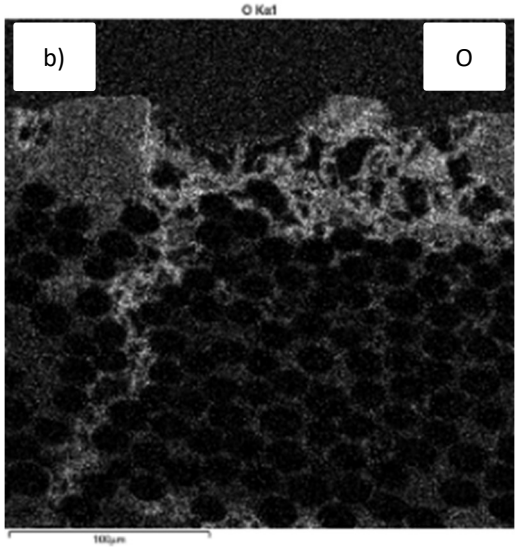

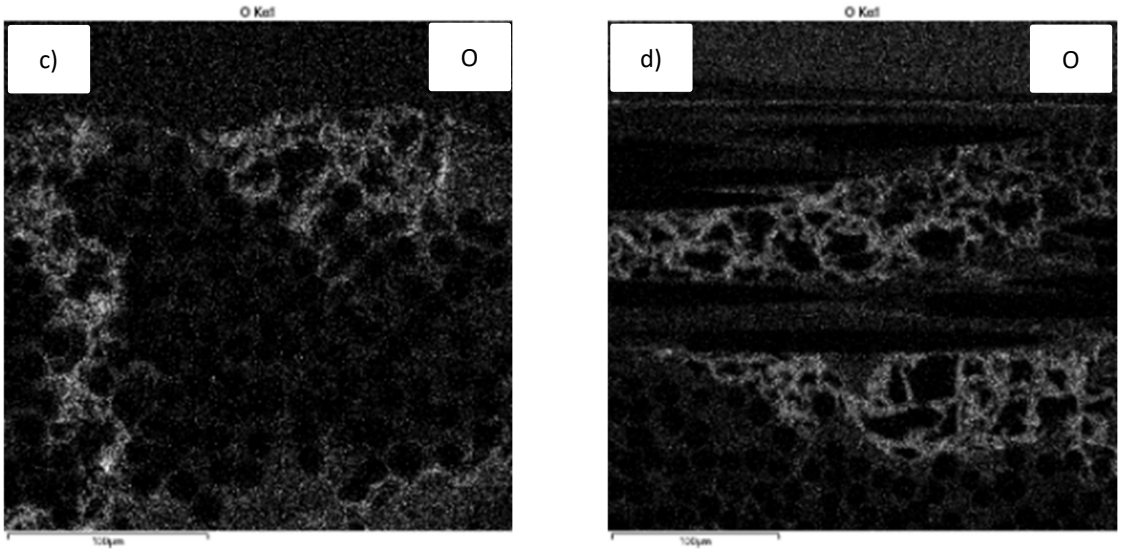

Figure 49 EDS maps for the composite oxidized at a temperature of 980 °C over the periods of a) 20 hours, b) 40 hours, c) 80 hours, d) 100 hours

The SiC fibers present in this material proved to be the most resistant to the oxidizing environment, as confirmed by spectrographic studies and EDS maps and SEM pictures (Figure 50 a and b). The coating on the fibers remained uniform, non-oxidized, and its thickness fell within the ranges previously measured for the material in its initial state. In some SEM images, a slight detachment of the coating from the fiber surface was observed; however, this is most likely an artifact of sample preparation rather than a consequence of oxidative degradation. This interpretation is further supported by spectrographic data, which indicate a consistently low oxygen content on the fiber surfaces. The protective performance of the fibers can be attributed to the engineered dual-layer interphase system composed of boron nitride (BN) and silicon nitride (Si_3N_4). Each layer plays a distinct yet complementary role in ensuring the structural and chemical integrity of the reinforcement under high-temperature oxidative conditions.

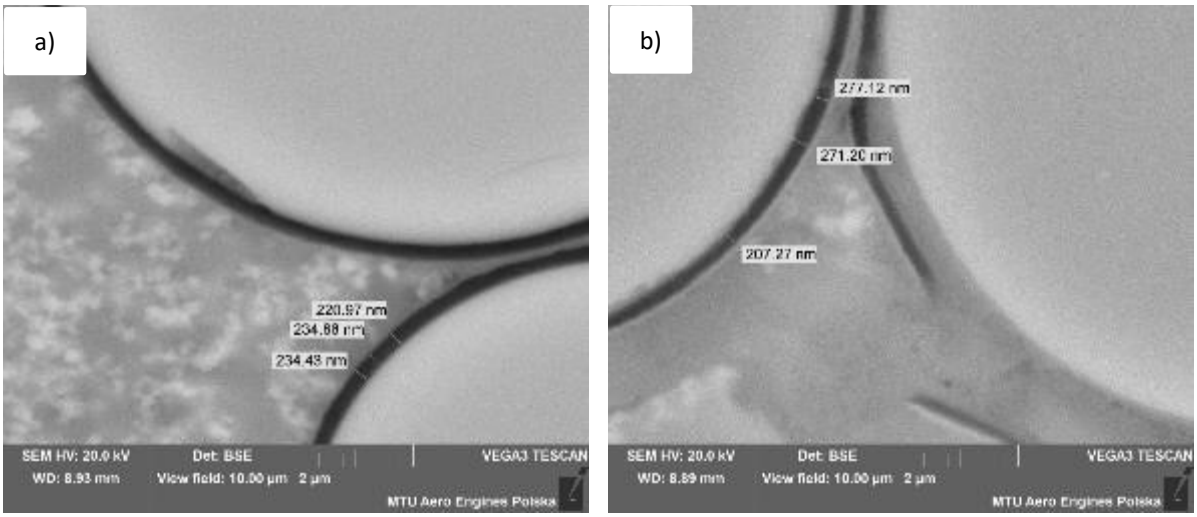

Figure 50 SEM images of fibers in the SiC/SiC material oxidized at a temperature of 980 °C for a) 20 hours, b) 40 hours, c) 80 hours, and d) 100 hours

Importantly, neither the elevated temperature of 980 °C nor the extended oxidation durations up to 100 hours had any observable detrimental effect on the integrity or functionality of these protective coatings. Throughout all tested conditions, the interphase layers remained chemically stable and structurally intact, effectively preventing oxygen ingress to the fiber surface. This highlights the exceptional thermal and oxidative stability of the BN/ Si_3N_4 interphase system and underscores its critical role in maintaining the long - term performance of SiC/SiC composites in harsh environments (especially at temperature up to 1000 °C).

The results of the study clearly indicate that temperature is the key factor influencing the oxidation process of the SiNC/SiC composite. Changes in the material, particularly matrix cracks, appear after just 20 hours, and further extending the time does not lead to additional changes. The SiC matrix is particularly susceptible to oxidation at high temperature, leading to the formation of a silica (SiO_2) layer that can embrittle the matrix and promote cracking. This behavior is strongly influenced by the processing route of the matrix. In PIP-derived SiC, the presence of residual carbon, oxygen, and amorphous phases makes the matrix more reactive and prone to oxidation-induced degradation. In contrast, CVI-processed SiC exhibits higher purity, crystallinity, and oxidation resistance, resulting in improved structural stability under thermal exposure. Therefore, the observed degradation in the current study is not only a function of temperature, but also of the inherent chemical and microstructural characteristics of the PIP-derived matrix.

6.2.2 Oxidation at 1100 °C

The oxidation process of the SiC/SiC composite at a temperature of 1100 °C proceeded under the same conditions and for the same durations as the oxidation process at 980 °C. As a result of oxidation at the higher temperature, the detachment of the composite layer closest to the oxygen exposure was also observed (Figure 51).

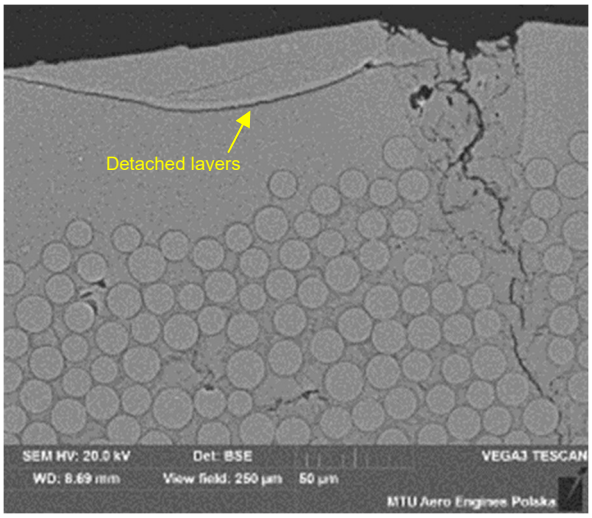

Figure 51 SEM picture of SiC/SiC composite tested at 980 ºC for 40h

Similar to the oxidation at 980 °C, the size and shape of the pores in the material did not change. The pores retained their original morphology and distribution, consistent with the pristine sample, indicating that oxidation at 1100 °C did not lead to pore growth or coalescence. However, pores located in close proximity to matrix cracks and matrix-rich pockets provided an easy path for oxygen propagation. In particular, pores situated within or adjacent to matrix cracks that reopened as a result of oxidation acted as preferential channels for oxygen ingress. These reopened cracks, often extending through matrix-rich zones, created interconnected pathways that facilitated deeper oxygen penetration into the composite structure. Furthermore, oxygen was observed to migrate along pore boundaries, suggesting that the internal pore network - although structurally unchanged - played a critical role in guiding the diffusion of oxidizing species. This interfacial migration along pore walls may have contributed to localized oxidation effects in the surrounding matrix, especially in areas with limited fiber reinforcement. Despite these transport phenomena, no significant increase in pore size or volume fraction was observed, and the pores maintained their original shape and distribution throughout the oxidation process. This confirms that the oxidation mechanism primarily involved crack-assisted oxygen transport rather than pore-driven degradation, and that the porous architecture remained stable under thermal exposure at 1100 °C. (Figure 52 a and b).

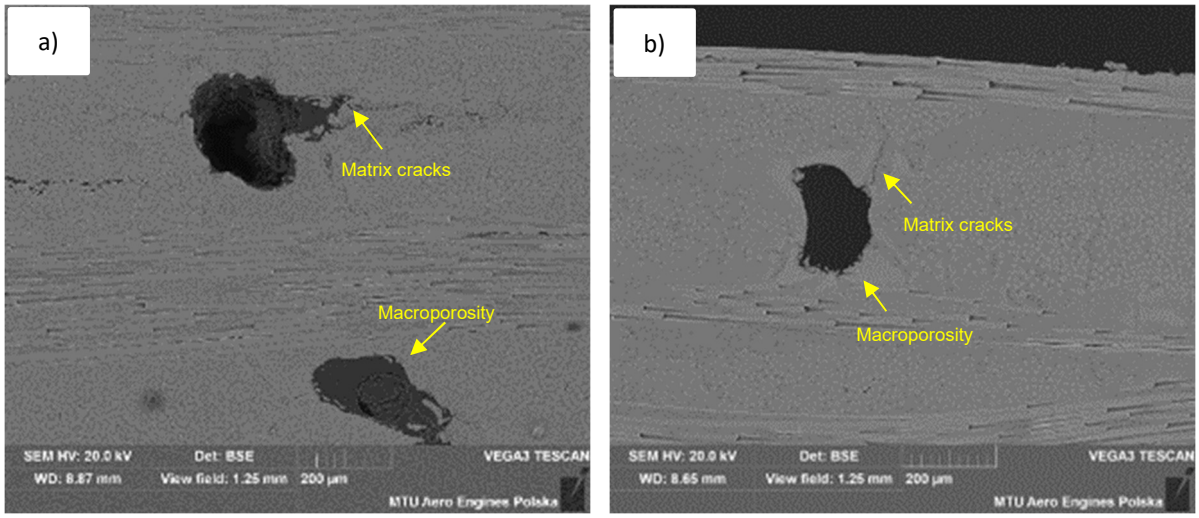

Figure 52 Macroporosity in SiC/SiC composite tested at 980ºC for a) 40h and b) 80h

Matrix-rich pockets located near the sample surface - thus being the most exposed to the oxidizing environment - exhibited significant cracking after oxidation at 1100 °C. These regions, already identified as structurally vulnerable due to their low fiber content and additionally due to chemistry, underwent extensive damage, with cracks propagating both transversely and longitudinally through the matrix. Importantly, this phenomenon was already observed after just 20 hours of oxidation, indicating that matrix-rich pockets are highly susceptible to early-stage oxidative degradation. This behavior is consistent with the mechanisms described earlier in the section on oxidation at 980 °C, where similar matrix-rich zones were shown to be prone to crack initiation due to thermal residual stresses. These stresses arise from the mismatch in the coefficient of thermal expansion (CTE) between the SiC matrix and the surrounding interphase materials, particularly in areas lacking fiber reinforcement. At 1100 °C, the elevated temperature further intensified these effects, leading to more pronounced crack formation in surface-adjacent matrix-rich pockets. The cracks in these regions not only facilitated oxygen ingress but also contributed to the formation of interconnected pathways that extended deeper into the material, accelerating localized oxidation processes (Figure 53 a and b).

The fibers did not undergo oxidation, as confirmed by spectrographic studies and EDS mapping. The cracks in the matrix were formed as a result of the oxidation process. Oxidation, as in the case of 980 °C, caused the opening of cracks that were formed during the matrix infiltration process and provided an easy path for oxygen diffusion (Figure 53).

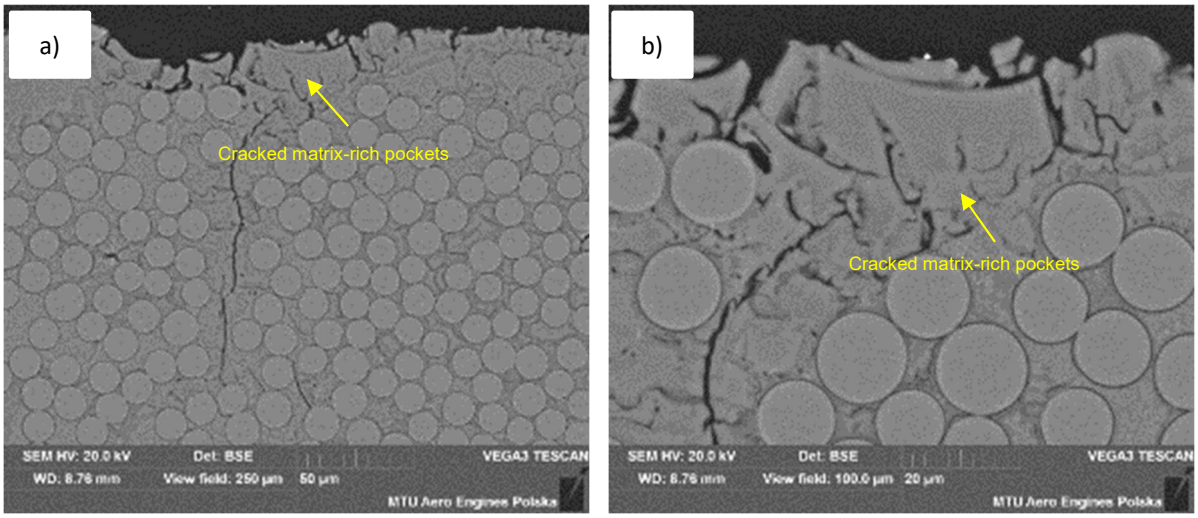

Figure 53 SEM pictures of SiC/SiC composite tested at 1100 °C for 20h, a) and b) cracked matrix-rich pockets.

At a temperature of 1100 °C, the formation of a SiO_2 layer can be observed, which is heterogeneous in its structure and increases in thickness and homogeneity with prolonged oxidation time. The SiO_2 layer does not adhere to the composite, it is chipped and broken. At the beginning of the oxidation process, the SiO_2 layer is barely noticeable, with a thickness ranging from 1 to 6 µm. Extending the oxidation time to 40 hours and 80 hours resulted in the formation of a thicker layer across the entire surface of the SiC/SiC composite. The layer formed during 80 hours is even 2-3 times thicker than the one formed during 40 hours. During 100 hours, due to significant oxidation of the material and detachment of parts of the composite near the oxidation surface, it is difficult to definitively determine the thickness of the layer, as it may have been detached along with the matrix material due to the oxidation process or sample preparation (Figure 54 a, b, c, d).

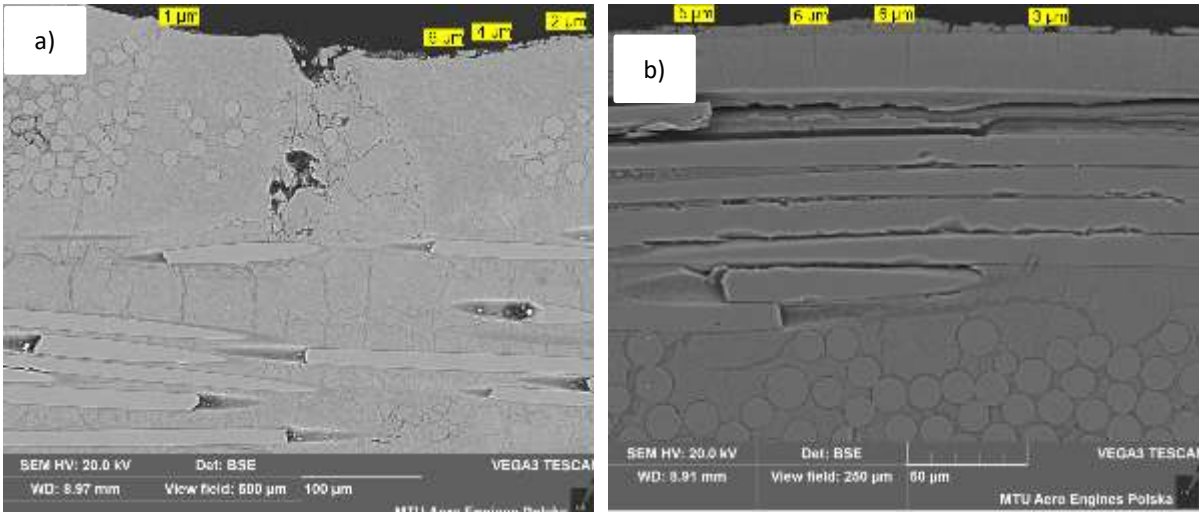

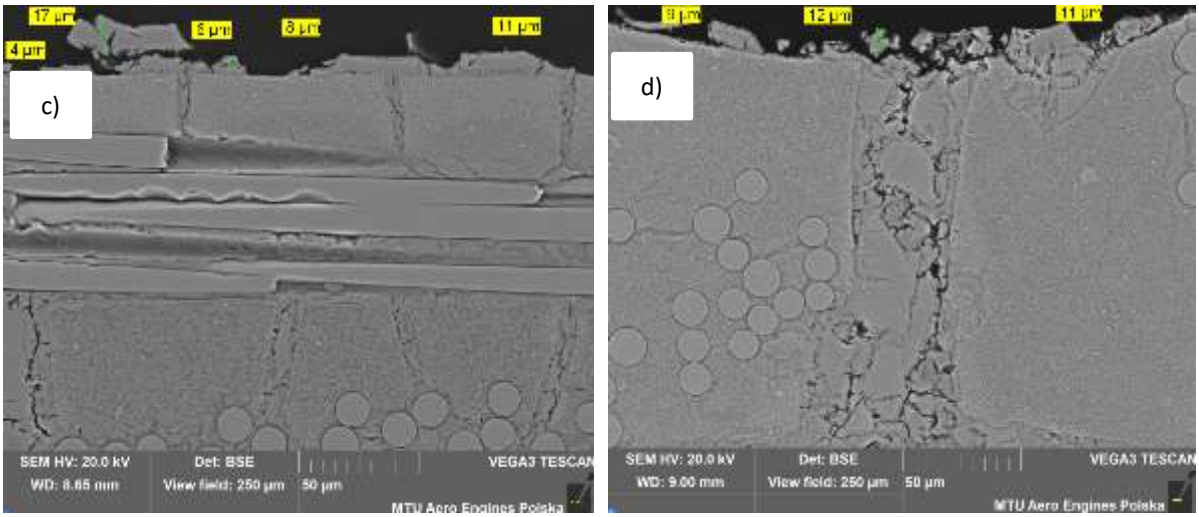

Figure 54 SEM pictures of SiC/SiC composite tested at 1100 ºC for a) 20h, b) 40h, c)80h and d) 100h

At 1100 °C, and especially after 100 hours of oxidation, the fibers began to show signs of oxidation as a direct consequence of the degradation of their protective coating. The loss of continuity and integrity of the BN/Si_3N_4 interphase allowed oxygen to reach the fiber surface, leading to gradual chemical degradation of the fiber material. In some cases, the presence of a distinct rim or halo around the fibers may indicate partial oxidation of the fiber surface, suggesting that the protective function of the interphase was no longer fully effective in those regions (Figure 55 b). In SEM images (Figure 55 a), the coating appears fractured, delaminated, and in some regions even partially vaporized. These damaged coatings were frequently observed in direct association with matrix cracks, which did not propagate along the fiber–coating interface, but rather along the fibers. The non-uniformity of the coating, along with its partial loss, is likely the result of oxidation and volatilization of boron and nitrogen species, particularly from the BN layer. This interpretation is supported by DSC results, which revealed exothermic peaks corresponding to oxidation reactions in this temperature range. At 1100 °C, BN oxidizes to form B_2O_3, a compound known to be volatile at elevated temperature, especially in open or cracked regions. Similarly, nitrogen-containing phases may decompose, releasing gaseous nitrogen oxides.

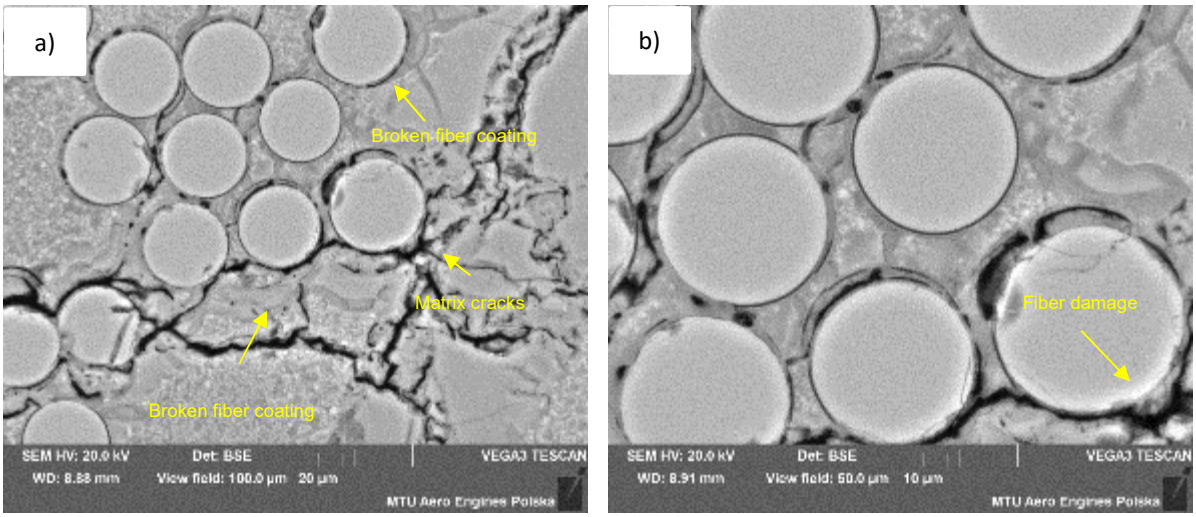

Figure 55 Broken fiber coating in SiC/SiC composite tested at 1100 °C for 100h

Furthermore, during oxidation for 100 hours, significantly increased oxidation of the SiC/SiC composite material was observed. The cracks in the matrix became much more visible (Figure 56 a, b). Longitudinal cracks connected with transverse cracks, allowing oxygen to migrate much deeper into the material. Additionally, these matrix cracks are thicker, and when a fiber is encountered along the crack path, and its coating is detached, the coating undergoes oxidation and degradation. Importantly, the matrix cracks were observed to propagate along the fiber direction rather than through the fibers themselves, which suggests that the fibers continued to act as effective barriers to crack growth. This behavior indicates that, despite partial degradation of the fiber coatings and significant matrix damage, the composite material still maintained its structural integrity and did not undergo catastrophic failure. The crack deflection along the fibers reflects the composite's inherent damage tolerance, which is a key design feature of SiC/SiC systems intended for high-temperature applications.

Previous oxidation studies of the SiC/SiC composite for 80 hours did not show such changes in the microstructure. The reason for this phenomenon may be related to differences in oxidation mechanisms with longer exposure times. In the case of 100 hours, the longer exposure time to high temperature may have caused more intense oxidation processes, leading to the formation of larger and more visible cracks and deeper oxygen migration into the material.

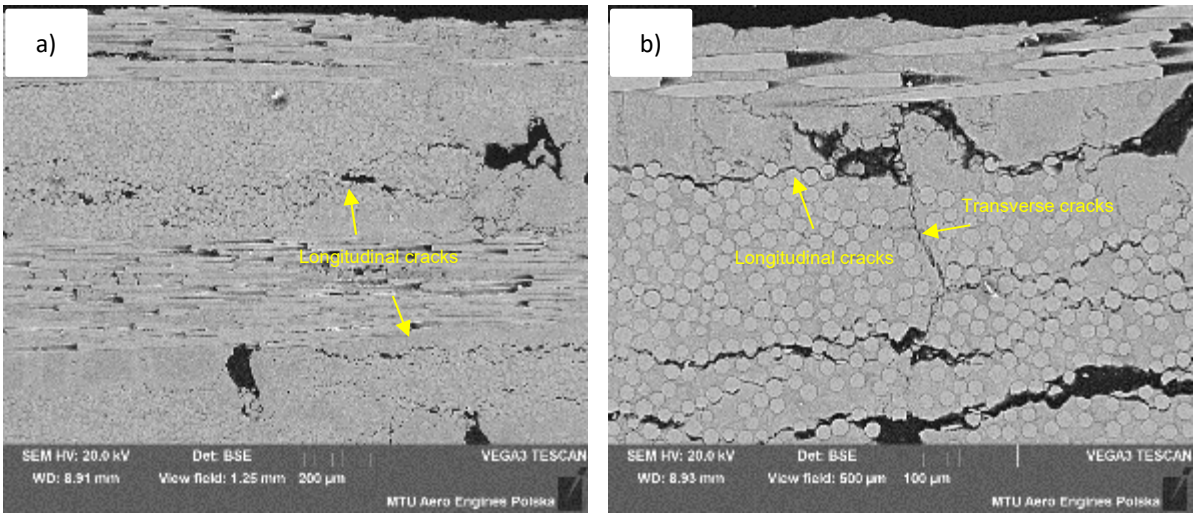

Figure 56 SEM Pictures of S200H composite tested at1100 °C for 100h a) view field:1,25 mm, b) view field 500 µm

All of these structural changes resulting from oxygen exposure-such as the formation of interconnected longitudinal and transverse cracks, partial degradation of fiber coatings, and matrix damage - collectively contributed to significant oxygen migration deep into the material, as clearly demonstrated by EDS elemental maps (Figure 57 a and b). These maps reveal elevated oxygen concentrations not only near the surface but also along crack paths and within matrix-rich regions, confirming that the crack network served as an effective conduit for oxygen ingress. The observed oxygen distribution supports the conclusion that prolonged oxidation at 1100 °C enabled deep penetration of oxidizing species, further accelerating local degradation processes.

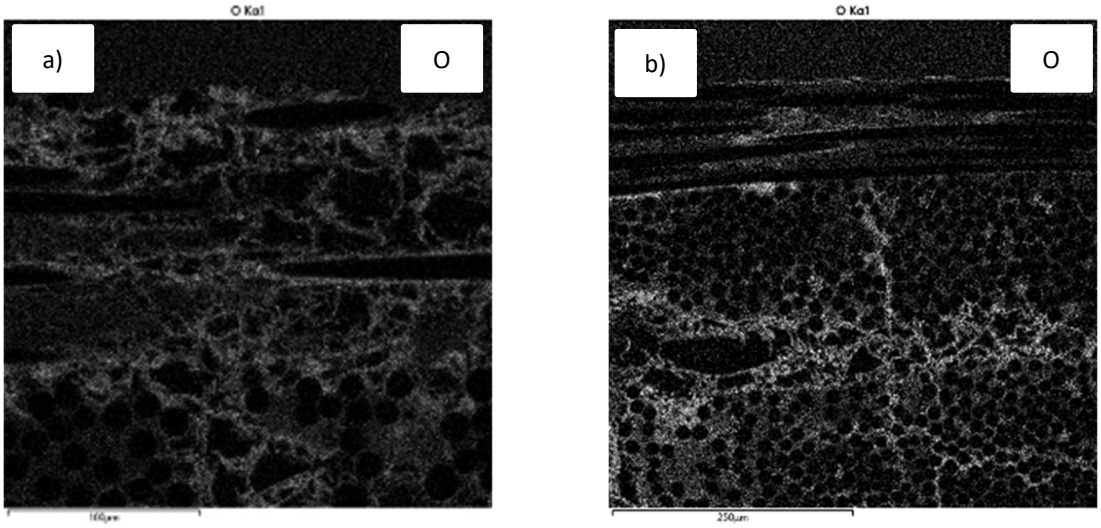

Figure 57 EDS Mapping for oxygen in SiC/SiC composite tested at 1100 °C

In comparison to oxidation at 980 °C, oxidation at 1100 °C resulted in the formation of a visible oxide layer on the surface of the SiC/SiC composite, which could be clearly observed using

scanning electron microscopy (SEM). Unlike the thin and barely detectable SiO_2 layer formed at 980 °C, the oxide scale at 1100 °C was thicker and more distinct, indicating more advanced surface oxidation. Moreover, this oxide layer was non-uniform along the length of the sample, with variations in thickness and morphology likely influenced by local differences in microstructure, surface roughness, and crack distribution. In addition to the surface oxidation, a clear increase in the cracking of matrix-rich pockets was observed, especially those located near the sample surface. These regions, already vulnerable due to their low fiber content, exhibited extensive cracking that was not present at 980 °C. Furthermore, the protective coating on the fibers began to undergo progressive degradation, particularly after prolonged exposure (e.g., 100 hours), which was not observed at the lower temperature. This degradation is closely related to the oxidation-induced chemical transformations of the BN and Si_3N_4 interphase layers. At elevated temperature, boron nitride (BN) oxidizes to form boron oxide (B_2O_3), which is volatile and can evaporate, especially in open or cracked regions. Similarly, silicon nitride (Si_3N_4) undergoes oxidation to form silica (SiO_2) and nitrogen-containing gases. These reactions not only reduce the protective capacity of the interphase but also contribute to the formation of porosity and local weakening of the fiber-matrix interface. The presence of a rim or halo around some fibers further supports the hypothesis of partial oxidation and volatilization of interphase components. Matrix cracks at 1100 °C were also significantly wider and more frequent, forming interconnected networks that facilitated deeper oxygen penetration into the material. Such extensive cracking and coating degradation were not observed at 980 °C, where oxidation reactions were either absent or much less intense. The higher temperature clearly accelerated the oxidation mechanisms, leading to more severe microstructural changes. Despite this advanced degradation, the composite did not suffer catastrophic failure. The SiC fibers remained uncracked and structurally intact, continuing to provide mechanical reinforcement. This highlights the material's inherent damage tolerance and the critical role of the fiber architecture and interphase design in maintaining the composite's integrity under aggressive oxidative conditions.

6.2.3 Oxidation in 1300 °C

As a result of the oxidation of the S200H composite at 1300 °C, the formation of oxidation-induced porosity can be observed. In SEM images (Figure 58 a and b), this porosity appears as fine, gray voids distributed within the matrix of the composite and its visible after 20h of oxidation. The matrix of the S200H material consists of an amorphous silicon carbonitride (SiNC)

phase, reinforced with dispersed Si_3N_4 fillers. The formation of these pores is attributed to several concurrent degradation mechanisms. The oxidation of the amorphous SiNC matrix leads to the breakdown of Si-C and Si-N bonds, resulting in the formation of a silica (SiO_2) network and the release of gaseous byproducts such as carbon monoxide (CO) and nitrogen (N_2). These gases, upon escaping the matrix, leave behind microvoids that accumulate over time. This transformation contributes to the development of amorphous regions and residual porosity. Furthermore, the evolution of gases during these oxidation reactions generates internal pressure within the composite, which can lead to the formation of microcracks and the expansion of existing pores [109]. This effect is exacerbated by the volume expansion associated with the formation of oxide phases, which introduces mechanical stresses into the matrix. These stresses can cause further microcracking, delamination, and interfacial debonding, all of which contribute to the progressive degradation of the material's microstructure. As oxidation time increases, both the size and density of the pores grow, indicating a time-dependent deterioration of the SiNC matrix and a continuous evolution of gaseous species. Notably, this porosity was most frequently observed near the surface of the sample, where oxygen exposure is most intense. It was also particularly concentrated in matrix-rich pockets and in areas where matrix cracking had occurred, suggesting that these regions are more susceptible to oxidative attack and gas accumulation.

Oxidation of the composite at a temperature of 1300 °C caused significant cracks in the SiC matrix. During oxidation for 20, 40, 80, or 100 hours, longitudinal and transverse cracks can be easily observed, which led to the diffusion of oxygen significantly deep into the material. As a result of oxidation at 1300 °C for just 20 hours, a large amount of oxygen paths migrating deep into the material can be observed. Increasing the oxidation time to 40 and 80 hours reveals an even greater amount of oxygen in the material and an enlargement of the cracks in the composite matrix (Figure 58 c and d).

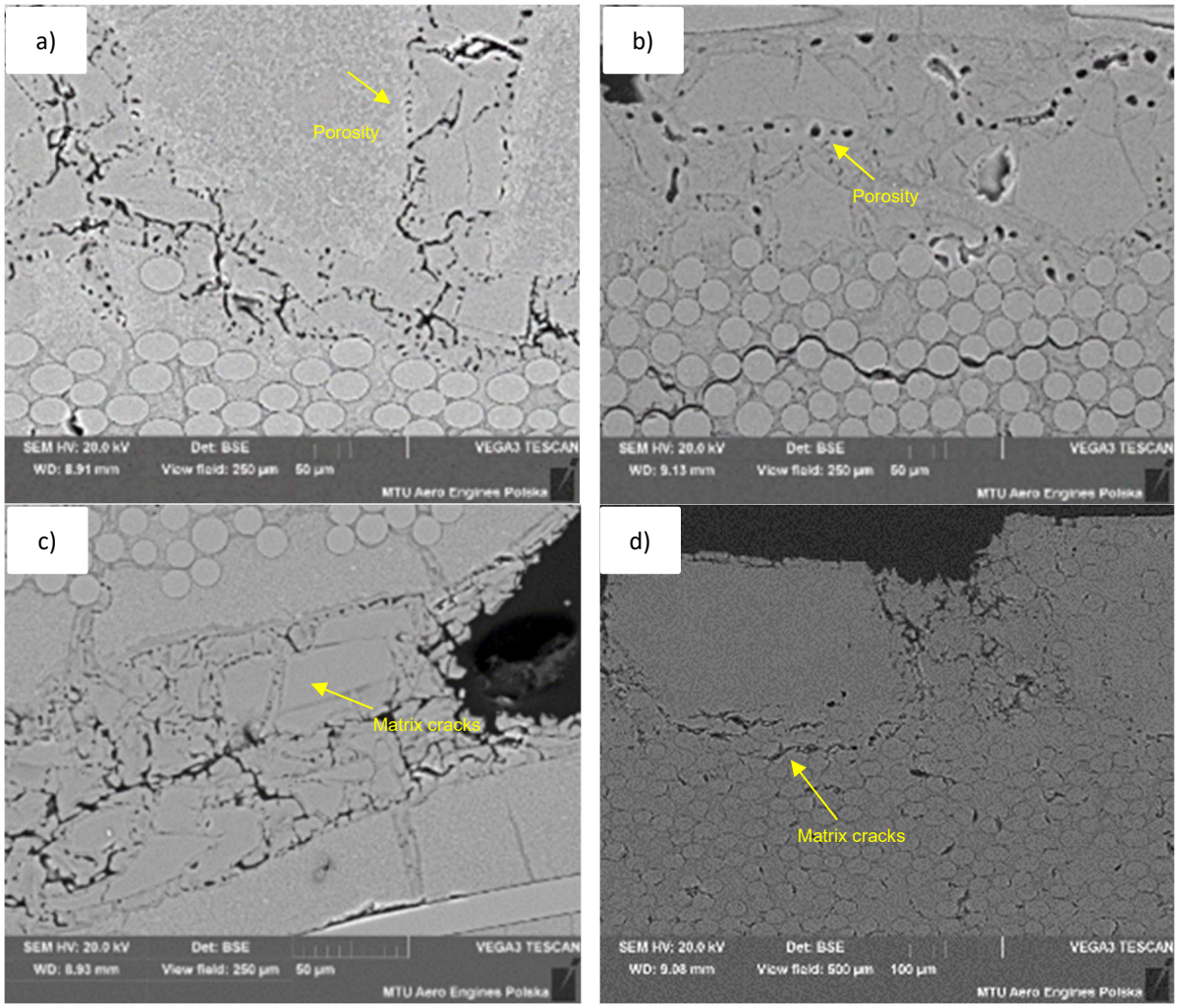

Figure 58 SEM pictures of SiC/SiC composite after 1300 ºC oxidation for a) 20h, b) 40h, c) 80h and d) 100h

The oxygen content in the fibers as a result of oxidation at 1300 °C for all oxidation times was at a similarly low level, as indicated by spectrographic measurements. However, SEM images show both the detachment of the coating from the fiber after just 40 hours of oxidation and further oxidation of the fibers that were stripped of their coating after 80 and 100 hours. The BN interphase, although effective elevated temperature, begins to oxidize. This reaction produces boron oxide (B_2O_3), which is a low-viscosity glass that can either volatilize or react with silica (SiO_2) present in the matrix to form borosilicate glass [110]. While this glassy phase may temporarily seal microcracks, it also contributes to the formation of amorphous regions and residual porosity. Moreover, the volatilization of B_2O_3 can leave behind voids and expose the underlying SiC fibers to further oxidation. The Si_3N_4 coating, although more thermally stable, also undergoes oxidation over time, forming a silica layer. This layer can initially act as a pro-

tective barrier, but under cyclic thermal or mechanical stress, it may crack or spall, compromising its protective function. Once the coatings are breached, oxygen can penetrate to the fiber surface, leading to oxidation of the SiC fibers themselves. This results in surface roughening, embrittlement, and eventual degradation of the fiber-matrix interface (Figure 59 d). Additionally, the thickness of the coating on fibers that had a uniform coating was similar to that measured for fibers that were not subjected to oxidation (Figure 59 a-h).

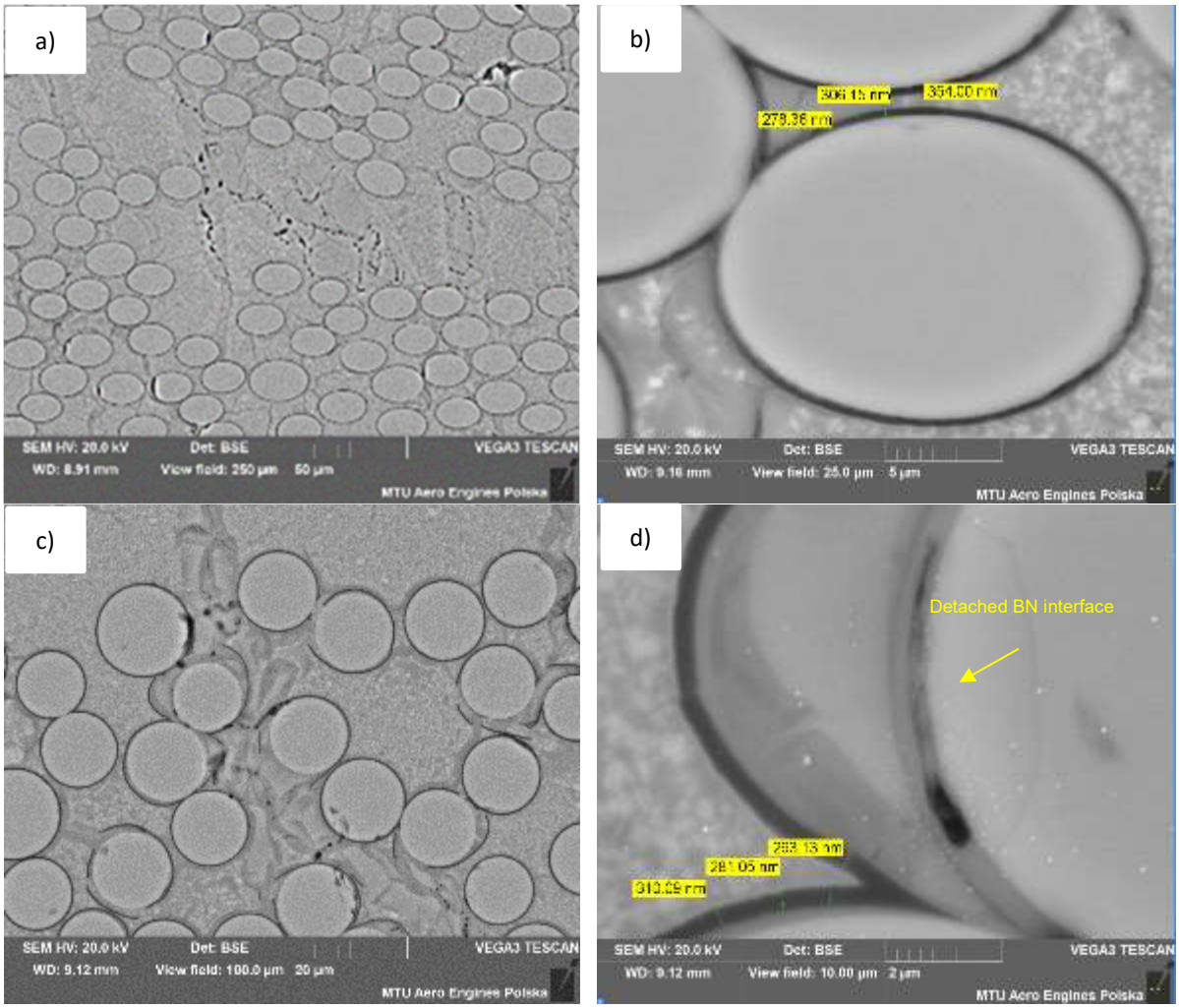

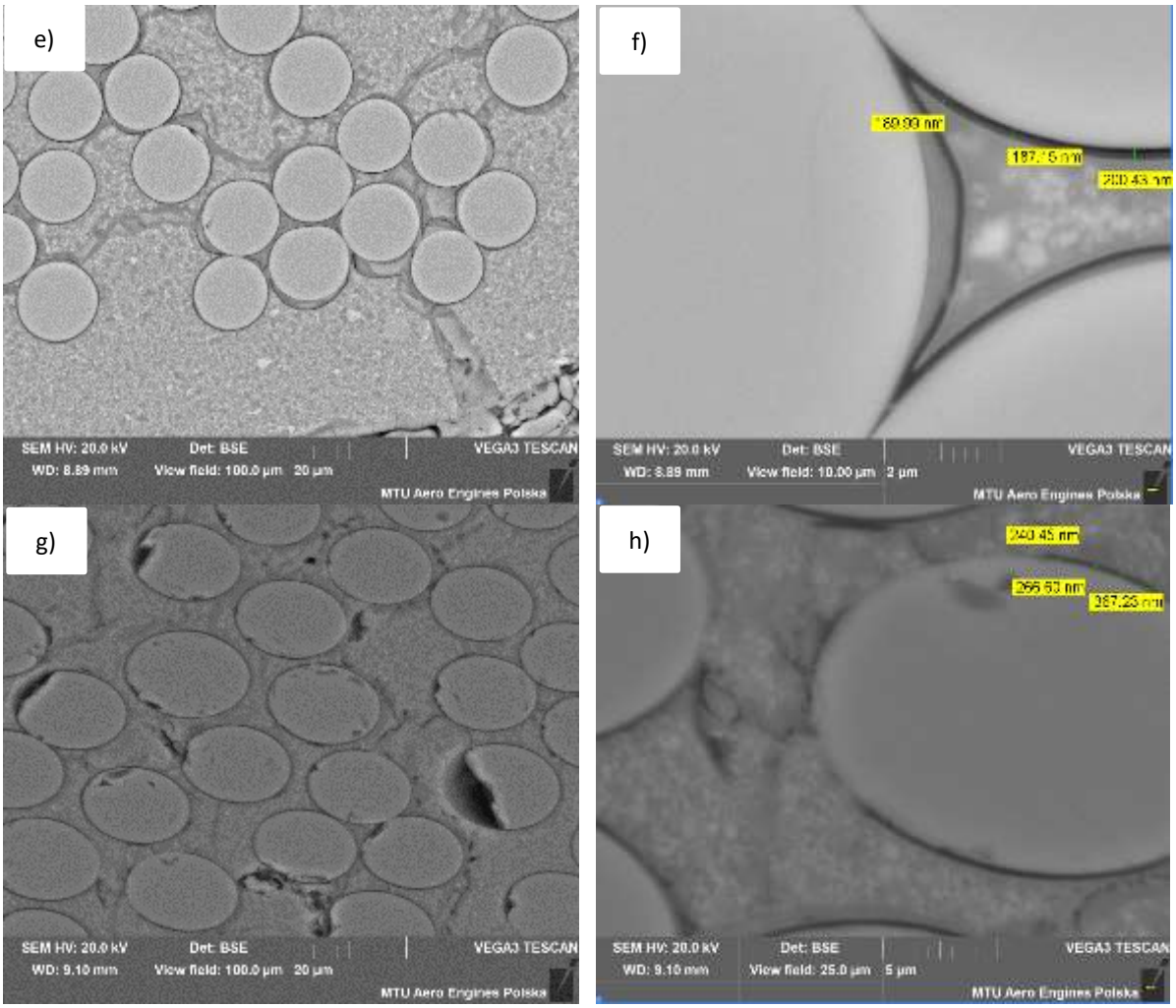

Figure 59 SEM pictures and fiber coating thickness measurements after oxidation at 1300 ºC for a) and b) 20h, c) and d) 40h, e) and f) 80h, g) and h) 100h

As a result of the oxidation process over 20 hours, an oxidizing layer formed on the surface of the composite, which was non-uniform. Its thickness ranged from 4 to 8 µm. Increasing the oxidation time led to the growth of the oxidizing layer to approximately 11 µm for 40 hours of oxidation and a similar value for 80 hours of oxidation. After 100 hours of oxidation at 1300 °C, a noticeable change in the morphology of the oxidizing layer can be observed. It is no longer unevenly distributed on the surface of the material but closely adheres to the composite and migrates inward (Figure 60 d). Its thickness is approximately 8 mm (Figure 60 a-d).

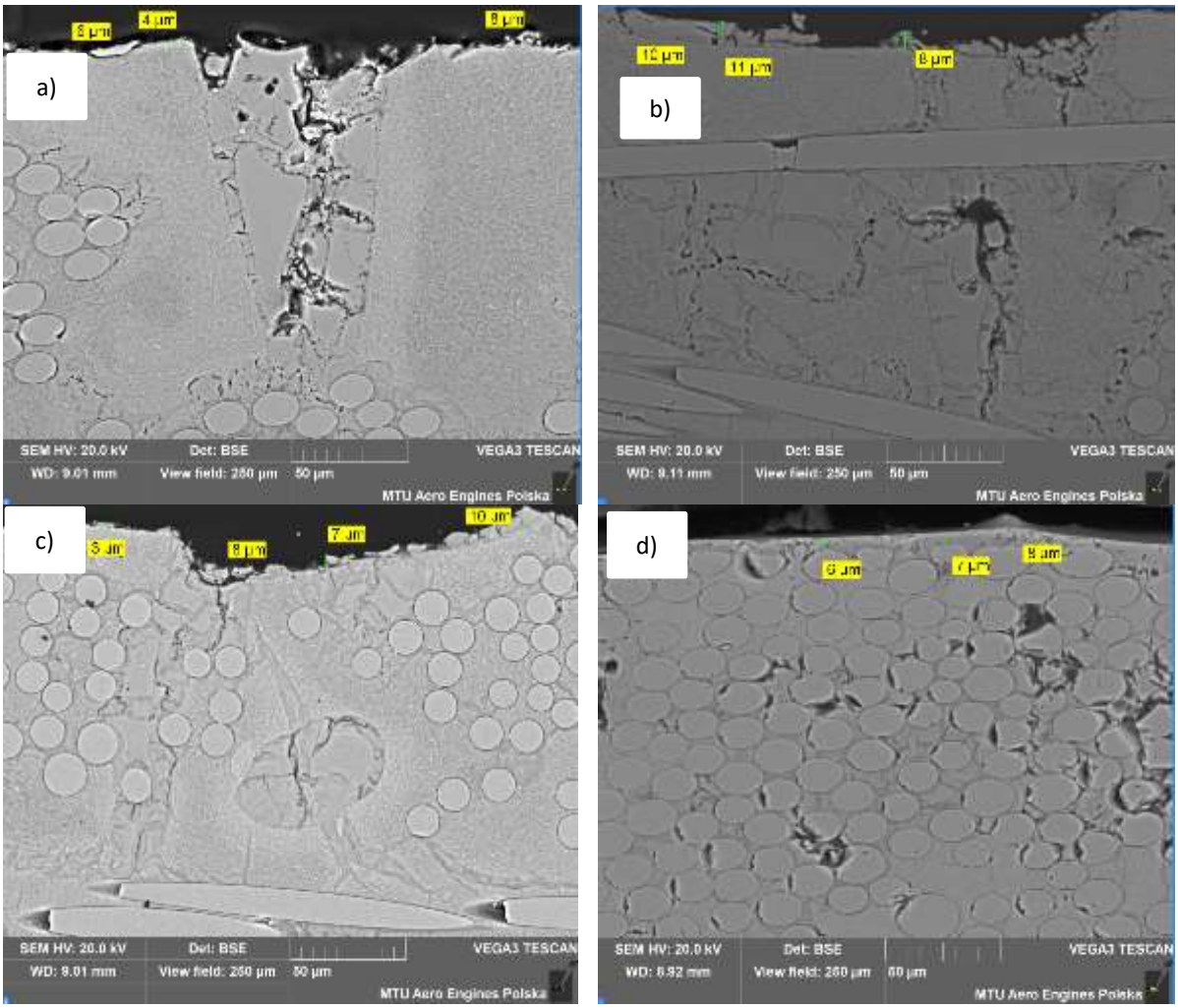

Figure 60 SEM pictures of oxide layer formed at 1300 ºC oxidation process during a) 20h, b) 40h, c), 80h and d) 100h

The greatest oxidation of the composite can be observed after 100 hours. Due to the significant oxidation, the material became brittle, making sample preparation very difficult. As can be observed, some fibers are broken or torn out, indicating severe structural degradation. In addition to the extensive oxidation of the matrix, the fibers themselves also show clear signs of damage. At 1300 °C, after 100 hours of exposure, the protective coatings on the fibers - particularly in regions close to the surface where oxygen ingress is most intense - undergo substantial degradation. The BN and Si_3N_4 interphases, which are designed to shield the fibers from oxidation, are no longer effective. As a result, the underlying SiC fibers become directly exposed to the oxidizing environment. This degradation leads to the breakdown of the fiber surface, and in many cases, the formation of a continuous SiO_2 layer that penetrates into the fiber structure. The infiltration of silica not only embrittles the fibers but also disrupts the fiber-matrix interface,

further compromising the mechanical integrity of the composite. These effects are most pronounced near the outer regions of the sample, where oxygen exposure is highest and the protective coatings are most vulnerable.

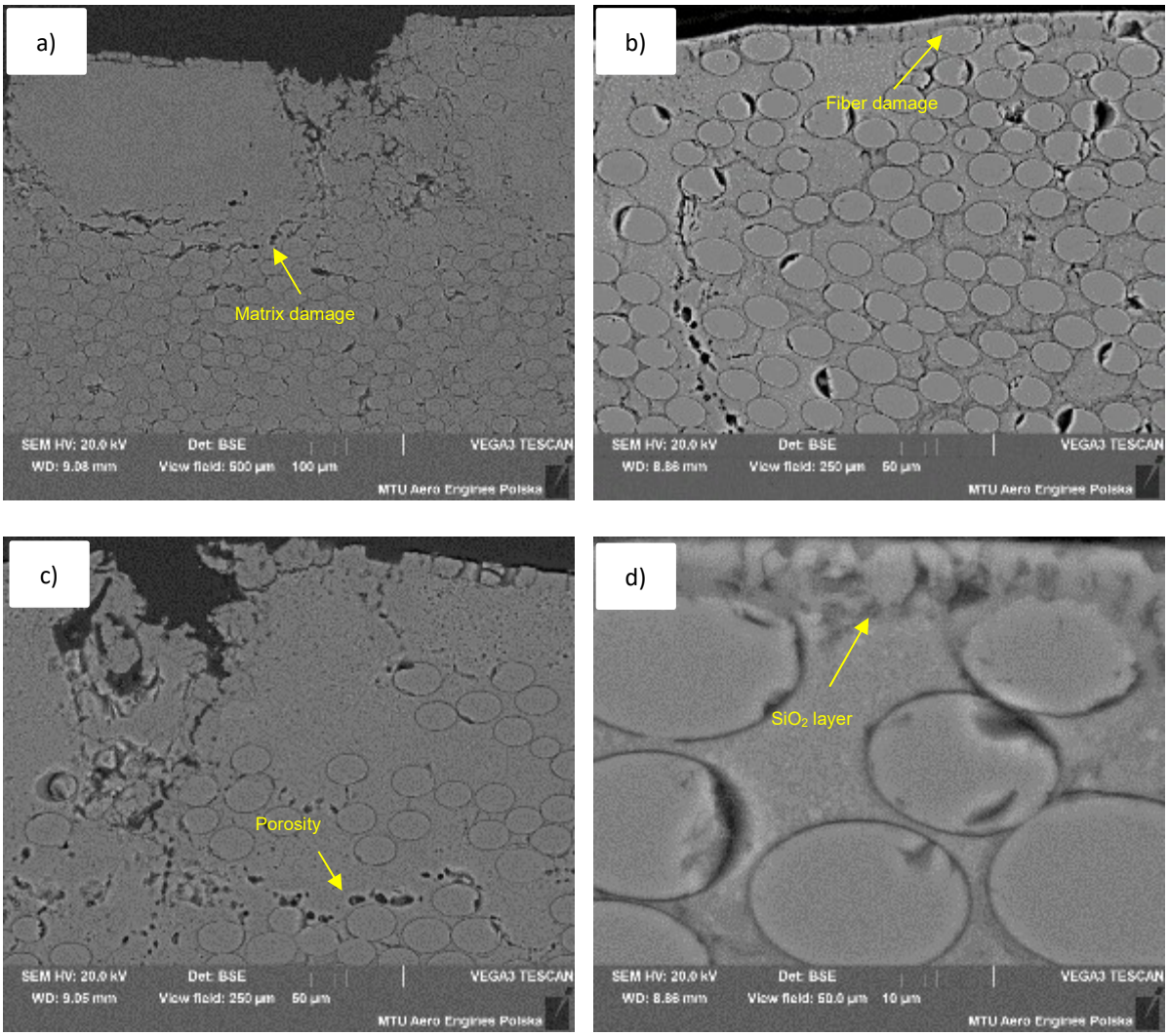

Figure 61 SEM pictures of S200H composite tested at 1300 °C after 100h a) vf: 500 µm, b) and c) vf: 250 µm, d) vf:50 µm

In addition to the observed structural degradation, oxidation at 1300 °C also resulted in significant oxygen migration into the bulk of the material, as confirmed by EDS oxygen mapping (Figure 62 a and b). The elemental distribution maps clearly show elevated oxygen concentrations not only near the surface but also deep within the matrix, indicating that oxygen diffusion progressed substantially during prolonged exposure.

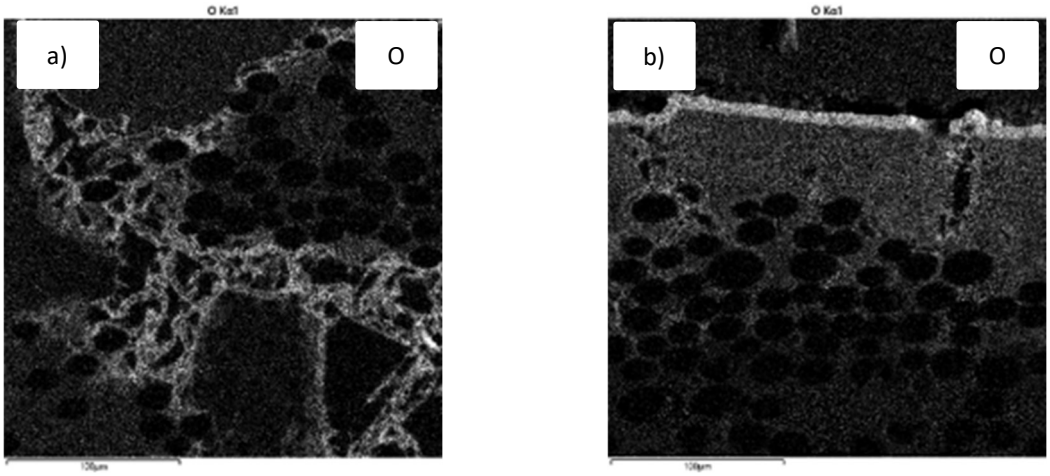

Figure 62 EDS Maps for oxygen for S200H composite tested at 1300 ºC, a) for 40h and b) for 100h

Similar to the behavior observed at lower oxidation temperature (980 and 1100 °C), oxygen migration was most pronounced in matrix-rich pockets and along matrix cracks. These regions, due to their higher glassy phase content and structural discontinuities, appear to act as preferential pathways for oxygen ingress. The presence of microcracks and amorphous zones likely facilitates faster diffusion, leading to localized oxidation and further degradation of the matrix and fiber coatings.

At 1300 °C, the oxidation of the SiC/SiC composite becomes significantly more aggressive and penetrative compared to lower temperature. After prolonged exposure (e.g., 100 hours), the material exhibits extensive microstructural degradation, both at the surface and within the bulk. A thick, continuous oxide scale forms on the surface, and oxygen diffusion into the interior of the composite is clearly evident, as confirmed by EDS oxygen mapping. These maps reveal deep oxygen penetration, particularly along matrix cracks and in matrix-rich pockets, which act as preferential diffusion pathways. The matrix undergoes severe oxidation, resulting in the formation of a dense SiO_2 network and the release of gaseous byproducts such as CO and N_2. These reactions contribute to the development of internal porosity and embrittlement. Cracking becomes widespread, with interconnected networks forming throughout the matrix, especially near the surface. These cracks not only weaken the structure but also facilitate further oxygen ingress. The fiber coatings, particularly BN and Si_3N_4, degrade substantially under these conditions. The BN interphase oxidizes to volatile B_2O_3, which either evaporates or reacts with SiO_2 to form borosilicate glass. This glassy phase, while potentially sealing cracks temporarily, contributes to interfacial porosity and local weakening. The Si_3N_4 coating also oxidizes, forming SiO_2 and releasing nitrogen-containing gases. As a result, the protective function of the

interphases is lost, and the underlying SiC fibers become exposed to oxidation. In many cases, a silica layer is observed penetrating into the fiber structure, indicating advanced degradation. Although the S200H composite, consisting of SiC fibers with a thermal stability up to 1600 °C and a matrix also known for its high-temperature resistance, is designed for elevated temperature applications, experimental results show that it undergoes progressive degradation due to oxidation already at lower temperature, such as those investigated in this study. Partial oxidation and microstructural changes were observed after exposure to 980 °C and 1100 °C, with more pronounced effects - including matrix cracking, porosity formation, and interphase degradation - appearing at 1300 °C. Despite these changes, the composite did not experience catastrophic failure, and the SiC fibers remained structurally intact, continuing to provide mechanical reinforcement. This demonstrates the material's inherent damage tolerance and confirms its potential for high - temperature applications. However, the observed degradation mechanisms-particularly the oxidation of the matrix and fiber coatings, oxygen ingress through cracks, and the formation of volatile or glassy oxidation products - highlight the limitations of unprotected use in harsh environments. Therefore, for applications such as aero-engine components, where the material is exposed to complex atmospheres, thermal gradients, and mechanical stresses, the use of environmental barrier coatings (EBCs) and thermal barrier coatings (TBCs) is strongly recommended. These protective layers can significantly enhance the oxidation resistance, reduce thermal loading, and extend the service life of the composite under real-world operating conditions.

Based on the results of microstructural analysis and the mechanisms occurring in the material during the oxidation of the SiC/SiC composite, as well as the observation that temperature-rather than time-is the primary driver of the oxidation process, the following degradation scheme for material has been proposed (Figure 63). This scheme describes the formation of open cracks in the matrix as the temperature increases, along with partial degradation of the fiber coating and the development of matrix porosity as a result of exposure to a temperature of 1300 °C. Additionally, the oxidation process leads to the formation of a homogeneous SiO_2 layer on the surface, which thickens progressively with increasing temperature.

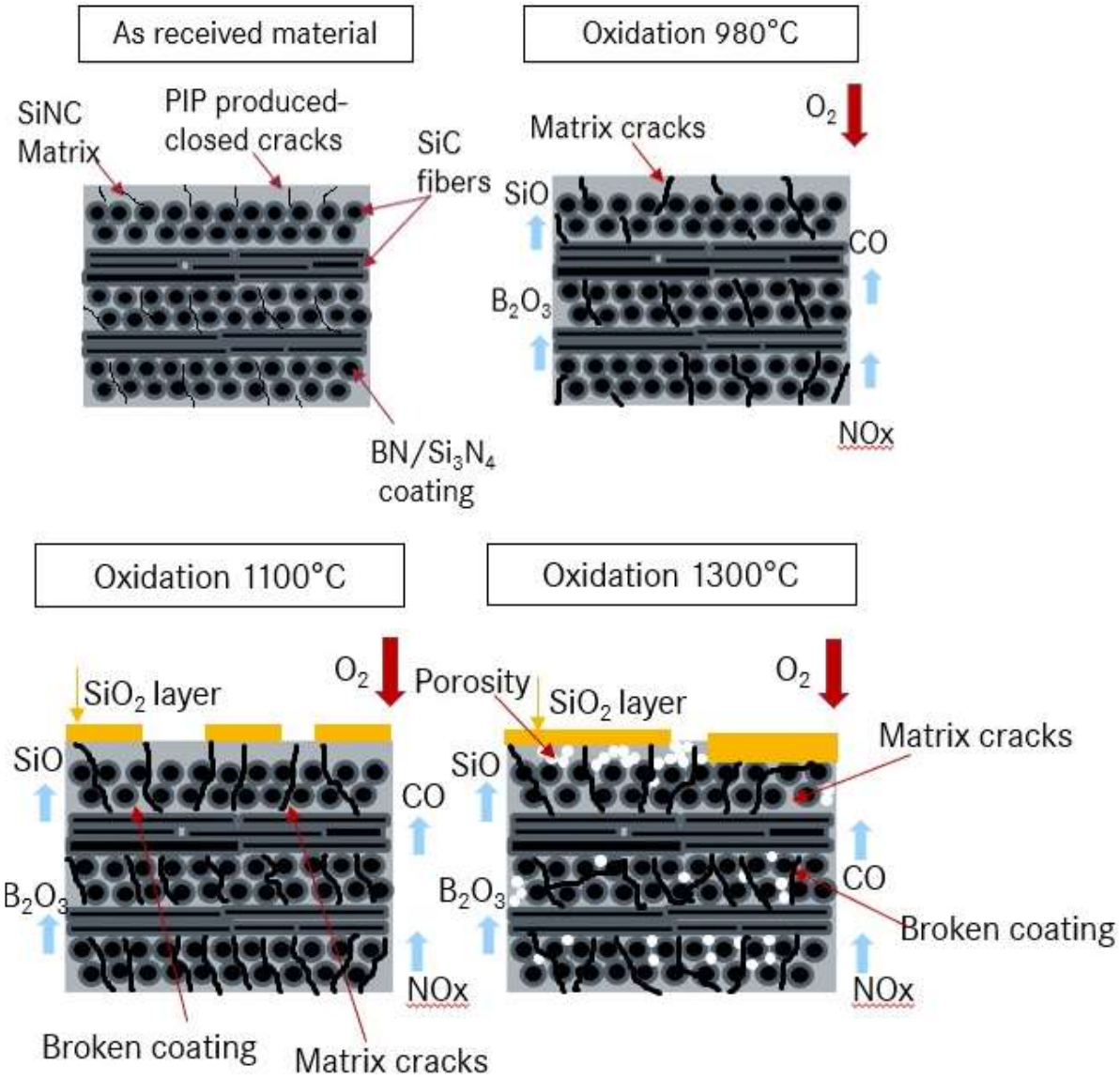

Figure 63 Degradation scheme for S200H material subjected to oxidation at 980, 1100 and 1300 °C

6.3 CMC composite after creep testing

To investigate the combined effects of oxygen exposure and mechanical stress on SiC/SiC composites, creep tests were performed at 980 and 1100 °C. These temperature were selected based on prior oxidation experiments conducted at 980, 1100, and 1300 °C, allowing for a direct comparison of microstructural changes induced by thermal oxidation and mechanical loading. This approach enables a deeper understanding of the degradation mechanisms affecting the composite under service-like conditions.

Creep tests were performed on 16 samples: 4 samples at a temperature of 980 °C and a maximum stress of 100 MPa, 4 at a temperature of 980 °C and a maximum stress of 200 MPa, 4 at

a temperature of 1100 °C and a maximum stress of 100 MPa, 2 at a temperature of 1100 °C and a maximum stress of 200 MPa, and 2 at a maximum stress of 150 MPa. The samples tested at a temperature of 980 °C and a maximum stress of 100 MPa reached a life of 200 hours without failure, while the samples at the same temperature but with a higher maximum stress of 200 MPa failed in the range of 33-106 hours (Figure 64). The samples that were tested at a higher temperature - 1100 °C, with a maximum stress of 100 MPa and 150 MPa, also reached a life of 200 hours without failure. However, increasing the stress to 200 MPa resulted in the samples failing in less than one hour.

The summary describing all samples after creep tests is presented in (Table 14).

Table 14 List of creep tested samples

Sample number	Test temperature [°C]	Stress max [MPa]	Life [hours]	Run out/broken	Creep strain at failure/run out [%]	Total strain at failure/ run out [%]
1	980	100	200	Run out	0,048	0,154
2	980	100	200	Run out	0,072	0,168
3	980	100	200	Run out	0,067	0,174
4	980	100	200	Run out	0,059	0,158
5	980	200	106,3	broken	0,14	0,37
6	980	200	79,5	broken	0,13	0,363
7	980	200	59,5	broken	0,14	0,373
8	980	200	33	broken	0,18	0,409
9	1100	100	200	Run out	0,193	0,291
10	1100	100	200	Run out	0,201	0,300
11	1100	100	200	Run out	0,198	0,295
12	1100	100	200	Run out	0,208	0,317
13	1100	200	0,73	broken	0,16	0,426
14	1100	200	0,27	broken	0,101	0,369
15	1100	150	200	Run out	0,428	0,605
16	1100	150	200	Run out	0,461	0,647

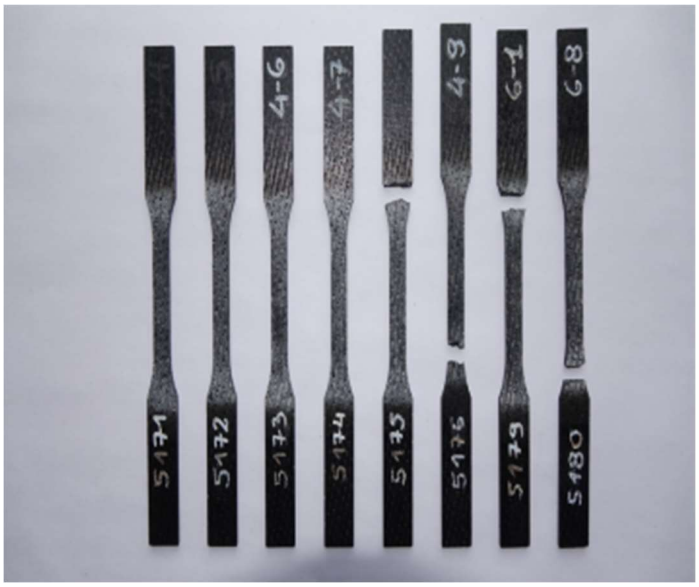

Figure 64 Samples after creep testing in the temperature 980 °C

Examples of plotted data recorded during the sample testing are presented below in Figure 65. It was observed, that the strain changed in the intervals:

- The initial increase during loading to given stress-loading strain.
- Once the creep test has started, the deformation increases further. This initial phase, often referred to as primary creep, is characterized by a strain rate decreasing over time (region I). For samples tested at 980 °C, this visible strain increase region is shorter. For samples tested at 1100 °C the transition to a linear increase of strain occurs after ~30-50 hours.
- Following this, the strain continues to increase at a slower and more stable rate. Although this phase resembles secondary creep, it is important to note that for SiC/SiC composites, a true steady-state creep regime is generally not observed [53, 111]. Instead, the strain rate remains variable over time, which is why this region is often referred to in the literature as pseudo-steady-state creep. In this study, the tests were terminated after 200 hours, and for samples that failed earlier, no tertiary creep - characterized by accelerating strain leading to rupture - was observed.
- The use of the terms primary, secondary, and tertiary creep in this context serves as a descriptive framework for interpreting the shape of the strain-time curves, rather than implying classical metallurgical creep behavior. This distinction is particularly relevant for ceramic matrix composites, where damage mechanisms such as oxidation and microcracking dominate over time-dependent plastic deformation.

- When the test time reached 200 hours, the unloading process started.

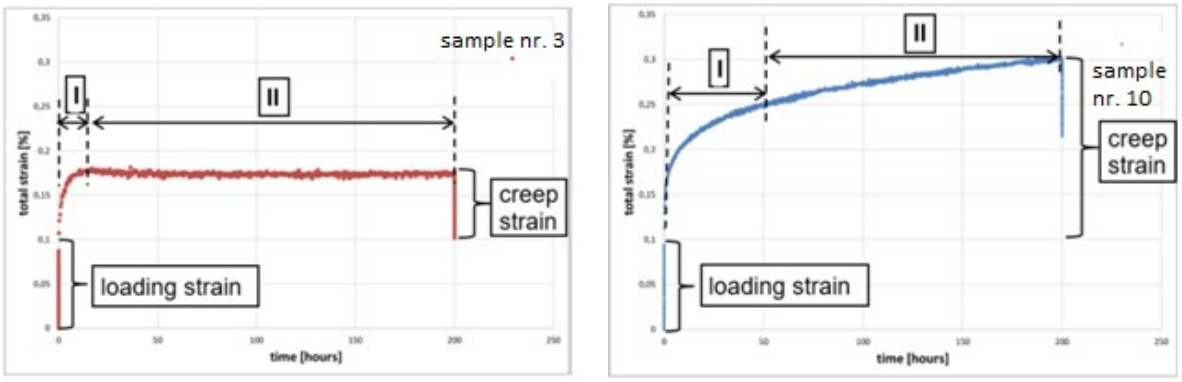

a) b)

Figure 65 Strain/time diagram for samples: a) 5173 tested at 980 °C, b) 5224 tested at 1100 °C.

Load/strain data were recorded during loading to desired stress level and during unloading of samples that met the criterion of 200 hours of running. Only the data points covering the loading and unloading periods were extracted from the raw data files.

The loading strain values were noted for all samples. The results of the loading strain for all samples are presented in Figure 66 and summarized in Table 15. Moreover, the stress-strain curves were plotted for loading interval (Figure 67). For all samples up to ~100 MPa the stress/strain dependence is close to the linear, so we can assume that material is in elastic stage. For tests at 1100 °C, the deviation from linearity starts from about 80 MPa. Above these load ranges, the specimens are in an inelastic state.

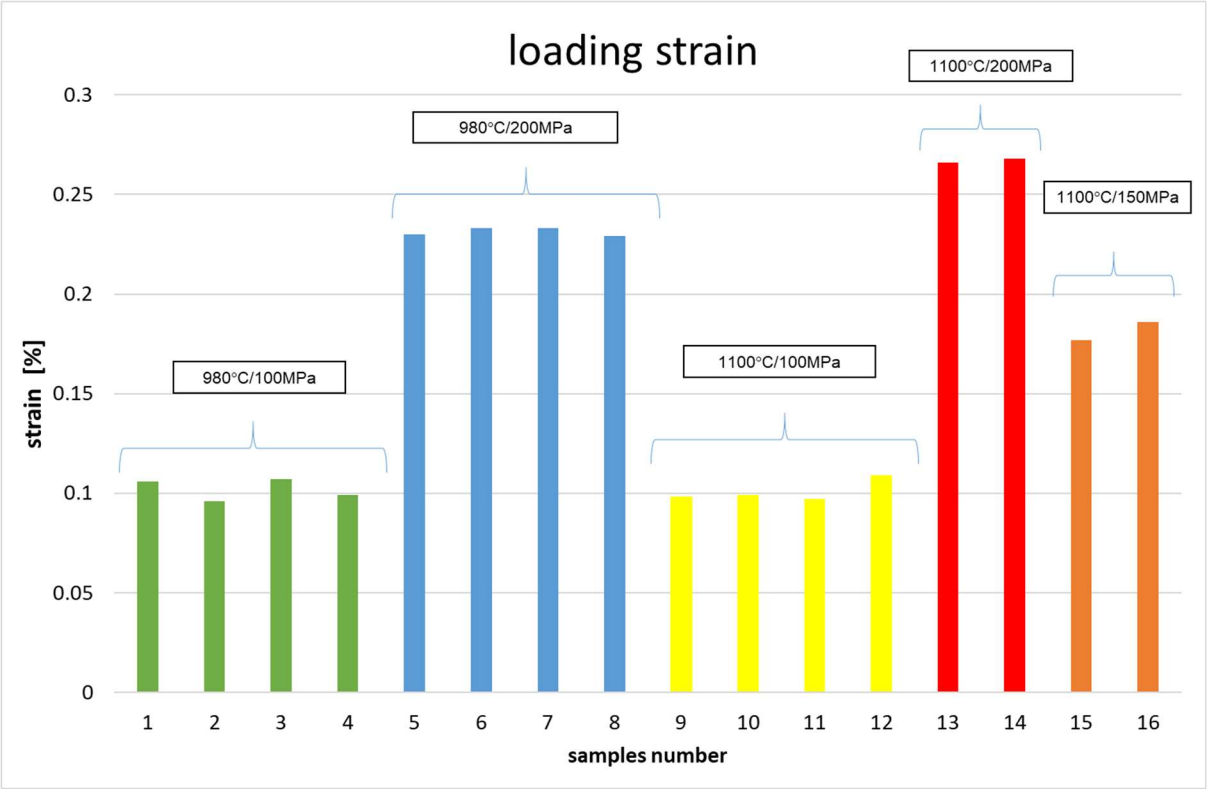

Figure 66 Loading strain from creep testing of S200H

Table 15 Summary of loading strain of S200H samples tested at different conditions

980 °C/100MPa		**980 °C/200MPa**		**1100 °C/100MPa**		**1100 °C/150MPa**		**1100 °C/200MPa**	
AV.	SD	AV.	SD	AV.	SD	AV.	SD	AV.	SD
0.102	0.005	0.231	0.002	0.101	0.006	0.182	0.006	0.267	0.001

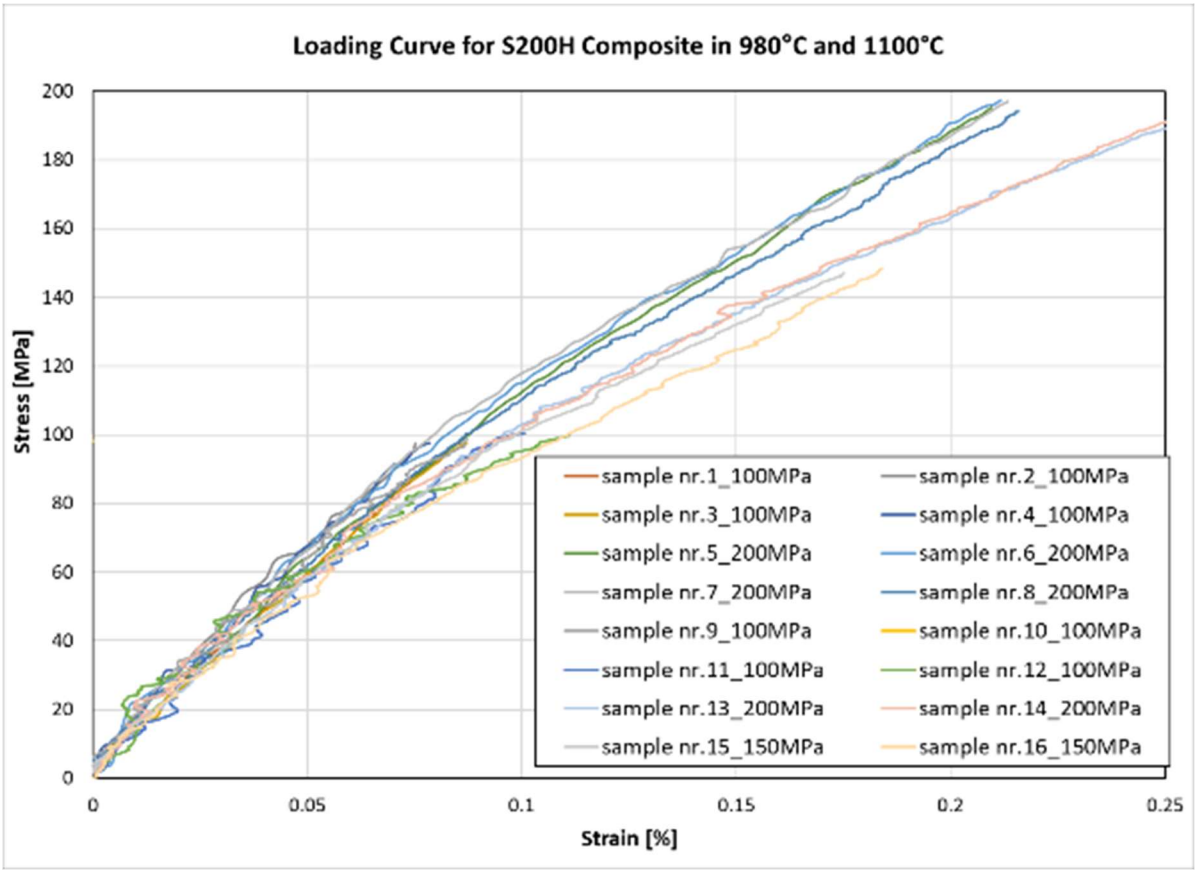

Figure 67 Stress/strain curves for loading interval

The strain obtained during loading to 100 MPa was independent of the temperature and was about 0.1% out both temperature: 980 and 1100 °C. In the case of samples tested under higher load, the dependence on temperature was visible. Samples tested at 1100 °C during the loading reached a slightly higher strain than samples tested at 980 °C. The values for samples from a given set (same stress and same temperature) showed a very small scatter of results between individual samples. Despite the small number of samples tested, homogeneity of the tested material can be assumed.

The data summary for loading strain, creep strain and total strain is presented in Figure 68.

The creep strain/time curves for samples tested at the same temperature are presented in Figure 69 and Figure 70. Figure 71 shows curves for two samples that failed after very short time.

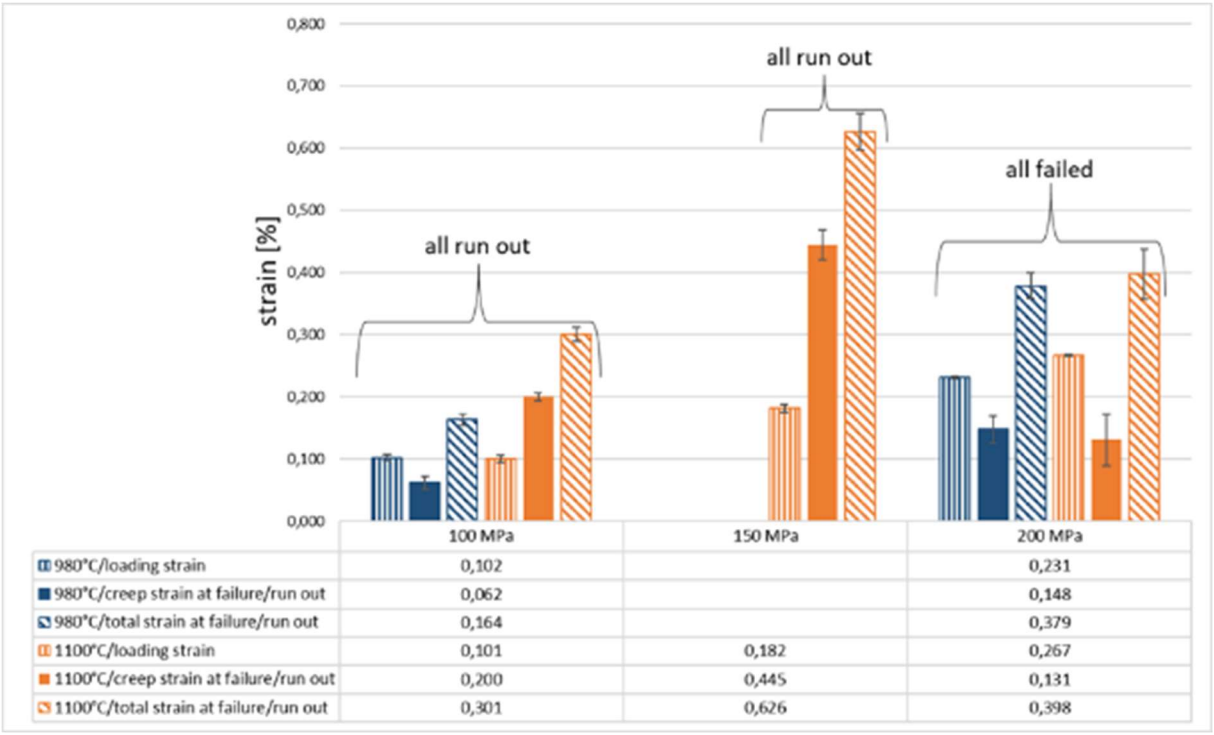

	100 MPa	150 MPa	200 MPa
980°C/loading strain	0,102		0,231
980°C/creep strain at failure/run out	0,062		0,148
980°C/total strain at failure/run out	0,164		0,379
1100°C/loading strain	0,101	0,182	0,267
1100°C/creep strain at failure/run out	0,200	0,445	0,131
1100°C/total strain at failure/run out	0,301	0,626	0,398

Figure 68 Comparison of loading strain/creep strain/total strain for S200H creep tested at 980 and 1100 °C

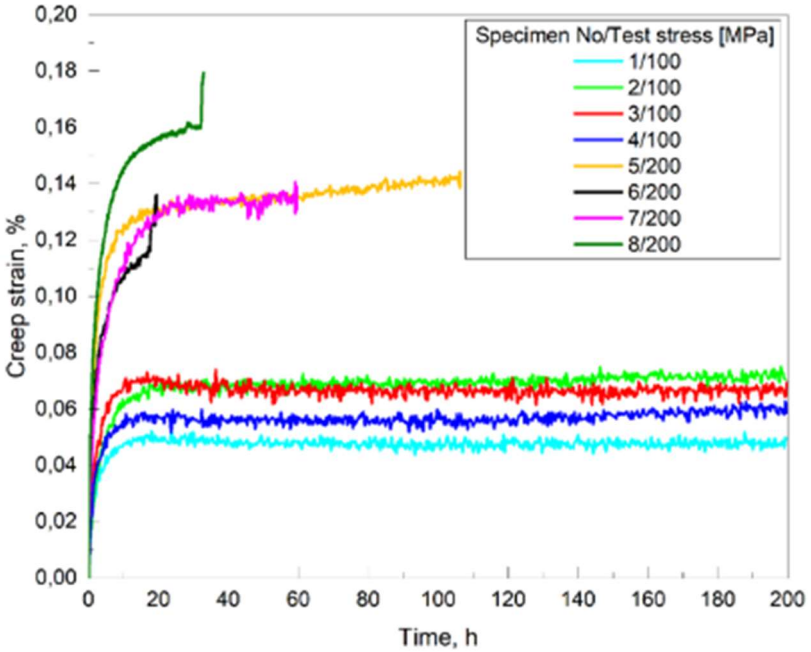

Figure 69 Strain/time creep curves of S200H tested at 980 °

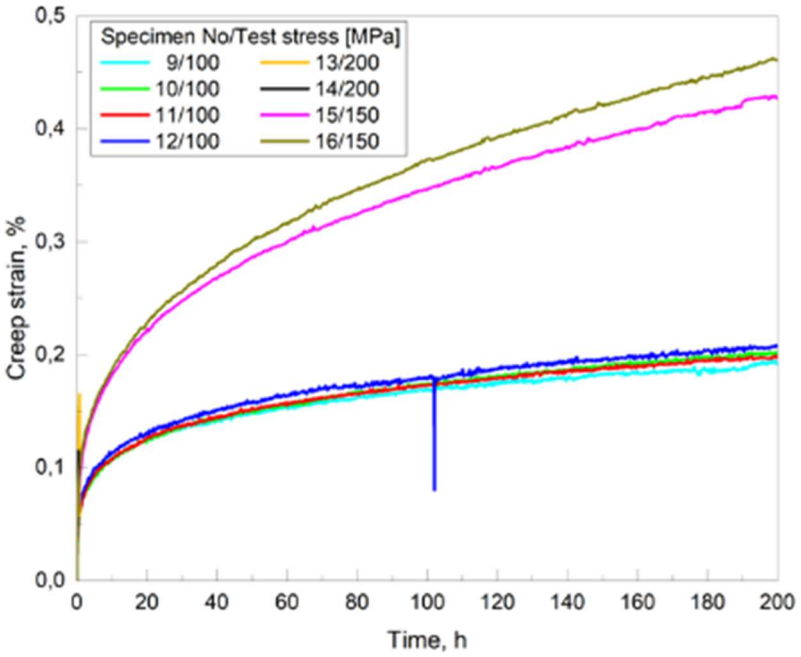

Figure 70 Strain/time creep curves of S200H tested at 1100 °C

All samples tested at 980 °C at 100 MPa ran out at 200 hours with a very slight increase in strain. The strain rate at 200 hours was close to zero for each samples. The samples tested under 200 MPa fractured after 33-106 hours, depending on the specimens.

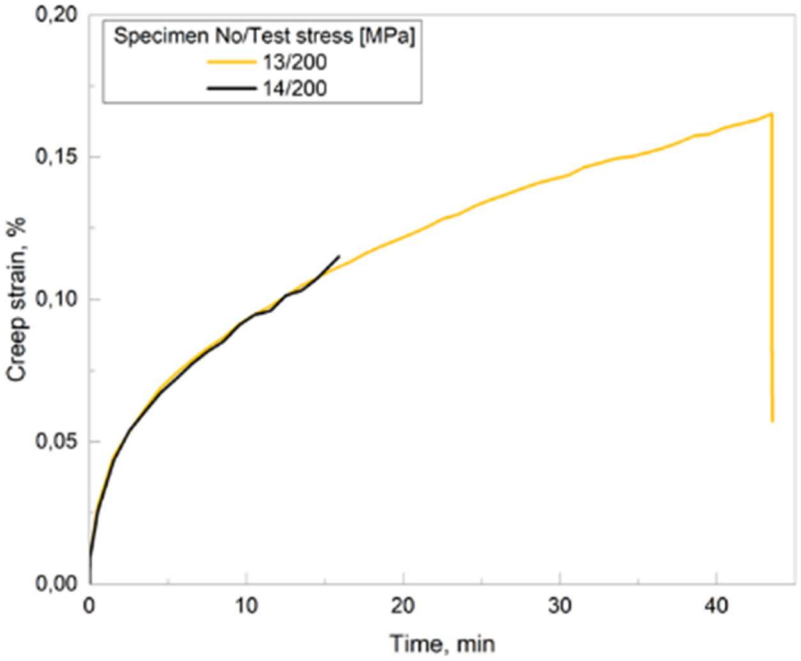

Figure 71 Strain/time creep curves of samples 13 and 14 tested at 1100 °C

Samples crept at 1100 °C at 100 MPa also ran out at 200 hours. During creep, samples reached ~0.2% creep strain (~0.3% total strain). The criterion of 200 hours was also reached by samples tested at 150 MPa. These samples crept up to ~0.45% creep strain (~0.6% total strain). The only

two samples that failed during the experiment are those tested at 1100 °C at 200 MPa. The rupture occurred after a very short time of testing, below 1 hour. The testing stress value was higher than matrix cracking strength of the S200H. Formation of cracks in the matrix under continuous load (200 MPa) and temperature (1100 °C) acting synergistically caused rapid material oxidation. Fiber coating could also oxidize and the pull out mechanism was hindered.

Fractographic images morphology of the surface after the rupture of SiC/SiC composite samples subjected to tensile testing at room temperature and creep testing at two different temperature (Figure 72). The fracture surface of the specimen tested at tension at room temperature (Figure 72 a) exhibits extensive fiber pull-out and pronounced splaying of the transverse tows. These features are indicative of weak interfacial bonding between the fibers and the matrix, consistent with a tough fracture response and minimal oxidation-related degradation [112].

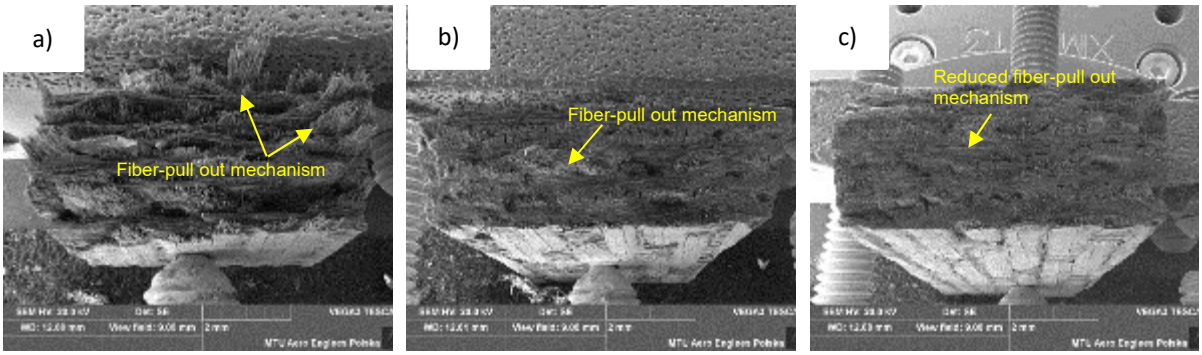

Figure 72 Fractographic images of SiC/SiC composite subjected to a) tensile test at room temperature, b) creep test at 980 °C and c) creep test at 1100 °C

However, in the specimens subjected to creep at elevated temperature (980 °C and 1100 °C), the fracture surfaces reveal significant changes in interfacial behavior. At 980 °C (Figure 72 b), Figure 73 a and b), the reduced fiber pull-out and smoother fracture surface suggest partial degradation of the Si_3N_4 outer layer, likely through oxidation to silica (SiO_2). This transformation is thermodynamically favored at intermediate temperature in air and leads to increased fiber-matrix bonding. The BN layer, while more oxidation-resistant under dry conditions, may still undergo partial removal or transformation, especially near surface-exposed regions.

At 1100 °C (Figure 72 c, Figure 73 c and d), the degradation is more advanced. The near-complete suppression of fiber pull-out and the brittle, planar fracture surfaces are consistent with extensive oxidation of both the Si_3N_4 and BN layers. The oxidation of BN likely proceeds via the formation of borosilicate glass or gaseous borohydroxides, particularly in the presence of moisture or at high oxygen partial pressure. The resulting glassy phases can infiltrate the

fiber-matrix interface, leading to mechanical lock-up and embrittlement. This is supported by the absence of splaying and the uniform fracture morphology observed in the high-temperature specimens. The spatial heterogeneity of oxidation - more severe near cut surfaces and less pronounced in the composite interior - is consistent with diffusion-limited ingress of oxidants. The degradation of the coatings, particularly the BN layer, is a critical factor in the observed embrittlement and strength loss at elevated temperature [110].

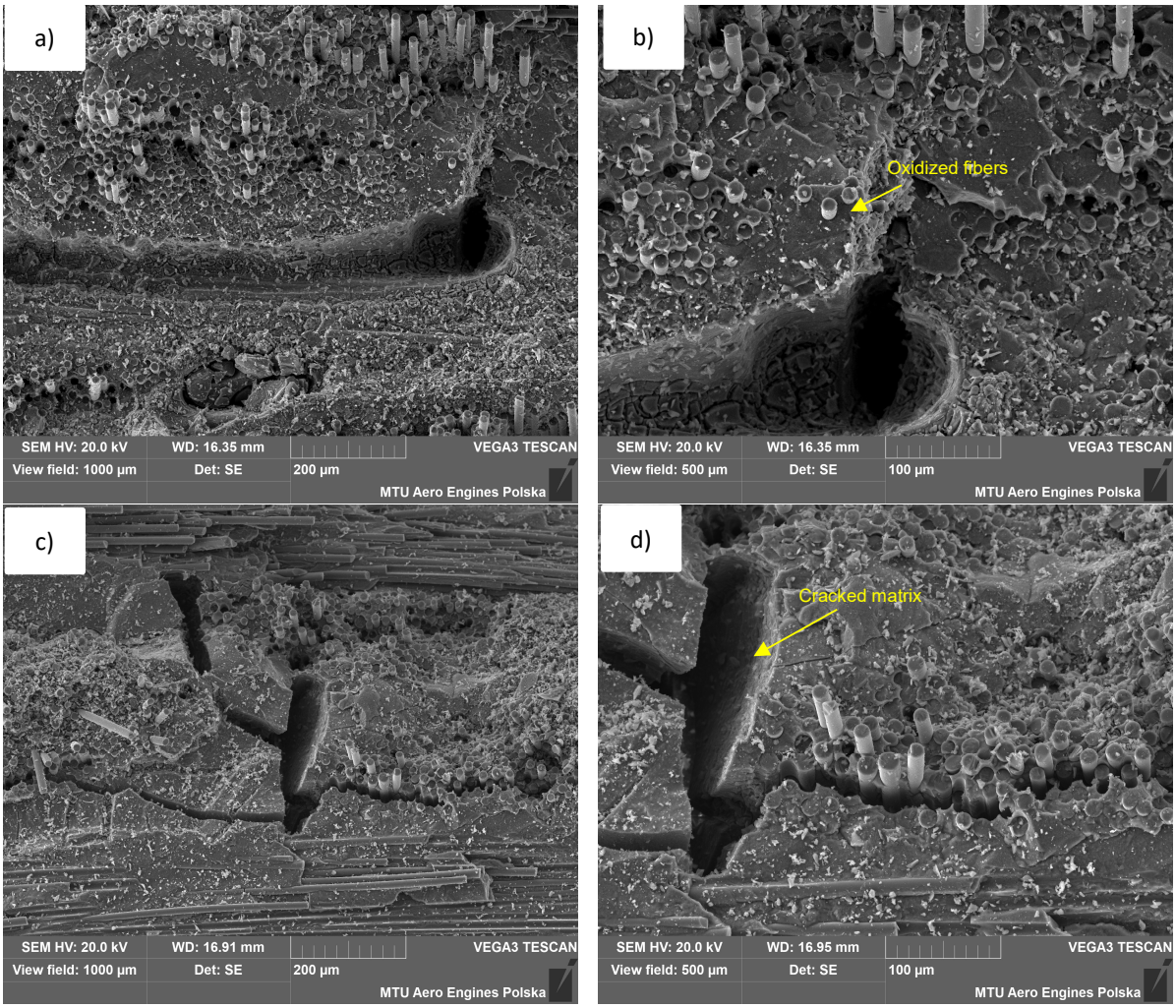

Figure 73 Fractographic images of SiC/SiC composite subjected to a), b) creep test at 980 °C and c), d) creep test at 1100 °C

Following the fractographic analysis of the fracture surfaces, scanning electron microscopy (SEM) was used to investigate the internal microstructure of the S200H composite. The SEM images revealed the presence of both longitudinal and transverse fibers, consistent with the 8-harness satin (8HS) weave architecture of the material. (Figure 74 and Figure 75). Porosity can be observed inside the tows and in the matrix Pores are spherical and elliptical in shape, elongated in one direction, longitudinal and perpendicular to the material plies (Figure 74 b and

Figure 75 b). Following the microstructural analysis, SEM observations revealed the presence of matrix cracking in all creep-tested specimens, regardless of the applied mechanical stress. Cracks were observed in samples tested at both 980 and 1100 °C, indicating that thermal exposure alone is sufficient to induce damage in the PIP-derived matrix (Figure 74 c, d and Figure 75 c, d). The cracks predominantly propagate along the fiber direction, following the architecture of the woven 8HS composite. This orientation suggests that the matrix is particularly susceptible to thermomechanical mismatch stresses along the fiber axis, possibly exacerbated by residual stresses from the PIP process and repeated thermal cycling.

In the specimens tested at 980 °C, the matrix cracks were relatively narrow and did not appear to compromise the integrity of the fiber coatings. The BN/Si_3N_4 interphase remained intact, and the cracks propagated adjacent to, but not through, the fiber coatings (Figure 74 e). Boron nitride is still visibly present and measurable (Figure 74 f). This behavior indicates that the interphase retained its protective function, effectively decoupling the fibers from the matrix and limiting the extent of oxidative damage.

In contrast, the specimens subjected to creep at 1100 °C exhibited more severe matrix degradation. The cracks were wider, more continuous (Figure 75 c, d), and in several cases, intersected the fiber coatings. SEM images revealed instances of coating delamination and partial removal, particularly in regions where the matrix crack intersected the fiber-matrix interface (Figure 75 e) . These observations suggest that at 1100 °C, the oxidation kinetics is sufficient to degrade the Si_3N_4 and BN layers, especially in areas exposed to oxygen ingress through open cracks. The delaminated coatings are likely the result of a combination of mechanical separation due to crack propagation and chemical degradation due to oxidation. The formation of low-viscosity borosilicate glass or volatilization of boron-containing species may further weaken the interfacial region, promoting coating detachment [110]. In some areas, remnants of the BN layer were observed displaced from the fiber surface, indicating that the interphase was no longer mechanically or chemically bonded to the fiber.

These findings are consistent with previous oxidation-only studies conducted at 980 and 1100 °C, where similar matrix cracking was observed. As described in chapter 9.2, the matrix exhibited crack formation even in the absence of mechanical loading. At 980 °C, the fiber coatings remained largely unaffected, with cracks propagating around the interphase. However, at 1100 °C, the coatings began to degrade, showing signs of oxidation and partial removal. The agreement between the oxidation-only and creep-tested specimens reinforces the conclusion

that matrix cracking and interfacial degradation are primarily thermally driven and become significantly more severe at higher temperature.

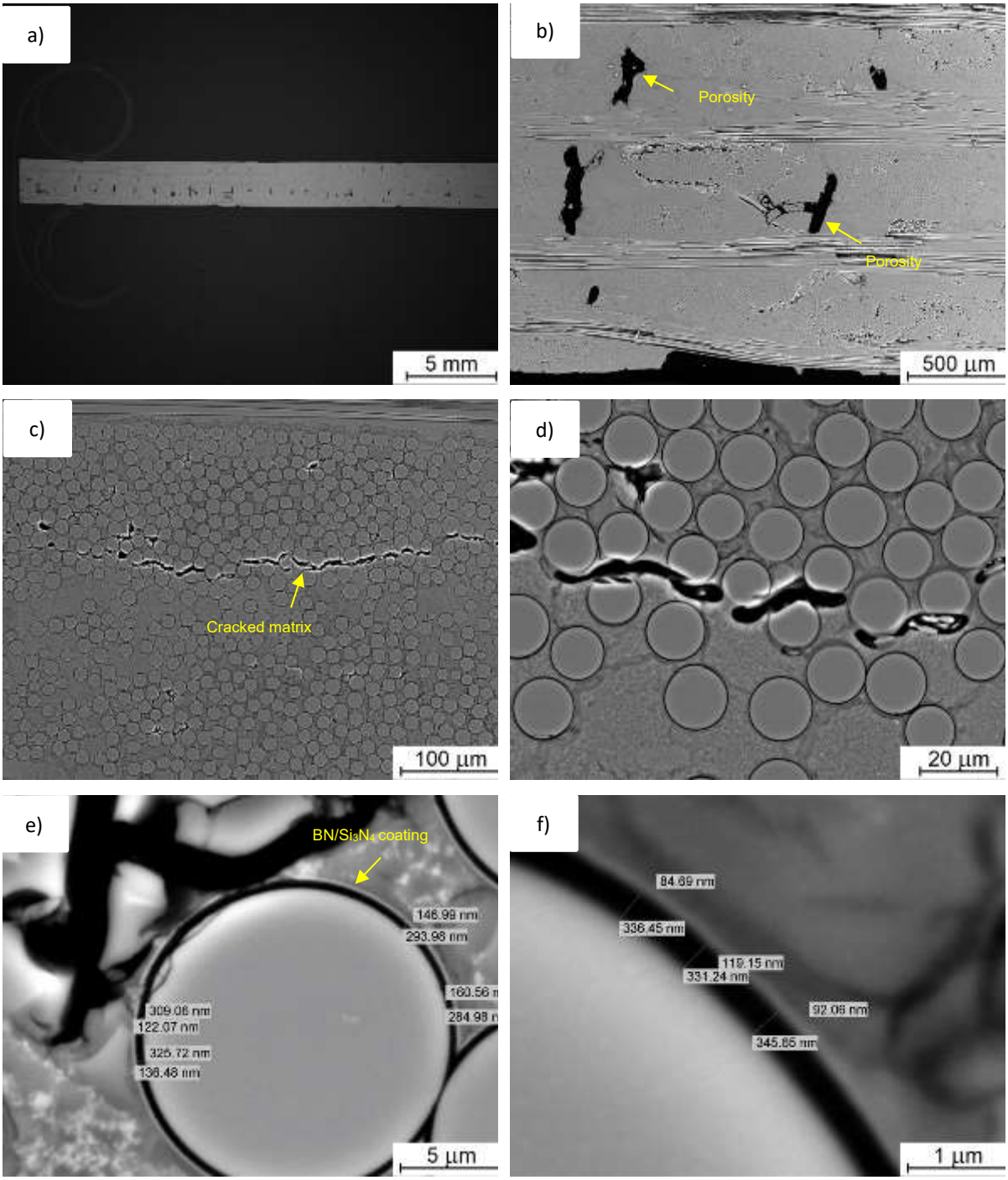

Figure 74 SEM pictures of S200H after creep test at 980 °C a) full cross-section, b) inter-laminar matrix pockets, c, d) open cracks, e, f) boron nitride coating

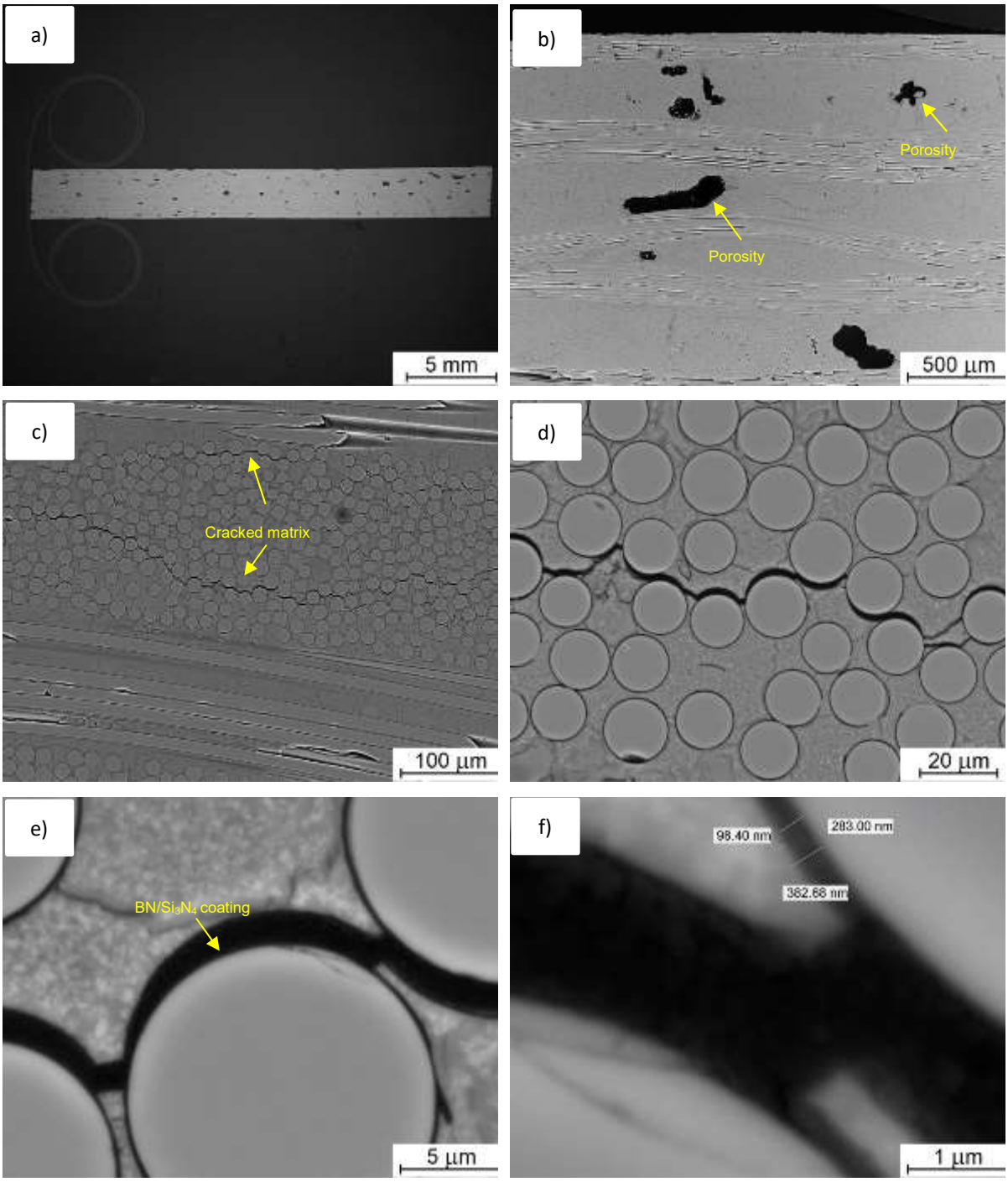

Figure 75 SEM pictures of S200H after creep test at 1100 °C a) full cross-section, b) inter-laminar matrix pockets, c, d) open cracks, e, f) boron nitride coating

Energy-dispersive X-ray spectroscopy (EDS) was applied to evaluate the elemental composition of the SiC/SiC composite after creep testing at 980 and 1100 °C. The analysis focused on the distribution of oxygen (O), nitrogen (N), carbon (C), and silicon (Si), with particular attention to the matrix and fiber interphase regions (Figure 76 and Figure 77). The EDS results clearly indicate that the material underwent oxidation during high-temperature exposure. The

highest concentration of oxygen was detected in the matrix, confirming the oxidation of the amorphous SiCN phase and the formation of silica (SiO_2). This is consistent with the SEM observations of matrix cracking and the known susceptibility of PIP-derived matrices to oxidative degradation. Elevated oxygen levels were also observed at the surface of the fiber coatings, particularly in the specimens tested at 1100 °C. This suggests that the outer Si_3N_4 layer of the coating began to oxidize under these conditions, potentially contributing to interfacial degradation. In contrast, the BN interphase remained largely chemically stable at 980 °C, with minimal oxygen detected in its vicinity. These findings are in agreement with previous microstructural observations. Together, the spectroscopic and imaging results provide a coherent picture of the oxidation behavior of the S200H composite under creep conditions, highlighting the temperature-dependent nature of matrix and interphase stability.

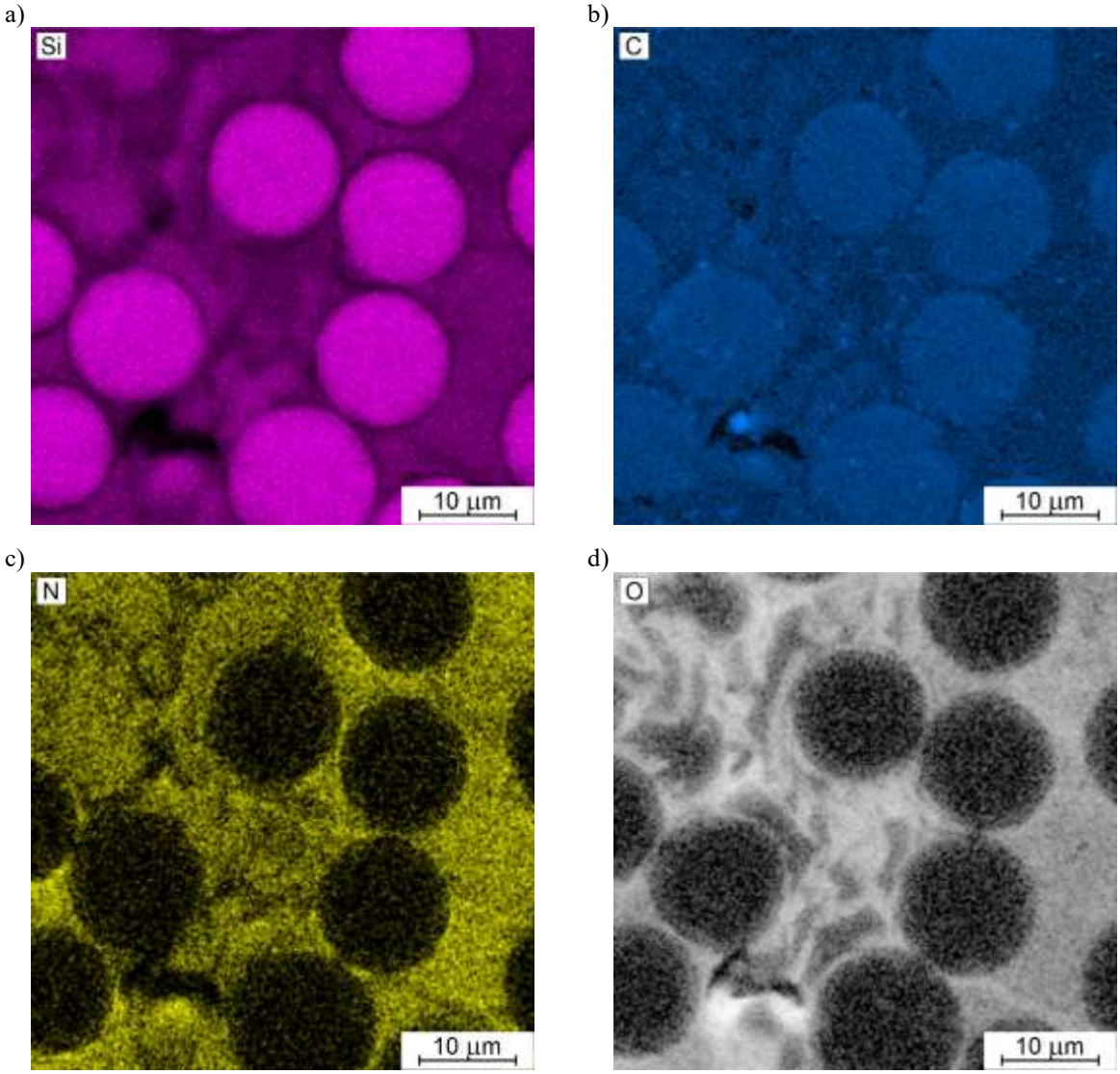

Figure 76 EDS elemental mapping of S200H after creep test at 980 °C a) Si, b) C, c) N, d) O

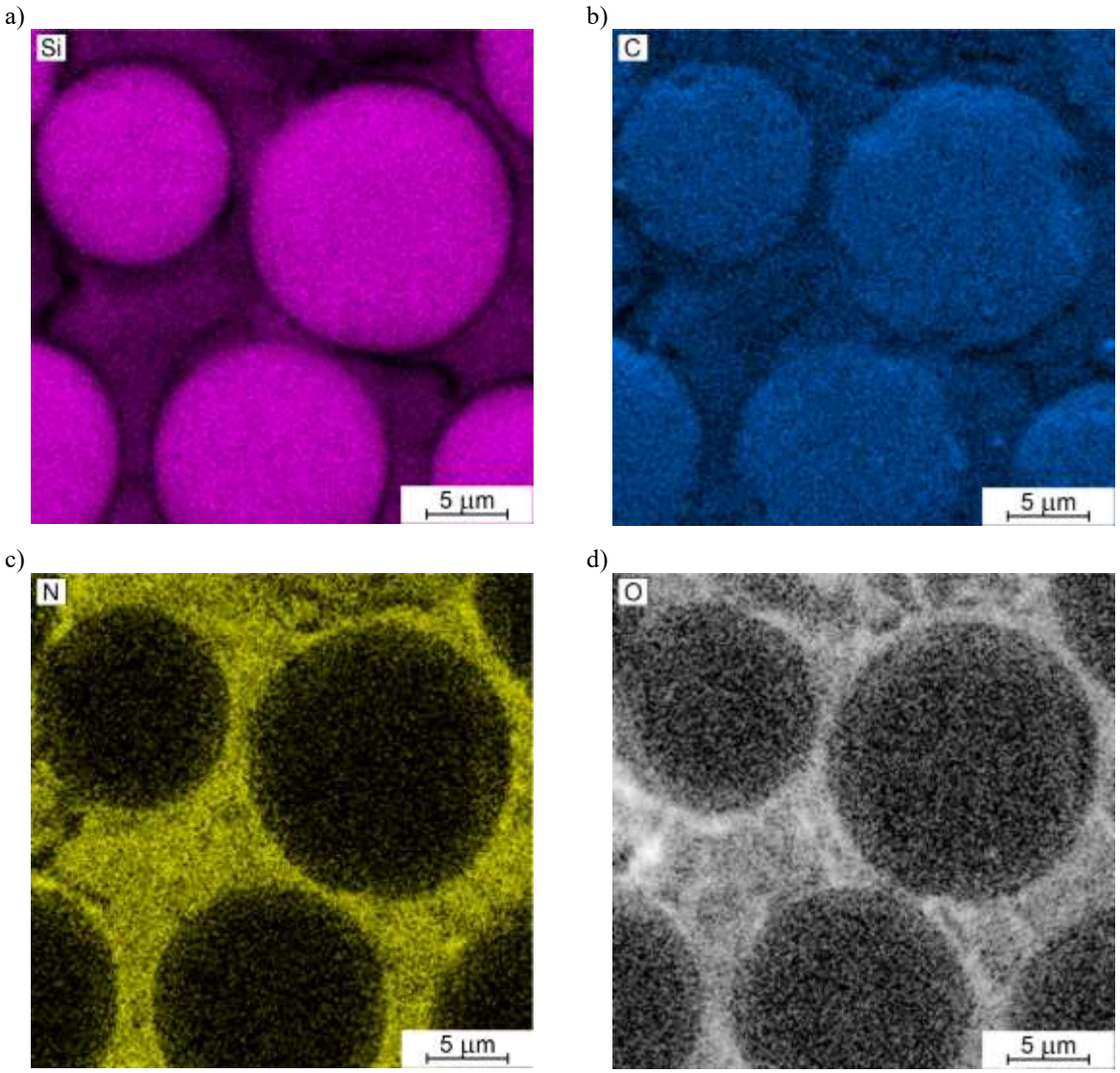

Figure 77 EDS elemental mapping of S200H after creep test at 1100 °C a) Si, b) C, c) N, d) O

Based on the conducted research, the following conclusions can be formulated:

- All samples tested at 100 MPa (4 at 980 °C and 4 at 1100 °C) ran out at 200 hours. At both temperature the loading strain was similar, but samples tested at higher temperature demonstrated three times higher creep strain during the creep testing. The behavior of individual samples in each test group was similar.
- For specimens that reached 200 hours of testing, a general tendency toward stiffness reduction was observed, regardless of the temperature. This decrease is most likely due to material oxidation and the development of microcracks in the matrix, leading to degradation of the composite's mechanical properties.

- At 150 MPa only two samples were tested at 1100 °C. Both samples run out at 200 hours. The values of loading, creep and total strain for both samples were similar. The total strain that the samples achieved at the end of the test was 0,605% and 0,647%, respectively.
- For samples tested at 200 MPa (4 at 980 °C and 2 at 1100 °C), the loading strain was slightly higher at higher temperature. The specimens tested at 980 °C failed after different times for individual samples in the range of 33-106 hours. The two specimens tested at 1100 °C failed very quickly (time below 1 hour of creep test). It is assumed that the load of 200 MPa exceeds the matrix cracking strength of S200H material.
- Cracks in the matrix were observed at both 980 and 1100 °C, regardless of the applied mechanical stress. These cracks propagated along the fibers and served as pathways facilitating oxygen ingress into the interior of the composite.
- At 980 °C, the BN/ Si_3N_4 coating remained intact, and the cracks bypassed the fiber-matrix interface. In contrast, at 1100 °C, the cracks penetrated the coating, leading to its delamination and oxidation, which resulted in local interfacial degradation and potential weakening of the mechanical properties.

6.4 Comparison of the microstructure of SiC/SiC composite after oxidation test and creep test

To deepen the understanding of degradation mechanisms in SiC/SiC composites, a comparative microstructural analysis was conducted on samples subjected to two distinct testing conditions: laboratory oxidation and creep testing. For the purpose of comparative analysis, samples of the SiC/SiC composite previously subjected to laboratory oxidation at 980 and 1100 °C for 100 hours were selected alongside samples exposed to creep testing at the same temperature but for duration of 200 hours. The creep tests were conducted under mechanical loads of 100 MPa at 980 °C and 150 MPa at 1100 °C, introducing both thermal and mechanical stress (Table 16)

Table 16 Selected SiC/SiC composite samples for comparative analysis of microstructural features.

Test	Temperature [°C]	Time [h]	Load [MPa]
Oxidation	980	100	-
Oxidation	1100	100	-
Creep	980	200	100
Creep	1100	200	150

The predefined view fields used for SEM imaging of oxidized and crept samples differ slightly, as the oxidation images were acquired earlier - prior to the establishment of standardized view field criteria. However, these differences are minor and do not affect the validity of the comparative microstructural analysis.

As shown in the SEM images below (Figure 78 a-j), both the oxidized samples and those subjected to creep testing exhibit longitudinal and transverse matrix cracks. The orientation and distribution of these cracks are similar in both cases, typically following the direction of the laminate architecture. Notably, the fiber coatings remain largely intact, indicating their stability and resistance to both oxidation and mechanical loading.

In addition to cracking behavior, the overall porosity of the matrix appears comparable between the oxidized and crept samples. No significant increase in pores density or size was observed, suggesting that prolonged exposure to elevated temperature and mechanical stress did not substantially alter the internal porosity of the composite. Furthermore, matrix-rich pockets-regions with locally higher matrix content - were present in both sets of samples and showed similar morphology and distribution.

These observations suggest that the primary factor contributing to matrix degradation is thermal exposure itself. The extended test duration in the creep experiments (200 hours) did not significantly increase the number of microstructural defects compared to the 100-hour oxidation tests.

Furthermore, the results confirm the high thermal and mechanical stability of the SiC fibers and their interfacial coatings at 980 °C, even under applied stress.

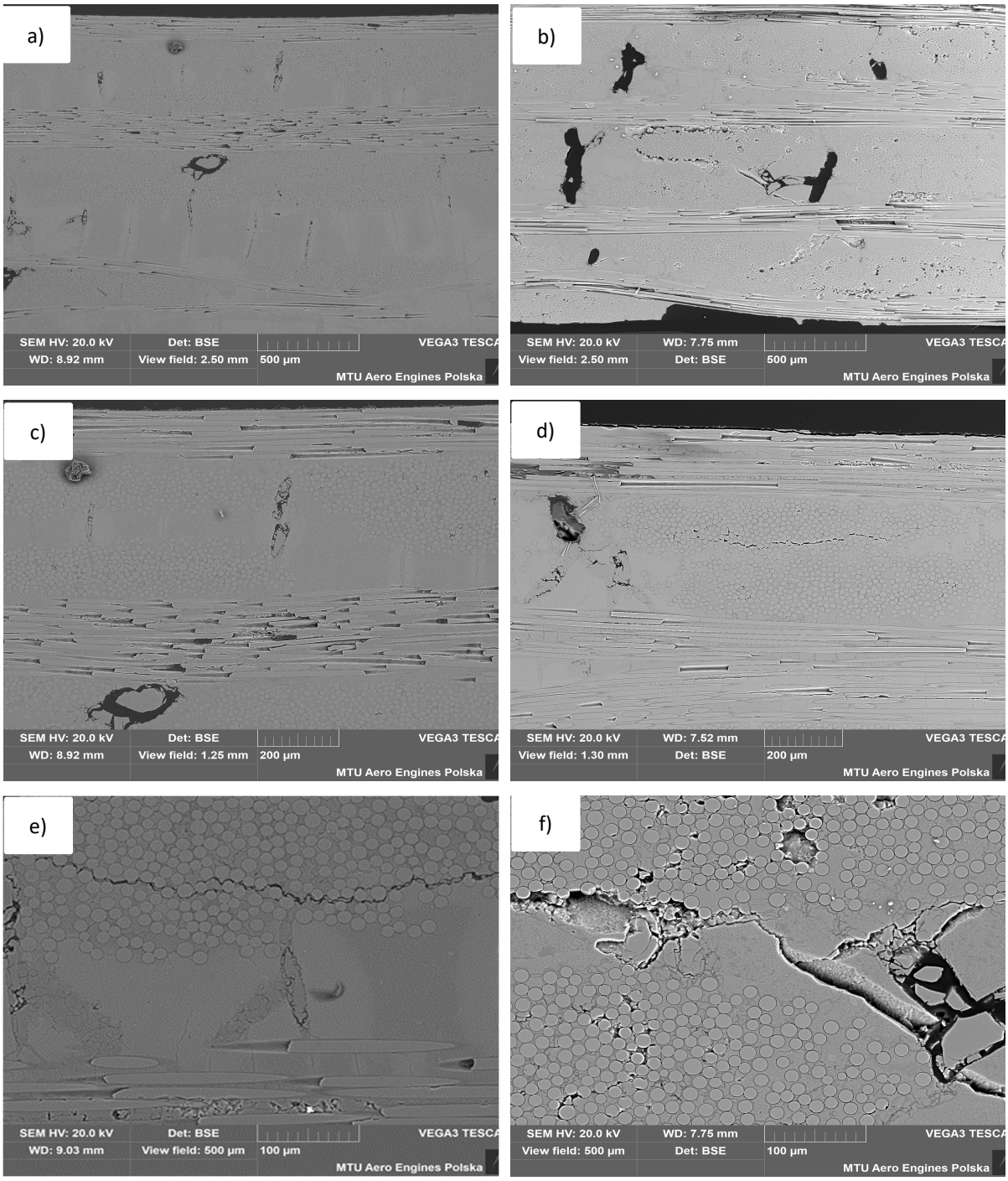

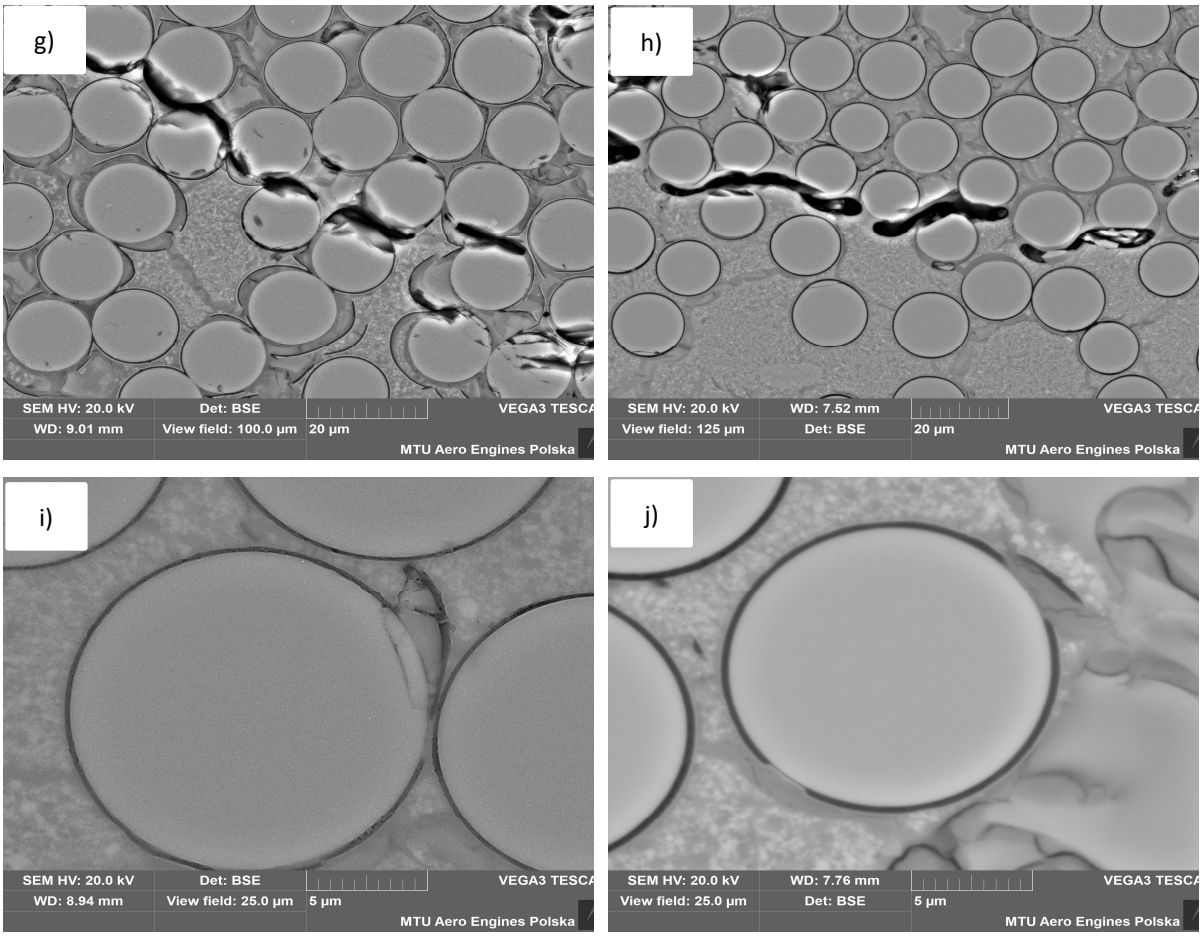

Figure 78 a), c), e), g), i) Microstructure od S200H composite tested atoxidation 980 °C for 100h and b), d), f), h), j) tested under creep conditions at 980 °C for 200h

In the comparative analysis between samples oxidized at 1100 °C for 100 hours and those subjected to creep testing at 1100 °C for 200 hours under 150 MPa, a surprising observation was made. The sample exposed solely to oxidation exhibited significantly more microstructural degradation, including a higher density of both longitudinal and transverse matrix cracks. These cracks were more extensive and uniformly distributed across the matrix compared to the crept sample (Figure 79 a, c, e, g, i). While the creep-tested sample also showed longitudinal and transverse matrix cracking, the extent of damage was notably lower (Figure 79 b, d, f, h, j). Moreover, the crack paths in the creep sample were observed to propagate through the fibers rather than along the fiber coatings, suggesting partial degradation of the interfacial layer due to oxidation under stress. In contrast, the oxidized sample revealed more severe damage to the fiber coatings themselves, with visible fragmentation and detachment, indicating that oxidation alone-without mechanical constraint-may lead to more aggressive coating degradation.

Additionally, the porosity levels and the presence of matrix-rich pockets remained comparable between the two samples, suggesting that the overall material architecture was not significantly altered by the different exposure conditions.

The unexpected differences observed in the SEM results where the sample subjected to oxidation (1100 °C, 100 h) shows more defects than the one exposed to creep (1100 °C, 200 h) can be attributed to differences in sample preparation and geometry. The samples used for oxidation tests were initially cut from a composite sheet, then exposed to the oxidation process, and afterward sectioned into smaller pieces for SEM analysis. This sequence likely introduced mechanical damage to the composite structure during cutting, exposing fibers and disrupting the protective matrix. As a result, oxygen could penetrate more easily, accelerating local degradation. Additionally, due to the small size of these samples, the relative contribution of surface porosity was significantly higher compared to larger specimens. In small samples, pores and microcracks occupy a proportionally larger area, which enhances oxygen diffusion and reactivity. These exposed features act as fast pathways for oxidation, especially at elevated temperature, leading to quicker and more intense degradation. Moreover, due to the small size of these samples, the oxidation process likely occurred more rapidly and uniformly, intensifying the formation of surface defects. In contrast, the creep-tested sample was a standard specimen that did not fail during the test (a run-out). It remained intact throughout the 200-hour creep exposure and was only sectioned for SEM analysis after the test. In this case, oxidation occurred more slowly and in a more controlled manner, as the surface was not mechanically disturbed prior to exposure. The larger size of the sample may have also limited oxygen diffusion into deeper layers, reducing the extent of degradation. Furthermore, the presence of mechanical stress during creep might have influenced the microstructure in a stabilizing way, potentially hindering the development of surface defects.

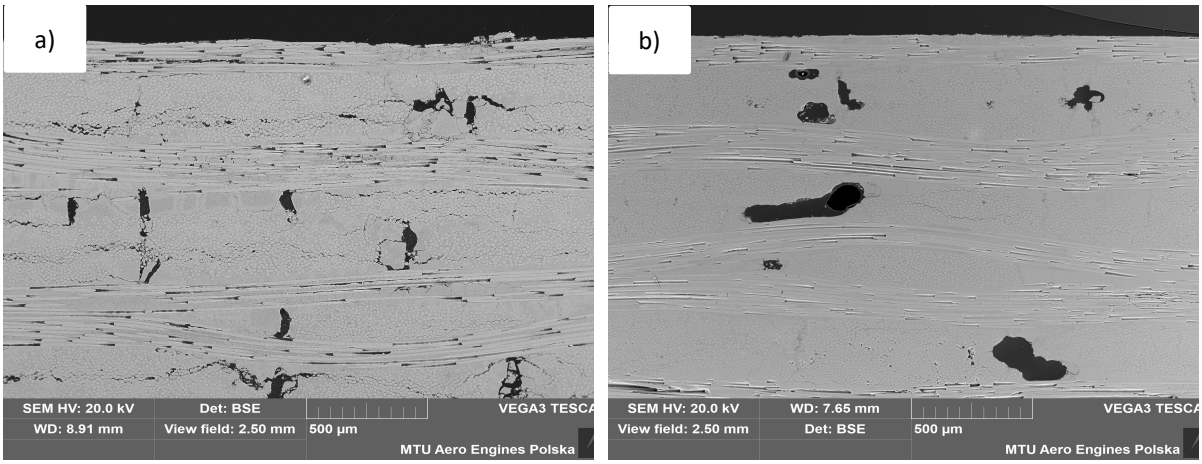

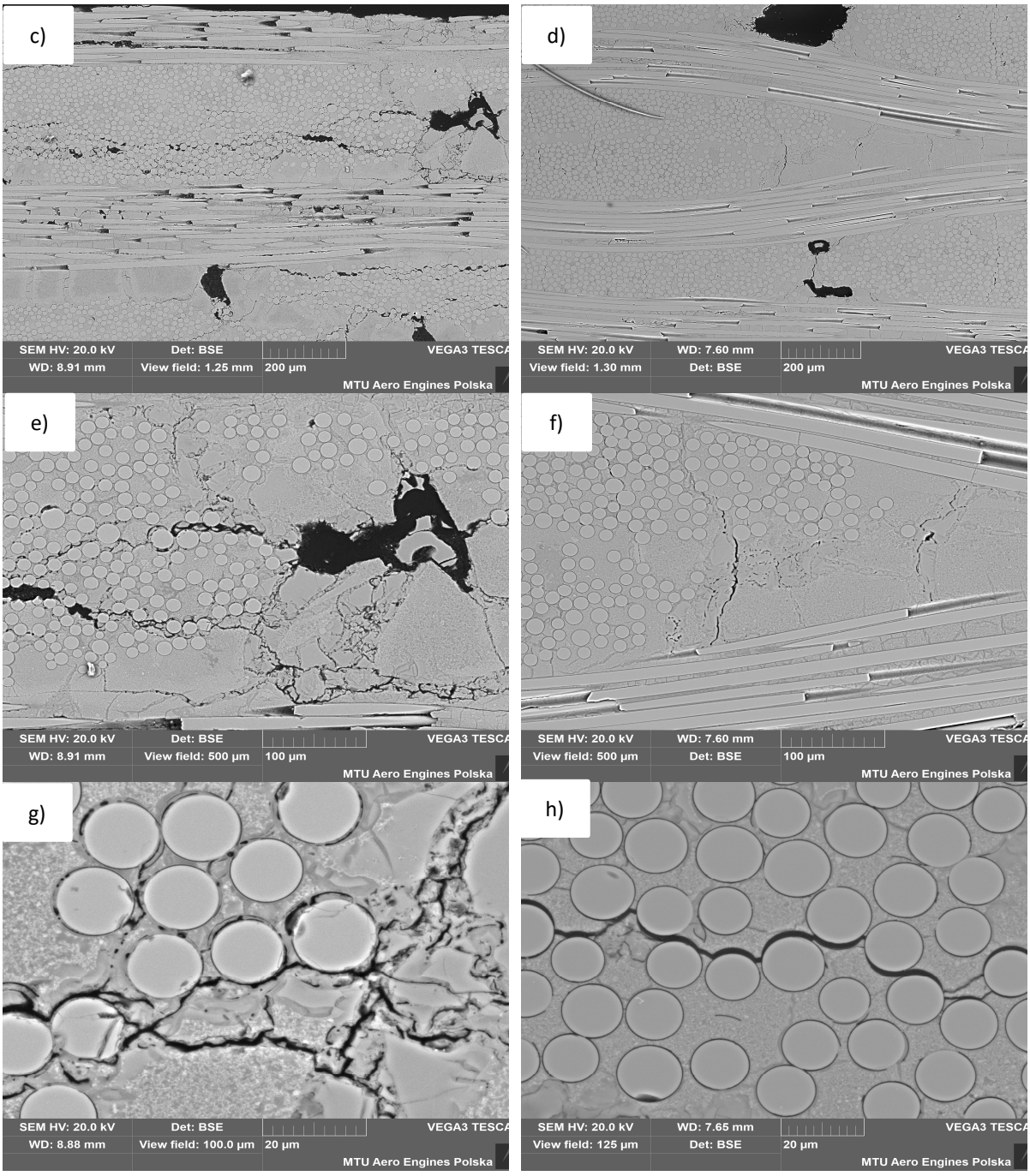
c)
SEM HV: 20.0 kV
Det: BSE
VEGA3 TESCA
WD: 8.91 mm
View field: 1.25 mm
200 µm
MTU Aero Engines Polska
d)
SEM HV: 20.0 kV
WD: 7.60 mm
VEGA3 TESCA
View field: 1.30 mm
Det: BSE
200 µm
MTU Aero Engines Polska
e)
SEM HV: 20.0 kV
Det: BSE
VEGA3 TESCA
WD: 8.91 mm
View field: 500 µm
100 µm
MTU Aero Engines Polska
f)
SEM HV: 20.0 kV
WD: 7.60 mm
VEGA3 TESCA
View field: 500 µm
Det: BSE
100 µm
MTU Aero Engines Polska
g)
SEM HV: 20.0 kV
Det: BSE
VEGA3 TESCA
WD: 8.88 mm
View field: 100.0 µm
20 µm
MTU Aero Engines Polska
h)
SEM HV: 20.0 kV
WD: 7.65 mm
VEGA3 TESCA
View field: 125 µm
Det: BSE
20 µm
MTU Aero Engines Polska

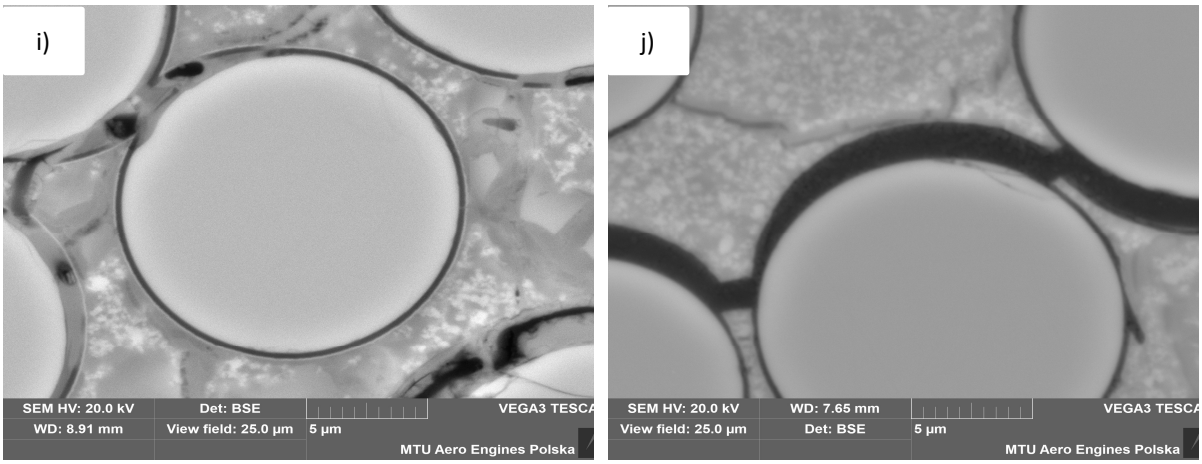

Figure 79 a), c), e), g), i) Microstructure of S200H composite tested oxidation at 1100 °C for 100h and b), d), f), h), j) tested under creep conditions at 1100 °C and 200h

6.5 SiC/SiC composite tested at engine atmosphere

As a complement to the investigation of pristine material behavior, laboratory-scale oxidation experiments, and creep testing, additional samples of the CMC composite were examined after direct exposure to conditions simulating those found in jet engine environment. These tests aimed to capture the combined effects of high temperature, pressure, and chemically reactive combustion products on the material's microstructure. Unlike controlled laboratory oxidation in static air, the engine-simulated conditions introduce dynamic factors such as gas flow, thermal cycling, and complex chemical species derived from jet fuel combustion.

The test was conducted as square cycles. One square cycle included 5 minutes of running on standby, followed by a step ramp-up (below 30 sec) to full power, a 5-minute holding time at speed, and a steep deceleration (below 30 sec). In total, the sample was tested for 200 hours. The maximum gas temperature reached during the test was 890 °C. During standby, the temperature was 790 K (520 °C) (Figure 80). The CMC part temperature is limited to the max. gas temperature. The CMC-part was tested directly in the Hot Gas Path as a hot-gas bearing liner segment.

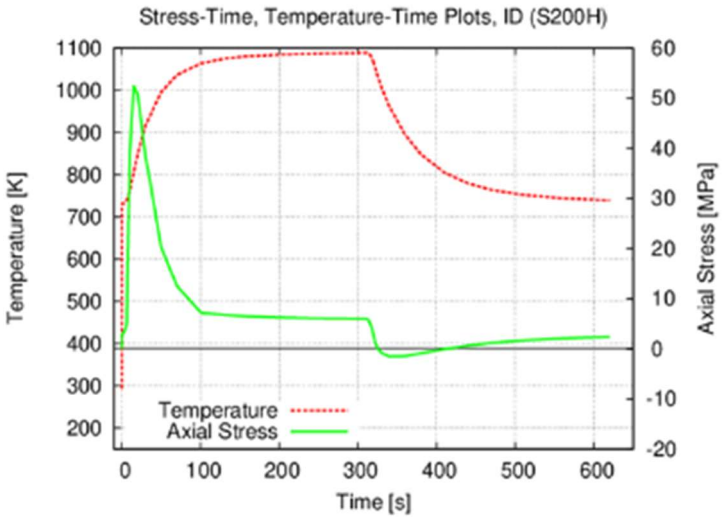

Figure 80 Conditions simulating the operating environment of an aircraft engine applied for testing the S200h sample

In a jet engine, materials are exposed to an extremely aggressive environment characterized not only by high temperature and pressures, but also by a chemically complex and reactive atmosphere. During operation, the temperature in the combustion chamber can exceed 1500 °C, while components such as turbine blades and liners are typically exposed to sustained temperature ranging from 900 to 1200 °C. High temperature is accompanied by pressures reaching up to 30–40 bar due to multi-stage air compression, which significantly increases the partial pressure of oxygen and accelerates oxidation reactions. Importantly, the oxidizing atmosphere in a jet engine is not composed of ambient air alone. It includes combustion products derived from jet fuel-typically kerosene-based hydrocarbons such as Jet A or Jet A-1. The combustion of kerosene produces a mixture of gases including CO_2, H_2O vapor, unburned hydrocarbons, NO_x, and SO_x, in addition to excess oxygen. Compared to oxidation in static air, this environment leads to the formation of different oxide species and more aggressive corrosion mechanisms. The presence of water vapor and sulfur compounds, for example, can significantly alter the oxidation kinetics and promote the formation of volatile or porous oxide scales [113]. Furthermore, the high gas velocity and pressure in the engine enhance the transport of reactive species to the material surface, intensifying oxidation and erosion. Frequent thermal cycling during flight operations induces thermal fatigue, contributing to crack initiation and propagation. Additionally, environmental contaminants such as salt particles, dust, and industrial pollutants may be ingested, leading to localized chemical attack and mechanical damage. These combined factors make the jet engine environment far more severe than static laboratory oxidation in air, and

must be considered when evaluating the long-term performance and degradation mechanisms of high-temperature materials such as SiNC/SiC composites.

The cutting plan for the CMC part tested under aircraft engine conditions has been proposed as shown in Figure 81 a and b. The part was embedded and subjected to microstructural analysis using Scanning Electron Microscopy.

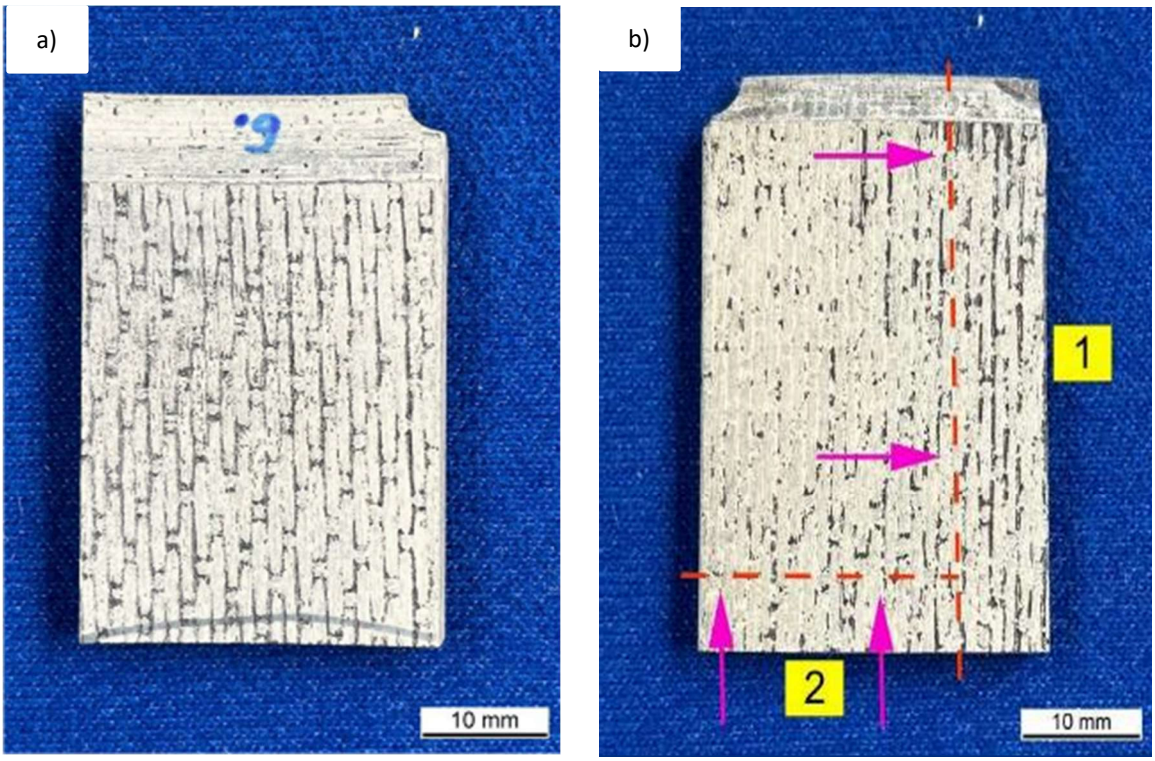

Figure 81 Cutting plan for CMC samples tested at aircraft engine environment a) and b).

The CMC sample exposed to engine conditions shows a significant transformation in surface color (Figure 81 a and b) compared to its pristine (Figure 11) and oxidized states (Figure 41 a). Initially, the pristine sample is black, reflecting the natural appearance of the SiC/Si_3N_4 composite. After oxidation, the surface turns gray with visible white deposits along the edges, indicating the onset of surface reactions and oxidation layer. However, after exposure to the engine environment, the sample becomes almost entirely white. This pronounced brightening is primarily the result of high-temperature exposure in an oxygen-rich and chemically aggressive environment. The surface undergoes extensive oxidation, leading to the formation of a light-colored oxide layer that covers the original dark material. Additionally, thermal decomposition of the nitride phase and the accumulation of light - colored residues from the engine atmosphere may further contribute to the whitening effect. The progression from black through gray to

nearly white clearly illustrates the increasing severity of environmental exposure and its impact on the surface chemistry and visual appearance of the composite material.

Two samples, 1 and 2, were subjected to microstructural analysis. They were cut according to the cutting plan (Figure 81 b). Their overview image can be seen in Figure 82 a and b.

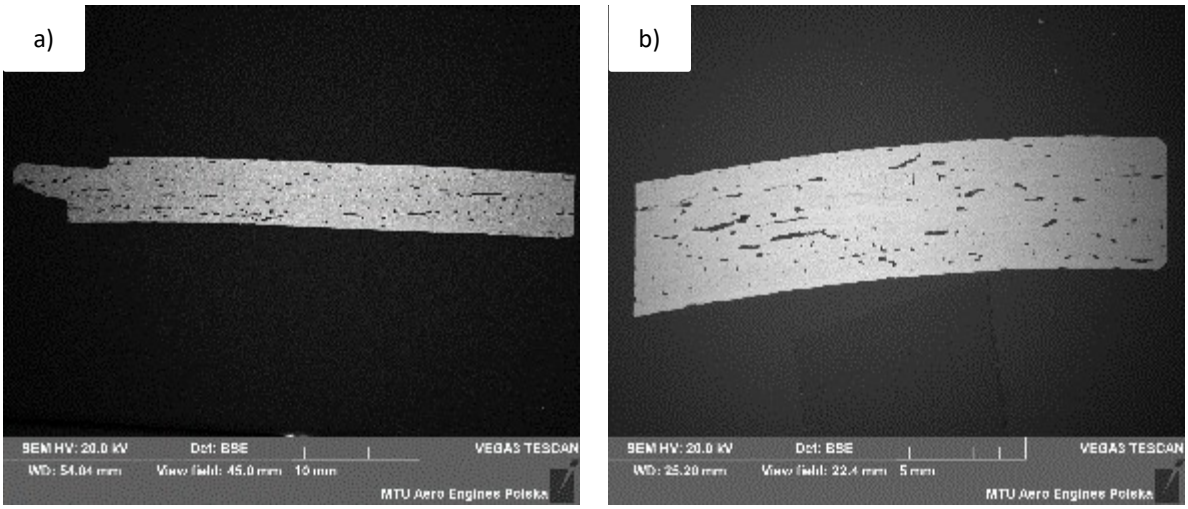

Figure 82 Overview of the S200H composite tested at aircraft engine conditions: a) sample number 1, b) sample number 2.

As revealed by SEM microstructural analysis, both samples exhibited the most intense oxidation near the surface exposed to the corrosive environment. The microstructure of this samples is presented in Figure 83 a and b. Sample 1 was cut in such a way that most of its volume represented the region most exposed to the corrosive environment. As a result, oxidation products such as the SiO_2 layer can be observed along three sides of the sample. Both samples exhibited significant oxidation of the SiNC matrix material.

Based on SEM microstructural analysis, both samples exhibited the most intense oxidation near the surfaces directly exposed to the corrosive environment. The oxidation layer formed on the surface appeared relatively uniform and continuous, with a thickness ranging from 8 to 10 µm (Figure 83 c). In contrast, in certain regions, a significantly thicker and more porous oxide layer was observed extending into the bulk of the material, with thicknesses between 33 and 44 µm (Figure 83 d). This variation in oxidation behavior is attributed to differences in the local microstructure of the composite. In areas where reinforcing fibers were present near the surface, the oxidation was limited to a thin external layer, likely due to the diffusion barrier effect of the fibers and their BN/Si_3N_4 coatings (Figure 83 c). In regions lacking fibers, oxygen could more easily penetrate into the material, resulting in deeper internal oxidation. Additionally, slight differences in exposure to the hot gas flow may have contributed to the observed asymmetry in

oxidation depth and morphology (Figure 83 d). The oxide layer that diffused into the bulk of the material exhibited a noticeably more porous structure compared to the compact surface layer. This difference is likely due to the nature of internal oxidation, where oxygen reacts with the matrix in a more dispersed manner, often leading to the formation of gas-filled voids and microcracks. In contrast, the surface layer grows in direct contact with the external environment, allowing for the formation of a denser and more continuous SiO_2 film. Additionally, the absence of reinforcing fibers in the internally oxidized region may have facilitated deeper oxygen penetration and less constrained oxide growth, contributing to the observed porosity.

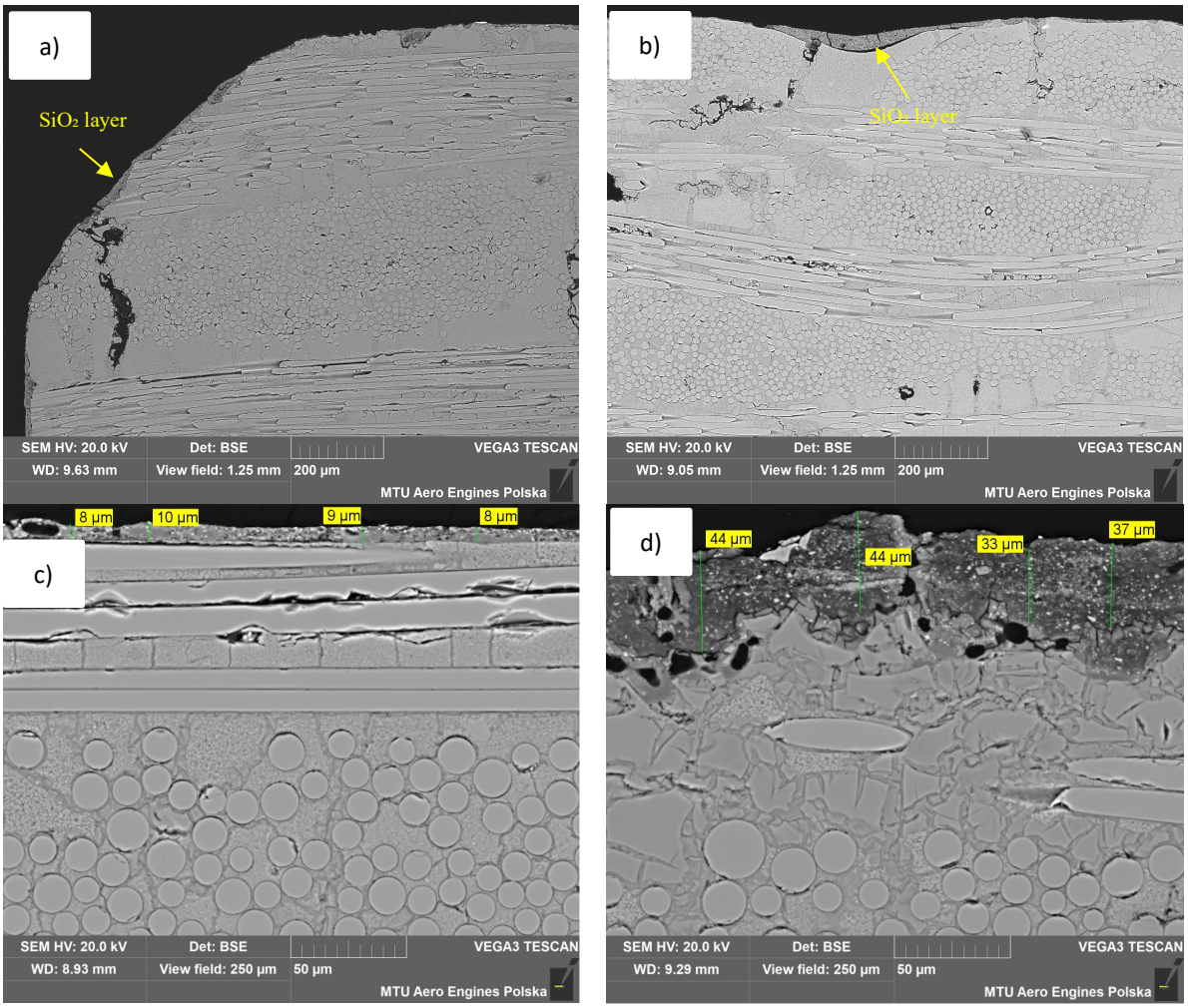

Figure 83 SEM pictures of S200H composite tested at aircraft conditions, a) and b) view field 1.25 mm, c) SiO_2 layer on the surface, d)SiO_2 layer in the material

To confirm the chemical composition of the coating, EDS mapping, as well as line and point measurements, were performed. Both point measurements and EDS maps revealed a high concentration of oxygen within the oxide layers formed in the material, both on the surface and in the layer that diffused into the bulk (Figure 84 a-d). Oxygen was found to migrate into the bulk

of the material through microcracks in the matrix, which were not open cracks but rather residual defects from the PIP process (Figure 84 a and c). This observation indicates that, although these cracks are not visibly open, they represent weak points within the S200H composite matrix and serve as pathways for oxidation, ultimately contributing to the degradation of the composite.

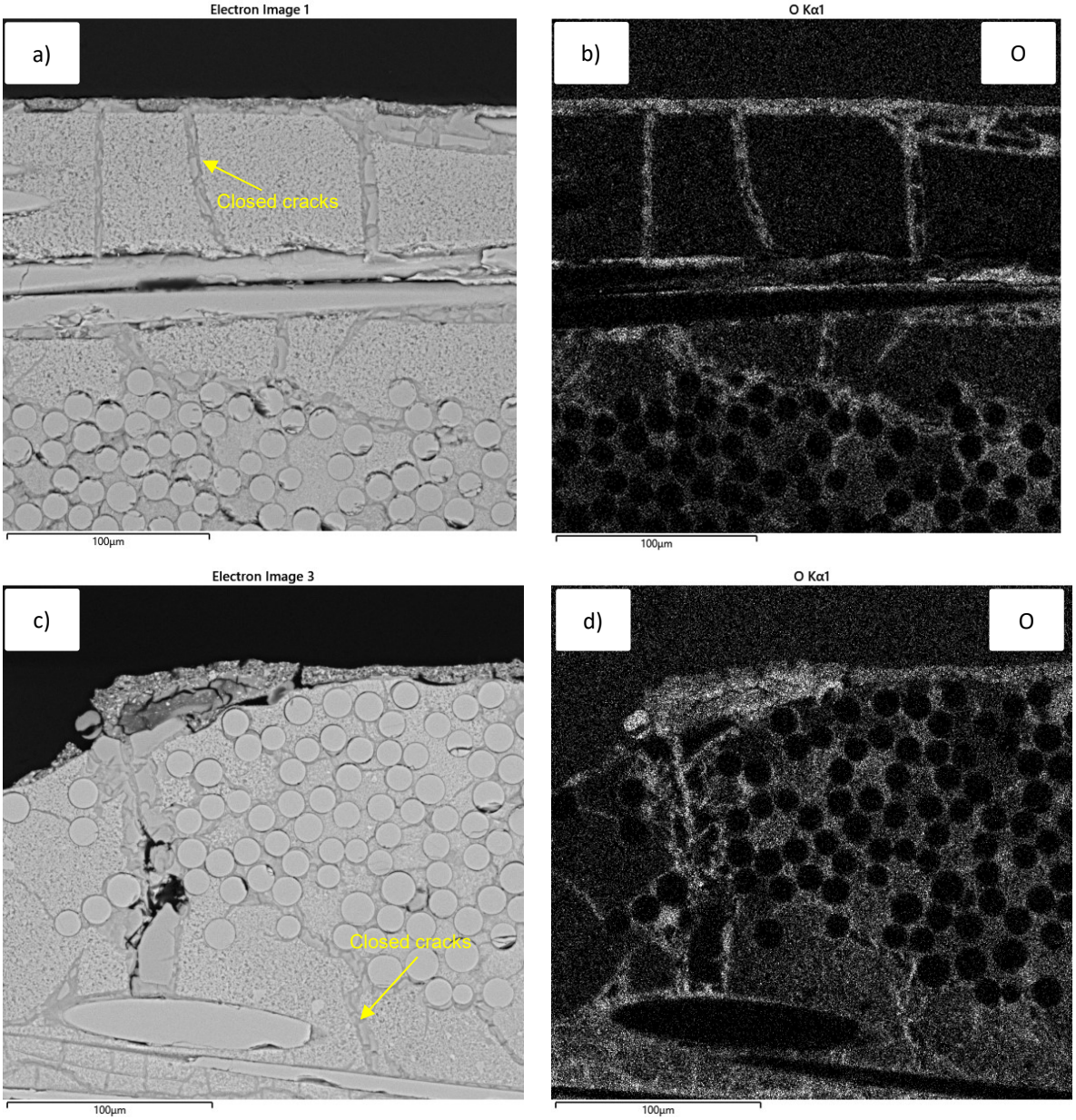

Figure 84 EDS analysis of S200H a) and c) selected area, b) and d) oxygen distribution

Linear measurements were performed to evaluate oxygen diffusion into the material (Figure 85). The results show that the highest oxygen concentration was observed in the oxide layer formed as a result of material oxidation, which had diffused into the underlying structure. Elevated oxygen levels were also detected in areas with structural defects such as porosity and

regions where fiber segments had been pulled out due to oxidation. In contrast, oxygen content was lower in fiber-rich zones and significantly higher in matrix-rich pockets. This measurement also reveals that, despite the absence of open cracks in the matrix, oxygen was able to diffuse deep into the material. This is most likely due to the lack of a continuous TBC (Thermal Barrier Coating) layer across the entire surface of the composite.

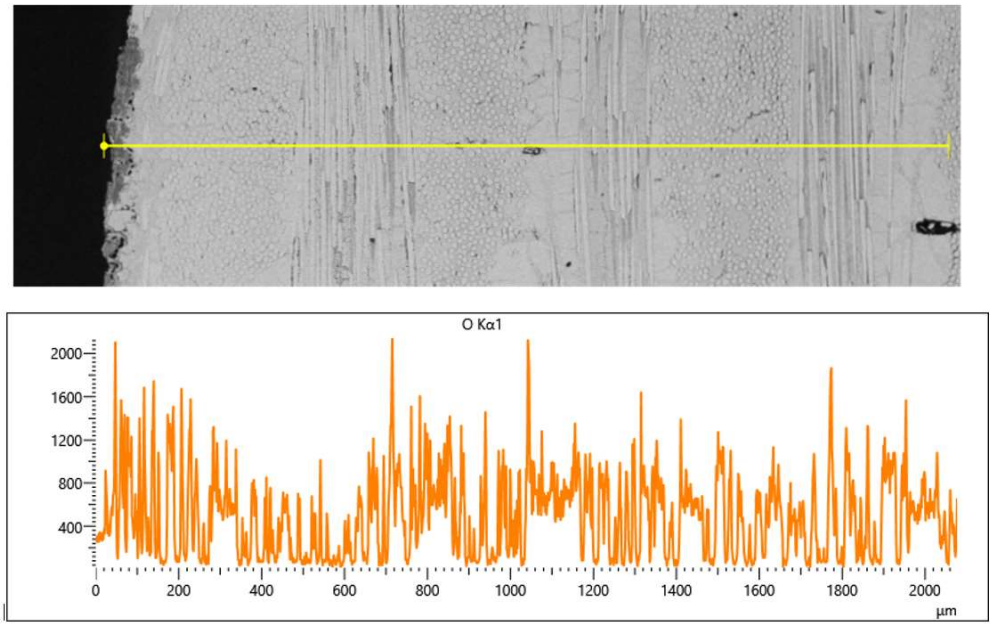

Figure 85 Line scans of S200H material

The SEM analysis revealed that the coating on the fibers of the S200H composite underwent partial degradation, oxidation, and detachment due to exposure to high temperature, a corrosive environment, and the mechanical stresses experienced during aircraft engine operation. Fibers situated near the surface exposed to the corrosive environment - regardless of their orientation, whether longitudinal or transverse - exhibited clear signs of partial degradation. In several instances, the fibers were visibly pulled out from the matrix, as illustrated in Figure 86 a and b. The protective coating originally present on the fibers has been extensively damaged and is no longer discernible in many regions. This loss of coating integrity has left the fibers vulnerable to environmental attack. Furthermore, detailed SEM observations revealed distinct signs of fiber degradation, including surface cracking and mechanical detachment. These features suggest that the combined effects of high temperature, oxidative atmosphere, and mechanical stresses contributed significantly to the deterioration of the fiber-matrix interface and the structural integrity of the fibers themselves.

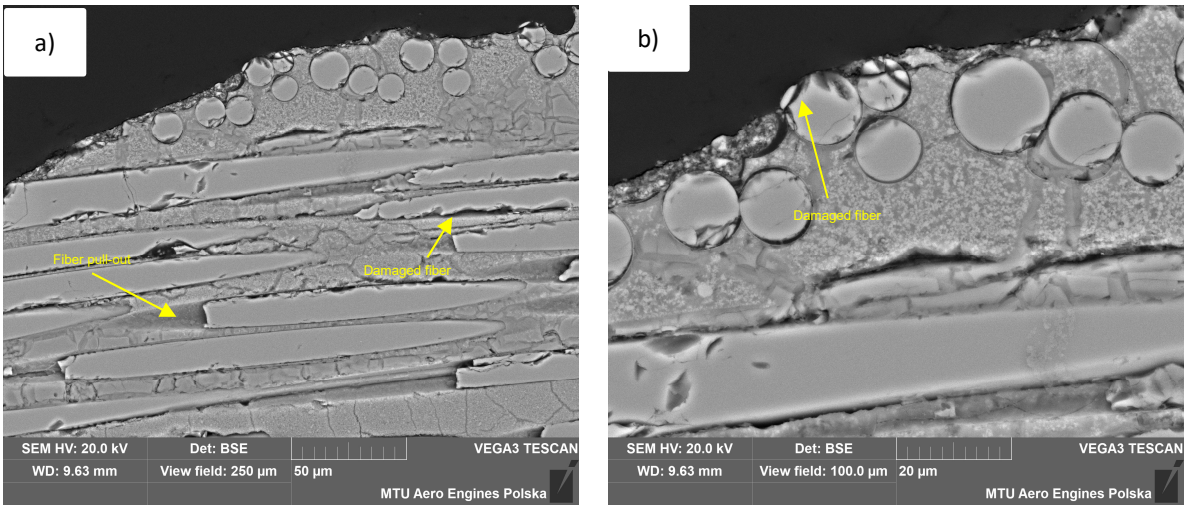

Figure 86 a) longitudinal and b) transverse fibers of the S200H material tested at aircraft engine environment

Fibers which were located deeper into the material appear to be fractured in some images, however, this is most likely a result of sample preparation rather than actual fiber damage (Figure 87). To verify this, linear measurements were performed on fibers oriented both transversely and longitudinally within the material. The results showed that the fibers themselves did not undergo significant oxidation and retained their structural integrity. The highest oxygen concentrations were observed in the fiber coatings, matrix and in areas where the coating had been stripped away (Figure 88 a and b).

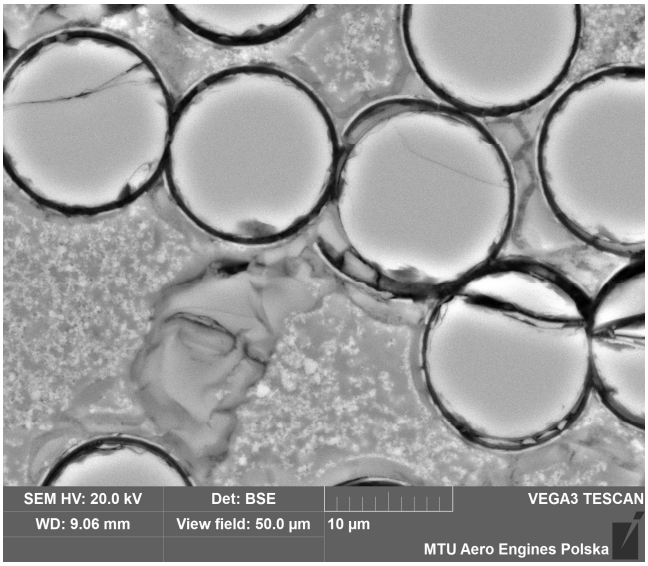

Figure 87 SiC fibers located deep in the sample

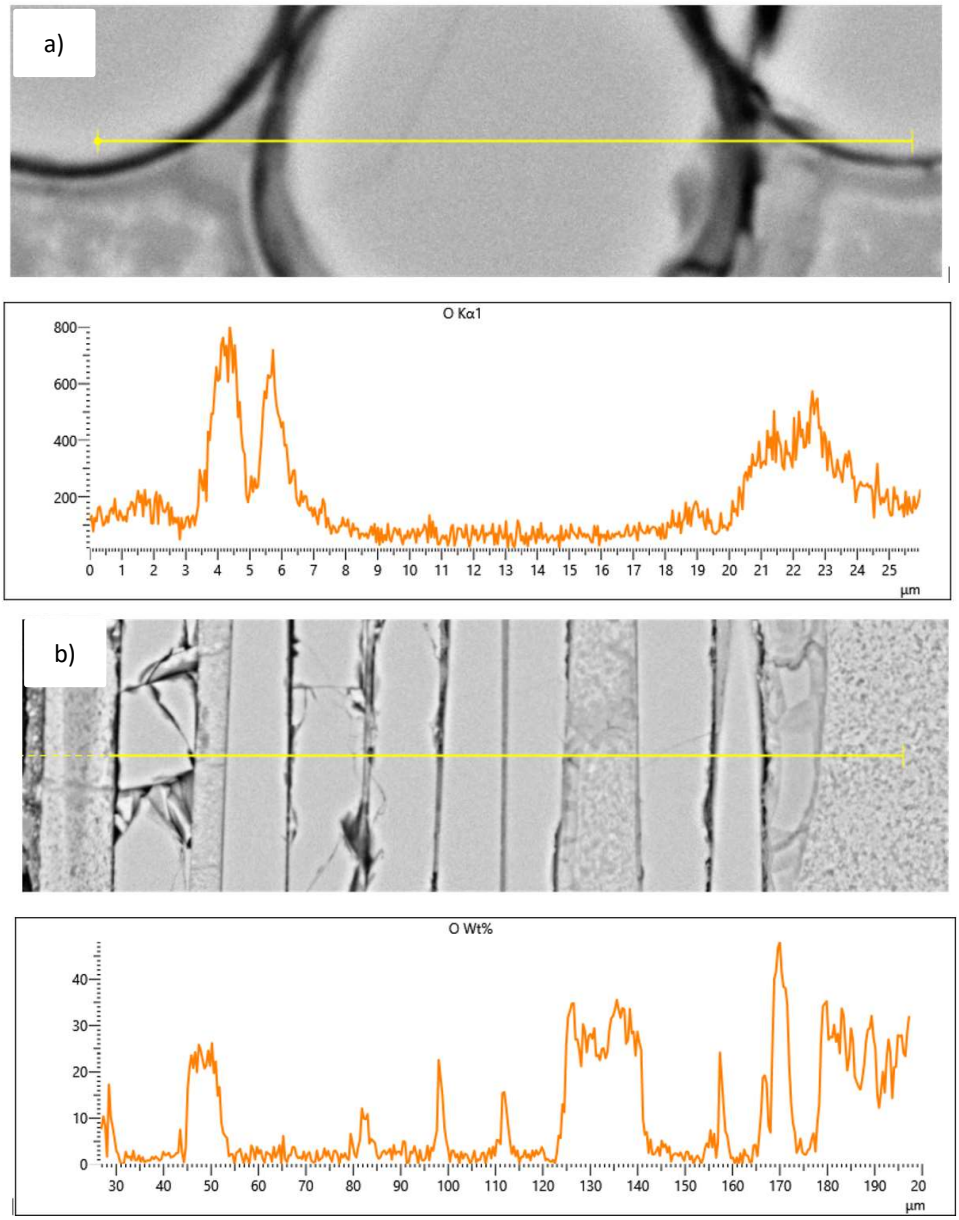

Figure 88 Line scan patterns of a) transverse and b) longitudinal fibers of the S200H material tested at aircraft engine environment

The samples were exposed to a temperature of 890 °C for 200 hours under conditions simulating both the mechanical stresses and the corrosive environment typical of aircraft engine operation. When comparing the microstructure of this material to that of the same composite subjected solely to oxidation at 980 °C for durations ranging from 20 to 100 hours, several significant differences can be observed.

Firstly, oxidation at the higher temperature of 980 °C led to the formation of open cracks in the SiNC matrix in certain areas - cracks that were not observed in the sample tested under simu-

lated engine conditions. Despite the longer exposure time and the additional influence of mechanical loading and a corrosive atmosphere, the sample tested at 890 °C did not exhibit such cracking. This supports the conclusion drawn from previous oxidation and creep studies that matrix degradation in this composite is primarily driven by temperature rather than time or stress. Consequently, increasing the operating temperature of the S200H material (980 °C to just 100 °C higher) can result in the formation of open cracks within the matrix.

Secondly, a thick SiO_2 layer was observed on the surface of the sample tested under engine-simulated conditions, whereas no such layer was detected in the samples oxidized at 980 °C. This difference is most likely due to the longer exposure time to the oxidizing environment (200 hours versus a maximum of 100 hours), which allowed for more extensive silica formation.

Thirdly, and most importantly, significant degradation of the fiber coating and partial degradation of the fibers themselves - particularly near the surface was observed in the sample tested under engine-like conditions. This phenomenon was not present in the samples subjected only to oxidation. These differences are attributed to the engine - simulated conditions. The composite was exposed not only to elevated temperature but also to mechanical stresses, including thermal gradients, vibration, and cyclic loading. These stresses can induce microcracking and strain at the fiber-matrix interface, compromising the integrity of the protective coatings. Such mechanical damage facilitates oxygen ingress and accelerates chemical degradation, even at temperature lower than those used in static oxidation tests. Applied mechanical stresses during the engine-simulated testing, likely accelerated the degradation processes at the fiber-matrix interface and contributed to the observed damage. What is more the atmosphere in engine-simulated testing is typically more chemically aggressive, involving flowing oxidizing gases and potentially reactive species such as moisture and CO_2. In contrast, the oxidation test at 980 °C was conducted in a controlled, static dry air environment. BN and Si_3N_4 coatings are relatively stable in dry air but can degrade in humid or chemically active atmospheres. BN, for instance, oxidizes to B_2O_3, which is volatile and can be removed from the surface under flowing conditions, while Si_3N_4 forms SiO_2, which may spall or become porous under stress. The engine-simulated test involved a longer exposure time (200 hours) compared to the oxidation test (100 hours). Prolonged exposure increases the likelihood of oxygen diffusion through microdefects in the coatings. Additionally, fibers located near the surface are more directly exposed to the environment, making them more susceptible to degradation. This surface accessibility plays a critical role in the extent of coating damage observed.

7 Summary

The increasing demand for high-performance materials in aerospace applications has led to the development and implementation of advanced ceramic matrix composites. Among them, SiC/SiC composites have emerged as promising candidates due to their high mechanical strength and thermal resistance at elevated temperature. This doctoral research investigates the mechanical and thermal resistance of the SiC/SiC (S200H) composite, with a particular focus on its applicability in aircraft engine components manufactured by MTU Aero Engines Polska. Conducted within the framework of an industrial PhD program, the study aims to bridge the gap between academic research and industrial application by developing microstructural evaluation criteria and analytical tools suitable for quality control and certification processes. The research methodology includes a comprehensive literature review, microstructure evaluation using advanced image analysis techniques, high-temperature creep testing, and heat treatment procedures.

Based on the adopted research hypotheses regarding the role of fibers, matrix, temperature, and mechanical stress in the degradation mechanisms of SiC/SiC composites, the following conclusions were formulated:

- Temperature is the dominant factor influencing oxidation behavior and microstructural degradation in SiC/SiC composites. While time contributes to damage, temperature drives the most significant changes.
- At 980 °C, oxidation is minimal, with negligible mass change and limited microstructural damage. The composite retains its integrity, and fiber coatings remain intact.
- At 1100 °C, oxidation becomes more pronounced. A non-uniform SiO_2 layer forms, and cracks in matrix-rich regions facilitate oxygen ingress. Partial degradation of BN/Si_3N_4 fiber coatings is observed.
- At 1300 °C, oxidation is aggressive and penetrative, leading to extensive matrix degradation, thick oxide scale formation, and increased porosity. Fiber coatings break down, exposing SiC fibers to direct oxidation.
- Despite severe oxidation at high temperatures, SiC fibers remain structurally intact, demonstrating the composite's damage tolerance and suitability for high-temperature applications.

- Oxidation kinetics follow a parabolic law, with deviations at 1300 °C. The calculated activation energy of 107 kJ/mol confirms the temperature dependence of the oxidation rate.
- Active oxidation mechanisms dominate at elevated temperatures, causing mass loss due to volatile species (e.g., SiO, CO, N_2), rather than protective oxide scale formation.
- Microstructural features, such as cracks and matrix-rich pockets, act as preferential pathways for oxygen diffusion, accelerating localized degradation.
- Mechanical stress affects degradation, especially at the fiber-matrix interface. Stress-induced damage includes coating delamination and fiber pull-out.
- The greater number of defects observed in the oxidized sample (1100 °C, 100 h) compared to the creep-tested sample (1100 °C, 200 h) can be attributed to differences in sample preparation and geometry. The small, pre - cut oxidation samples were more susceptible to mechanical damage and oxygen ingress. In contrast, the larger, intact creep-tested sample experienced slower and more controlled oxidation, highlighting the significant influence of sample geometry and preparation on degradation mechanisms.
- Exposure to jet engine - like conditions resulted in more severe surface oxidation and fiber coating degradation than static oxidation, even at slightly lower temperatures. This was attributed to reactive species, gas flow, and thermal cycling, which accelerated degradation mechanisms.
- In some regions, internal oxidation penetrated deeply into the matrix, especially where fiber reinforcement was absent. Fiber coatings experienced significant degradation, including oxidation, detachment, and mechanical damage, compromising the protective function of the BN/Si_3N_4 interphase.
- These findings highlight the critical importance of protective coatings and environmental barrier systems for SiC/SiC composites in aerospace applications, where combined thermal, chemical, and mechanical stresses accelerate material degradation.

Bibliography

[1] Washburn, E. W., Ries, H., & Day, A. L. (1920). Report of the committee on the definition of the term ceramics. Journal of the American Ceramic Society, 3(7), 526-542. https://doi.org/10.1111/j.1151-2916.1920.tb17297.x.
[2] Baker, A., Dutton, S., & Kelly, D. (2004). Composite materials for aircraft structures (2nd ed.). AIAA. ISBN: 9781563475405 .
[3] Daniel, I. M., & Ishai, O. (1994). Engineering mechanics of composite materials. Oxford University Press. ISBN: 9780195075069 .
[4] Krenkel, W. (Ed.). (2008). Ceramic matrix composites: Fiber reinforced ceramics and their applications. Wiley-VCH. https://doi.org/10.1002/9783527622412.
[5] Raether, F. (2013). Ceramic matrix composites-An alternative for challenging construction tasks. Ceramic Applications, 1(1), 23-30. .
[6] Zok, F. W. (2006). Ceramic matrix composites. Journal of the American Ceramic Society, 89(11), 3309-3324
[7] Flores, O. R., Bordia, R. K., Nestler, D., Krenkel, W., & Motz, G. (2014). Ceramic fibers based on SiC and SiCN systems: Current research, development, and commercial status. Advanced Engineering Materials, 16(6), 624-630. https://doi.org/10.1002/adem.201400069.
[8] Okamura, K., Shimoo, T., Suzuya, K., & Suzuki, K. (2006). SiC-Based Ceramic Fibers Prepared via Organic-to-Inorganic Conversion Process-A Review. Journal of the Ceramic Society of Japan, 114, 445-450. https://doi.org/10.2109/jcersj.114.445.
[9] Bunsell, A., & Piant, A. (2006). A review of the development of three generations of small diameter silicon carbide fibers. Journal of Materials Science, 41, 823-830. https://doi.org/10.1007/s10853-006-6566-z.
[10] DiCarlo, J. A. (2013). Materials and Structures Division. NASA Glenn Research Center.
[11] Ichikawa, H. (2006). Development of high performance SiC fibers derived from polycarbos-ilane using electron beam irradiation curing-A review. Journal of the Ceramic Society of Japan, 114(1330), 445-450. https://doi.org/10.2109/jcersj.114.455
[12] Ishikawa, T. (2005). Polymeric and inorganic fibers. In J. J. M. Baltussen (Ed.), Polymeric and inorganic fibers (Vol. 178, pp. 109-144). Springer. ISBN: 9783540315711
[13] Takeda, M., Sakamoto, J., Saeki, A., Imai, Y., & Ichikawa, H. (1995). High performance silicon carbide fiber Hi-Nicalon for ceramic matrix composites. Ceramic Engineering and Science Proceedings, 16(4), 37-44. https://doi.org/10.1002/9780470314715.ch3.
[14] Takeda, M., Sakamoto, J., & Ichikawa, H. (1996). Mechanical and structural analysis of silicon carbide fiber Hi-Nicalon Type S. Ceramic Engineering and Science Proceedings, 17(4), 35-42. https://doi.org/10.1002/9780470314876.ch2
[15] Yun, H. M., & DiCarlo, J. A. (2002). Tensile behavior of as-fabricated and burner-rig exposed SiC/SiC composites with Hi-Nicalon Type S fibers. Ceramic Engineering and Science Proceedings, 23(3), 571-578. https://doi.org/10.1002/9780470294741.ch67
[16] Ichikawa, H. (2007). High performance SiC fibers from polycarbosilane for high temperature applications. Key Engineering Materials, 352, 59-64. https://doi.org/10.4028/www.scientific.net/KEM.352.59.
[17] Cannon, R. M., Rhodes, W. H., & Heuer, A. H. (1979). Plastic deformation of fine-grained alumina: I, interface-controlled diffusional creep. Journal of the American Ceramic Society, 63(1-2), 46-53. https://doi.org/10.1111/j.1151-2916.1980.tb10648.x
[18] DiCarlo, J. A. (n.d.). SiC fiber creep and rupture models for understanding CMC behavior above 1400 °C. NASA Technical Memorandum.
[19] Morscher, G. N., & DiCarlo, J. A. (1992). A simple test for thermo-mechanical evaluation of ceramic fibers. Journal of the American Ceramic Society, 75(1), 136-140. https://doi.org/10.1111/j.1151-2916.1992.tb05455.x

[20] Pezzotti, G., Kleebe, H. J., Nishimura, H., & Ota, K. (2001). Grain-boundary viscosity of preoxidized and nitrogen-annealed silicon carbides. Journal of the American Ceramic Society, 84(10), 2371-2376. https://doi.org/10.1111/j.1151-2916.2001.tb01017.x
[21] Ishikawa, T. (2005). Advances in inorganic fibers. Advances in Polymer Science, 178, 109-144. ISBN : 3540240160 (hbk.)
[22] Sacks, M. D., Toreki, W., Batish, C. D., & Choi, G. J. (1998). Preparation of boron-doped silicon carbide SiC fibers. U.S. Patent No. 5,851,942.
[23] Lipowitz, J., Rabe, J. A., Zangvil, A., & Xu, Y. (1997). Structure and properties of Sylramic™ silicon carbide fiber-A polycrystalline, stoichiometric β-SiC composition. Ceramic Engineering and Science Proceedings, 18(3), 147-157. https://doi.org/10.1002/9780470294437.ch16
[24] Lipowitz, J., & Rabe, J. A. (1994). Preparation of polycrystalline ceramic fibers. U.S. Patent No. 5,279,780.
[25] Ishikawa, T. (2019). Ceramic fibers and their applications. Jenny Stanford Publishing. https://doi.org/10.1201/9780429341885.
[26] DiCarlo, J. A., Yun, H. M., Morscher, G. N., & Bhatt, R. T. (2005). SiC/SiC composites for 1200 °C and above. In N. Bansal (Ed.), Handbook of ceramic composites (pp. 77–98). Kluwer Academic Publishers. https://doi.org/10.1007/0-387-23986-3_4
[27] Yun, H. M., Wheeler, D., Chen, Y., & DiCarlo, J. A. (2005). Thermo-mechanical properties of Super Sylramic SiC fibers. Ceramic Engineering and Science Proceedings, 26(2), 59–65.
[28] Bhatt, R. T., Sola, F., Evans, L. J., Rogers, R. B., & Johnson, D. F. (2021). Microstructural, strength, and creep characterization of Sylramic™, Sylramic™-iBN and Super Sylramic™-iBN SiC fibers. NASA Technical Report.
[29] Dong, S. M., Chollon, G., Labrugère, C., Lahaye, M., Guette, A., Bruneel, J. L., Couzi, M., & Naslain, R. (2001). Characterization of nearly stoichiometric SiC ceramic fibers. Journal of Materials Science, 36, 2371–2381. https://doi.org/10.1023/A:1017988827616
[30] Pujar, V. V., & Morscher, G. N. (2007). Tensile creep behavior of melt-infiltrated SiC composites for gas turbine engine applications. ASME Turbo Expo 2007, Paper GT2007-27491. https://doi.org/10.1115/GT2007-27491
[31] Morscher, G. N., & Pujar, V. (2006). Creep and stress-strain behavior after creep for SiC fiber-reinforced melt-infiltrated SiC matrix composites. Journal of the American Ceramic Society, 89(5), 1652–1658. https://doi.org/10.1111/j.1551-2916.2006.00939.x
[32] Dunn, D. (2010). The effect of fiber volume fraction in HiPerComp SiC-SiC composites (Doctoral dissertation, Alfred University, NY).
[33] Yun, H. M., DiCarlo, J. A., & Bhatt, R. T. (2005). Advanced SiC/SiC ceramic composites for air-breathing and rocket propulsion engine components. JANNAF Conference Proceedings, Charleston, SC.
[34] Lee, K. N. (2014). Environmental barrier coatings for SiCf/SiC. In N. P. Bansal & J. Lamon (Eds.), Ceramic Matrix Composites (pp. 430–451). John Wiley & Sons. https://doi.org/10.1002/9781118832998.ch15
[35] Luthra, K. L., & Corman, G. S. (2006). Melt infiltrated (MI) SiC/SiC composites for gas turbine applications. In W. Krenkel, R. Naslain, & H. Schneider (Eds.), High Temperature Ceramic Matrix Composites (pp. 744–753). Wiley-VCH. https://doi.org/10.1002/3527605622.ch113
[36] Corman, G., Upadhyay, R., Sinha, S., Sweeney, S., Wang, S., Biller, S., & Luthra, K. (2016). Selected applications of ceramics and composite materials. In L. D. Madsen & E. B. Svedberg (Eds.), Materials Research for Manufacturing (pp. 59–91). Springer.
[37] Naslain, R. (2003). Design, preparation and properties of non-oxide CMCs for application in engines and nuclear reactors: An overview. Elsevier. https://doi.org/10.1016/S0266-3538(03)00230-6
[38] DiCarlo, J. A., Yun, H. M., Morscher, G. N., & Bhatt, R. T. (2005). SiC/SiC composites for 1200 °C and above. In N. Bansal (Ed.), Handbook of ceramic composites (pp. 77–98). Kluwer Academic Publishers. https://doi.org/10.1007/0-387-23986-3_4
[39] Knauf, M. W. (2010). Fatigue behaviour of a SiC/SiC composite at 1000 °C in air and in steam (Master's thesis). Air Force Institute of Technology.
[40] Karadimas, G., & Salonitis, K. (2023). Ceramic matrix composites for aero engine applications-A review. Applied Sciences, 13(5), 3017. https://doi.org/10.3390/app13053017

[41] Morscher, G. (2014). Stress-environmental effects on fiber-reinforced SiC-based composites. In Ceramic Matrix Composites: Materials, Modeling and Technology. https://doi.org/10.1002/9781118832998.ch11
[42] Nasiri, N. A., et al. (2016). Oxidation behavior of SiC/SiC ceramic matrix composites in air. Journal of the European Ceramic Society, 36, 3293–3302. https://doi.org/10.1016/j.jeurceramsoc.2016.05.051
[43] Morscher, G. N. (1997). Tensile stress rupture of SiCf/SiCm minicomposites with carbon and boron nitride interphase at elevated temperature in air. Journal of the American Ceramic Society, 80(8), 2029–2042
[44] Ogbuji, L. U. J. T. (1998). A passive mode of oxidation degradation in a SiC-SiC composite. Journal of the American Ceramic Society, 81(11), 2777–2784.
[45] Jacobson, N. S., Morscher, G. N., Bryant, D. R., & Tressler, R. E. (1999). High-temperature oxidation of boron nitride: II. Boron nitride layers in composites. Journal of the American Ceramic Society, 82(6), 1473–1482.
[46] Morscher, G. N., & Cawley, J. D. (2002). Intermediate temperature strength degradation in SiC/SiC composites. Journal of the European Ceramic Society, 22(14–15), 2777–2788. https://doi.org/10.1016/S0955-2219(02)00144-9
[47] Costello, J., & Tressler, R. (1986). Oxidation kinetics of silicon carbide crystals and ceramics: I, in dry oxygen. Journal of the American Ceramic Society, 69(9), 674–681. https://doi.org/10.1111/j.1151-2916.1986.tb07470.x
[48] Schiroky, G. H. (1987). Oxidation behavior of chemically vapor-deposited silicon carbide. Advanced Ceramic Materials, 2(2), 137-141. https://doi.org/10.1111/j.1551-2916.1987.tb00069.x.
[49] Narushima, T., Goto, T., & Hirai, T. (1989). High-temperature passive oxidation of chemically vapor deposited silicon carbide. Journal of the American Ceramic Society, 72(8), 1386-1390. https://doi.org/10.1111/j.1151-2916.1989.tb07658.x.
[50] Kleykamp, H., Schauer, V., & Skokan, A. (1995). Oxidation behaviour of SiC fibre reinforced SiC. Journal of Nuclear Materials, 227(1-2), 130-137. https://doi.org/10.1016/0022-3115(95)00133-6.
[51] Sheldon, B. W., Sun, E. Y., Nutt, S. R., & Brennan, J. J. (1996). Oxidation of BN-coated SiC fibers in ceramic matrix composites. Journal of the American Ceramic Society, 79(2), 539-543. https://doi.org/10.1111/j.1151-2916.1996.tb08163.x.
[52] Ashby, M. F. (2014). Materials (p. 336). Oxford: Elsevier. ISBN 978-0-08-097773-7 .
[53] Lamon, J. (2019). Review: Creep of fibre-reinforced ceramic matrix composites. International Materials Reviews, 64(1), 1-35. https://doi.org/10.1080/09506608.2018.1564182.
[54] Carrère, P., & Lamon, J. (2003). Creep behavior of a SiC/Si-B-C composite with a self-healing multilayered matrix. Journal of the European Ceramic Society, 23(6), 1105-1114. https://doi.org/10.1016/S0955-2219(02)00273-X.
[55] Wilshire, B., & Bache, M. R. (2007). Creep damage resistance of ceramic-matrix composites. Journal of the European Ceramic Society, 27(16), 4603-4611. https://doi.org/10.1016/j.jeurceramsoc.2007.03.029.
[56] Zhu, S., Mizuno, M., Kagawa, Y., Nagano, Y., & Kaya, H. (1998). Creep and fatigue behavior in an enhanced SiC/SiC composite at high temperature. Journal of the American Ceramic Society, 81(9), 2269-2277. https://doi.org/10.1111/j.1151-2916.1998.tb02621.x.
[57] Chermant, J. L., Boitier, G., Darzens, S., Farizy, G., & Vicens, J. (2002). State of the art of damage-creep in ceramic matrix composites. In Creep and Fracture of Engineering Materials and Structures (pp. 45-60).
58 Chermant, J. L., Boitier, G., Darzens, S., et al. (2002). The creep mechanism of ceramic matrix composites at low temperature and stress, by a material science approach. Journal of the European Ceramic Society, 22, 2443–2460. https://doi.org/10.1016/S0955-2219(02)00103-6
[59] Jones, R. H., & Henager, C. H. Jr. (2005). Subcritical crack growth processes in SiC/SiC ceramic matrix composites. Journal of the European Ceramic Society, 25(10), 1717-1722. https://doi.org/10.1016/j.jeurceramsoc.2004.12.015.

[60] European Committee for Standardization. (2007). Advanced technical ceramics-Mechanical properties of ceramic composites at high temperature under inert atmosphere-Determination of creep behaviour (NF EN 13235). Classification index: B 43-351.
[61] Homes, J. W. (1992). A technique for tensile fatigue and creep testing of fiber-reinforced ceramics. Journal of Composite Materials, 26(7), 916-933. https://doi.org/10.1177/00219983920260060
[62] Morscher, G. N., John, R., Zawada, L., et al. (2011). Creep in vacuum of woven Sylramic-iBN melt-infiltrated composites. Composites Science and Technology, 71(1), 52-59. https://doi.org/10.1016/j.compscitech.2010.10.003
[63] Bodet, R., Bourrat, X., Lamon, J., et al. (1995). Tensile creep behavior of a silicon carbide-based fiber with a low oxygen content. Journal of Materials Science, 30(3), 661-677. https://doi:10.1007/BF00356326.
[64] Bodet, R., Lamon, J., Jia, N., et al. (1996). Microstructure stability and creep behavior of Si-C-O (Nicalon) fibers in carbon monoxide and argon environments. Journal of the American Ceramic Society, 79(10), 2673-2683. https://doi.org/10.1111/j.1151-2916.1993.tb06608.x
[65] Simon, G., & Bunsell, A. R. (1984). Creep behaviour and structural characterization at high temperature of Nicalon SiC fibres. Journal of Materials Science, 19(11), 3658-3670.
[66] Lavaste, V., Besson, J., Berger, M. H., et al. (1995). Elastic and creep properties of alumina-based single fibers. Journal of the American Ceramic Society, 78(11), 3081-3087. https://doi.org/10.1111/j.1151-2916.1995.tb09086.x
[67] Yun, H. M., Goldsby, J. C., & DiCarlo, J. A. (1994). Tensile creep and stress-rupture behavior of polymer-derived SiC fibers. NASA Technical Memorandum 106692.
[68] Sauder, C., & Lamon, J. (2007). The tensile creep behavior of SiC-based fibers with low oxygen content. Journal of the American Ceramic Society, 90(4), 1146-1156. https://doi.org/10.1111/j.1551-2916.2007.01535.x
[69] Yun, H. M., & DiCarlo, J. A. (1996). Time/temperature dependent tensile strength of SiC and Al_2O_3-based fibers. Ceramic Transactions, 74, 17-26.
[70] Chermant, J. L., Boitier, G., Darzens, S., et al. (2002). The creep mechanism of ceramic matrix composites at low temperature and stress, by a material science approach. Journal of the European Ceramic Society, 22, 2443–2460. https://doi.org/10.1016/S0955-2219(02)00103-6
[71] Zhu, S., Mizuno, M., Kagawa, Y., et al. (1999). Creep and fatigue behavior in Hi-Nicalon™-fiber-reinforced silicon carbide composites at high temperature. Journal of the American Ceram-ic Society, 82(1), 117-128. https://doi.org/10.1111/j.1151-2916.1999.tb01731.x.
[72] Zhu, S., Mizuno, M., Nagano, Y., Kagawa, Y., & Kaya, H. (1997). Tensile creep behavior of SiC/SiC composite at elevated temperature. Composites Science and Technology, 57(12), 1629-1637.
[73] Morscher, G. N., & Pujar, V. V. (2006). Creep and stress-strain behavior after creep for SiC fiber-reinforced, melt-infiltrated SiC matrix composites. Journal of the American Ceramic Society, 89(5), 1652-1658. https://doi.org/10.1111/j.1551-2916.2006.00939.x
[74] Pandey, V. (2000). Quasi-static and creep behavior of enhanced C/SiC ceramic matrix compo-sites (Master's thesis). Virginia Polytechnic Institute and State University, Blacksburg, VA.
[75] Ruggles-Wrenn, M. B. (2015). Environmental effects on oxide/oxide composites. In N. P. Bansal & J. Lamon (Eds.), Ceramic matrix composites: Materials, modeling, technology and applications (Chapter 10, pp. 295-333). Wiley.
[76] Wu, X., & Holmes, J. W. (1995). Tensile creep and creep-strain recovery behavior of silicon carbide fiber-calcium aluminosilicate matrix ceramic composites. Journal of the American Ceramic Society, 78(10), 2695-2700.
[77] Zhu, S., Mizuno, M., Kagawa, Y., Cao, J., & Kaya, H. (1998). Creep and fatigue behavior in an enhanced SiC/SiC composite at high temperature. Journal of the American Ceramic Society, 81(9), 2269-2277. https://doi.org/10.1111/j.1151-2916.1998.tb02621.x
[78] . Zhu, S., & Kagawa, Y. (2001). Evaluation of creep behavior in SiC/SiC ceramic matrix composites. Seisan Kenkyu, 53(9), 466-469.
[79] . Lamouroux, F., Steen, M., & Valles, J. L. (1994). Uniaxial tensile and creep behavior of an alumina fiber-reinforced ceramic matrix composite: I. Experimental study. Journal of the European Ceramic Society, 14(6), 529-537. https://doi.org/10.1016/0955-2219(94)90124-4.

[80] . Jia, N., Bodet, R., & Tressler, R. E. (1993). Effects of microstructural instability on the creep behavior of SiC-C-O (Nicalon) fibers in argon. Journal of the American Ceramic Society, 76(12), 3051-3060. https://doi.org/10.1111/j.1151-2916.1993.tb06608.x
[81] Lamouroux, F., Steen, M., & Valles, J. L. (1994). Uniaxial tensile and creep behaviour of an alumina fiber-reinforced ceramic matrix composite: I. Experimental study. Journal of the European Ceramic Society, 14, 529–537. https://doi.org/10.1016/0955-2219(94)90124-4
[82] Chermant, J. L., & Holmes, J. (1995). Elevated temperature creep and cyclic creep behavior of fiber-reinforced ceramics. In High Temperature Ceramic-Matrix Composites I (pp. 95-106). American Ceramic Society. https://doi.org/10.1080/09506608.2018.1564182
[83] DiCarlo, J. A., Yun, H. M., & Hurst, J. B. (2004). Fracture mechanisms for SiC fibers and SiC/SiC composites under stress-rupture conditions at high temperature. Applied Mathematics and Computation, 152(2), 473-481. https://doi.org/10.1016/S0096-3003(03)00570-8
[84] Forio, P., Lavaire, F., & Lamon, J. (2004). Delayed failure at intermediate temperature (600 °C-700 °C) in air in silicon carbide multifilament tows. Journal of the American Ceramic Society, 87(5), 888-893. https://doi.org/10.1111/j.1551-2916.2004.00888.x.
[85] Gauthier, W., & Lamon, J. (2009). Delayed failure of Hi-Nicalon and Hi-Nicalon S multifilament tows and single filaments at intermediate temperature (500-800 °C). Journal of the American Ceramic Society, 92(3), 702-709. https://doi.org/10.1111/j.1551-2916.2009.02924.x
[86] Gauthier, W., Lamon, J., & Pailler, R. (2009). Oxidation of silicon carbide fibers in air at intermediate temperature during static fatigue. Journal of the American Ceramic Society, 92(3), 702-709. https://doi.org/10.1111/j.1551-2916.2009.03180.x
[87] Rugg, K. L., Tressler, R. E., Bakis, C. E., et al. (1999). Creep of SiC/SiC microcomposites. Journal of the European Ceramic Society, 19(14-15), 2285-2296. https://doi.org/10.1016/j.jeurceram-soc.2020.07.012
[88] Boitier, G. (1997). Comportement en fluage et microstructure de composites C/SiC 2,5D [Doctoral dissertation, University of Caen, France]..
[89] Darzens, S. (2000). Fluage en traction sous argon et microstructure de composites SiC/SiBC [Doctoral dissertation, University of Caen, France]
[90] SAE International. (2017). Ceramic matrix composites (Vol. 5 of 6). SAE International.
[91] Descamps, P., Tirlocq, J., & Cambier, F. (n.d.). Ceramic matrix composites: Properties and applications. In F. L. Riley (Ed.), 3rd European Symposium on Engineering Ceramics (pp. 109-125). Springer.
[92] Chen, S., & Zeng, Y. (2021). Static and dynamic oxidation behavior of silicon carbide at high temperature. Journal of Materials Science, 41(11), 5445-5456. https://doi.org/10.1016/j.jeurceram-soc.2021.04.040
[93] Liu, P. S., & Chen, G. F. (2014). Porous materials: Processing and applications. Elsevier.
[94] Sympatec. (n.d.). Particle shape. Retrieved from https://www.sympatec.com/en/particle-measurement/glossary/particle-shape/ .
[95] Hua, Y., Zhang, L., Cheng, L., Li, Z., & Du, J. (2010). Microstructure and mechanical properties of SiCp/SiC and SiCw/SiC composites by CVI. Journal of Materials Science, 45(2), 392-398.
[96] Lu, G. Q., & Xiao, Z. M. (1999). Mechanical properties of porous materials. Journal of Porous Materials, 6(6), 359-368.
[97] Filipuzzi, L., Camus, G., Naslain, R., & Thebault, J. (1994). Oxidation mechanisms and kinetics of 1D-SiC/C/SiC composite materials: 1. An experimental approach. Journal of the American Ceramic Society, 77(2), 459-466. https://doi.org/10.1111/j.1151-2916.1994.tb07015.x
[98] Becher, P. F. (1993). Crack bridging processes in toughened ceramics. In B. R. Lawn & R. F. Cook (Eds.), Toughening mechanisms in quasi-brittle materials (pp. 19-33). Springer.
[99] Aghaeian, S., Sloof, W. G., Mol, J. M. C., & Böttger, A. J. (2022). Initial high-temperature oxidation behavior of Fe-Mn binaries in air: The kinetics and mechanism of oxidation. Oxidation of Metals, 98(1-2), 217-237. https://doi.org/10.1007/s11085-022-10115-5.
[100] Singhal, S. C. (1976). Oxidation kinetics of hot-pressed silicon carbide. Journal of Materials Science, 11(7), 1246-1253.

[101] Smialek, L. S., Robinson, R. C., Opila, E. J., Fox, D. S., & Jacobson, N. S. (1999). SiC and Si_3N_4 recession due to SiO scale volatility under combustion conditions. NASA Technical Report.
[102] Ogbuji, L., & Opila, E. (1995). A comparison of the oxidation kinetics of SiC and Si_3N_4. Journal of the Electrochemical Society, 142(3), 925-930. https://doi.org/10.1002/chin.199529024
[103] Narushima, T., Goto, T., & Hirai, T. (1989). High temperature passive oxidation of chemically vapor deposited silicon carbide. Journal of the American Ceramic Society, 72(8), 1386-1390. https://doi.org/10.1111/j.1151-2916.1989.tb07658.x
[104] Liu, D. (1997). Oxidation of polycrystalline alpha silicon carbide. Ceramics International, 23(5), 425-436. https://doi.org/10.1016/S0272-8842(96)00051-X.
[105] . Fox, D. S., et al. (2004). Paralinear oxidation of silicon nitride in water vapor/oxygen environment. NASA Technical Report.
[106] Dang, X., Zhao, D., Guo, T., Fan, X., Xue, J., Ye, F., Liu, Y., & Cheng, L. (2022). Oxidation behaviors of carbon fiber reinforced multilayer SiC-Si_3N_4 matrix composites. Journal of Advanced Ceramics, 11(2), 354-364. https://doi.org/10.1007/s40145-021-0539-1.
[107] Katoh, Y., et al. (2014). Continuous SiC fiber, CVI SiC matrix composites for nuclear applications: Properties and irradiation effects. Journal of Nuclear Materials, 448(1-3), 448-476. https://doi.org/10.1016/j.jnucmat.2013.06.040
[108] Bernachy-Barbe, F., Gélébart, L., Bornert, M., Crépin, J., & Sauder, C. (2015). Anisotropic damage behavior of SiC/SiC composite tubes: Multiaxial testing and damage characterization. Composites Part A: Applied Science and Manufacturing, 76, 281-288. https://doi.org/10.1016/j.compositesa.2015.04.022
[109] Singh, A., Kumari, J., Debnath, N. K., & Chaturvedi, R. K. (2023). Tribology and surface topographical analysis of in-situ formed BN and Si_3N_4 in SiC-Al_2O_3 ceramic composites. https://doi.org/10.21203/rs.3.rs-3175770/v1
110 Poerchke, D. L., Rossol, M. N., & Zok, F. W. (2016). Intermediate temperature oxidative strength degradation of a SiC/SiC composite with a polymer-derived matrix. Journal of the American Ceramic Society, 99(3), 1004-1013. https://doi.org/10.1111/jace.14741
[111] Chermant, J. L., Boitier, G., Darzens, S., et al. (2002). The creep mechanism of ceramic matrix composites at low temperature and stress, by a material science approach. Journal of the European Ceramic Society, 22(14-15), 2443-2460. https://doi.org/10.1016/S0955-2219(02)00103-6
[112] Zielinska, P., Kloc, A., & Motyka, M. (2025). Influence of the creep on microstructure and mechanical properties of SiC/SiC composite. Archives of Metallurgy and Materials, 70(3), 1479-1486. https://doi.org/10.24425/amm.2025.155497
[113] . Fan, M., et al. (2024). Advances in human-machine cooperation-based aircraft artificial environment assessment and regulation technologies. Energy and Built Environment. https://doi.org/10.1016/j.enbenv.2024.04.005

Abstract

This doctoral dissertation investigates the thermal and mechanical behavior of the S200H composite, with particular emphasis on its applicability in aerospace environments. The research was conducted within the framework of an industrial PhD program in collaboration with MTU Aero Engines Polska, aiming to support the implementation of advanced composite materials in aircraft engine components.

A comprehensive experimental methodology was employed, including light and electron microscopy, thermal analysis, X-ray diffraction, Archimedes density measurements, heat treatment procedures, and mechanical creep testing. The oxidation behavior of the composite was examined at three temperature - 980, 1100, and 1300 °C - each for durations of 20, 40, 80, and 100 hours. Creep tests were performed at 980 and 1100 °C under various stress conditions to evaluate time-dependent deformation and damage mechanisms. To complement the creep experiments, an additional sample was analyzed after exposure to a simulated jet engine environment. This test provided insight into the material's performance under combined thermal, chemical, and mechanical stresses typical of aerospace service conditions. The microstructural analysis revealed advanced oxidation effects, coating degradation, and localized damage mechanisms that were not observed under static laboratory conditions.

The results confirmed that temperature is the dominant factor influencing microstructural degradation, with oxidation effects intensifying significantly at 1300 °C. SiC fibers demonstrated high structural stability across all conditions, while the matrix exhibited susceptibility to oxidation, particularly in fiber-depleted regions. The BN/Si_3N_4 dual-layer fiber coating provided effective protection at temperature around 1000ºC but degraded under prolonged exposure, leading to interfacial weakening.

This study contributes to the understanding of degradation mechanisms in SiC/SiC composites and supports their integration into high-temperature aerospace applications. The findings provide a foundation for the development of microstructural evaluation criteria and protective strategies for ceramic composites operating in chemically aggressive and mechanically demanding environments.

Streszczenie

Niniejsza rozprawa doktorska dotyczy analizy właściwości cieplnych i mechanicznych kompozytu S200H – o osnowie ceramicznej SiC wzmacnianego włóknami SiC (SiC/SiC), w aspekcie jego zastosowania w branży lotniczej. Badania zostały przeprowadzone w ramach programu „Doktorat wdrożeniowy", we współpracy z firmą MTU Aero Engines Polska, a ich celem było wsparcie implementacji technologii zaawansowanych materiałów kompozytowych do produkcji komponentów silników lotniczych.

W pracy przyjęto kompleksową metodologię badawczą, obejmującą mikroskopię świetlną i elektronową, analizę cieplną, dyfraktometrię rentgenowską, pomiary gęstości metodą Archimedesa, obróbkę cieplną oraz próby pełzania. Proces utleniania kompozytu badano w temperaturze 980, 1100 i 1300 °C, dla czasów ekspozycji wynoszących 20, 40, 80 i 100 h. Próby pełzania przeprowadzono w temperaturze 980 i 1100°C, dla różnych wartości naprężeń, w celu określenia żarowytrzymałości materiału oraz scharakteryzowania mechanizmów jego zniszczenia.

Uzupełnieniem badań wytrzymałościowych były próby w środowisku symulującym warunki pracy silnika lotniczego. Uzyskane wyniki umożliwiły ocenę właściwości użytkowych kompozytów SiC/SiC w warunkach złożonego obciążenia cieplnego, mechanicznego i chemicznego, typowych dla eksploatacji w lotnictwie. Na podstawie analizy obrazów mikrostruktury ujawniono zaawansowane efekty utleniania, degradację powłok ochronnych oraz mikrouszkodzenia, które nie obserwowano po badaniach laboratoryjnych w warunkach statycznych.

Analiza otrzymanych rezultatów badań potwierdziła, że temperatura ekspozycji materiału jest głównym czynnikiem wpływającym na degradację jego mikrostruktury, przy czym efekty utleniania znacząco nasilają się powyżej 1300°C. Włókna wzmacniające SiC cechuje duża trwałość w przyjętych warunkach badań, natomiast osnowa jest podatna na utlenianie, szczególnie w obszarach o mniejszej objętości względnej włókien. Dwuwarstwowa powłoka ochronna BN/Si3N4 skutecznie chroni włókna w temperaturze do ok. 1000ºC, choć może ulegać degradacji w przypadku długotrwałej ekspozycji.

Rozprawa doktorska wnosi istotny wkład w zrozumienie mechanizmów degradacji kompozytów SiC/SiC, przybliżając ich zastosowanie w wysokotemperaturowych aplikacjach lotniczych. Uzyskane wyniki stanowią podstawę opracowania kryteriów oceny mikrostruktury materiałów ceramicznych oraz strategii ich ochrony w środowiskach agresywnych chemicznie, w warunkach dużego obciążenia cieplnego i mechanicznego.